Development and Application of a Model for the Cross-Flow Induced by Mixing Vane Spacers in Fuel Assemblies

Zur Erlangung des akademischen Grades

Doktor der Ingenieurwissenschaften

der Fakultät für Maschinenbau

Karlsruher Institut für Technologie (KIT)

genehmigte

Dissertation

von

Dipl.-Ing. Markus Zimmermann

Eidesstattliche Erklärung

Hiermit erkläre ich, dass ich die vorliegende Arbeit selbständig angefertigt und keine anderen als die angegebenen Quellen und Hilfsmittel benutzt, sowie die wörtlich und inhaltlich übernommenen Stellen als solche kenntlich gemacht und die Satzung des Karlsruher Institutes für Technologie (KIT) zur Sicherung guter wissenschaftlicher Praxis in der jeweils gültigen Fassung beachtet habe.

Rückersdorf, 1. März 2015

Dipl.-Ing. Markus Zimmermann

Kurzfassung

In Reaktorbrennelementen werden Gitterabstandhalter mit Mischfähnchen verwendet, durch die der Queraustausch von Masse, Impuls und Energie zwischen den einzelnen Unterkanälen verstärkt wird. Dadurch wird die Temperaturverteilung innerhalb der Stabbündel gleichmäßiger. Für die thermo-hydraulische Auslegung von Brennelementen werden von den Herstellerfirmen Unterkanalanalyseprogramme eingesetzt, welche die Massenstrom- und Temperaturverteilung im Reaktorkern berechnen können. Diese Unterkanalanalyseprogramme berechnen Unterkanal-gemittelte Werte und verwenden empirische Korrelationen, um mikroskopische Effekte, wie z.B. Wandreibung, turbulente Mischung oder den Wärmeübergang, zu berücksichtigen. Experimentelle Untersuchungen deuten auf eine starke drallbehaftete Strömung im Nachlauf eines Mischfähnchengitters hin. In der freien Literatur wurde kein Modell gefunden, das diesen Dralleffekt auf den Queraustausch berücksichtigt.

Es wurden systematische CFD Untersuchungen in einer 5×5 Stabbündelgeometrie durchgeführt, die ein Mischfähnchengitter enthält. Die Strömungsbedingungen decken den einphasigen und zweiphasigen Bereich ab mit Dampfanteilen zwischen $\alpha_g = 0\% - 15\%$. Ein nicht-lineares k-ε Turbulenzmodell mit kubischen Koeffizienten wurde für die Simulation der Stabbündel-typischen Strömungsphänomene, wie z.B. Sekundärströmungen und anisotrope Turbulenz, verwendet. Eine detaillierte Analyse des Impulsgleichgewichts in der Spaltregion zeigt, dass die Drallströmung in den Unterkanälen aufgrund der Mischfähnchen die Querströmung stark beeinflusst. Basierend auf den Ergebnissen der CFD Simulationen wurde ein neues Modell entwickelt, das den auf diese Weise erzwungenen Queraustausch vorhersagen kann. Dieses Modell wurde in das Unterkanalanalyseprogramm COBRA-FLX^TM implementiert, das von AREVA GmbH entwickelt wurde und genutzt wird. Das neue Modell stellt eine signifikante Verbesserung der Vorhersagen des Queraustauschs und der Massenstromverteilung innerhalb eines Stabbündels im Nachlauf eines Mischfähnchengitters dar.

Abstract

Grid spacers with mixing vanes are used in nuclear fuel assemblies to increase the lateral cross-flow between sub-channels that homogenizes the temperature distribution within the fuel rod bundle. For the thermal-hydraulic design of such fuel bundles, sub-channel analysis codes are used to predict the mass and temperature distribution within the reactor core. These analysis codes compute sub-channel averaged values and contain empirical correlations to include the effects of microscopic flow phenomena such as wall friction, turbulent mixing or heat transfer. Experimental investigations show a strong swirling flow in the vicinity of a mixing vane spacer. No model was found in open literature that accounts for the swirling flow effect on the lateral cross-exchange of mass, momentum or energy.

Systematic CFD investigations of the flow in a 5×5 rod bundle geometry containing a single spacer grid with split-type mixing vanes were performed with single-phase and two-phase flow conditions and with void fractions ranging between $\alpha_g = 0\% - 15\%$. A cubic non-linear k-ε turbulence model was used to simulate the typical rod bundle flow effects such as secondary flow and non-isotropic turbulence. A detailed analysis of the forces and flows in the gap showed that mixing vane induced swirling flow in the sub-channels strongly affect the inter-sub-channel cross-flow. A new model was developed based on the CFD simulation results to predict the forced cross-flow between the sub-channels. This model was implemented into the sub-channel analysis code COBRA-FLX$^{\text{TM}}$ that was developed and is used by AREVA GmbH. The new model significantly improves the predictions for the cross-flow and mass flow distribution within the rod bundle in the vicinity of the mixing vane spacer grid.

Contents

List of Figures

List of Tables

Nomenclature

Only the most important symbols that appear several times are explained here. For special symbols see Nomenclature of the respective equations.

Latin symbol	Description	Unit
A	Cross section	$\mathrm{m^2}$
c_p	Specific heat at constant pressure	$\mathrm{kJ/kgK}$
C	Coefficient	-
d	Diameter	m
F	Force	N
$\vec{g}$	Gravity vector	$\mathrm{m^2/s}$
G	Mass flux	$\mathrm{kg/m^2s}$
h	Enthalpy	$\mathrm{J/kg}$
j	Superficial velocity	$\mathrm{m/s}$
k	Turbulent kinetic energy	$\mathrm{m^2/s^2}$
l	Length	m
$\dot{m}$	Axial mass flow	$\mathrm{kg/s}$
$\dot{M}$	Momentum	Pa
n	Number	-
$\vec{n}$	Normal vector	-
p	Rod pitch; perimeter	m
P	Pressure	Pa
Pr	Prandtl number	-
q''	Heat flux	$\mathrm{W/m^2}$
$\dot{q}$	Specific heat	$\mathrm{W/kg}$
r	Radius	m
Re	Reynolds number	-
s	Gap width	m
S	Source term	-
S_{ij}	Strain rate tensor	$\mathrm{m/s}$
Sc	Schmidt number	-
t	Time	s
T	Temperature	K
$\vec{u}$	Velocity vector	$\mathrm{m/s}$
v'	Specific volume	$\mathrm{m^3/kg}$

Latin symbol	Description	Unit
V	Volume	m^3
w	Cross-flow per unit length	kg/ms
x_e	Thermodynamic equilibrium quality	-
x_f	Flow quality	-
x, y, z	Positions in cartesian coordinate system	m
y^+	Dimensionless wall distance	-

Greek symbol	Description	Unit
α	Volume fraction	-
β	Thermal expansion coefficient	1/K
γ	Mixing vane angle	deg
Γ	Circulation	m^2/s
δ	Sub-channel centroid distance	m
δ_{ij}	Kronecker Delta	-
Δ	Difference operator	-
ϵ	Blockage ratio	-
ε	Turbulent dissipation rate	$\mathrm{m}^2/\mathrm{s}^3$
η	Kolmogorov length scale	m
Θ	Lateral momentum mapping function	-
κ	Von Kármán constant	-
λ	Thermal conductivity	W/mK
μ	Viscosity	Pas
ρ	Density	kg/m^3
σ	Surface tension	N/m
σ_D	Standard deviation	-
τ	Stress	Pa
ω	Specific dissipation	1/s
Ω	Vorticity	1/s
Ω_{ij}	Rotation rate tensor	m/s

Subscripts	Description
$[\ ]_{ax}$	Axial direction
$[\ ]_b$	Bubble related
$[\ ]_c$	Continuous phase
$[\ ]_d$	Dispersed phase
$[\ ]_f$	Friction term
$[\ ]_g$	Gas phase
$[\ ]_{grid}$	Grid related
$[\ ]_{hyd}$	Hydraulic diameter
$[\ ]_i$	Sub-channel i
$[\ ]_{ij}$	Interface between sub-channels

Subscripts	Description
$[\ ]_j$	Sub-channel j
$[\ ]_l$	Liquid phase
$[\ ]_{lat}$	Lateral direction
$[\ ]_m$	Mixture
$[\ ]_r$	Relative
$[\ ]_{rod}$	Rod related
$[\ ]_{sat}$	Saturated
$[\ ]_t$	Turbulent
$[\ ]_{tm}$	Turbulent mixing
$[\ ]_{vane}$	Mixing vane related
$[\ ]_{vd}$	Void drift
$[\ ]_w$	Wall related
$[\ ]_x, [\ ]_y, [\ ]_z$	Component in x-direction

Superscripts	Description
$[\ ]^+$	Dimensionless term
$[\ ]'$	Turbulent fluctuation term
$[\ ]^{SP}$	Single-phase
$[\ ]^{TP}$	Two-phase

Abbreviations	Description
BWR	Boiling Water Reactor
CFD	Computational Fluid Dynamics
CHF	Critical Heat Flux
COBRA	Coolant Boiling in Rod Arrays
DES	Detached Eddy Simulation
DNB	Departure from Nucleate Boiling
DNS	Direct Numerical Simulation
EVM	Eddy Viscosity Model
FDM	Finite Difference Method
FVM	Finite Volume Method
LDV	Laser Doppler Velocimetry
LES	Large Eddy Simulation
LWR	Light Water Reactor
PIV	Particle Image Velocimetry
PWR	Pressurized Water Reactor
RANS	Reynolds Averaged Navier Stokes
RSM	Reynolds Stress Model

Acknowledgment

Chapter 1

Introduction

1.1 Motivation

Worldwide growing energy demand The worldwide demand for primary energy will grow within the next decades. This has mainly two reasons: (1) The total population of the earth will grow until 2040 up to over 9 billion people[1] and (2) the energy consumption per capita will rise due to increasing industrialization in emerging countries despite the energy-saving efforts in some industrialized countries. Figure 1.1 shows the outlook of the total primary energy demands until 2040.

ExxonMobil [28]
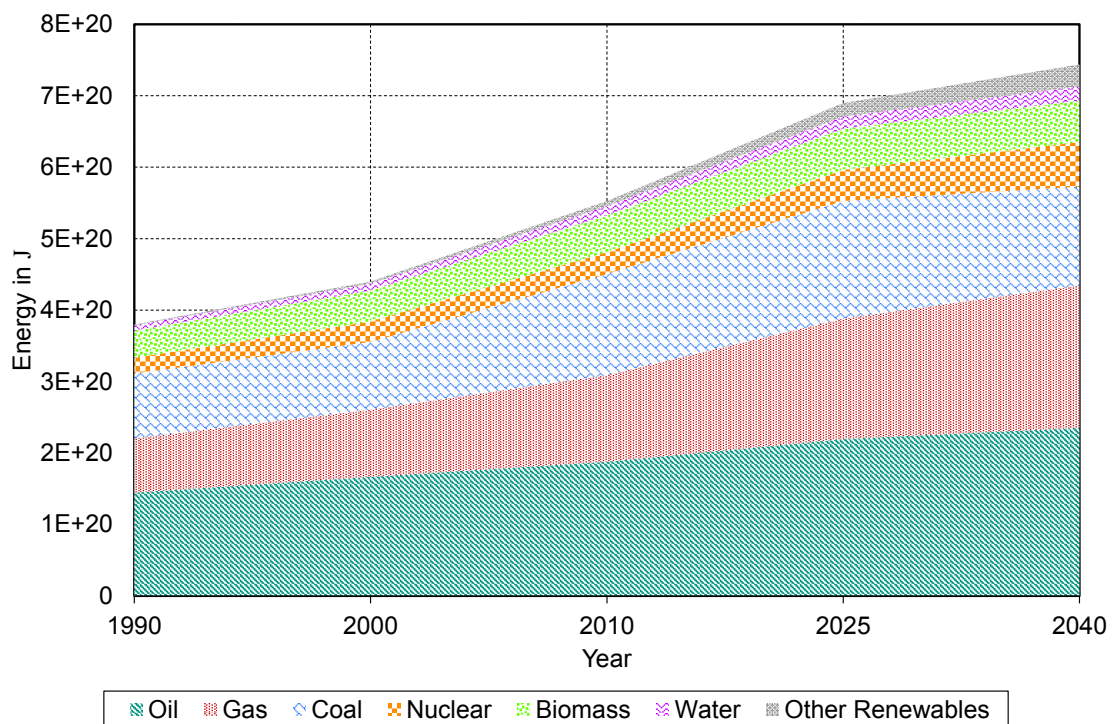
Fig. 1.1: Worldwide primary energy demand - prognosis

---

[1]http://esa.un.org/wpp/unpp/panel_population.htm, 26.03.2014

The major part of primary energy will be gained from fossil fuels such as oil, natural gas or coal. Meanwhile the available reserves of fossil fuels are limited. The strongest increase is expected in the renewable energy sector, namely hydro-power, wind and solar energy or bio mass. Nuclear energy is very controversial but its importance will grow worldwide from a total energy share of 5.55% in 2010 to 8.37% in 2040. Also the reserves of nuclear fuel, such as uranium, are limited. Reserves are all economically and technically extractable resources. Resources are all known or suspected and potentially extractable sources. A simple method to calculate the range of all reserves and resources is to divide the amount of reserves by the amount of the yearly consumption. This method neglects all changes of reserves and consumption, but it is a good first order approximation to show the limitation of fossil fuels. Figure 1.2 shows the range of reserves and resources of uranium, coal, gas and oil based on the data of 2007. Except coal, all reserves will be exhausted in the following 60 years if the discovery of new resources and the growth of reserves fits the growth of energy demands. The energy suppliers are facing therefore following challenges:

1. Secure the energy supply for the growing population

2. Find substitutes for depleting fossil fuels

3. Increase the efficiency of fuel usage, also in nuclear energy

4. Limit the impact on the global climate

Bundesanstalt für Geowissenschaften und Rohstoffe (BGR) [11]
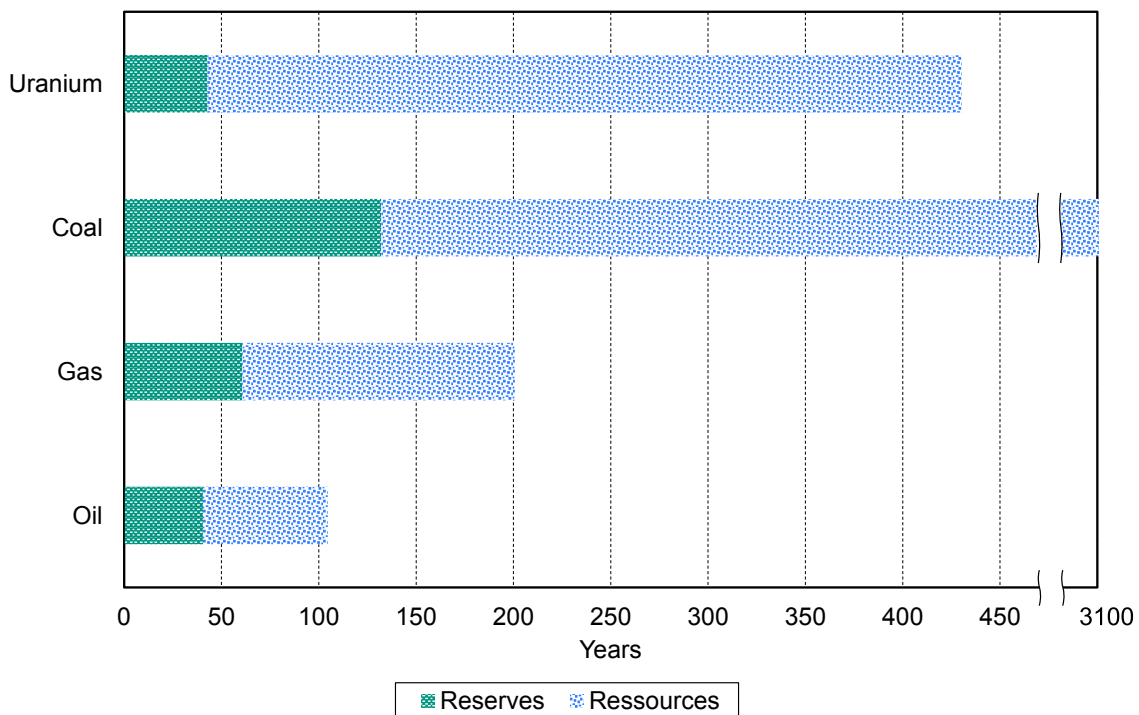
Fig. 1.2: Worldwide range of fuel reserves (as part of resources) and resources, based on data of 2007

The challenge of climate change Due to the usage of fossil fuels, there is an increase of the carbon dioxide (CO_2) concentration in the atmosphere. Compared to the average value in the pre-industrial age before 1750, until 2012 the average atmospheric concentration raised about 40% from $280\,\mathrm{ppm}$ to $392.6\,\mathrm{ppm}$[2]. It is consensus in the majority of the scientific community that this high concentration results in an increase of the average global temperature and an increase of the temperature differences (greenhouse effect). As a result there will be more extreme weather conditions, rising sea-levels and a loss of agricultural areas[3]. Although all relevant effects are not yet completely understood, different scenarios predict an increase of the average surface temperature between $2 - 6\,^\circ\mathrm{C}$ along the 21st century[4]. It is assumed that human activity is the primary driver of this climatic change. Therefore a $2\,^\circ\mathrm{C}$ target was formulated which describes the goal of international climate policy to limit the global warming up to two degrees compared to the level before the begin of industrialization. One of the main tasks to achieve this goal is the reduction of CO_2 emissions due to the replacement of fossil fuels by low-carbon fuels such as renewable energies or nuclear fuels.

Expansion of nuclear energy Nuclear power plants emit less CO_2, have low fuel cost and have a high availability. In the year 2014, there are 437 operating nuclear power plants and 72 are under construction[5]. Furthermore, 174 reactors are planned and 299 are proposed[6], mainly in China, India, Russia and USA. The numbers of new grid connections and new constructions are growing for years, except after the Fukushima accident in 2011, as Fig. 1.3 shows. Some countries, such as Germany, have decided to shut down all their nuclear power plants and to focus on renewable energies. Other countries, such as UAE and Belarus, are currently constructing new nuclear plants and some more countries have plans to construct new reactors. Most likely the worldwide number of plants will increase. At the same time the serious accidents of Three Mile Island in 1979, Chernobyl in 1986 and Fukushima in 2011 show that more research has to be done to increase safety and efficiency and to solve the problem of the final repository of radioactive waste.

Increasing safety and efficiency of nuclear reactors Most of the worldwide operating reactors are Light Water Reactors (LWR) which are divided into two groups: Pressurized Water Reactors (PWR) and Boiling Water Reactors (BWR). The main difference between them is that the steam in a BWR is directly generated in the primary loop and then led to the turbines. In a PWR plant the coolant is always subcooled, and the heat is transferred via a steam generator to a secondary loop which is connected with the turbine. The heat in a nuclear plant is generated due to the fission reaction in the fuel pellets which contain enriched uranium dioxide (UO_2). These pellets are enclosed by a cladding tube, the fuel rod (sketched in Fig. 1.4a) which is about $4\,\mathrm{m}$ long. Usually 14×14 up to 18×18 fuel rods (in a PWR, depending on manufacturer) are assembled into fuel rod bundles (Fig. 1.4b) that are supported by grid spacers.

---

[2]Blasing [9]
[3]http://en.wikipedia.org/wiki/Effects_of_global_warming, 26.03.2014
[4]http://earthobservatory.nasa.gov/Features/GlobalWarming/page5.php, 26.03.2014
[5]http://www.iaea.org/pris, 26.03.2014
[6]http://www.world-nuclear.org/info/Facts-and-Figures/World-Nuclear-Power-Reactors-Archive/Reactor-Archive-August-2014/, 13.10.2014
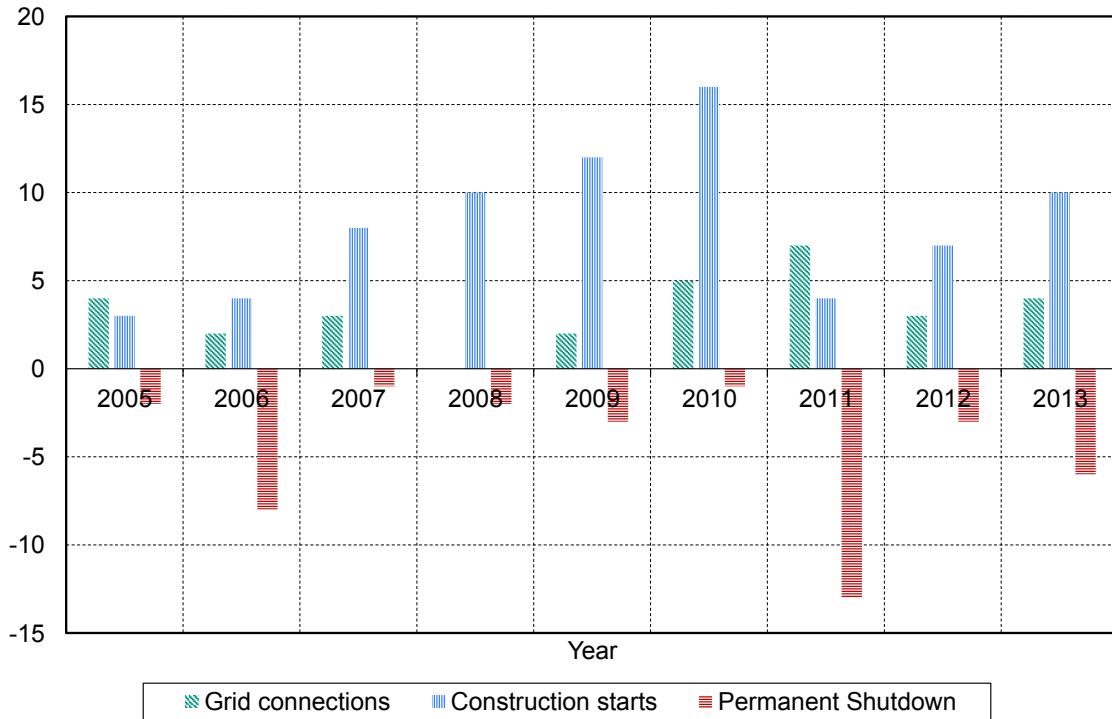
Fig. 1.3: Status changes of nuclear power plants worldwide

The coolant flows in the spaces between the fuel rods that are named sub-channels. In a BWR, there is a bounding box around the single fuel elements, but not in a PWR. The reactor core is composed of a few hundred fuel rod bundles (Fig. 1.4c).

| (a) Fuel rod | (b) Fuel rod bundle with spacers | (c) Reactor core |
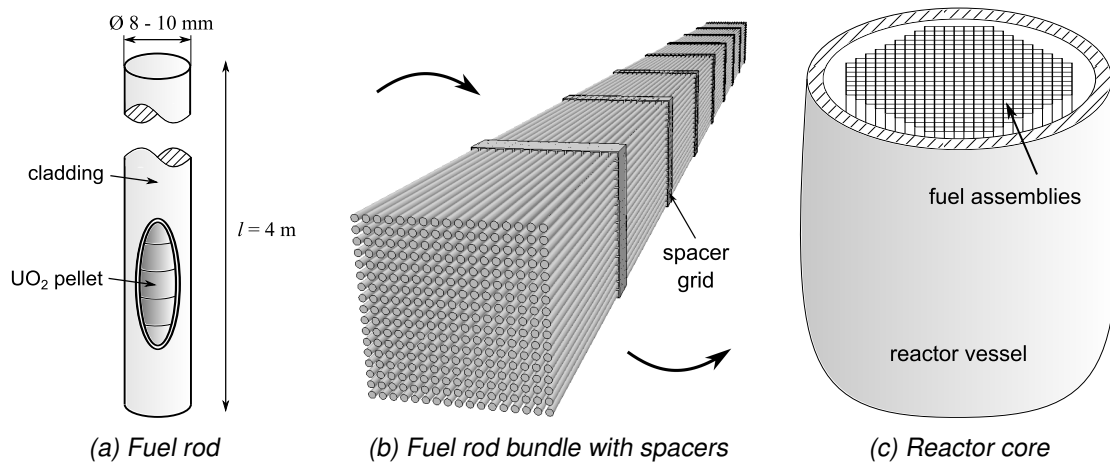
Fig. 1.4: Sketches of assemblies in a Light Water Reactor core

One of the main design criteria for LWR is to avoid boiling crisis. There are two kinds of boiling crisis: the first is called *Departure from Nucleate Boiling (DNB)*. It happens, if the evaporation rate at the fuel rod surface is high enough that a vapor film is generated at the rod surface. The second kind of boiling crisis occurs in an annular flow regime, where a high vapor mass flux is in the core flow and the liquid covers the rod surface. If the liquid film on the heated surface disappears locally, then this is called a *Dry-out*. The heat removal by vapor is much

4

less effective than by liquid. The danger of a boiling crisis is that the heat transfer declines sharply and thereby the heat cannot be dissipated. The cladding of the fuel rods can be destroyed under these circumstances.

Within the reactor core the temperature distribution is not constant. It has the shape of a Bessel function in the radial direction and of a cosine function in the axial direction which is the main flow direction of the coolant. One mechanism that helps to remove the heat from the core center is the inter-sub-channel cross-exchange. Due to lateral transport of mass, momentum and energy the central sub-channels with the highest temperatures can be cooled by the surrounding sub-channels. It is one goal in the nuclear energy research to understand and to improve this cross-exchange.

Advanced design of fuel rod bundles and spacer devices to improve the cross-exchange between sub-channels For the cross-flow enhancement so-called mixing vanes are attached at the downstream edge of grid spacers and their effects are analyzed with experiments and numerical simulation tools, which can calculate the distribution of the coolant flow and the temperature depending on the operating conditions. These tools solve a system of linear equations derived from the Navier-Stokes equations, the continuity condition and the conservation equation for energy. They are called sub-channel analysis codes, because the nodalization of the control volumes is based on the individual sub-channels within a rod bundle that are connected with each other via the gaps. The inter-sub-channel cross-exchange terms serve as sources and sinks in the mass, momentum and energy conservation equation. Effects that take place on smaller length scales, such as turbulent mixing and heat transfer, can not be resolved directly and therefore they must be modeled using empirical correlations. Empirical models are usually obtained from experiments or increasingly from numerical simulations with high-resolution grids. One effect that will be numerically investigated in this work, is the forced cross-exchange and turbulent mixing induced by mixing vanes on grid-spacers under single- and two-phase flow conditions.

1.2 State of the art

1.2.1 Experimental investigations

Flow structure of rod bundle flow

The understanding of flow and temperature distribution in a rod bundle during operation is of great importance for the safety and economical design of nuclear reactors and have been therefore subject of numerous experimental investigations. Rod bundle flow is characterized by a high turbulence level. Turbulence describes the velocity fluctuation over time around a mean value. Turbulence is random, diffusive and dissipative. Reynolds [85] showed that turbulence can be described by a single dimensionless number that is now known as the *Reynolds number Re*. It represents the ratio between inertial forces and viscous forces, see Eq. 1.1. For a two-phase flow, the Reynolds number can be defined using the two-phase mass

flux and a viscosity of the mixture that can be defined as shown in Eq. 1.2. In a round tube the flow is fully turbulent, if the Reynolds number becomes $Re > 4000$. At typical reactor operating conditions, the Reynolds number is between $Re = 400000 \ldots 700000$. These high turbulent conditions are enhancing heat transfer and fluid mixing.

$$Re = \frac{\rho u l}{\mu} \tag{1.1}$$

$$\mu_{2ph} = \frac{u_g}{u} \cdot \mu_g + \frac{u_l}{u} \cdot \mu_l \tag{1.2}$$

Density ρ in $\mathrm{kg/m^3}$, velocity u in $\mathrm{m/s}$, characteristic length l in m, dynamic viscosity μ in Pas

In the past, some additional flow phenomena were discovered that occur in rod bundle flow. Nikuradse [72] discovered secondary flow motions in non-circular channels by evaluating velocity profiles and photographic studies. Secondary flows also occur in sub-channel geometries. Compared to the axial velocity, the secondary flow velocity is very small: $u_{lat}/u_{ax} < 0.5\%$[7] and it grows with p/d-ratio[8]. Secondary flow cells, as shown in Fig. 1.5a, were first quantitatively measured by Vonka [128] with a Laser-Doppler-Velocimetry (LDV) system. Reichardt [83] discovered the non-isotropic behavior of the turbulent fluctuations close to a solid wall. This means that turbulent quantities are different depending on their direction.

The turbulent structure of a rod bundle flow depends on the Reynolds number Re and the pitch-to-diameter-ratio p/d[9]. Levchenko et al. [58] measured a non-uniform distribution of the wall shear stress τ_w around the rod perimeter. τ_w is lower in the gap area and higher in the open channel area. The maximum wall shear stress was found not to be at the symmetry-line what is assumed to be an effect of the secondary flow. Rehme [79] showed the strong anisotropy of turbulence in sub-channel flow. It is increased with decreasing p/d. This was confirmed by other authors[10].

(a) Secondary flow structures   (b) Flow pulsation in narrow gaps
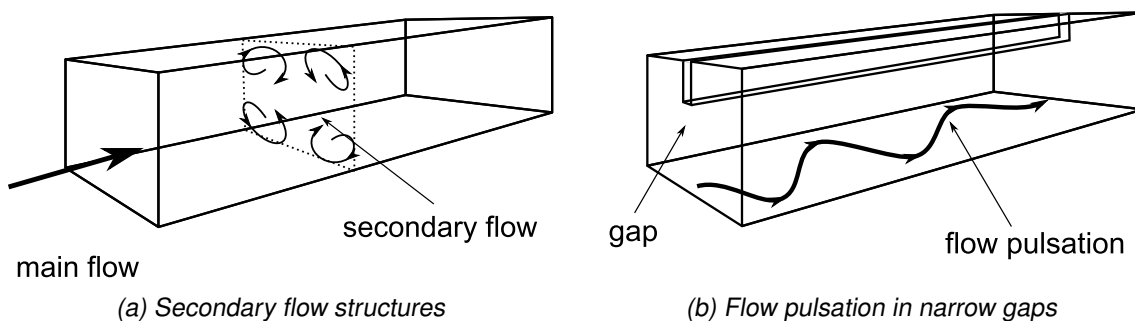
Fig. 1.5: Characteristic flow phenomena in sub-channels of fuel rod bundles

With introduction of the modern LDV measurement techniques Rowe et al. [98] measured velocity profiles of a isothermal water flow in a 3×2.5 rod bundle. A macroscopic flow pulsation in the gap region of the tightly packed rod bundle was observed. Later, Möller [71] measured

---

[7]Trupp and Azad [122]

[8]Carajilescov [14]

[9]Eifler and Nijsing [27]

[10]Hooper [35], Hooper et al. [36], Renksizbulut and Hadaller [84], Krauss [49]

the frequencies of this flow pulsation and showed their dependency on the p/d-ratio. The flow pulsation phenomenon, illustrated in Fig. 1.5b, is made responsible for an increasing of the turbulent mixing rate in tightly-packed rod bundles with $p/d < 1.2$[11]. Table 1.1 lists an overview of some experimental works on turbulent rod bundle flow without spacers.

Tab. 1.1: List of selected experimental investigations in rod bundle geometries without spacers

Reference	Geometry	Fluid	Flow conditions	Data
Eifler and Nijsing [27]	interior sub-channel hexagonal $p/d = 1.025 \ldots 1.15$	water	$Re = 13000 \ldots 54000$	velocity, pressure
Levchenko et al. [58]	interior sub-channel hexagonal $p/d = 1.05 \ldots 1.2$	air	$Re = 34000 \ldots 50000$	velocity, wall shear stress
Rowe et al. [98]	3×2.5 bundle square $p/d = 1.125 \ldots 1.25$	water	$Re = 50000 \ldots 200000$	velocity, turbulence intensity
Trupp and Azad [122]	7-rod bundle hexagonal $p/d = 1.2 \ldots 1.5$	air	$Re = 12000 \ldots 84000$	velocity, Reynolds stress, wall shear stress, friction factor
Carajilescov [14]	interior sub-channel hexagonal $p/d = 1.123$	water	$Re = 7900 \ldots 27000$	velocity, Reynolds stress
Rehme [77, 78, 81, 82]	wall sub-channel $p/d = 1.03 \ldots 1.4$	air	$Re = 59700 \ldots 194000$	velocity, wall shear stress, pressure, Reynolds stress
Hooper [35], Hooper et al. [36]	2×3 bundle $p/d = 1.107 \ldots 1.194$	air	$Re = 22600 \ldots 207600$	velocity, wall shear stress, Reynolds stress
Renksizbulut and Hadaller [84]	6-rod bundle $p/d = 1.15$	water	$Re = 500000$	velocity, wall shear stress, turbulence intensity
Vonka [128]	interior sub-channel hexagonal $p/d = 1.3$	air	$Re = 60000 \ldots 175000$	velocity
Krauss [49]	37-rod bundle hexagonal $p/d = 1.03 \ldots 1.12$	air	$Re = 38000 \ldots 70000$ isothermal and heated	velocity, temperature, wall shear stress, Reynolds stress

---

[11]Meyer [69]

Influence of grid spacers

The position of fuel rods in a rod bundle is supported by grid spacers. Those spacers block the sub-channel flow area partially and induce a large pressure drop that depends on the blockage ratio ϵ (Eq. 1.3)[12]. The developed thermal and hydrodynamic boundary layer is disrupted[13] and the turbulence intensity is increased[14] by the grid spacers.

$$\epsilon = \frac{A_{grid}}{A} \tag{1.3}$$

Projected area in flow direction of the grid A_{grid} in m^2, sub-channel cross section A in m^2

Rowe and Angle [96] found a 25% increased cross-mixing-level in a geometry with wart-type spacers compared to a bare rod bundle, because of the increased turbulence intensity. Rowe and Chapman [97] report that this increase depends on the Reynolds number. From the downstream edge of the grid, turbulence intensity declines rapidly towards a level that is lower than that in fully developed flow. Subsequently the turbulence intensity increases upon the level of fully developed flow. This behavior was confirmed by experiments performed by Caraghiaur [13]. Table 1.2 lists a number of literature references for experimental investigations in rod bundles with grid spacers.

Tab. 1.2: List of selected experimental investigations with grid spacers

Reference	Geometry	Fluid	Flow conditions	Data
Rowe and Chapman [97]	3×2.5 bundle square $p/d = 1.25$	water	$Re = 100000$	velocity, turbulence intensity
Rehme [80]	12-rod bundle diff. spacers $p/d = 1.39$	water	$Re = 4000\ldots70000$	pressure
Herkenrath et al. [32]	4×4 bundle diff. spacers $p/d = 1.3$ (PELCO-S) $p/d = 1.33$ (EUROP)	water	$P = 70\,\text{bar}$ (PELCO-S, EUROP) $P = 160\,\text{bar}$ (EUROP)	enthalpy, pressure
Caraghiaur [13]	24-rod bundle spacer	water	$Re = 10000\ldots50000$	velocity, pressure, turbulence intensity

Influence of mixing vanes on spacers

Spacer grids with mixing vanes are used in commercial nuclear reactors since many years. Their main purpose is to increase the Critical Heat Flux (CHF), which is one of the most im-

---

[12]Rehme [78]
[13]Holloway et al. [34]
[14]Caraghiaur [13]

portant design criteria for water cooled reactors. This type of spacer has a great impact on the coolant distribution within a rod bundle. In addition to the typical spacer grid effects, the mixing vanes significantly increase the cross-flow and, as consequence, the enthalpy mixing[15].

Rosal et al. [90] showed in experiments with a 3×3 and a 4×4 rod bundle at PWR-conditions that the presence of mixing vanes increases the DNB-ratio. The DNB-ratio is defined to be the Critical Heat Flux (CHF) where Departure from Nucleate Boiling (DNB) occurs, divided by the operational heat flux. A high DNB-ratio means therefore a high safety margin. De Crécy [24] showed that the positions of the initial DNB are mostly on the central rod in a 5×5 rod bundle, if no mixing vanes are used. With mixing vanes, this position can be on one of the surrounding rods as well. This indicates a more homogeneous temperature distribution caused by the vanes. In most cases the DNB-ratio was increased and only under special conditions with low mass flow the CHF could be decreased with mixing vanes.

As a result of the investigations a large number of different mixing vane designs was developed during the recent decades. There are "split-type" mixing vanes[16] for the generation of a large inter-sub-channel cross-flow, "swirl-type" mixing vanes[17] for the generation of swirling flow within the sub-channel to increase the heat transfer from the fuel rods and there are other kinds of vanes. Figure 1.6 shows the swirl and split vane geometries. There are many different shapes of mixing vanes and often, the specific geometric configuration of the vanes are proprietary.

(a) Split vane type   *(b) Swirl vane type*
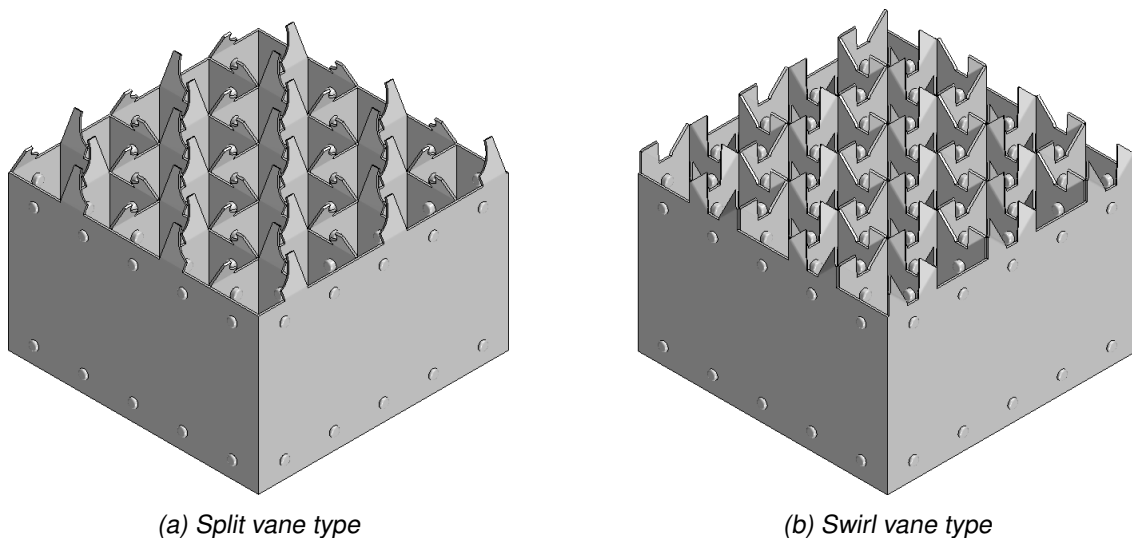
Fig. 1.6: Geometry of different mixing vane spacer types

Shen et al. [110] and later Shin and Chang [111] performed experiments with rod bundle flow to determine the influence of the angle γ of the mixing vane deviation from the axial flow direction. Shen et al. [110] measured the mixing rates of water in a 4×4 rod bundle, whereas Shin and Chang [111] investigated the CHF in a 2×2 rod bundle with R134a. It was noted that there is an optimum angle around $\gamma \approx 30°$ with a maximum of mixing or a maximum increase of CHF. Yang et al. [133] and Yang and Chung [132] could measure detailed axial velocity and

---

[15]Chung et al. [20]
[16]Chang et al. [16], sometimes also called "small scale vortex flow mixing vanes" [56]
[17]sometimes also called "large scale vortex flow mixing vanes" [56]

turbulence distribution with a LDV system in a 5×5 rod bundle with $\gamma = 22°$ mixing vanes in water under environmental conditions. The turbulence behind the grid was found to be more isotropic and with a much higher intensity than before the grid. The region of influence was extended to 20 hydraulic diameters downstream of the spacer grid. McClusky et al. [65] used the *Particle Image Velocimetry* (PIV) method to measure the velocity and vorticity of water flow in a 5×5 rod bundle. It was shown that the mixing vanes induce a strong swirling flow. The core of the vortex was initially centered in a sub-channel and traveled towards a rod surface further downstream. The decay of the angular momentum was compared with a Lamb-Oseen-Vortex. In a later investigation by McClusky et al. [66] with a different grid a different vortical structure was found. Two co-rotating vortices were shed from the mixing vane tips which later merged into one vortex.

Holloway et al. [33] investigated the influence of mixing vane grids on the heat transfer. The same bundle as by McClusky et al. [66] was used, but with 8 different spacer grids. It was found that the spacer grids can increase the heat transfer due to an increase of turbulence intensity. A model that is based on the grid blockage ratio was developed that accounts for the increased heat transfer. Table 1.3 gives an overview over selected experimental works about the flow in rod bundles with mixing vane spacers.

A great challenge for experimental investigators is the reproduction of typical reactor operating conditions with pressures about $P = 165\,\text{bar}$ and heat fluxes about $q'' = 1\,\text{MW/m}^2$. In experimental facilities typically an electrical resistance heating is used. This means high costs and a large technical effort for the electrical insulation. As shown in Tab. 1.3 some authors use different fluids such as the refrigerants R134a or R12. With R134a, only $\approx 10\,\%$ of the heat flux and about $20\,\%$ of the pressure compared to a water loop is necessary to simulate reactor operating conditions. Scaling models are further needed to transfer the results from the model fluid to water. Other authors use environmental conditions with much lower temperatures and pressures. Only few experimental data are available with a rod bundle geometry and reactor operating conditions with water or water / vapor. Another challenge is the measurement of the flow properties. Often, the experimental data are not detailed enough to determine the specific effect of the mixing vanes alone.

1.2.2 Computational investigations

Experimental facilities are less flexible in operating conditions, test section geometry and they are expensive. Due to these reasons and because of an increasing quality of flow modeling and enhanced computational capacity, there is a growing trend to complement experimental investigations by numerical simulations. While the first numerical investigations were limited to small flow domains of only a small part of one sub-channel and poor model quality, Li and Gao [61] were recently able to simulate a full scale 17×17 fuel rod assembly with spacer grids.

The quality and applicability of fluid flow models has increased strongly over the last years. During the 1970s the k-ε turbulence model was developed by Jones and Launder [43] to predict the turbulent quantities and it was used by Seale [109] who performed as one of the first detailed 3D analyses of the turbulence in sub-channel flow. He found that secondary flows do not contribute significantly to the turbulent mixing. The isotropic k-ε model was not able to

Tab. 1.3: List of selected experimental investigations with mixing vane spacers

Reference	Geometry	Fluid	Flow conditions	Data
Rosal et al. [90]	3×3 bundle $d = 12.7\,\mathrm{mm}$ $p/d = 1.316$		$T = 495\ldots 604\,\mathrm{K}$ $P = 103\ldots 165\,\mathrm{bar}$ sinusoidal axial heat flux	CHF
Shen et al. [110]	4×4 bundle $p/d = 1.375$ $\gamma = 0\ldots 35°$	water	$Re = 14200$	velocity
Yang et al. [133], Yang and Chung [132]	5×5 bundle $d = 9.5\,\mathrm{mm}$ $p/d = 1.347$ $\gamma = 22°$	water	$T = 298\ldots 303\,\mathrm{K}$	velocity, pressure, turbulence
De Crécy [24]	5×5 bundle $d = 9.5\,\mathrm{mm}$ $p/d = 1.326$	R12	$P = 81\ldots 172\,\mathrm{bar}$ $G = 980\ldots 5590\,\mathrm{kg/m^2 s}$	CHF
McClusky et al. [65, 66], Holloway et al. [33]	5×5 bundle $d = 9.5\,\mathrm{mm}$ $p/d = 1.326$ div. grids	water	$T = 293\,\mathrm{K}$ $Re = 28000\ldots 42000$	velocity, vorticity, heat transfer, pressure
Shin and Chang [111]	2×2 bundle $d = 9.5\,\mathrm{mm}$ $p/d = 1.332$ $\gamma = 20\ldots 40°$	R134a	$P = 14.67\ldots 25.67\,\mathrm{bar}$ $G = 1000\ldots 1800\,\mathrm{kg/m^2}$	CHF
Chang et al. [16]	5×5 bundle $d = 25.4\,\mathrm{mm}$ $p/d = 1.304$ $\gamma = 30°$	water	$Re = 50250$ $T = 308\,\mathrm{K}$ $P = 1\,\mathrm{bar}$	velocity, turbulence intensity
Rubin et al. [100]	5×5 bundle $d = 9.5\,\mathrm{mm}$ $p/d = 1.326$ $\gamma = 28°$	water	$P = 48\ldots 165\,\mathrm{bar}$ $q'' = 350\ldots 1500\,\mathrm{kW/m^2}$	density, CHF
Dominguez-Ontiveros et al. [25]	5×5 bundle	water	$Re = 2000\ldots 16300$	velocity

reproduce the experimentally measured high mixing rates[18]. To overcome this, Seale [109] proposed the use of anisotropy factors. Due to the insufficiency of the k-ε model in special flow cases, other models have been developed and applied to rod bundle flow simulations. Rapley and Gosman [76] used a simplified algebraic Reynolds stress model to simulate secondary flows. They could outline the importance of secondary flows for the wall shear stress distribution when they compared their predictions to experimental data.

At the beginning of the history of numerical researches the computational domains were lim-

---

[18]Seale [108]

ited to only one sub-channel or the symmetric part of one sub-channel, using periodic boundary conditions. Karoutas et al. [44] used this method to compare numerical predictions with previously produced experimental results in a rod bundle with mixing vane spacers. Using the k-ε turbulence model, he was able to reproduce the swirling flow qualitatively, but the comparison with the experimentally measured axial and lateral velocity profiles showed only a rough consistency. Due to the use of infinitesimal thin surfaces of the grid spacer, there was an inaccurate prediction of the pressure drop, because the flow blockage was ignored.

CFD was used further to find optimized mixing vane configurations. In [38] and In et al. [39] simulated a single sub-channel of one grid span with periodic boundaries. They found a good agreement of the simulation results compared to the experimental data of Karoutas et al. [44] and Yang and Chung [132]. The turbulent kinetic energy in the gap region was found to be under-predicted, because of the isotropic k-ε model. Comparing the swirling flow strength, the cross-flow and the pressure drop, the optimum angle was found to be $\gamma = 35°$. Similar investigations were performed by Cui and Kim [23], Kim and Seo [47] and Lee and Choi [56].

Baglietto et al. [6] proposed a modified non-linear k-ε model with additional quadratic coefficients that is able to predict secondary flow patterns in sub-channel flow. This model was used by Merzari et al. [68] for simulating the flow pulsation in a tightly packed rod bundle with the unsteady Reynolds averaged Navier-Stokes (URANS) approach.

A great challenge is the correct simulation of swirling flow as it occurs behind mixing vane spacers. The standard k-ε model fails in this task. The SST k-ω turbulence model of Menter [67] is recommended by some authors[19] to correctly predict the swirling flow and heat transfer. Detailed experimental data is needed for further investigations. PIV and LDV measurements of the flow structure behind mixing vane grids, as they were performed by Dominguez-Ontiveros et al. [25], Chang et al. [16] and others, can be used to benchmark the CFD results. Detailed experimental data of velocity, turbulence or void fraction distribution in two-phase flow with swirl under high pressure conditions are still less available in the literature. Table 1.4 shows an overview over the development and application of CFD-methods to rod bundle flows.

1.2.3 Modeling of inter-sub-channel cross-exchange

The major interest in sub-channel experiments and simulations is devoted to investigate the pressure losses, the heat transfer and the inter-sub-channel cross-exchange which are very important for the design of reactor cores. Cross-exchange means the travel of mass, momentum and energy from one sub-channel into another via the gap. Rogers and Todreas [88] mention various mixing phenomena in sub-channel flow:

- **Turbulent Mixing**: Due to turbulent fluctuations, there is a lateral movement of fluid particles. The same mass that is transported over the gap is replaced by an equal mass from the adjacent sub-channel, so there is no net mass transfer in single-phase flow.

- **Diversion Cross-flow**: A directed flow into lateral direction evolves from a lateral pressure difference. This pressure difference can be induced by a spacer grid with a different

---

[19]Tseng et al. [123], Ákos Horváth and Dressel [48]

Tab. 1.4: List of selected computational investigations with mixing vane spacers

Reference	Code	Geometry	Flow conditions	Models	Mesh
Karoutas et al. [44]	CFDS-Flow3D	single sub-channel $d = 9.53\,\text{mm}$ $p/d = 1.333$	$Re = 94900$ $P = 4.83\,\text{bar}$ $T = 299.82\,\text{K}$	water Std. k-ε	infinite thin spacer
In [38], In et al. [39]	CFX 4.2	single sub-channel	$Re = 65000$	water Std. k-ε	infinite thin spacers $y^+ = 15\ldots50$
Kim and Seo [47]	CFX 5.6	$d = 9.53\,\text{mm}$ $p/d = 1.333$	$u_b = 6.79\,\text{m/s}$ $q'' = 30\,\text{kW/m}^2$	water Std. k-ε	
Lee and Choi [56]	Fluent	17×17 bundle $d = 10.6\,\text{mm}$ $p/d = 1.373$	$Re = 542000$ $P = 100\,\text{bar}$ $T = 315\,°\text{C}$	water RSM	structured $y^+ = 200$
Alleborn et al. [1]	STAR-CD	$d = 7.7\,\text{mm}$ $l = 0.457\,\text{m}$	$P = 138\,\text{bar}$ $G = 940\ldots2650\,\text{kg/m}^2\text{s}$	two-phase water Kurul-Podowski bulk boiling	
Gandhir and Hassan [30]	Open-FOAM	Geometry used by Dominguez-Ontiveros et al. [25]	$Re = 23000$	water RKE, SST	trimmed hexaeder
Podila et al. [75]	Fluent 14	Geometry used by Chang et al. [16]	$Re = 50250$ $T = 308\,\text{K}$ $P = 1\,\text{bar}$	water RSM, Std. k-ε	hybrid $y^+ = 30$

channel blockage or by different heat fluxes and therefore a different density and void distribution in the sub-channels. The diversion cross-flow can be calculated from a lateral momentum balance. There is a resistance to diversion cross-flow that comes from the lateral pressure loss when the flow travels through the gap.

- **Flow Scattering**: An increase of the turbulent mixing caused by the turbulence enhancement when flow passes through spacer grids or other channel baffles which break up streamlines.

- **Flow Sweeping**: An artificially generated amplification of the convective cross-flow. Flow sweeping can be induced by wire-wrap spacers or by spacer grids with mixing vanes. This effect plays a major role and is used specifically to strengthen the transverse exchanges.

Later, Lahey and Moody [50] postulated the Void Drift phenomena, which occurs only under two-phase flow conditions. It was determined that void tends to travel into regions with a higher mass flux. All phenomena are summarized in Tab. 1.5 and are further discussed afterwards.

Tab. 1.5: Types of rod bundle mixing phenomena

	Natural	Artificial
Not directed	Turbulent Mixing	Flow Scattering
Directed	Diversion Cross-flow Void Drift	Flow Sweeping

Turbulent mixing

Turbulent mixing is described as diffusive transportation process that equalizes gradients of density, velocity or enthalpy. The molecular diffusion is negligible small compared to the turbulent diffusion. This type of cross-exchange always takes place in a turbulent flow, even under steady-state conditions. Due to turbulent mixing, there is a mass flow $\dot{m}_{tm,k}$, a force $F_{tm,k}$ or a heat flux $\dot{Q}_{tm,k}$ in each phase k opposite to the direction of the corresponding gradient and proportional to the exchange Area A_{ij}, see Eq. 1.4 – 1.6. In single-phase flow under isothermal conditions, there is no net transverse mass flow or heat flux, because the density and enthalpy are constant.

$$\dot{m}_{tm,k} = D_t \frac{\partial\,(\alpha_k\rho_k)}{\partial\,y} A_{ij} \tag{1.4}$$

$$F_{tm,k} = \nu_t \frac{\partial\,(\alpha_k\rho_k u_k)}{\partial\,y} A_{ij} \tag{1.5}$$

$$\dot{Q}_{tm,k} = a_t \frac{\partial\,(\alpha_k\rho_k h_k)}{\partial\,y} A_{ij} \tag{1.6}$$

Diffusion coefficients D_t, ν_t and a_t in $\mathrm{m^2/s}$, phase k volume fraction α, phase k density ρ in $\mathrm{kg/m^3}$, phase k velocity u in $\mathrm{m/s}$, phase k enthalpy h in $\mathrm{J/kg}$ and exchange area A_{ij} in $\mathrm{m^2}$

The relation between the different diffusion coefficients for mass and momentum is expressed as turbulent Schmidt number Sc_t (Eq. 1.7) and for energy and momentum as turbulent Prandtl number Pr_t (Eq. 1.8). The functional relations for Sc_t and Pr_t are not completely understood and so they are often treated as constant and close to unity. With these two numbers, only the diffusion coefficient ν_t remains that needs to be modeled. In CFD, ν_t is calculated from the turbulence model. In case of the standard k-ε model it is calculated with Eq. 1.9.

$$Sc_t = \frac{\nu_t}{D_t} \tag{1.7}$$

$$Pr_t = \frac{\nu_t}{a_t} \tag{1.8}$$

$$\nu_t = \frac{\mu_t}{\rho} = C_\mu \frac{k^2}{\varepsilon} \tag{1.9}$$

Diffusion coefficients D_t, ν_t, a_t in m²/s, turbulent viscosity μ_t in Pas, density ρ in kg/m³, turbulent viscosity coefficient $C_\mu = 0.09$, turbulent kinetic energy k in m²/s², turbulent dissipation rate ε in m²/s³

In sub-channel codes, there are no turbulence models and the turbulent mixing is considered by an empirical correlation, where the turbulent diffusion is assumed to be proportional to the average mass flux $\overline{G}$, see Eq. 1.10 that is derived in Rowe and Angle [94]. The lateral turbulent mixing length Δy is not known for sure, but [94] showed that it is proportional to the gap width s. In the past many experiments have been performed to determine the turbulent mixing coefficient C_β[20]. It was found to be a function of gap width s, the Reynolds number Re and the flow regime. Some model proposals that can be found in literature are presented in Tab. 1.6.

$$\nu_t = C_\beta \Delta y \frac{\overline{G}}{\rho_m} \tag{1.10}$$

Turbulent mixing coefficient C_β, lateral mixing length Δy in m, average mass flux of two adjacent channel $\overline{G}$ in kg/m²s, channel average density ρ_m in kg/m³

Tab. 1.6: Different models for the single-phase turbulent mixing coefficient

Reference	Model
Rowe and Angle [94]	$C_\beta^{SP} = 0.0062 \cdot \frac{d_{hyd}}{s} \cdot Re^{-0.1}$
Rogers and Roseheart [87]	$C_\beta^{SP} = \frac{1}{2} \cdot 0.0058 \cdot \left(\frac{s}{d}\right)^{-1.46} \cdot Re^{-0.1} \cdot \left[1 + \left(\frac{d_{hyd,j}}{d_{hyd,i}}\right)^{1.5}\right] \cdot \frac{d_{hyd,i}}{d}$
Sadatomi et al. [102]	$C_\beta^{SP} = 0.00562 \cdot \left(\frac{d_{hyd}}{s}\right) \cdot \frac{Re^{-0.125}}{F_i^*} + 0.0018 \cdot \left(\frac{s}{d}\right)^{-0.52}$

Rowe and Angle [94] investigated the energy transfer between two connected and heated channels under several flow conditions. They found that in single-phase flow the mixing rate is nearly independent from the gap width and only slightly dependent on Reynolds number. In two-phase flow, there is a dependency on gap width, mass flux and steam quality. The mixing rate was usually higher in two-phase flow and only smaller for very high void fractions. They also recognized a flow oscillation, but could not explain this phenomenon. Their proposed turbulent mixing model (Tab. 1.6) is the base for a number of following models, sometimes extended by other authors.

Castellana et al. [15] measured sub-channel exit temperatures to determine the turbulent mixing in a 5×5 rod bundle with flow conditions that are similar to reactor operating conditions.

---

[20]sometimes also referred as Stanton number St

It was found that turbulent mixing is increased with onset of wall boiling and that the mixing rate grows with increasing steam quality. It is believed that the mutual interaction between the continuous phase and the vapor bubbles increase the turbulent fluctuations. Faya et al. [29] considered this effect with a two-phase multiplier Θ^{TP}, according to the model of Beus [8] (Eq. 1.12).

$$C_\beta^{TP} = \Theta^{TP} \cdot C_\beta^{SP} \tag{1.11}$$

$$\Theta^{TP} = \begin{cases} 1 + \frac{\Theta^{TP}(x_e = x_m) - 1}{x_m} \cdot x_e & , x_e < x_m \text{ (bubbly and slug flow regime)} \\ 1 + \left(\Theta^{TP}(x_e = x_m) - 1\right) \cdot \frac{\left(1 - \frac{x_0}{x_m}\right)}{\left(\frac{x_e}{x_m} - \frac{x_0}{x_m}\right)} & , x_e \geq x_m \text{ (annular flow regime)} \end{cases} \tag{1.12}$$

$$\frac{x_0}{x_m} = 0.57 \cdot Re^{0.0417} \tag{1.13}$$

$$x_m = \frac{0.4 \cdot \sqrt{\rho_l \cdot g \cdot d_{hyd} \left(\rho_l - \rho_g\right)} + 0.6 \cdot G}{G \cdot \left(\sqrt{\rho_l / \rho_g} + 0.6\right)} \tag{1.14}$$

Single-phase turbulent mixing coefficient C_β^{SP}, two-phase mixing multiplier Θ^{TP}, steam quality x_e, Reynolds number Re, liquid phase and vapor phase density ρ_l and ρ_g in kg/m³, gravitational acceleration g in m/s², hydraulic diameter d_{hyd} in m, mass flux G in kg/m²s

Beus [8] model consists of two regions: (1) The bubbly-slug flow region with a linear increase of the two-phase multiplier with steam quality x_e until a maximum at the point $x_e = x_m$ and (2) the annular flow region with a hyperbolic decrease of the two-phase multiplier if the steam quality exceeds the maximum point. Figure 1.7 shows the two-phase multiplier development with steam quality. The maximum point is assumed to be at the transition from slug flow to annular flow and is calculated with the correlation from Wallis [130] in Eq. 1.14. Other investigators found this maximum before this transition somewhere in the slug flow region[21].
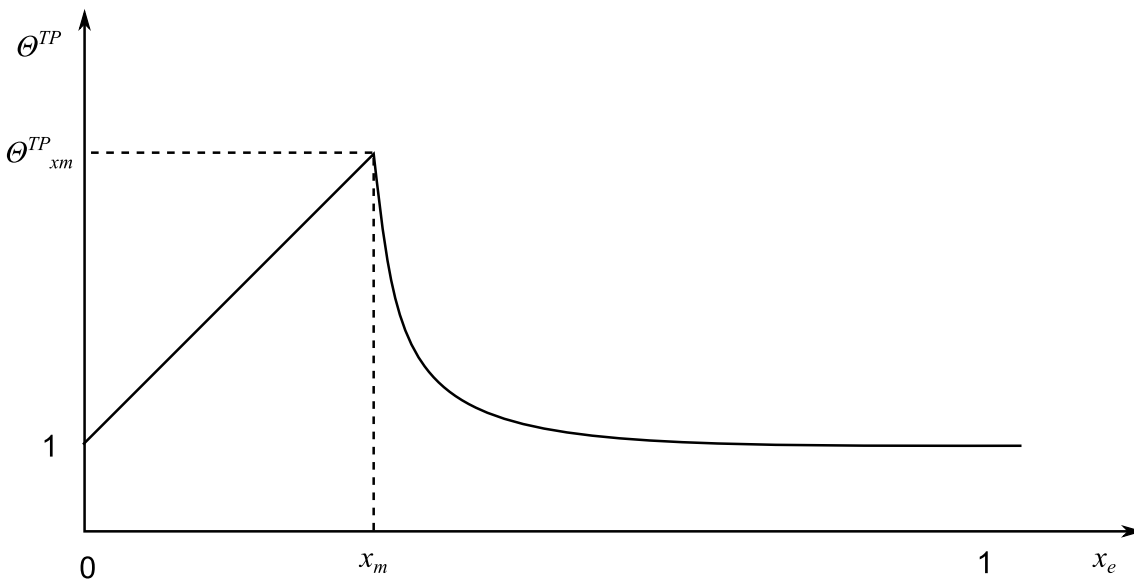
Fig. 1.7: Two-phase multiplier for turbulent mixing coefficient according to Faya et al. [29]

---

[21]Rowe and Angle [96]

Seale [108] showed with rod bundle experiments in air flow and with different gap-widths that the measured mixing rates were higher than they could be explained alone by turbulent diffusion. He also found a slightly decrease of mixing rates with Reynolds number and a strong increase if the gap-width got smaller. He attributed this to the strong anisotropy of the flow.

Kawahara et al. [45] performed detailed measurements of the mixing rates in air-water flow through two rectangular channels at different flow regimes. It was confirmed that turbulent mixing depends strongly on the flow regime. A bubbly flow had similar mixing-rates like a single-phase flow. In the slug flow regime, the mixing rates became 7-times higher than in single-phase flow and in annular flow the mixing rates decreased again towards the level of single-phase flow. Table 1.7 provides an overview over some experimental investigations about turbulent mixing rates.

Void drift

In sub-channel flow under boiling conditions, there is a formation of small vapor bubbles. These bubbles are in the flow field subjected to various forces that strive for an equilibrium state. The bubbles are moved therefore until the equilibrium state is reached. This phenomenon is called void drift.

Van der Ros [124] performed measurements at two connected square-channels with an air-water mixture under environmental conditions. From the results he concluded that the mixing of the vapor fraction behaves like a diffusion process, whereas the liquid phase mixing was dominated by the diversion cross-flow. The cross-mixing of vapor was increased with gap width and heat flux and decreased with liquid velocity.

A large number of experiments was performed by Sadatomi et al. [101] in two connected circular channels and by Sadatomi et al. [104] in a 2×3 rod bundle with air-water flow. The trend was observed that the void fraction is greater in the channels with a greater axial velocity than in channels with a smaller axial velocity. The void drift phenomenon was also observed in rod bundle flow experiments by Herkenrath et al. [32] as well as in different geometries such as eccentric annulus[22]. It was observed that vapor tends to move to regions of higher velocity, away from the wall towards the channel center. Lahey and Moody [50] suggested that void drift is a diffusion process and the driving gradient is the difference between the current and an equilibrium void distribution in two adjacent sub-channels i and j (Eq. 1.15).

$$\dot{m}_{vd,g} = C_\beta^{vd} \frac{\overline{G}}{\rho_m} \rho_g [(\alpha_j - \alpha_i) - (\alpha_j - \alpha_i)_{EQ}] A_{ij} \qquad (1.15)$$

Void drift mixing coefficient C_β^{vd}, average mass flux $\overline{G}$ in kg/m²-s, mixture density ρ_m and gas phase density ρ_g in kg/m³, void fraction α, interface area A_{ij} in m²

Obviously, void drift is not present in single-phase flow. According to Sugawara and Miyamoto [115] the void drift effect plays a role only in the bubbly and slug flow regime when the vapor phase is dispersed. In the 3×3 rod bundle experiments by Lahey et al. [51] and the PELCO-

---

[22]Lahey et al. [52]

Tab. 1.7: Selection of experimental investigations on turbulent mixing

Reference	Geometry	Fluid	Flow conditions	Data
Rowe and Angle [94]	interior sub-channels $p/d = 1.035\ldots 1.149$	water	$Re = 42870\ldots 398160$	enthalpy difference
Roidt et al. [89]	interior sub-channel hexagonal $d = 63.5\,\text{mm}$	air	$Re = 67900$	tracer concentration
Castellana et al. [15]	5×5 bundle $p/d = 1.33$	water	$P = 103\,\text{bar}$ $Re = 90000\ldots 490000$	enthalpy difference
Seale [108]	wall sub-channels $p/d = 1.1\ldots 1.833$	air	$Re = 34400\ldots 300000$	tracer concentration
Sadatomi et al. [102]	two circular channels	water	environmental conditions $Re = 5000\ldots 66000$	tracer concentration
Kawahara et al. [45]	2 square channels	air and water	environmental conditions	tracer concentration
Cheng and Müller [18]	7-rod bundle hexagonal $p/d = 1.147$ grid spacer wire wraps	R12	$P = 1\ldots 30\,\text{bar}$	enthalpy difference
Sadatomi et al. [103]	2×3 bundle $p/d = 1.25$	air and water	environmental conditions	tracer concentration
Kawahara et al. [46]	2 interior sub-channels hexagonal $p/d = 1.083$	air and water	environmental conditions	tracer concentration
Ylönen et al. [134]	5×5 bundle $p/d = 1.36$	water	isothermal $Re = 8800\ldots 46000$	tracer concentration

S 4×4[23] experiments the exit steam quality in the corner sub-channel was much lower than expected by an energy balance. That shows that the void drift mechanism has a great impact on the enthalpy distribution.

Some authors use the same value for the diffusion coefficient for Void Drift and Turbulent Mixing. However, because that are different mechanisms, they can't always be the same. Other authors suggest to use different values [24]. Hence, there are two unknown terms: the equilibrium void fraction distribution $(\alpha_j - \alpha_i)_{EQ}$ and the void drift coefficient C_β^{vd} that have to

---

[23]Herkenrath et al. [32]
[24]Sato [107], Ninokata et al. [73]

be modeled. The common approach for the void drift mixing coefficient is to use the product of a two-phase multiplier function and the single-phase turbulent mixing coefficient.

Levy [59] assumed that the equilibrium void fraction difference is proportional to the mass flux difference (Eq. 1.16). This model doesn't account for geometry. Another model was published by Rowe et al. [99] (Eq. 1.17) which accounts for geometry, but not for mass flow effects.

$$\frac{(\alpha_{g,j} - \alpha_{g,i})_{EQ}}{\overline{\alpha_g}} = C_M \frac{G_j - G_i}{\overline{G}} \tag{1.16}$$

$$\frac{(\alpha_{g,j} - \alpha_{g,i})_{EQ}}{\overline{\alpha_g}} = (1 - \overline{\alpha_g}) \left(\frac{\overline{d}_{hyd}}{d_{hyd,j}} - \frac{\overline{d}_{hyd}}{d_{hyd,i}} \right) \tag{1.17}$$

Proportionality constant $C_M = 1.4$, mass flux G in $^{kg}/_{m^2s}$, void fraction α_g, hydraulic diameter d_{hyd} in m

Hotta et al. [37] developed a model to account for many hydraulic effects, such as surface tension, lift force, wall effects and static pressure gradient. It is based on three fundamental effects that were identified in a large experimental data base including the General Electric 3×3[25], PELCO-S 4×4, EUROP 4×4[26] experiments and the experiments accomplished by Sadatomi et al. [103]. These effects, shown in Eq. 1.18 are:

- **Fluid dynamic effect:** The equilibrium void distribution depends mainly on fluid dynamic properties such as the gradient of mass flow rate, clustering, collision and deformation of bubbles. It depends on fluid properties like surface tension, density or viscosity. It can be expressed as function of the void fraction.

- **Geometrical effect:** Bubble migration is dominated by the surface tension σ and the local turbulent velocity field near solid boundaries. As consequence, their arrangement plays a major role for the equilibrium void distribution.

- **Narrow gap effect:** In bubbly flow, the bubbles tend to flow along the center line of each sub-channel and have a small probability to cross the gap into a neighbor sub-channel.

A different approach for modeling void drift was published by Bellil et al. [7]. He suggested that the local effect of lift force is the physical origin of the void drift effect. He calculated the lateral velocity of the bubble from a force balance accounting for the viscous resistance. The resulting void drift mass flow term is written in equation 1.20 using the relative velocity between the phases defined in equation 1.21 by a correlation from Wallis [130].

---

[25]Lahey et al. [51]
[26]Herkenrath et al. [32]

$$\left[(\alpha_g\rho_g)_i - (\alpha_g\rho_g)_j\right]_{EQ} = (1 - C_{\Omega,ij})\left(\underbrace{C_{p,ij}\frac{G_i^2/\rho_{m,i} - G_j^2/\rho_{m,j}}{G_i^2/\rho_{m,i} + G_j^2/\rho_{m,j}}}_{\text{fluid dynamic effect}} - \underbrace{C_{s,ij}\frac{(\sigma/d_b)_i - (\sigma/d_b)_j}{(\sigma/d_b)_i + (\sigma/d_b)_j}}_{\text{geometrical effect}}\right) \quad (1.18)$$

$$\cdot (\alpha_g\rho_g)_i + \underbrace{\Omega_{ij}\left[(\alpha_g\rho_g)_i - (\alpha_g\rho_g)_j\right]}_{\text{narrow gap effect}}$$

$$C_{\Omega,ij} = 0.5C_{\Omega,0}\left[1 - \tanh\left(\frac{\pi(\alpha_g - \alpha_{tr})}{\alpha_{g,i} - \alpha_{g,j}}\right)\right] \quad (1.19)$$

Mass flux G in kg/m²s, mixture density ρ_m and gas phase density ρ_g in kg/m³, surface tension σ in N/m, bubble diameter d_b in m, void fraction α_g, C_p, C_s and $C_{\Omega,ij}$ are three characteristic parameters that depend on void fraction and channel geometry and have to be identified experimentally

$$\dot{m}_{vd,g} = \rho_g\left(\alpha_i\frac{C_L d_b^2 \rho_l}{18\mu_l}u_r\frac{u_{l,i} - u_{l,j}}{\delta_{ij}}\right)A_{ij} \quad (1.20)$$

$$u_r = 1.53\left(\frac{\rho_l - \rho_g}{\rho_l^2}\sigma g\right)^{0.25} \quad (1.21)$$

Liquid density ρ_l and gas phase density ρ_g in kg/m³, surface tension σ in N/m, void fraction α, lift force coefficient C_L, bubble diameter d_b in m, liquid dynamic viscosity μ_l in Pas, phase-pair relative velocity u_r and liquid velocity u_l in m/s, gravitational acceleration g in m/s², interface area A_{ij} in m², centroid distance between sub-channels δ_{ij} in m

Pang [74] performed a numerical study on the void drift phenomenon to determine a correlation for the void fraction difference at equilibrium state $(\alpha_j - \alpha_i)_{EQ}$ and for the void drift coefficient C_β^{vd}. He also found a close relationship between the lift force and the void drift.

Diversion cross-flow

The diversion cross-flow velocity can be calculated from a lateral momentum balance. Usually, the gravity plays no role, because the lateral flow is orthogonal to the gravity vector. The shear forces within the fluid are small and often neglected. Only the lateral pressure gradient and the forces on the rod surface in lateral direction need to be considered in the force balance. The forces on the rod surface act in the opposite direction of the lateral pressure gradient and can be therefore considered as resistance ΔP_r to cross-flow. The lateral resistance coefficient C_{ij} is defined by Eq. 1.22.

$$\Delta P_r = \frac{1}{2}C_{ij}\rho u_{lat}^2 \quad (1.22)$$

Lateral resistance coefficient C_{ij}, density ρ in kg/m³, lateral velocity u_{lat} in m/s

Tapucu [118] performed measurements of the lateral flow velocity to determine C_{ij}. He used two rectangular, parallel channels that were connected by a lateral slot. In single-phase flow

he noted that C_{ij} is a function of the ratio of lateral velocity and axial donor channel velocity. Not many other experimental investigations about this topic were found in the literature. In sub-channel codes, the lateral resistance coefficient is often assumed to be constant.

Flow scattering

Due to the partial channel blockage by the grid spacer the fluid streamlines are disturbed and hence the turbulence is increased locally. As consequence, both the turbulent mixing rate and the pressure drop are increased. If there is a different channel blockage in adjacent sub-channels and therefore a different pressure drop, this will result in an additional diversion cross-flow that evolves from the induced lateral pressure gradient.

An approach for modeling the spacer effect is suggested by Avramova [5]. It uses multiplier functions $\Theta_{tm,grid}$ and $\Theta_{vd,grid}$ for turbulent mixing and void drift respectively. The multiplier functions depend on the axial position z behind a grid spacer, the blockage ratio ϵ and the mixing vane angle γ. Figure 1.8 shows qualitatively what is expected for the distribution of the multiplier functions, according to experimental data. The magnitude is expected shortly behind the downstream edge of the spacer grid and then it decreases exponentially. The magnitude increases with the angle of the mixing vanes and with the blockage ratio of the spacer grid.

$$C_\beta^{grid} = \Theta_{tm,grid}(z, \gamma, \epsilon) \cdot C_\beta \tag{1.23}$$

$$C_\beta^{sp,vd} = \Theta_{vd,grid}(z, \gamma, \epsilon) \cdot C_\beta^{vd} \tag{1.24}$$

Mixing rate multiplier function for grid spacers $\Theta_{tm,grid}$ and $\Theta_{vd,grid}$, axial position z in m, mixing vane angle γ in deg, spacer blockage ratio ϵ, turbulent mixing coefficient C_β and void drift coefficient C_β^{vd}
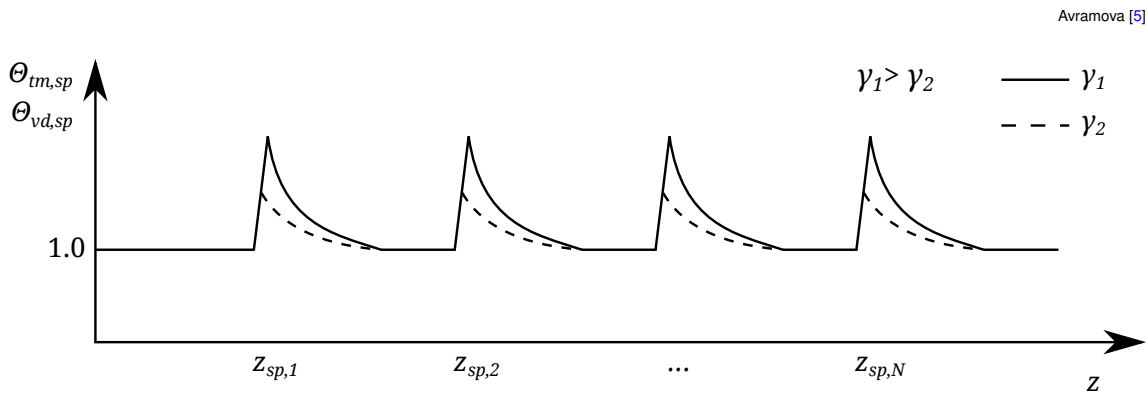
Fig. 1.8: Qualitative trend of locally increased cross-exchange due to spacer grids

Flow sweeping

Flow Sweeping means a convective flow between two connected sub-channels that is induced artificially by geometrical features such as wire wraps or mixing vanes at the downstream edge

of grid spacers. Therefore it is also denoted as forced cross-flow sometimes. Physically it can be distinguished between two effects of mixing vanes:

- Sweeping of a fraction of flow into the adjacent sub-channel due to flow guidance and therefore an introduction of a lateral pressure force on the surface of the mixing vane

- Creation of a swirling flow within the sub-channel that results in a high lateral velocity component in the sub-channel center

Avramova [5] has shown that the diffusive effect (enhanced turbulent mixing) and the convective effect (flow sweeping) of grid spacers with mixing vanes have to be modeled separately. While the diffusive effect is integrated in the spacer grid multiplier function Θ_{sp}, the convective effect requires an additional model. The approach of Avramova [5] is to model the lateral momentum transfer due to mixing vanes with the lateral cross-flow velocity u_{lat} that is gained by means of CFD simulations (Eq. 1.25). It was found that this cross-flow velocity can change its direction depending on the axial position behind the spacer grid. This is due to a movement of the vortex created by the mixing vanes within the channel.

$$\dot{I}_{mv} = C_{grid}^2 u_{ax,i}^2 \rho_{m,i} A_{ij} \tag{1.25}$$

$$C_{grid} = \frac{u_{lat}^{CFD}}{u_{ax}^{CFD}} \tag{1.26}$$

Lateral velocity coefficient from CFD simulations C_{grid}, axial velocity u_{ax} and lateral velocity u_{lat} in $\mathrm{m/s}$, density ρ in $\mathrm{kg/m^3}$, lateral cross-exchange area A_{ij} in $\mathrm{m^2}$

1.2.4 Concluding remarks

The flow in rod bundles has been investigated experimentally for many decades. In recent years, there is a trend to numerical flow simulations. This method provides more detailed results and an easier handling of different geometries or operating conditions, but it is only as good as the models used in those simulations. A comparison of the CFD results with experimental data for validation is therefore essential. In two-phase flow of water-vapor under high pressure conditions less experimental data are available. As consequence, the CFD models used for these conditions are of limited reliability. The following flow phenomena could be discovered experimentally and reproduced by CFD simulations:

- The turbulence is strongly *anisotropic* in rod bundle flow. Special turbulence models have to be used to account for this anisotropy, such as Reynolds stress models or non-linear k-ε models.

- In non-circular channels, there are *secondary flows* that influence the wall shear stress distribution. Secondary flows can be predicted with non-isotropic turbulence models.

- In a tight bundle configuration with $p/d < 1.2$ periodic, large scale *flow pulsations* in the gap area can occur that influence the turbulent mixing.

- Turbulence is a diffusional mixing process. In two-phase flow, there is a strong dependency on the flow regime that is determined from the void fraction.

- Spacer grids increase the *pressure drop* due to channel blockage and increase the turbulent intensity downstream due to flow redistribution. This can enhance the heat transfer.

- Mixing vanes induce a strong *swirling flow* that increases the cross-flow.

- In two-phase flow the void was found to travel towards regions of higher mass flux.

Sub-channel codes contain several empirical correlations to consider those effects. In the literature no correlation was found to consider the swirling flow effect on inter-sub-channel mixing. The empirical models used in sub-channel analysis tools need parameters that depend strongly on the specific geometry and flow conditions and have to be determined experimentally or by means of CFD simulations.

1.3 Aim and structure of this work

This work is aimed to improve the understanding of the Flow Sweeping effect in rod bundle flow with mixing vane spacers. Therefore a detailed investigation of the cross-flow in the vicinity of such spacers by means of CFD simulations both for single and two-phase flow conditions at BWR and PWR pressure level will be performed. The key parameters of geometry and flow conditions that have an impact on the cross-flow development shall be examined and a model will be developed to predict the cross-flow. This model will be applied to a sub-channel analysis code for a validation with experimental data. Furthermore the CFD simulation method is documented in order to derive empirical model coefficients as input parameters for sub-channel codes. This work is concerned with following tasks, depicted in Fig. 1.9:

1. Verification of the CFD simulation model setup by comparison with experimental data

2. Systematical investigation of the influence of split-type mixing vane spacers on the cross-flow and turbulent mixing under single-phase and two-phase flow conditions by means of CFD simulations with the tool STAR-CCM+® 9.02.005

3. Postulate a new model to consider the forced cross-flow in the sub-channel-analysis tool COBRA-FLX™ based on the CFD simulation results

4. Development of a method for determination of model coefficients from CFD results, which can be used as input for COBRA-FLX™

5. Validation of the COBRA-FLX™ predictions including the newly proposed model
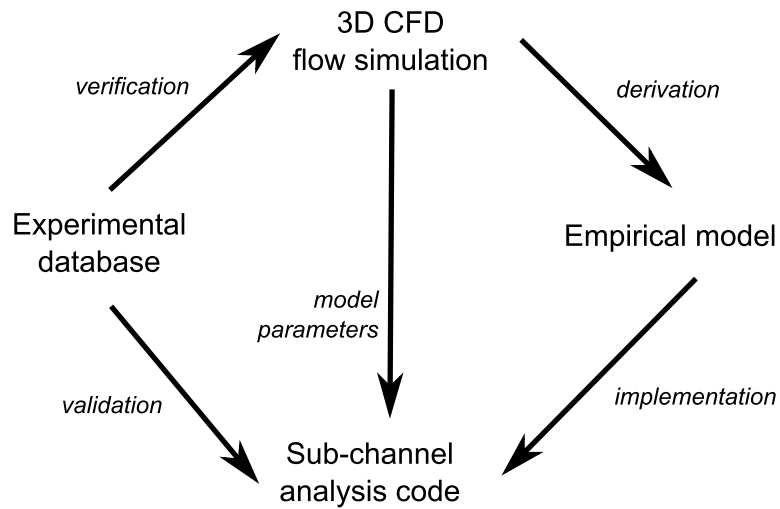
Fig. 1.9: Main tasks of this work

The theoretical backgrounds of the models used in STAR-CCM+® 9.02.005 and in COBRA-FLX^{TM} will be given in chapter 2. In chapter 3 a detailed description of the CFD simulation setup and the simulation results is given. The derivation of the new forced cross-flow model and its implementation into the COBRA-FLX^{TM}source code is discussed in chapter 4. There is also a comparison of the predictions by the new and the previous version with experimental data. Chapter 5 provides a summary and an outlook on work that can be done in the future to enhance the proposed model approach.

Chapter 2

Theoretical backgrounds of fluid flow modeling and simulation

This chapter is dealing with the mathematical formulation of fluid flow. First, a set of equations is presented that describes the coolant flow behavior. Afterwards, the numerical approaches for the solution of this set of equations are shown. Some of these numerical approaches require additional closure equations, which are explained in detail on the example of the simulation programs used in this work.

2.1 Mathematical model of fluid flow

The fluid is assumed to be a continuous Newtonian fluid. In Newtonian fluids the shear stress τ is proportional to the shear rate S_{ij}. The proportionality factor is called the dynamic viscosity μ, see Eq. 2.1. For simplicity an in-compressible fluid is assumed which means mathematically that $\nabla \cdot \vec{u} = 0$.

$$\tau = \mu \cdot S_{ij} \tag{2.1}$$

$$S_{ij} = \left(\frac{\partial u_i}{\partial x_j} + \frac{\partial u_j}{\partial x_i} \right) \tag{2.2}$$

Dynamic viscosity μ in Pas, shear rate S_{ij} in s^{-1}, velocity u in m/s, length x in m

The fluid is considered in a control volume shown in Fig. 2.1. The fluid can pass over the boundaries of the control volume. Its behavior is described in terms of three conservation equations: the conservation of mass, momentum and energy. These equations are based on the 1$^{\text{st}}$ law of thermodynamics and Newtons 2$^{\text{nd}}$ law. They are discussed for single-phase and two-phase conditions in the following sections.
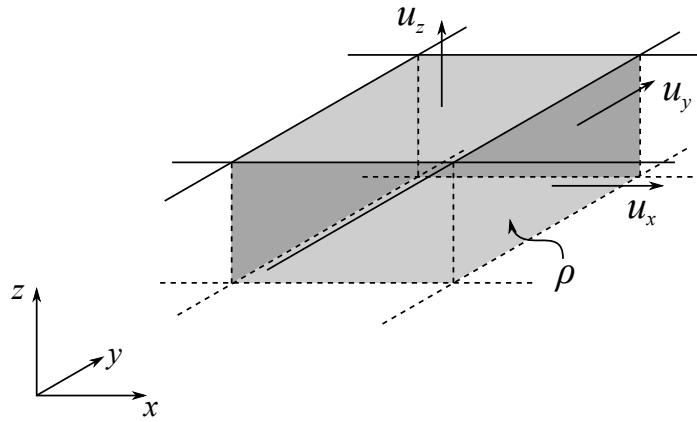
Fig. 2.1: Control volume for conservation equations

2.1.1 Single-phase flow

In single-phase flow, the whole control volume is occupied by only one continuous fluid either completely as liquid or completely as evaporated phase.

Mass conservation equation

The mass conservation equation postulates that the rate of temporal change of mass in a control volume equals the sum of in-coming and out-going mass flows. With the previous mentioned assumptions, the mathematical expression of this law is given for a Cartesian coordinate system in Eq. 2.3 for compressible and in Eq. 2.4 for in-compressible fluids. In the following, only in-compressible fluids will be considered.

$$\frac{\partial \rho}{\partial t} + \frac{\partial \rho \cdot u_x}{\partial x} + \frac{\partial \rho \cdot u_y}{\partial y} + \frac{\partial \rho \cdot u_z}{\partial z} = 0 \tag{2.3}$$

$$\frac{\partial u_x}{\partial x} + \frac{\partial u_y}{\partial y} + \frac{\partial u_z}{\partial z} = \nabla \vec{u} = 0 \tag{2.4}$$

Density ρ in $\mathrm{kg/m^3}$, time t in s, velocity u in $\mathrm{m/s}$, length x, y and z in m

Momentum conservation equation

The momentum conservation equation describes the motion of a Newtonian fluid. For the three directions in space, the equations were formulated by Claude Louis Marie Henri Navier and George Gabriel Stokes and are known therefore as the Navier-Stokes equations. The change of momentum in space and time equals the sum of forces acting on the bounding surfaces of the control volume and on the mass of the control volume. The forces considered are the pressure forces and the shear forces as well as body forces, such as the gravitational force. The formulation of the Navier-Stokes equations in a Cartesian coordinate system is given in Eq. 2.5 – 2.7. The Navier-Stokes equations are non-linear partial differential equations

due to the convective acceleration term. Currently, there is no analytic solution found and these equations have to be solved numerically.

$$\rho \cdot \left(\frac{\partial u_x}{\partial t} + u_x \cdot \frac{\partial u_x}{\partial x} + u_y \cdot \frac{\partial u_x}{\partial y} + u_z \cdot \frac{\partial u_x}{\partial z} \right) = -\frac{\partial P}{\partial x} + \mu \left(\frac{\partial^2 u_x}{\partial x^2} + \frac{\partial^2 u_x}{\partial y^2} + \frac{\partial^2 u_x}{\partial z^2} \right) + F_{V,x} \quad (2.5)$$

$$\rho \cdot \left(\frac{\partial u_y}{\partial t} + u_x \cdot \frac{\partial u_y}{\partial x} + u_y \cdot \frac{\partial u_y}{\partial y} + u_z \cdot \frac{\partial u_y}{\partial z} \right) = -\frac{\partial P}{\partial y} + \mu \left(\frac{\partial^2 u_y}{\partial x^2} + \frac{\partial^2 u_y}{\partial y^2} + \frac{\partial^2 u_y}{\partial z^2} \right) + F_{V,y} \quad (2.6)$$

$$\rho \cdot \left(\frac{\partial u_z}{\partial t} + u_x \cdot \frac{\partial u_z}{\partial x} + u_y \cdot \frac{\partial u_z}{\partial y} + u_z \cdot \frac{\partial u_z}{\partial z} \right) = -\frac{\partial P}{\partial z} + \mu \left(\frac{\partial^2 u_z}{\partial x^2} + \frac{\partial^2 u_z}{\partial y^2} + \frac{\partial^2 u_z}{\partial z^2} \right) + F_{V,z} \quad (2.7)$$

Density ρ in kg/m³, time t in s, velocity u in m/s, pressure P in Pa, dynamic viscosity μ in Pas, volumetric force F_V in N/m³, length x, y and z in m

Energy conservation equation

Equation 2.8 shows the thermal enthalpy conservation equation for laminar flow. The change of thermal enthalpy is caused by the convective mass fluxes over the boundaries of the control volume that carry enthalpy with them. Other sources or sinks are the heat fluxes over solid boundaries, a volumetric heat source $\dot{q}_s$ in the inner volume or viscous dissipation Φ_e. The dissipation function Φ_e in Eq. 2.9 means physically the conversion of friction losses into thermal energy. It contains only quadratic terms which are always positive, so this is an irreversible process.

$$\rho \cdot \left(\frac{\partial h}{\partial t} + u_x \cdot \frac{\partial h}{\partial x} + u_y \cdot \frac{\partial h}{\partial y} + u_z \cdot \frac{\partial h}{\partial z} \right) = \left(\frac{\partial P}{\partial t} + u_x \cdot \frac{\partial P}{\partial x} + u_y \cdot \frac{\partial P}{\partial y} + u_z \cdot \frac{\partial P}{\partial z} \right)$$
$$+ \left[\frac{\partial}{\partial x} \left(\lambda \cdot \frac{\partial T}{\partial x} \right) + \frac{\partial}{\partial y} \left(\lambda \cdot \frac{\partial T}{\partial y} \right) + \frac{\partial}{\partial z} \left(\lambda \cdot \frac{\partial T}{\partial z} \right) \right] \quad (2.8)$$
$$+ \rho \cdot \dot{q}_s + \mu \cdot \Phi_e$$

$$\Phi_e = 2 \cdot \left[\left(\frac{\partial u_x}{\partial x} \right)^2 + \left(\frac{\partial u_y}{\partial y} \right)^2 + \left(\frac{\partial u_z}{\partial z} \right)^2 \right]$$
$$+ \left(\frac{\partial u_y}{\partial x} + \frac{\partial u_x}{\partial y} \right)^2 + \left(\frac{\partial u_z}{\partial y} + \frac{\partial u_y}{\partial z} \right)^2 + \left(\frac{\partial u_x}{\partial z} + \frac{\partial u_z}{\partial x} \right)^2$$
$$- \frac{2}{3} \cdot \left(\frac{\partial u_x}{\partial x} + \frac{\partial u_y}{\partial y} + \frac{\partial u_z}{\partial z} \right)^2$$

$$(2.9)$$

Density ρ in kg/m³, time t in s, velocity u in m/s, enthalpy h in J/kg, pressure P in Pa, dynamic viscosity μ in Pas, temperature T in K, thermal conductivity λ in W/mK, energy source $\dot{q}_s$ in W/kg, length x, y and z in m

2.1.2 Two-phase flow

In two-phase flow, both the liquid (index l) and the gas phase (index g) occupy the control volume at the same time. The description of two-phase flow is more complex than the modeling of single-phase flow. According to the different possible phase distributions which are divided into several flow regimes, there are different modeling approaches. In this subsection, the different flow regimes in vertical two-phase flow are presented and afterwards the corresponding conservation equations.

Flow regimes

The different two-phase flow regimes can be determined using the superficial velocities j_g and j_l (Eq. 2.10 and 2.11) that depend on the void fraction (Eq. 2.12) and the phase velocities. The flow regime transition is very complex and depends on several parameters. In the literature, different transition criteria were defined. Figure 2.2 shows the transition criteria developed by Taitel et al. [117] and Mishima and Ishii [70] for round tubes arranged in a flow regime map. For rod bundle geometries, the transition criteria were defined by Venkateswararao et al. [126]. Figure 2.3 shows the most mentioned flow regimes which are:

- **Bubbly flow:** At low gas volume fraction (= void fraction), the gas phase is dispersed into small bubbles. The bubble shape and bubble size distribution depends on the particular flow condition.

- **Slug flow:** At raised void fractions, large Taylor-bubbles appear that are separated by liquid slugs. Large pressure oscillations can be caused by slug flow.

- **Churn turbulent flow:** After a further increase of void fraction, the slug flow becomes unstable and turns into a turbulent churn flow.

- **Annular flow:** At very high gas flows, the pipe wall is covered by a liquid film, whereas the gas phase is located in the channel center.

- **Droplet flow:** The liquid film is completely evaporated and the remaining liquid phase is dispersed into small droplets.

$$j_g = \alpha_g u_g \tag{2.10}$$

$$j_l = (1 - \alpha_g)u_l \tag{2.11}$$

$$\alpha_g = \frac{V_g}{V_g + V_l} \tag{2.12}$$

Volume occupied by liquid V_l and gas V_g in $\mathrm{m^3}$, liquid and gas velocity u_l and u_g in $\mathrm{m/s}$
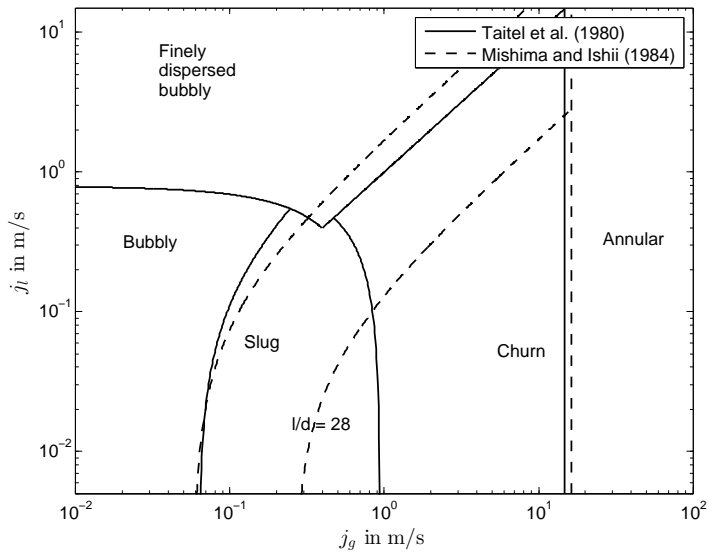
Fig. 2.2: Flow regime map for vertical upward flow in a circular channel
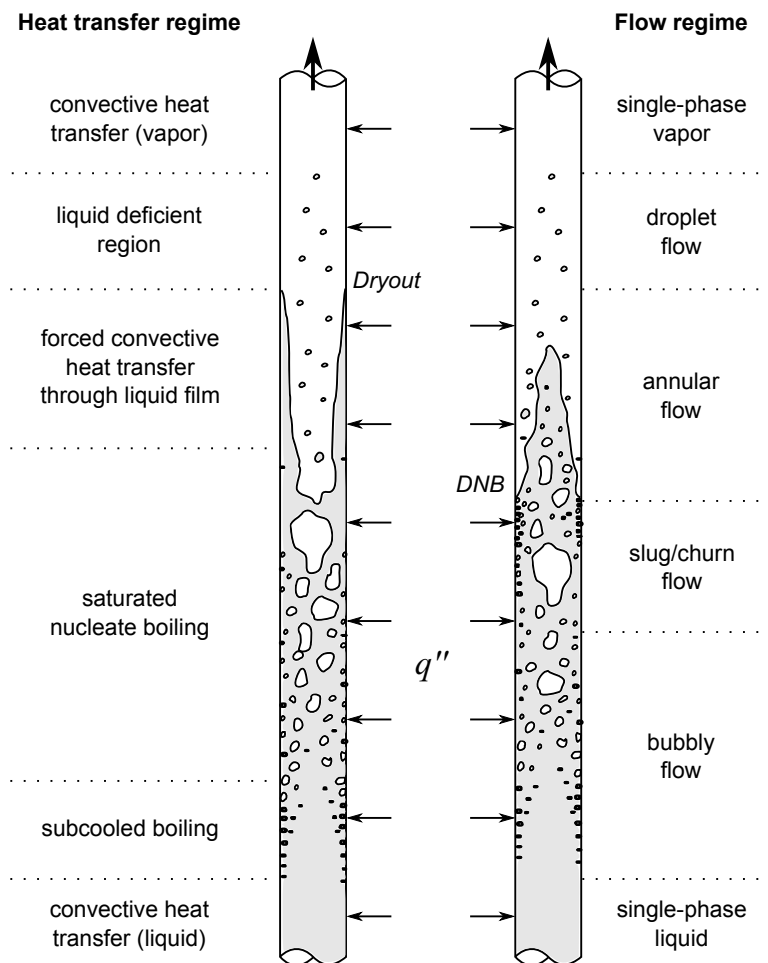
Fig. 2.3: Flow and heat transfer regimes in vertical upward flow in a circular channel

29

Two-fluid model

The two-fluid model is the most general model for the description of two-phase flow. It provides conservation equations for each phase. Both phases share the same pressure field, i.e. $P_g = P_l = P$. The phases can exchange mass, momentum and energy between each other. These exchange terms will occur as source terms in the conservation equations. For the mass conservation equation of both phases they are noted as S_ρ in Eq. 2.13 and 2.14:

$$\frac{\partial}{\partial t}(\alpha_g \rho_g A) + \nabla(\alpha_g \rho_g \vec{u}_g A) = S_{\rho,g} \tag{2.13}$$

$$\frac{\partial}{\partial t}\left[(1 - \alpha_g)\rho_l A\right] + \nabla\left[(1 - \alpha_g)\rho_l \vec{u}_l A\right] = S_{\rho,l} \tag{2.14}$$

Time t in s, void fraction α_g, density ρ in kg/m³, area A in m², velocity vector $\vec{u}$ in m/s, mass flow source term S_ρ in kg/s

In the momentum conservation equations that are written in Eq. 2.15 and 2.16, the momentum transfer due to phase-change is denoted as $S_{\dot{M}}$. Additional shear stress terms occur on the phase interface due to an inter-phase momentum transfer.

$$\frac{\partial}{\partial t}(\alpha_g \rho_g \vec{u}_g A) + \nabla(\alpha_g \rho_g \vec{u}_g \vec{u}_g A) = -\alpha_g \nabla P A - \tau_{w,g} A_{w,g}$$
$$- \tau_{i,l} A_{ij} - \alpha_g \rho_g \vec{g} A + S_{\dot{M},g} \tag{2.15}$$

$$\frac{\partial}{\partial t}\left[(1 - \alpha_g)\rho_l \vec{u}_l A\right] + \nabla\left[(1 - \alpha_g)\rho_l \vec{u}_l \vec{u}_l A\right] = -(1 - \alpha_g)\nabla P A - \tau_{w,l} A_{w,l}$$
$$- \tau_{i,g} A_{ij} - (1 - \alpha_g)\rho_l \vec{g} A + S_{\dot{M},l} \tag{2.16}$$

Time t in s, void fraction α_g, density ρ in kg/m³, area A in m², velocity vector $\vec{u}$ in m/s, pressure P, solid shear stress τ_w and shear stress on phase interface τ_i in Pa, area of solid surface A_w and phase interface area A_{ij} in m², gravity vector $\vec{g}$ in m/s², momentum source term $S_{\dot{M}}$ in N

The energy conservation equation is not further discussed here. Obviously, the separated formulation of the two-fluid model contains more unknown terms than the single-phase model and more unknown terms than available equations. Closure relations are required for those unknown terms that depend on flow regime. The number of unknowns can be decreased if the mixture equations of the two-fluid model is used. Therefore a formulation for the density of the mixture ρ_m and the mass flow of the mixture $\dot{m}_m$ is given in Eq. 2.17 and 2.18.

$$\rho_m = \alpha_g \rho_g + (1 - \alpha_g)\rho_l \tag{2.17}$$

$$\dot{m}_m = \left[\alpha_g \rho_g u_g + (1 - \alpha_g)\rho_l u_l\right] \cdot A \tag{2.18}$$

$$x_f = \frac{\alpha_g \rho_g u_g}{\alpha_g \rho_g u_g + (1 - \alpha_g) \cdot \rho_l u_l} \tag{2.19}$$

Void fraction α_g, density ρ in kg/m³, velocity u in m/s, area A in m²

The mass conservation equation for the two-phase mixture is the sum of Eq. 2.13 and 2.14 with the formulations of the mixture density for mass and the mixture mass flow. Dividing through the flow area A would yield:

$$\frac{\partial}{\partial t}\rho_m + \frac{1}{A}\nabla \dot{m}_m = 0 \tag{2.20}$$

Density ρ in $\mathrm{kg/m^3}$, area A in $\mathrm{m^2}$, mass flow $\dot{m}$ in $\mathrm{kg/s}$

The two-phase mixture formulation of the momentum equation is the sum of the phase momentum equations. The two-phase mixture momentum density (Eq. 2.23) is denoted as specific volume v'. Because of the summation the phase interchange terms disappear. This yields:

$$\frac{\partial \dot{m}_m}{\partial t} + \nabla v' \frac{\dot{m}_m^2}{A} = -\nabla PA - \tau_w A_w - \rho_m \vec{g}A \tag{2.21}$$

$$v' = \frac{1}{\rho_{m,i}} \tag{2.22}$$

$$\rho_{m,i} = \left[\frac{x_f^2}{\alpha_g \rho_g} + \frac{(1-x_f)^2}{(1-\alpha_g)\rho_l} \right]^{-1} \tag{2.23}$$

Time t in s, mass flow of the mixture $\dot{m}_m$ in $\mathrm{kg/s}$, specific volume v' in $\mathrm{m^3/kg}$, area A in $\mathrm{m^2}$, pressure P and wall shear stress τ_w in Pa, gravity $\vec{g}$ in $\mathrm{m/s^2}$, flow quality x_f, void fraction α_g, density ρ in $\mathrm{kg/m^3}$

In the next sections, the general numerical solution methods are discussed and the closure relations of the numerical tools used in this work are presented in particular.

2.2 Numerical solution methods

With the previously mentioned sets of conservation equations the flow behaviour can be simulated within a defined flow domain and with given boundary conditions. According to the desired grade of accuracy and the available computational capacity, different numerical solution methods can be applied that are discussed in this section. Figure 2.4 compares the different solution methods in the dimensions accuracy and efficiency. A high efficiency means here a low computational effort to gain the solution of the flow problem.

2.2.1 Direct Numerical Simulation (DNS)

The DNS is the most exact way of numerical simulation. It works without averaging or model approximations and resolves all motions in the fluid down to the smallest length scales. The results of a DNS simulation are considered as equivalent to experimental results with the advantage of a high spatial and temporal resolution of flow parameters. Only approximation errors, arising from differentiation, exist. The solution domain has to be as large as the largest
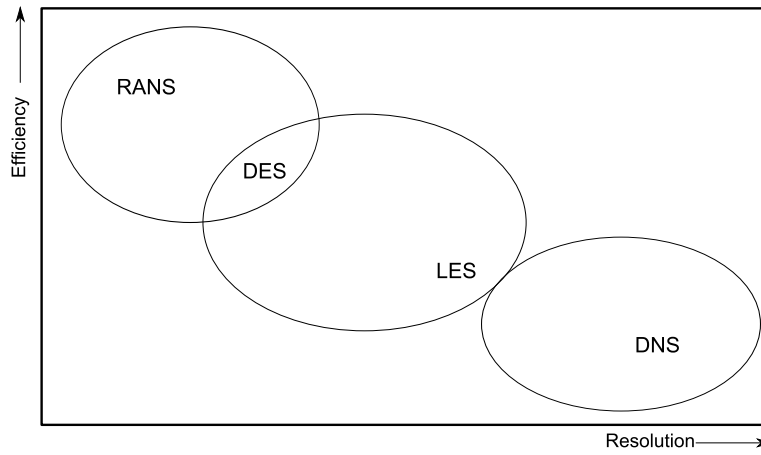
Fig. 2.4: Resolution and accuracy of different numerical solution approaches

possible turbulent structure. This size is usually determined by the geometric length scale l. For a full resolution of the dissipation effect, the maximum distance between grid cells is determined by the smallest turbulent length scale which can be estimated by the Kolmogorov length scale η. The number of cells n needed for the computational grid is then proportional to l/η (Eq. 2.24).

$$n \approx \frac{l}{\eta} \tag{2.24}$$

$$\eta = \left(\frac{\nu^3}{\varepsilon}\right)^{1/4} \tag{2.25}$$

$$\varepsilon \approx \frac{u'^3}{l} \tag{2.26}$$

$$Re_l = \frac{u'l}{\nu} \tag{2.27}$$

$$n \propto Re_l^{3/4} \tag{2.28}$$

Geometric length scale l in m, Kolmogorov length scale η in m, kinematic viscosity ν in m²/s, turbulent dissipation rate ε in m²/s³, velocity fluctuation u' in m/s

The Reynolds number Re_l in Eq. 2.27 is defined with the velocity fluctuation u' and is therefore about $1-5\,\%$ compared to the Reynolds number with the common definition using the mean velocity. Nevertheless, in all three dimensions the total number of cells correlates with $Re_l^{9/4}$ (isotropic turbulence) and so the DNS is practically applicable only for small regions at low Reynolds numbers and less turbulence and it is mostly used for academic purposes.

2.2.2 Large Eddy Simulation (LES)

Turbulent flows contain a large continuous spectrum of velocity and pressure fluctuations, shown in Fig. 2.5. The large scale turbulent eddies carry the most of the energy and are essential for the transport of conservation variables. The effect of the small-scale turbulent eddies is mostly dissipation. Smagorinsky [112] proposed to simulate only the large scale

eddies directly and to use a subgrid-scale turbulence model to capture the effect of the small eddies. It is therefore a compromise between more accurate DNS and more effective RANS method. Mathematically, LES means a low pass filtering of the conservation equations by a filter function which eliminates the small scales of turbulence. Only the large turbulence scales are resolved. Figure 2.5 shows the application range of the subgrid-scale turbulence models within the turbulent spectrum in LES, compared to the RANS and DNS method.
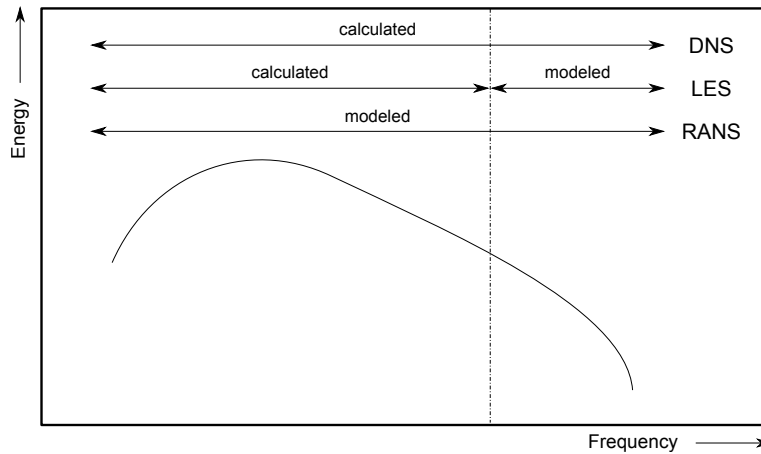
Fig. 2.5: Turbulent spectrum and application of turbulence models

2.2.3 Reynolds Averaged Navier-Stokes (RANS)

For engineering applications the full resolution in time and space of turbulent eddies is usually not necessary. Often, only the mean values are interesting. Therefore, the Navier-Stokes equations are time-averaged by the Reynolds-averaging method over a sufficiently large time intervall. The velocity u can be described by the time-mean value $\overline{u}$ and the fluctuation u', see Eq. 2.29 and Fig. 2.6. When applying this method to the velocity correlations within the Navier-Stokes equations, Eq. 2.30 shows that additional correlation terms appear that represent the effects of the turbulent fluctuations and that have to be modeled by a turbulence model. Here a constant density is assumed.

$$u(x,t) = \overline{u}(x) + u'(x,t) \tag{2.29}$$

$$\rho \overline{u_x u_y} = \rho \overline{(\overline{u_x} + u'_x)(\overline{u_y} + u'_y)} = \rho \overline{u_x u_y} + \underbrace{\rho \overline{u'_x u'_y}}_{\text{Reynolds stress}} \tag{2.30}$$

Time average velocity $\overline{u}$ and velocity fluctuation u' in $^{\mathrm{m}}/_{\mathrm{s}}$, density ρ in $^{\mathrm{kg}}/_{\mathrm{m}^3}$

2.2.4 Detached Eddy Simulation (DES)

In a Detached Eddy Simulation, the flow region is divided into two regions: a near-wall region and an open-flow region. In the near wall region, the RANS-method is applied and in the

open-flow region the LES method is used. DES is therefore a hybrid version from LES and RANS. The DES uses the Spalart-Allmaras turbulence model.
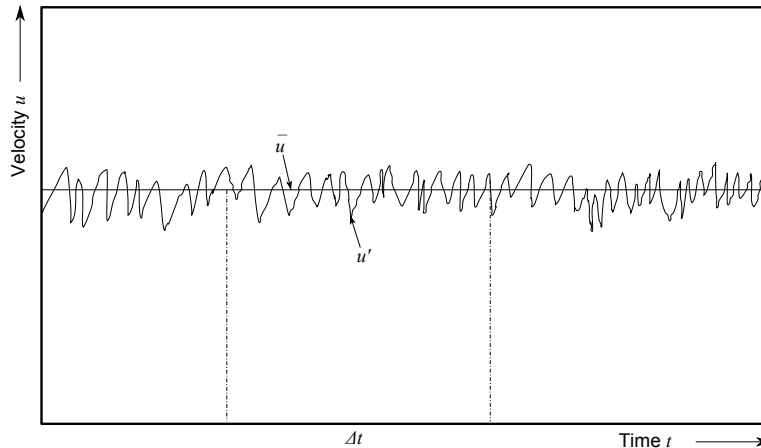
Fig. 2.6: Time averaged velocity within a fluctuating velocity field

Two major groups of turbulence models exist: (1) The Eddy Viscosity Models (EVM), assuming isotropic turbulence and (2) Reynolds Stress turbulence Models (RSM), providing a more detailed description of the Reynolds stress terms. More details on turbulence models are given in the section about STAR-CCM+® 9.02.005.

2.3 Description of STAR-CCM+® 9.02.005

STAR-CCM+® 9.02.005 is a commercial CFD software package distributed by CD-adapco. It is based on its predecessor STAR-CD but with a new object oriented client-server architecture. It provides a graphical user interface with complete meshing, modeling and visualization environment. It provides equations for the LES, DES and RANS approach, approximated by the Finite Volume Method (FVM). In the following, the RANS approach of STAR-CCM+® 9.02.005 will be presented and its closure relations will be discussed. Afterwards, the meshing models and solution scheme of STAR-CCM+® 9.02.005 will be introduced.

2.3.1 Basic conservation equations

The two-fluid formulation of the RANS equations used in STAR-CCM+® 9.02.005 is given for phase i in Eq. 2.31 for the mass conservation and in Eq. 2.32 for the momentum conservation. Equation 2.31 contains a source term for the interphase mass transfer rate $\dot{m}_{ij}$ that appears also in the momentum equation. This term represents the phase change of mass due to boiling or condensation. Equation 2.32 contains an additional source term for the interphase momentum transfer $\dot{M}_{ij}$ which appears because of the phase interactions. The turbulent shear stress tensor τ_t appears due to the Reynolds averaging. The closure relations for the last two mentioned terms are discussed in the following section. The STAR-CCM+® 9.02.005 version of the energy equation was not used in this work and will not be presented here.

$$\frac{\partial}{\partial t}\alpha_i\rho_i + \nabla \cdot \alpha_i\rho_i\vec{u}_i = \dot{m}_{ij} \tag{2.31}$$

$$\frac{\partial}{\partial t}\alpha_i\rho_i\vec{u}_i + \nabla \cdot (\alpha_i\rho_i\vec{u}_i\vec{u}_i) = -\alpha_i\nabla P + \alpha_i\rho_i\vec{g}$$
$$+ \nabla\left[\alpha_i \cdot (\tau_i + \tau_{t,i})\right] + \dot{M}_{ij} + \dot{m}_{ij}\vec{u}_j - \dot{m}_{ji}\vec{u}_i \tag{2.32}$$

$$\sum_i \alpha_i = 1 \tag{2.33}$$

Time t in s, volume fraction of phase i α_i, density ρ in kg/m³, velocity vector $\vec{u}$ in m/s, volumetric inter-phase mass transfer rate $\dot{m}_{ij}$ in kg/m³s, pressure P in Pa, gravity vector $\vec{g}$ in m/s², viscous shear stress τ and turbulent shear stress τ_t in Pas, interphase momentum transfer $\dot{M}_{ij}$ in kg/m²s²

2.3.2 Closure relations

The set of equations to be solved is not closed, because there are more unknown terms than available equations. Additional relations have to be found for modeling the turbulent stress tensor τ_t and the inter-phase momentum transfer $\dot{M}_{ij}$. STAR-CCM+® 9.02.005 usually provides a small selection of models to be used as closure relations and the user can select the most appropriate for the specific flow case. In the following subsections, only the closure relations that were selected for this work are presented.

Turbulence modeling

STAR-CCM+® 9.02.005 offers several turbulence models, each appropriate for special flow cases. The turbulence model has to be selected in conjunction with the wall treatment. Basically, two kinds of meshes can be distinguished: (1) The low-y^+-mesh with a full resolution of the hydrodynamic boundary layer at smooth walls and (2) the high-y^+-mesh that uses wall functions. Table 2.1 gives an overview over available models for the RANS approach in STAR-CCM+® 9.02.005. Some models will be presented more in detail.

The standard k-ε model was developed in the 1970s by Launder and Spalding [54] who used the Boussinesq-approximation to compute the Reynolds stresses (Eq. 2.34). This approach assumes an isotropic distribution of turbulence. It produces good results in fully-developed turbulent pipe flow in regions that are far away from a solid wall. In the following years, this model has become established as the standard for industrial applications. Several enhancements were added over time. The realizability option (Eq. 2.36) prevents an overestimation of the turbulent viscosity in stagnation points[1], e.g. in spacer grids.

---

[1]Durbin [26]

Tab. 2.1: Turbulence models available in STAR-CCM+® 9.02.005

Model family	Model	Wall treatment	Flow conditions	Flow condition
k-ε	standard	high-y^+	single and two-phase	circular pipe flow far away from no-slip walls
	standard low-Re	low, all-y^+	single-phase	viscous sub-layer
	standard two-layer	all-y^+	single and two-phase	circular pipe flow with wall
	AKN low-Re	low, all-y^+	single-phase	compact heat exchangers
	V2F	low, all-y^+	single-phase	heat transfer, skin friction and flow separation
	Elliptic Blending	low, all-y^+	single-phase	More accuate than standard k-ε, more stable than SST
	realizable	high-y^+	single and two-phase	more accurate than standard k-ε
	realizable two-layer	all-y^+	single and two-phase	
k-ω	standard	low, high and all-y^+	single-phase	boundary layers under adverse pressure gradients
	SST	low, high and all-y^+	single-phase	
Spalart-Allmaras	standard	low, all-y^+	single-phase	attached boundary layers and flows with mild separation
	High-Re	high-y^+	single-phase	Used for DES
Reynolds stress	linear pressure strain	high-y^+	single and two-phase	Anisotropic turbulent flows in non-circular channels
	linear pressure strain two-layer	all-y^+	single and two-phase	
	quadratic pressure strain	high-y^+	single and two-phase	
Turbulence response	Issa		two-phase	Dispersed phase in two-phase flow with low void fraction
	Tchen		two-phase	

36

$$-\rho\overline{u'_i u'_j} = \mu_t S_{ij} - \frac{2}{3}\rho k \delta_{ij} \tag{2.34}$$

$$\mu_t = C_\mu \cdot \rho \cdot k \cdot t_t \tag{2.35}$$

$$t_t = \min\left[\max\left(\frac{k}{\varepsilon}, \sqrt{\frac{\mu}{\rho \cdot \varepsilon}}\right), \frac{2}{C_T S_{ij}}\right] \tag{2.36}$$

Density ρ in kg/m³, Reynolds stress $\overline{u'_i u'_j}$ in m²/s², turbulent viscosity μ_t and dynamic viscosity μ in Pas, shear rate S_{ij} in s⁻¹, turbulent kinetic energy k in m²/s², Kronecker delta δ_{ij}, coefficient $C_\mu = 0.09$, turbulent time scale t_t in s, turbulent dissipation rate ε in m²/s³, time scale coefficient $C_T = 0.6$

In Equation 2.37 and 2.38 the two-phase formulation of the k-ε model is given. In case of a single-phase flow, the volume fraction of the liquid phase becomes $\alpha_l = 1$ and of the vapor phase $\alpha_g = 0$ and there is also no mass exchange between the phases, e.g. $m_{ij} = m_{ji} = 0$.

$$\frac{\partial}{\partial t}\int_V \alpha_i \rho k \cdot dV + \int_A \alpha_i \rho k \vec{u} \cdot dA = \int_A \alpha_i\left(\mu + \frac{\mu_t}{\sigma_k}\right)\nabla k \cdot dA$$
$$+ \int_V \alpha_i \left[G_k + G_b - \rho(\varepsilon + Y_M) + S_k\right]_i \cdot dV \tag{2.37}$$
$$+ \sum_{i \neq j}(\dot{m}_{ij}k_j - \dot{m}_{ji}k_i)$$

$$\frac{\partial}{\partial t}\int_V \alpha_i \rho \varepsilon \cdot dV + \int_A \alpha_i \rho \varepsilon \vec{u} \cdot dA = \int_A \alpha_i\left(\mu + \frac{\mu_t}{\sigma_\varepsilon}\right)\nabla \varepsilon \cdot dA$$
$$+ \int_V \alpha_i \frac{1}{T_t}\left[C_{\varepsilon 1}(G_k + C_{\varepsilon 3}G_b) - C_{\varepsilon 2}\rho\varepsilon + S_\varepsilon\right]_i \cdot dV \tag{2.38}$$
$$+ \sum_{i \neq j}(\dot{m}_{ij}\varepsilon_j - \dot{m}_{ji}\varepsilon_i)$$

Time t in s, phase i volume fraction α, density ρ in kg/m³, turb. kinetic energy k in m²/s², turb. dissipation rate ε in m²/s³, volume V in m³, velocity vector $\vec{u}$ in m/s, area A in m², dynamic viscosity μ and turbulent viscosity μ_t in Pas, model coefficients $\sigma_k = 1.0$, $\sigma_\varepsilon = 1.3$, $C_{\varepsilon 1} = 1.44$, $C_{\varepsilon 2} = 1.92$, production terms G_k and G_b defined in Eq. 2.39 and 2.40, dilatation dissipation Y_M in m²/s³ (Eq. 2.41), source terms S_k and S_ε in kg/ms³ (Eq. 2.42 – 2.43), mass change due to phase transformation $\dot{m}_{ij}$ in kg/m³s

- The turbulent production G_k describes the generation of turbulence due to the presence of velocity gradients and shear stress. In in-compressible fluids it is computed with Eq. 2.39.

- The buoyancy production G_b occurs in flows with a temperature gradient and is computed with Eq. 2.40.

- The dilatation dissipation Y_M plays a role in compressible flows. According to the model of Sarkar and Balakrishnan [106], the dilatation dissipation is computed by Eq. 2.41.

- The Particle induced turbulence source terms occur in bubbly two-phase flows or in multi-component flows. It was experimentally observed that bubbles can induce an

additional turbulent kinetic energy in the continuous phase resulting from the phase-velocity difference. It can be modeled as source term S_k for Eq. 2.37 and S_ε in Eq. 2.38 according to the model of Troshko and Hassan [121].

$$G_k = \mu_t \cdot \frac{\partial u_i}{\partial x_j} \cdot S_{ij} \tag{2.39}$$

$$G_b = \beta_t \frac{\mu_t}{Pr_t}(\nabla T \cdot \vec{g}) \tag{2.40}$$

$$Y_M = \frac{C_M k\varepsilon}{c^2} \tag{2.41}$$

$$S_k = F_D^{ij} \cdot (u_j - u_i) \tag{2.42}$$

$$S_\varepsilon = \frac{C_{pit}S_k}{t_b} \tag{2.43}$$

$$t_b = \frac{2 \cdot C_{VM}^{ij} \cdot d_b}{3 \cdot C_D^{ij} \cdot |u_j - u_i|} \tag{2.44}$$

Turbulent viscosity μ_t in Pas, velocity u in m/s, length x in m, shear rate S_{ij} in s^{-1}, thermal expansion coefficient β_t, turbulent Prandtl number Pr_t, temperature T in K, gravity vector $\vec{g}$ in m/s², $C_M = 2$, turb. kinetic energy k in m²/s², turb. dissipation rate ε in m²/s³, speed of sound c in m/s, drag force F_D^{ij} in N (Eq. 2.80), phase velocities u in m/s, calibration constant $C_{pit} = 0.45$, bubble pseudo-turbulence dissipation relaxation time t_b in s, virtual mass coefficient C_{VM}^{ij} (Eq. 2.94), bubble diameter d_b in m, drag force coefficient C_D^{ij} (Eq. 2.80)

Reynolds Stress Models (RSM) provide a transport equation (Eq. 2.45) for each of the unique components of the Reynolds stress tensor τ_t. Therefore they account for the turbulence anisotropy and produce the most accurate predictions of the turbulence field. For the computation of the turbulent dissipation rate, the same transport equation as in the k-ε model is used (Eq. 2.38). Overall seven additional equations have to be solved that requires much more computational cost compared to the two-equation k-ε model. Equation 2.45 is formulated for the single-phase case. The Reynolds stress models of Speziale et al. [114] (SSG) and Gibson and Launder [31] (GL) that are available in STAR-CCM+® 9.02.005. They differ mainly in modeling the pressure strain term Φ_r, but this is not discussed here in detail.

$$\frac{\partial}{\partial t} \int_V \rho \overline{u_i' u_j'} \cdot dV + \int_A \rho \overline{u_i' u_j'} u \cdot dA = \int_A D_r \cdot dA$$
$$+ \int_V \left[G_k + G_b - \frac{2}{3}\rho \delta_{ij}(\varepsilon + Y_M) + \Phi_r + S_r \right] \cdot dV \tag{2.45}$$

$$D_r = \left(\mu + \frac{\mu_t}{\sigma_r} \right) \nabla \overline{u_i' u_j'} \tag{2.46}$$

Time t in s, density ρ in kg/m³, volume V in m³, area A in m², Reynolds stress diffusion D_r in kg/s³, dynamic viscosity μ and turbulent viscosity μ_t in Pas, turbulent Schmidt number $\sigma_r = 0.82$, production terms G_k and G_b defined in Eq. 2.39 – 2.40, turbulent dissipation rate ε in m²/s³, dilatation dissipation Y_M in m²/s³ (Eq. 2.41), pressure strain Φ_r in kg/ms³, source term S_r in kg/ms³

The SST k-ω model is an alternative two-equation eddy viscosity model that solves transport equations for the turbulent kinetic energy k (Eq. 2.49) and the specific dissipation rate ω (Eq. 2.50). The original k-ω model was formulated by Wilcox [131]. It gives better results than the k-ε model in the near-wall region, but in regions far from the wall it is less accurate. To overcome this, Menter [67] proposed to use a blending function as function of the wall distance y. The model uses a cross-diffusion term D_ω far from walls, but not near the wall. This approach blends virtually a k-ε model in the far-field with a k-ω model near the wall. The relation for turbulent viscosity μ_t is given in Eq. 2.47 with a modified turbulent time scale t_t in Eq. 2.48.

$$\mu_t = \rho k t_t \tag{2.47}$$

$$t_t = \min\left(\frac{1}{\omega}, \frac{0.31}{S_{ij} \cdot \tanh\left\{ \left[\max\left(\frac{2\sqrt{k}}{0.09\omega y_w}, \frac{500\mu}{\rho y_w^2 \omega} \right) \right]^2 \right\}} \right) \tag{2.48}$$

Density ρ in kg/m^3, turbulent kinetic energy k in m^2/s^2, turbulent time scale t_t in s, specific dissipation rate ω in s^{-1}, shear rate S_{ij} in s^{-1}, wall distance y_w in m, dynamic viscosity μ in Pas

The transport equation for the turbulent kinetic energy k in Eq. 2.49 is similar to that of the k-ε model. It is shown here for the single-phase case. Additional terms, such as dilatation dissipation, vortex-stretching modification or free-shear modification are not included in Eq. 2.49 and 2.50 for simplicity.

$$\frac{\partial}{\partial t} \int_V \rho k \cdot dV + \int_A \rho k \vec{u} \cdot dA = \int_A (\mu + \mu_t \sigma_k) \nabla k \cdot dA$$
$$+ \int_V (G_k - 0.09 \cdot \rho \omega k + S_k) \cdot dV \tag{2.49}$$

$$\frac{\partial}{\partial t} \int_V \rho \omega \cdot dV + \int_A \rho \omega \vec{u} \cdot dA = \int_A (\mu + \mu_t \sigma_\omega) \nabla \omega \cdot dA$$
$$+ \int_V (G_\omega - C_\beta \rho \omega^2 + D_\omega + S_\omega) \cdot dV \tag{2.50}$$

Time t in s, density ρ in kg/m^3, turbulent kinetic energy k in m^2/s^2, specific dissipation rate ω in s^{-1}, volume V in m^3, velocity vector $\vec{u}$ in m/s, area A in m^2, dynamic viscosity μ and turbulent viscosity μ_t in Pas, model coefficients σ_k, σ_ω, C_β (Eq. 2.55), production terms G_k (Eq. 2.39) and G_ω (Eq. 2.51), cross derivative D_ω (Eq. 2.52), source terms S_k in kg/ms^3 and S_ω in kg/m^3s^2

The production term for the specific dissipation G_ω for in-compressible fluids and the cross-derivative are defined in Eq. 2.51 and 2.52. The latter is calculated with the blending function F_1 (Eq. 2.53) that depends on the wall distance y.

$$G_\omega = \rho \cdot \gamma_\omega S_{ij}^2 \tag{2.51}$$

$$D_\omega = 2 \cdot (1 - F_1) \cdot \rho \sigma_{\omega,2} \frac{1}{\omega} \nabla k \cdot \nabla \omega \tag{2.52}$$

$$F_1 = \tanh\left\{ \left[\min\left(\max\left(\frac{\sqrt{k}}{0.09\omega y_w}, \frac{500\mu}{\rho y_w^2 \omega} \right), \frac{2k}{y_w^2 \cdot C_{D,\omega}} \right) \right]^4 \right\} \tag{2.53}$$

$$C_{D,\omega} = \max\left(\frac{1}{\omega} \nabla k \cdot \nabla \omega, 10^{-20} \right) \tag{2.54}$$

Density ρ in kg/m³, blending coefficient γ_ω (Eq. 2.55), shear rate S_{ij} in s^{-1}, blending function F_1, model coefficient $\sigma_{\omega,2} = 0.856$, specific dissipation rate ω in s^{-1}, turbulent kinetic energy k in m²/s², wall distance y_w in m, dynamic viscosity μ in Pas

The model coefficients in Eq. 2.49 – 2.51 have different values in the near-wall region and in the far-field and they are also calculated by the blending function F_1. Each coefficient ϕ is calculated by Eq. 2.55.

$$\phi = F_1 \cdot \phi_1 + (1 - F_1) \cdot \phi_2 \tag{2.55}$$

Blending function F_1 (Eq. 2.53), coefficients for each region $C_{\beta,1} = 0.075$, $C_{\beta,2} = 0.0828$, $\sigma_{k,1} = 0.85$, $\sigma_{k,2} = 1.0$, $\sigma_{\omega,1} = 0.5$, $\sigma_{\omega,2} = 0.856$, $\gamma_{\omega,1} \approx 0.5532$, $\gamma_{\omega,2} \approx 0.4404$

A non-linear k-ε model   accounts for turbulence anisotropy. Lien et al. [62] constituted a non-linear extension for the standard k-ε model by adding quadratic and cubic functions of the strain and rotation rate tensors to the Boussinesq approximation (Eq. 2.34). Compared to a full Reynolds stress model, much computational effort can be saved, but the used model coefficients are strictly empirical and do not directly represent the physical background.

$$\begin{aligned}
-\rho \overline{u_i' u_j'} = {} & \mu_t S_{ij} - \frac{2}{3}\rho k \delta_{ij} - C_1 \cdot \mu_t \frac{k}{\varepsilon} \cdot \left(S_{ik}S_{kj} - \frac{1}{3}\delta_{ij}S_{ik}S_{kj} \right) \\
& - C_2 \cdot \mu_t \frac{k}{\varepsilon} \cdot \left(\Omega_{ik}S_{kj} - \frac{1}{3}\delta_{ij}\Omega_{ik}S_{kj} \right) \\
& - C_3 \cdot \mu_t \frac{k}{\varepsilon} \cdot \left(\Omega_{ik}\Omega_{kj} - \frac{1}{3}\delta_{ij}\Omega_{ik}\Omega_{kj} \right) \\
& - C_4 \cdot \mu_t \frac{k^2}{\varepsilon^2} \cdot \left[(S_{ik}S_{kj}) \cdot \Omega_{ik} + \Omega_{kj} \cdot (S_{ik}S_{kj}) \right] \\
& - C_5 \cdot \mu_t \frac{k^2}{\varepsilon^2} \cdot \left(S_{ik}S_{kj} - \Omega_{ik}\Omega_{kj} \right) \cdot S_{ij}
\end{aligned} \tag{2.56}$$

Turbulent viscosity μ_t in Pas, shear rate S_{ij} and rotation rate Ω_{ij} in s^{-1}, density ρ in kg/m³, turbulent kinetic energy k in m²/s², turbulent dissipation rate ε in m²/s³, Kronecker delta δ_{ij}

The coefficients used in this equations are given in Eq. 2.57 – 2.62. The variable C_μ in Eq. 2.57 replaces the constant value in Eq. 2.35 for the turbulent viscosity. The non-linear model co-

efficients were adopted for sub-channel flow by Baglietto et al. [6] to predict secondary flow patterns and a proper wall shear stress distribution, according to experimental data.

$$C_\mu = \frac{C_{a0}}{C_{a1} + C_{a2} \cdot S_{NL} + C_{a3} \cdot \Omega_{NL}} \tag{2.57}$$

$$C_1 = \frac{C_{NL1}}{(C_{NL6} + C_{NL7} \cdot S_{NL}) \cdot C_\mu} \tag{2.58}$$

$$C_2 = \frac{C_{NL2}}{(C_{NL6} + C_{NL7} \cdot S_{NL}) \cdot C_\mu} \tag{2.59}$$

$$C_3 = \frac{C_{NL3}}{(C_{NL6} + C_{NL7} \cdot S_{NL}) \cdot C_\mu} \tag{2.60}$$

$$C_4 = C_{NL4} \cdot C_\mu^2 \tag{2.61}$$

$$C_5 = C_{NL5} \cdot C_\mu^2 \tag{2.62}$$

$$S_{NL} = \frac{k}{\varepsilon} \cdot \sqrt{\frac{1}{2} \cdot S_{ij} S_{ij}} \tag{2.63}$$

$$\Omega_{NL} = \frac{k}{\varepsilon} \cdot \sqrt{\frac{1}{2} \cdot \Omega_{ij} \Omega_{ij}} \tag{2.64}$$

Model coefficients $C_{NL1} = 0.8$, $C_{NL2} = 11.0$, $C_{NL3} = 4.5$, $C_{NL4} = -10.0$, $C_{NL5} = -2.0$, $C_{NL6} = 1000.0$, $C_{NL7} = 1.0$, $C_{a0} = 0.667$, $C_{a1} = 3.9$, $C_{a2} = 1.0$, $C_{a3} = 0.0$, turbulent kinetic energy k in $\mathrm{m^2/s^2}$, turbulent dissipation rate ε in $\mathrm{m^2/s^3}$, shear rate S_{ij} and rotation rate Ω_{ij} in $\mathrm{s^{-1}}$

A turbulence response model is used in dispersed two-phase flow with low void fraction. The model of Issa and Oliveira [40] couples the turbulence field of dispersed phase to the turbulence field of the continuous phase by the turbulence response coefficient C_t that is defined as the ratio of the dispersed phase velocity fluctuations to the continuous phase velocity fluctuations. The dispersed phase turbulence parameters are calculated with Eq. 2.65 – 2.68.

$$\mu_{t,d} = \frac{\rho_d}{\rho_l} \cdot C_t^2 \cdot \mu_{t,c} \tag{2.65}$$

$$C_t = \frac{u_d'}{u_c'} \tag{2.66}$$

$$k_d = C_t^2 \cdot k_c \tag{2.67}$$

$$\varepsilon_d = C_t^2 \cdot \varepsilon_c \tag{2.68}$$

Index d = dispersed phase, index c = continuous phase, density ρ in $\mathrm{kg/m^3}$, turbulence response coefficient C_t =, velocity fluctuation u' in $\mathrm{m/s}$, turbulent viscosity μ_t in Pa, turbulent kinetic energy k in $\mathrm{m^2/s^2}$, turbulent dissipation rate ε in $\mathrm{m^2/s^3}$

Wall functions

Von Kármán [127] proposed that the average velocity of a turbulent flow at a certain point is proportional to the logarithm of the distance from that point to the wall. This is known as the law of the wall (Eq. 2.69). In the viscous sub-layer in the region $0 < y^+ \leq 5$ the shear stress is dominant and the velocity is proportional to the wall distance.

$$u^+ = \begin{cases} y^+ & , 0 < y^+ \leq 5 \text{ (viscous sublayer)} \\ \frac{1}{\kappa} \cdot \ln(y^+) + C^+ & , y^+ > 30 \text{ (log-law-region)} \end{cases} \tag{2.69}$$

Von Kármán constant $\kappa = 0.41$, wall function constant $C^+ = 5.0$, dimensionless wall distance y^+ (Eq. 2.71)

With this assumption it is possible to model the velocity gradient in those regions without applying a full mesh resolution in this region. The law of the wall is valid for fully developed turbulent flow that is mainly parallel to a hydraulically smooth wall. The velocity gradient in stagnation flow cannot be predicted by this model. Figure 2.7 shows the velocity distribution as function of the wall distance.

$$u^+ = \frac{u}{u_\tau} \tag{2.70}$$

$$y^+ = \frac{y_w u_\tau \rho}{\mu} \tag{2.71}$$

$$u_\tau = \sqrt{\frac{\tau_w}{\rho}} \tag{2.72}$$

$$\tau_w = \mu \left(\frac{\partial u}{\partial y_w} \right)_{y_w=0} \tag{2.73}$$

Velocity u and friction velocity u_τ in m/s, wall distance y_w in m, density ρ in kg/m³, dynamic viscosity μ in Pas, wall shear stress τ_w in Pa
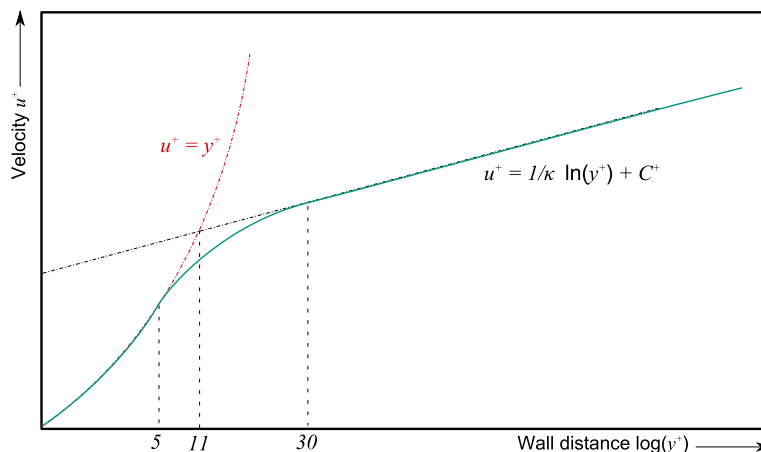
Fig. 2.7: Dimensionless velocity u^+ as function of the wall distance y^+

Interaction length scale

The interaction length scale represents the size of bubbles in dispersed two-phase flows in terms of the Sauter mean diameter d_S (Eq. 2.74). In STAR-CCM+® 9.02.005 the S-γ [63] model is used that solves a transport equation to compute the interfacial area density S_2 (Eq. 2.75). There are additional models to compute the breakup and coalescence source terms in Eq. 2.75. The source term due to mass transfer S_m occurs only in boiling flows.

$$d_S = \frac{6\alpha_g}{\pi S_2} \tag{2.74}$$

$$\frac{\partial \rho^{2/3} S_2}{\partial t} + \nabla \cdot (\alpha_g S_2 \vec{u}_g) = \rho^{2/3} \cdot (S_{br} + S_{co} + S_m) \tag{2.75}$$

Void fraction α_g, density ρ in kg/m³, time t in s, gas velocity vector $\vec{u}_g$ in m/s, source terms for bubble breakup S_{br}, coalescence S_{c0} and mass transfer S_m in m/s

Inter-phase momentum transfer

The momentum transfer $\dot{M}_{ij}$ in Eq. 2.32 between the phases is modeled as the sum of different volumetric forces, as shown in Eq. 2.76. The forces have different physical meanings and are discussed in the following paragraphs. These are the drag force F_D^{ij}, the turbulent dispersion force F_{TD}^{ij}, the virtual mass force F_{VM}^{ij}, the lift force F_L^{ij} and the wall lubrication force F_{WL}^{ij}.

$$\dot{M}_{ij} = F_D^{ij} + F_{TD}^{ij} + F_{VM}^{ij} + F_L^{ij} + F_{WL}^{ij} \tag{2.76}$$

Drag force F_D^{ij}, turbulent dispersion force F_{TD}^{ij}, virtual mass force F_{VM}^{ij}, lift force F_L^{ij}, wall lubrication force F_{WL}^{ij} in N/m³

In the bubbly flow regime the flow conditions can be described by several dimensionless numbers. The bubble Reynolds number Re_b (Eq. 2.77) describes the drag of bubbles of size d_b. The Morton number Mo (Eq. 2.78) is used to determine the transition between Reynolds dependent behavior and surface tension dominated behavior. The Eötvös number Eo (Eq. 2.79) describes the shape and drag of deformed bubbles.

$$Re_b = \frac{\rho_c u_r d_b}{\mu_c} \tag{2.77}$$

$$Mo = \frac{\vec{g} \cdot \mu_c^4}{\rho_c \cdot \sigma^3} \tag{2.78}$$

$$Eo = \frac{\vec{g} \cdot (\rho_l - \rho_g) \cdot d_b^2}{\sigma} \tag{2.79}$$

Continuous phase density ρ_c in kg/m³, bubble diameter d_b in m, continuous phase dynamic viscosity μ_c in Pas, relative velocity u_r in m/s, surface tension σ in N/m, gravitational acceleration $\vec{g}$ in m/s²

The drag force   on a bubble or particle arises from the relative velocity between the two phases. The drag force model of Bozzano and Dente [10] (Eq. 2.81) was selected, because it covers a wide range of bubbly flow regimes and bubble shapes. It can be used for highly viscous flows and also for low and high pressure water systems.

$$F_D^{ij} = \frac{3}{4} C_D^{ij} \rho_c |u_j - u_i|(u_j - u_i) \frac{\alpha_c \cdot \alpha_d}{d_b} \tag{2.80}$$

$$C_D^{ij} = f_D \cdot \left(\frac{a}{R_0}\right)^2 \tag{2.81}$$

$$f_D = \left(\frac{48}{Re_b}\right) \cdot \frac{1 + 12Mo^{1/3}}{1 + 36Mo^{1/3}} + 0.9 \cdot \frac{Eo^{3/2}}{1.4 \cdot (1 + 30Mo^{1/6}) + Eo^{3/2}} \tag{2.82}$$

$$\left(\frac{a}{R_0}\right)^2 = \frac{10 \cdot (1 + 1.3Mo^{1/6}) + 3.1 \cdot Eo}{10 \cdot (1 + 1.3Mo^{1/6}) + Eo} \tag{2.83}$$

Drag force coefficient C_D^{ij}, continuous phase density ρ_c in kg/m³, phase velocity u in m/s, continuous phase volume fraction α_c, bubble diameter d_b in m, bubble Reynolds number Re_b (Eq. 2.77), Morton number Mo (Eq. 2.78), Eötvös number Eo (Eq. 2.79)

The equilibrium between drag force and buoyancy force results in a terminal velocity:

$$u_{t,\infty}^2 = \frac{4 \cdot \Delta\rho \cdot \vec{g} \cdot d_b}{3 \cdot \rho_c \cdot C_D^{ij}} \tag{2.84}$$

Phase pair density difference $\Delta\rho$ and continuous phase density ρ_c in kg/m³, gravitational acceleration $\vec{g}$ in m/s², bubble diameter d_b in m, drag force coefficient C_D^{ij} (Eq. 2.81)

Drag correction terms are used to reproduce experimental terminal velocities correctly as a function of bubble concentration. In a bubble swarm, there are mutual interactions between the bubbles and the continuous phase. According to Richardson and Zaki [86], the main effect of increased bubble concentration is hindering. The terminal velocity decreases faster than would be expected from buoyancy reduction. This effect is captured by a correction factor α_c^n (Eq. 2.85). The original model is modified in STAR-CCM+® 9.02.005 to gain exact continuity between the Reynolds number ranges (Eq. 2.86).

$$\frac{u_t}{u_{t,\infty}} = \alpha_c^n \tag{2.85}$$

$$n = \max \begin{cases} \min \begin{cases} 4.65 \\ \min(4.35 \cdot Re_\infty^{-0.03}, 4.45 \cdot Re_\infty^{-0.1}) \end{cases} \\ 2.39 \end{cases} \tag{2.86}$$

$$Re_\infty = \frac{Re_b}{\max(\alpha_c, 0.34)} \tag{2.87}$$

Terminal velocity u_t in m/s, drag correction exponent n, single bubble Reynolds number Re_∞, bubble Reynolds number Re_b, continuous phase volume fraction α_c

The turbulent dispersion force   redistributes non-uniformities in phase concentrations due to turbulent fluctuations. It is therefore directed into all directions. The turbulence dispersion arises from the Reynolds averaging of the laminar drag force formulation. A derivation for Eq. 2.88 is given in Burns et al. [12]. This force is usually modeled separately from the drag force. In STAR-CCM+® 9.02.005, the turbulent dispersion force is modeled with a effective turbulent Prandtl number σ_α that signifies the ratio of momentum diffusivity over the volume fraction diffusivity due to continuous phase velocity fluctuations.

$$F_{TD}^{ij} = \frac{\mu_{t,c}}{\rho_c \sigma_\alpha} \cdot \left(\frac{\nabla \alpha_d}{\alpha_d} - \frac{\nabla \alpha_c}{\alpha_c} \right) \tag{2.88}$$

$$\sigma_\alpha = \frac{1}{\left(1 + \frac{\tau_R}{\tau_T}\right) \cdot \left(1 + \frac{\rho_c \cdot C_{VM}^{ij}}{\rho_d + \rho_c \cdot C_{VM}^{ij}}\right)} \tag{2.89}$$

$$\tau_R = \frac{\rho_d \alpha_d}{C_{cd}^D} \cdot \left(1 + \frac{\rho_c}{\rho_d} \cdot C_{VM}^{ij}\right) \tag{2.90}$$

$$\tau_T = C_\mu \cdot \frac{k_c}{\varepsilon_c} \tag{2.91}$$

Index c = continuous phase, index d = dispersed phase, turbulent viscosity μ_t in Pas, density ρ in kg/m³, turbulent Prandtl number for volume fraction σ_α, volume fraction α, particle relaxation time τ_R and eddy viscosity time scale τ_T in s, virtual mass coefficient C_{VM}^{ij} (Eq. 2.94), coefficients C_{cd}^D, $C_\mu = 0.09$, turbulent kinetic energy k in m²/s², turbulent dissipation rate ε in m²/s³

The virtual mass force   is an additional resistance on a particle that is accelerated because the surrounding continuous phase is also accelerated due to the no-slip condition at the phase interface. This force can influence the trajectory of bubbles in swirling flow. Auton et al. [4] suggested that the virtual mass force is proportional to the difference of the acceleration between the two phases (Eq. 2.92). The virtual mass coefficient C_{VM}^{ij} is either constant for a spherical particle (Eq. 2.94) or a function of the dispersed phase volume fraction, as proposed by Zuber [136] (Eq. 2.95).

$$F_{VM}^{ij} = C_{VM}^{ij} \cdot \rho_c \alpha_d (\vec{a}_j - \vec{a}_i) \tag{2.92}$$

$$\vec{a}_k = \left(\frac{D\vec{u}}{Dt} \right)_k \tag{2.93}$$

$$C_{VM}^{ij} = 0.5 \tag{2.94}$$

$$C_{VM}^{ij} = 0.5 \cdot \frac{1 + 2\alpha_d}{1 - \alpha_d} \tag{2.95}$$

Virtual mass coefficient C_{VM}^{ij}, continuous phase density ρ_c in kg/m³, dispersed phase volume fraction α_d, acceleration $\vec{a}$ in m/s², velocity $\vec{u}$ in m/s, time t in s

The lift force is working on a bubble perpendicular to the relative velocity, if the continuous phase is swirling or non-uniform. It is defined by Auton et al. [4] to be proportional to the cross product of the phase relative velocity $\vec{u}_r$ with the continuous phase velocity curl (Eq. 2.96). The lift force coefficient can be set to $C_L^{ij} = 0.25$, following Lance and Bateille [53]. The lift force model of Tomiyama et al. [119] accounts for the bubble size and distortion, which is described by the Eötvös number Eo and was therefore selected for this work.

$$F_L^{ij} = C_L^{ij} \cdot \alpha_d \rho_c [\vec{u}_r \times (\nabla \times \vec{u}_c)] \tag{2.96}$$

$$C_L^{ij} = \begin{cases} 0.288 \cdot \tanh\left[0.121 \cdot \max(Re_b, 7.374)\right] & , Eo_d < 4 \\ 0.00105 \cdot Eo_d^3 - 0.0159 \cdot Eo_d^2 - 0.0204 \cdot Eo_d + 0.474 & , 4 \leq Eo_d \leq 10.7 \\ -0.27 & , 10.7 < Eo_d \end{cases} \tag{2.97}$$

$$Eo_d = Eo \times \left(\frac{1}{1 + 0.163 \cdot Eo^{0.757}} \right)^{-2/3} \tag{2.98}$$

Lift coefficient C_L^{ij}, continuous phase density ρ_c in kg/m³, dispersed phase volume fraction α_d, continuous phase velocity $\vec{u}$ and phase relative velocity $\vec{u}_r$ in m/s, Eötvös number Eo, bubble Reynolds number Re_b

The wall lubrication force prevents bubbles from touching the wall. Antal et al. [2] proposed that the bubbles close to the wall experience a force from the fluid flowing asymmetrically around the bubble, so it is similar to lift force, but only present in the near-wall region.

$$F_{WL}^{ij} = -C_{WL}^{ij} \cdot y_w \cdot \alpha_d \cdot \rho_c \cdot \frac{\vec{u}_{r,p}^2}{d_b} \cdot \vec{n} \tag{2.99}$$

$$\vec{u}_{r,p} = \vec{u}_r - (\vec{u}_r \cdot \vec{n}) \cdot \vec{n} \tag{2.100}$$

$$C_{WL}^{ij} = \max\left[C_{w1} + \left(\frac{C_{w2}}{y_w} \right) \cdot d_b, 0 \right] \tag{2.101}$$

Wall lubrication coefficient C_{WL}^{ij}, wall distance y_w in m, dispersed phase volume fraction α_d, continuous phase density ρ_c in kg/m³, phase pair relative velocity $\vec{u}_r$ and relative velocity parallel to the wall $\vec{u}_{r,p}$ in m/s, bubble diameter d_b in m, wall normal vector $\vec{n}$, model coefficients $C_{w1} = -0.01$ and $C_{w2} = 0.05$

2.3.3 Meshing

For the numerical solution the fluid region has to be divided into discrete control volumes. This step is commonly called "meshing". STAR-CCM+® 9.02.005 offers different types of meshing models, listed in Tab. 2.2. All models produce unstructured meshes of the fluid region. This has the advantage that mesh generation is automated, controlled only by a couple of parameters. The drawback compared to a manual mesh generation is that there is less accessibility to the individual mesh node distribution.

Tab. 2.2: Meshing models in STAR-CCM+® 9.02.005

Model	Description	Example
Surface Meshing Models		
Surface Remesher	Discretization of the surface of a flow region by triangular elements	
Surface Wrapper	Mapping of the integral volume within a surface shell	
Volume Meshing Models		
Tetrahedral Mesh	Fills the control volume with tetrahedral cells	
Polyhedral Mesh	Fills the control volume with polygonal cells	
Advancing Layer Mesh	Creates a layer of prismatic cells growing from solid surfaces and fills the remaining volume with polygonal cells	
Trimmer Mesh	Creates a mesh of hexagonal cells that are trimmed by the boundaries of the region	
Special Models for Volume Mesh		
Prism-Layer Mesh	Creates layers of prismatic cells orthogonal to a wall boundary	
Extruder Mesh	The shape of the mesh on a boundary can be extruded to a specified length with a user-defined node distribution	
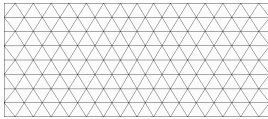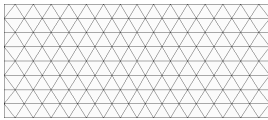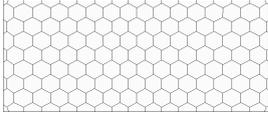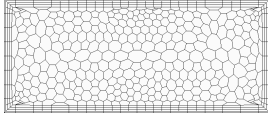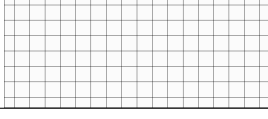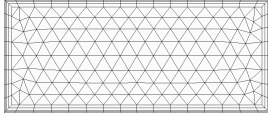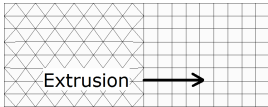
A good mesh is essential for a good convergence of the solution and a good reliability of the results. Therefore the mesh has to match two requirements: (1) A sufficient resolution and (2) a good quality. In CFD, next to the model errors that can occur in RANS-simulations, the discretization of the fluid region is the major error source. The required mesh resolution is correlated to the flow conditions and the set of model equations used in the simulation. In DNS simulations, the mesh resolution has to be fine enough to cover the whole turbulence length scale spectrum. Also in RANS simulations the results will vary with mesh resolution, if the mesh is not fine enough to resolve large gradients of velocity or temperature. For regions close to a solid surface, wall functions can be used for a reduction of required resolution. The mesh resolution is limited by the computational capacity and the optimum mesh cell size with low discretization errors has to be found iteratively.

The mesh quality will influence the stability of the calculation. It can be described by various criteria that are listed below. STAR-CCM+® 9.02.005 offers a mesh diagnostics tool and

quality indicators to calculate and to visualize the mesh quality. For poor surface meshes a repair tool is included which can manually fix some meshing errors. Poor volume meshes can be fixed only by changing the meshing parameters and re-running the mesh generation. The mesh quality has to be checked before the simulation run. Often, large residuals remain in cells of poor quality.

- **Negative volume cells:** A mesh containing negative volume cells would be invalid and no simulation can be run. Negative volume cells must not exist in a valid mesh.

- **Cell skewness angle:** Angle between face normal and connection between cell centroids. It should not be larger than $85\,°$.

- **Face validity:** The ideal value is 1 if the face normals pointing outward of cell centroid. If some face normals pointing towards the cell centroid, then the face validity is smaller than 1.

- **Volume change:** The ratio of the volume of two neighbor cells should not be smaller than 10^{-6}. A perfect value would be 1 if both cells have the same size.

- **Cell quality:** Criterion that evaluates the relative geometric distribution of cell centroids of the neighbor cells and of cell face orientation. Flat cells with non-orthogonal faces would have a low cell quality, whereas a value of 1 would be perfect.

2.4 Description of COBRA-FLX^{TM}

COBRA-FLX^{TM} is a thermal-hydraulic analysis and design program based on COBRA 3CP and developed by AREVA GmbH[2]. It is used for the thermal-hydraulic design of PWRs. It calculates the local DNB-ratio in a fuel pin. Within AREVA it is the standard tool for evaluation of thermal-hydraulic experiments. It provides a steady state and transient full core and sub-channel analysis with flexible geometry specifications and is able to calculate cross-flow effects and pressure drops. There is a choice of different correlations for turbulent mixing, friction factor or CHF that can be selected by the user.

The first version of COBRA (Coolant Boiling in Rod Arrays) was developed in the 1960s within a cooperative programme between the USA and Canada for the development of heavy water reactors. It was later extended and sold to other institutions where the code was further developed. Table 2.3 shows the development path from the first version towards COBRA-FLX^{TM}. Within this path, many other developments branched off that are not shown here.

2.4.1 Basic conservation equations

The fluid in COBRA-FLX^{TM} is considered as single component two-phase mixture of liquid and vapor in thermodynamic equilibrium. Variations of fluid and flow properties across the flow

---

[2]Leberig et al. [55]

Tab. 2.3: Historical development of COBRA-FLX^{TM}

Year	Version	Institution	Reference
1967	COBRA	Batelle Northwest Lab.	Rowe and Angle [95]
1970	COBRA-II	Batelle Northwest Lab.	Rowe [91]
1971	COBRA-III	Batelle Northwest Lab.	Rowe [92]
1973	COBRA-III C	Batelle Northwest Lab.	Rowe [93]
1980	COBRA-III C / MIT	MIT	Loomis and Hinkle [64]
1981	COBRA-III C / MIT-2	MIT	Jackson and Todreas [41]
1986	COBRA 3-CP	Siemens / KWU	Veloso and Mistelberger [125]
2009	COBRA-FLX	AREVA	Leberig et al. [55]

channel normal to the mean flow direction are neglected. The effects of these microscopic phenomena are considered by empirical correlations for the friction factor, heat transfer or turbulent mixing. The mean flow direction is the axial direction parallel to the rod walls and the lateral velocity components are assumed to be small. Considering the magnitude of the axial velocity u_z component to be of order 1 and the magnitude of the lateral velocity components u_x and u_y to be of order δ and assuming that $\delta \ll 1$, the velocity correlation term $u_x \cdot u_y$ in the momentum conservation equation is considered as δ^2 and is therefore neglected as being very small. As consequence, the momentum conservation equation system is reduced to only two equations accounting for the axial and the lateral momentum. The axial component of the velocity will be denoted therefore as u_{ax} and the lateral component as u_{lat}. The local composition of the fluid is described by the space averaged volume fraction α_g, defined in Eq. 2.12.

The following conservation equations for mass, momentum and energy will be given in their final discretized form as they are used in COBRA-FLX^{TM}. These equations are derived from the standard conservation equations (Eq. 2.4, 2.5–2.7 and 2.8) including additional assumptions that will be listed in this section. The Navier-Stokes equations are averaged by the sub-channel geometry approach and applied to a control volume shown in Fig. 2.8.

The bounding surfaces are the rod surfaces and the imaginary fluid-fluid interfaces in the gap area. The sub-channels can exchange mass, momentum or energy over these fluid interfaces in the gap. The terms in the basic conservation equations will be therefore integrated over the whole control volume. The Gauß theorem (Eq. 2.102) is used to transform the spatial gradients in these equations. The resulting integration over the bounding surfaces of the control volume gives the transport of the flow properties into and out of the control volume.

$$\int_V \nabla \Phi \, dV = \oint_A \Phi \cdot \vec{n} \, dA \tag{2.102}$$

Volume V in m^3, fluid property Φ, area A in m^2, surface normal vector $\vec{n}$
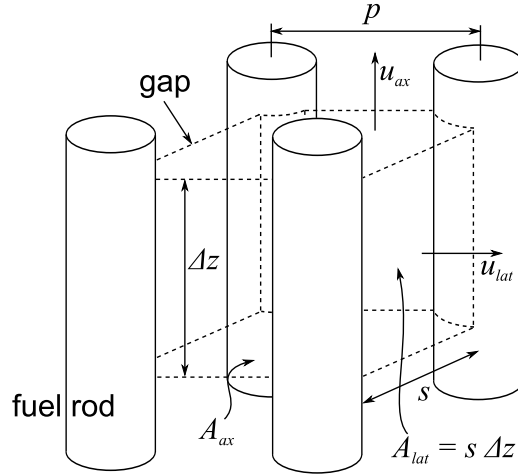
Fig. 2.8: Sub-channel control volumes with main geometric parameters

Mass conservation equation

Applying the volume averaging and the Gauß theorem to the mass conservation equation and considering the lateral cross-flow through the gap area A_{lat} yields:

$$\frac{\partial}{\partial t} \int_V \rho \, dV + \oint_{A_{ax}} \rho \left(u_{ax} \cdot \vec{n} \right) dA_{ax} + \oint_{A_{lat}} \rho \left(u_{lat} \cdot \vec{n} \right) dA_{lat} = 0 \qquad (2.103)$$

Time t in s, volume V in m^3, density ρ in kg/m^3, area A in m^2, velocity u in m/s, surface normal vector $\vec{n}$

The fluid is considered as single-component two-phase mixture. Both phases share the same pressure and velocity field. The mixture density is defined in Eq. 2.104. The flow components considered are the axial mass flow $\dot{m}$ and the sum of all lateral cross-flows through the gaps, denoted as w (Eq. 2.106). A sign convention e_k is used for each gap to determine the direction of the cross-flow, according to the sub-channel numbering used in COBRA-FLX$^{\text{TM}}$. Performing the integrations in Eq. 2.103, substituting the mass flow and cross-flow terms, dividing by the axial node distance Δz and taking the limit as Δz approaches zero, yields the differential form of the mass conservation equation used in COBRA-FLX$^{\text{TM}}$, shown in Eq. 2.107.

$$\rho_m = \alpha_g \cdot \rho_g + (1 - \alpha_g) \cdot \rho_l \qquad (2.104)$$

$$\dot{m} = \rho_m u_{ax} A \qquad (2.105)$$

$$w = \rho_m u_{lat} s \qquad (2.106)$$

$$A \frac{\partial}{\partial t} \rho_m + \frac{\partial}{\partial z} \dot{m} + \sum_k e_k w = 0 \qquad (2.107)$$

Axial sub-channel cross section A in m^2, time t in s, void fraction α_g, density of the gas phase ρ_g and the liquid phase ρ_l in kg/m^3, axial direction z in m, axial mass flow $\dot{m}$ in kg/s, sign convention e_k, lateral cross-flow w in kg/ms, axial velocity u_{ax} and lateral velocity u_{lat} in m/s, gap width s in m

Axial momentum equation

The derivation of the COBRA-FLX$^{\text{TM}}$ formulation of the axial momentum balance equation follows the same steps as the mass conservation equation. The local instantaneous Navier-Stokes equation for a two-phase mixture is presented in Eq. 2.21 with $\dot{m} = \rho \vec{u} A$. In the sub-channel approach, this formulation is averaged over the sub-channel control volume. The Gauß theorem is used to transform the volume integrals of the spatial gradients into surface integrals. This step gives the transport over the bounding surfaces:

$$\frac{\partial}{\partial t} \int_V \rho \vec{u} \, dV + \int_A \rho \vec{u}(\vec{u}\vec{n}) dA = - \int_A P \vec{n} \, dA - \int_{A_{rod}} \tau \vec{n} \, dA_{rod} + \int_V \rho \vec{g} \, dV \qquad (2.108)$$

Time t in s, volume V in m^3, sub-channel cross-section A in m^2, velocity vector $\vec{u}$ in m/s, two-phase specific volume for momentum v' in m^3/kg, surface normal vector $\vec{n}$, pressure P in Pa, shear stress τ in Pa, density ρ in kg/m^3, gravity vector $\vec{g}$ in m/s^2

The axial component of Eq. 2.108 is developed performing the integrations and using the following assumptions:

- The volume integral of the transient term is:

$$\frac{\partial}{\partial t} \int_V \rho \vec{u} \, dV = A \Delta z \frac{\partial}{\partial t} \rho u_{ax} \qquad (2.109)$$

Time t in s, volume V in m^3, sub-channel cross-section A in m^2, density ρ in kg/m^3, velocity u in m/s, axial node distance Δz in m

- The momentum flux in the axial direction, accounting for axial and lateral convection, is:

$$\int_A \rho \vec{u}(\vec{u}\vec{n}) dA = \left[\left(\rho u_{ax}^2 A \right)_{z+\Delta z} - \left(\rho u_{ax}^2 A \right)_z \right] + \sum_k e_k \rho u_{ax} u_{lat} s \Delta z \qquad (2.110)$$

Density ρ in kg/m^3, velocity u in m/s, sub-channel cross-section A in m^2, axial node distance Δz and gap width s in m, sign convention for cross-flow e_k

- The pressure forces on the bounding surfaces in axial direction are:

$$\int_A P \vec{n} \, dA = A \left(P_{z+\Delta z} - P_z \right) \qquad (2.111)$$

Sub-channel cross-section A in m^2, pressure P in Pa, surface normal vector $\vec{n}$, axial node distance Δz in m

- Gravity is the only significant body force term. The volume integral of the body force is:

$$\int_V \rho \vec{g} \, dV = -A \rho \Delta z g \cos(\Theta) \qquad (2.112)$$

Volume V in m^3, density ρ in kg/m^3, gravity vector $\vec{g}$ in m/s^2, sub-channel cross-section A in m^2, axial node distance Δz in m, angle between rod bundle and gravity vector Θ

- Viscous shear stresses between fluid elements are assumed to be small compared to the shear stress on solid surfaces and are therefore neglected. Only the turbulent shear stresses between the fluid interfaces in the gaps are considered. They are modeled using an empirical expression for the turbulent fluctuation mass flow per unit length w' that is scaled with the axial velocity difference of two connected sub-channels i and j:

$$\int_{A_{fluid}} \tau_t \vec{n} dA_{fluid} = -C_t \Delta z \sum_k w' \Delta u_{ax} \tag{2.113}$$

$$\Delta u_{ax} = \left[\left(\frac{\dot{m}}{\rho_m A} \right)_i - \left(\frac{\dot{m}}{\rho_m A} \right)_j \right] \tag{2.114}$$

$$w' = C_\beta \cdot s \cdot \overline{G} \tag{2.115}$$

$$\overline{G} = \frac{1}{2} \cdot \left[\left(\frac{\dot{m}}{A} \right)_i + \left(\frac{\dot{m}}{A} \right)_j \right] \tag{2.116}$$

Area of the gaps A_{fluid} and axial sub-channel cross section A in m^2, turbulent shear stress τ_t in Pa, surface normal vector $\vec{n}$, local velocity gradient coefficient C_t, axial node distance Δz in m, turbulent mixing mass flow per unit length w' in kg/ms, axial velocity difference Δu_{ax} in m/s, mixture density ρ_m in kg/m^3, axial mass flow $\dot{m}$ in kg/s, turbulent mixing coefficient C_β, average mass flux $\overline{G}$ in kg/m^{2}s, wetted perimeter p_w in m

- The shear stress on solid surfaces is modeled with the lumped parameter C_f and C_d represents the effects of local changes in the flow channel geometry. The two-phase friction is modeled using a multiplier function C_ϕ^2 for the single-phase wall friction coefficient:

$$\int_{A_{rod}} \tau \vec{n} dA_{rod} = -\frac{1}{2} \left(\frac{C_f C_\phi^2 \Delta z}{d_{hyd}} + C_d \right) \cdot \rho u_{ax}^2 A \tag{2.117}$$

Area of rod surfaces A_{rod} in m^2, viscous shear stress τ in Pa, surface normal vector $\vec{n}$, single-phase wall friction coefficient C_f, two-phase friction multiplier C_ϕ^2, local loss coefficient C_d, hydraulic diameter d_{hyd} in m, density ρ in kg/m^3

Putting Eq. 2.109 − 2.117 into Eq. 2.108, dividing by Δz and taking the limit as Δz approaches zero yields:

$$A \frac{\partial}{\partial t} \rho u_{ax} + \frac{\partial}{\partial z} \rho u_{ax}^2 A + \sum_k e_k \rho u_{ax} u_{lat} s = -A \frac{\partial}{\partial z} P - \frac{1}{2} \left(\frac{C_f C_\phi^2}{d_{hyd}} + \frac{C_d}{\Delta z} \right) \cdot \rho u_{ax}^2 A$$
$$-C_t \sum_k w' \left[\left(\frac{\dot{m}}{\rho_m A} \right)_i - \left(\frac{\dot{m}}{\rho_m A} \right)_j \right] - A \rho g \cos(\Theta) \tag{2.118}$$

Time t in s, sub-channel cross-section A in m^2, velocity u in m/s, single-phase wall friction coefficient C_f, two-phase friction multiplier C_ϕ^2, local loss coefficient C_d, hydraulic diameter d_{hyd} and gap width s in m, density ρ in kg/m^3, sign convention e_k, pressure P in Pa, velocity gradient coefficient C_t, turbulent mixing w' in kg/ms (Eq. 2.115), gravitational acceleration g in m/s^2, angle of sub-channel to gravitational direction Θ in °

The formulation of the two-phase momentum flux is further modified by substitution of the two-phase momentum formulations given in Eq. 2.119 and 2.120. Then, the product rule is

applied to the convection term and the derivative of the mass flow is substituted by the mass conservation equation (Eq. 2.107):

$$\rho u_{ax}^2 A = \frac{\dot{m}^2 v'}{A} \tag{2.119}$$

$$\rho u_{ax} u_{lat} s = \frac{\dot{m} w v'}{A} \tag{2.120}$$

$$\frac{\partial}{\partial z} \rho u_{ax}^2 A = \frac{\partial}{\partial z} \left(\frac{\dot{m}^2 v'}{A} \right) \tag{2.121}$$

$$= \dot{m}^2 \frac{\partial}{\partial z} \left(\frac{v'}{A} \right) + 2\dot{m} \frac{v'}{A} \frac{\partial}{\partial z} \dot{m} \tag{2.122}$$

$$= \dot{m}^2 \frac{\partial}{\partial z} \left(\frac{v'}{A} \right) - 2u_{ax} A \frac{\partial}{\partial t} \rho_m - 2u_{ax} \sum_k e_k w \tag{2.123}$$

$$u_{ax} = \dot{m} \frac{v'}{A} \tag{2.124}$$

Density ρ in kg/m³, velocity u in m/s, cross-section A in m², gap width s in m, mass flow $\dot{m}$ in kg/s, time t in s, sign convention e_k, diversion cross-flow w in kg/ms (Eq. 2.106), two-phase specific volume for momentum v' in m³/kg (Eq. 2.22)

Putting Eq. 2.123 into Eq. 2.118 would give the final form of the axial momentum balance equation in the differential form that is used in COBRA-FLX^{TM}. It contains already the empirical modeling approaches that are accounting for the shear stress on solid surfaces, the turbulent mixing and two-phase pressure drop. These correlations contain model coefficients that need additional closure relations. The turbulent mixing term w' is responsible for carrying momentum between the sub-channels i and j.

$$\frac{\partial}{\partial t} \dot{m} - 2u_{ax} A \frac{\partial \rho_m}{\partial t} - 2u_{ax}^* \sum_k e_k w + \sum e_k \frac{\dot{m}}{A} w v' =$$
$$-A \frac{\partial P}{\partial z} - \frac{1}{2} \cdot \left(\frac{C_f}{d_{hyd}} \cdot \frac{C_\phi^2}{\rho_l} + \frac{C_d}{\Delta z} v' \right) \cdot \frac{\dot{m}^2}{A} - \dot{m}^2 \frac{\partial}{\partial z} \frac{v'}{A} \tag{2.125}$$
$$-C_t \cdot \sum_k w' \left[\left(\frac{\dot{m}}{\rho_m A} \right)_i - \left(\frac{\dot{m}}{\rho_m A} \right)_j \right] - A \rho_m g \cos(\Theta)$$

Time t in s, mass flow $\dot{m}$ in kg/s, axial velocity u_{ax} in m/s, axial sub-channel cross section A in m², mixture density ρ_m and liquid density ρ_l in kg/m³, sign convention e_k, diversion cross-flow w in kg/ms (Eq. 2.106), specific volume v' in m³/kg (Eq. 2.22), axial direction z in m, pressure P in Pa, friction coefficient C_f, hydraulic diameter d_{hyd} in m, two-phase friction coefficient C_ϕ, local loss coefficient C_d, velocity gradient coefficient C_t, turbulent mixing w' in kg/ms (Eq. 2.115), gravitational acceleration g in m/s², angle of sub-channel to gravitational direction Θ in °

Lateral momentum equation

The control volume for the lateral component of Eq. 2.108 is different as for the axial component as Fig. 2.9 shows. The differences to the assumptions of the axial momentum balance are:

- The time derivative is integrated as follows:

$$\frac{\partial}{\partial t} \int_V \rho \vec{u} dV = sl\Delta z \frac{\partial}{\partial t} \rho u_{lat} \tag{2.126}$$

  Time t in s, volume V in m³, density ρ in kg/m³, velocity u in m/s, axial node distance Δz, gap width s and lateral length of control volume l in m

- The lateral momentum is zero at the sub-channel centers, i.e. there is no lateral momentum flux over the side control sections and only the axial component is considered. The axial velocity is the mean value of the two adjacent sub-channels i and j:

$$\int_A \rho \vec{u}(\vec{u}\vec{n}) dA = \left[(\rho u_{lat} u_{ax}^*)_{z+\Delta z} - (\rho u_{lat} u_{ax}^*)_z\right] \cdot sl \tag{2.127}$$

$$u_{ax}^* = \frac{1}{2} \cdot \left(u_{ax,i} + u_{ax,j}\right) \tag{2.128}$$

  Density ρ in kg/m³, velocity u in m/s, sub-channel cross-section A in m², axial node distance Δz, gap width s and lateral length l in m

- The pressure forces on the bounding surfaces in lateral direction are the sub-channel averaged pressures of the adjacent sub-channels i and j:

$$\int_A P\vec{n} dA = -\left(P_j - P_i\right) \cdot s\Delta z \tag{2.129}$$

  Sub-channel cross-section A in m², pressure P in Pa, surface normal vector $\vec{n}$, axial node distance Δz and gap width s in m

- The lateral resistance coefficient represents all form drag and viscous shear stress caused by the rod geometry

$$\int_{A_{rod}} \tau \vec{n} dA_{rod} = -\frac{1}{2} C_{ij} \rho u_{lat}^2 s\Delta z \tag{2.130}$$

  Area of rod surfaces A_{rod} in m², viscous shear stress τ in Pa, surface normal vector $\vec{n}$, cross-flow resistance coefficient C_{ij}, density ρ in kg/m³, lateral velocity u_{lat} in m/s, axial node distance Δz and gap width s in m

- The turbulent shear stress in lateral direction and the viscous drag on fluid interfaces is neglected

- Gravity is neglected as it is assumed to be perpendicular to the lateral direction
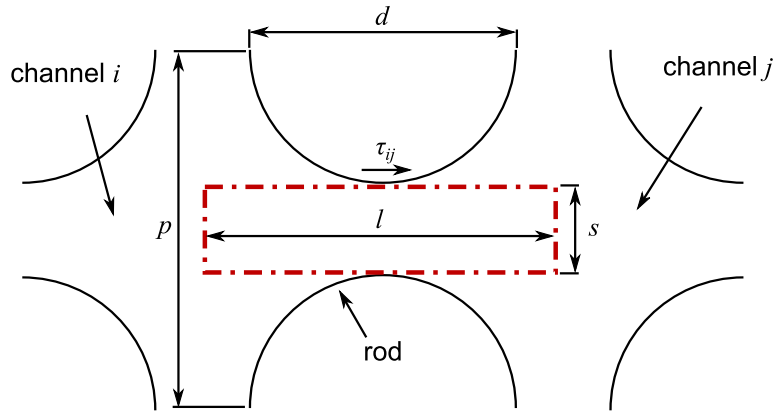
Fig. 2.9: Control volume for lateral momentum conservation equation in COBRA-FLX^{TM}

Putting Eq. 2.126 – 2.130 into Eq. 2.108, dividing by $l \cdot \Delta z$ and taking the limit as Δz approaches zero yields:

$$s \frac{\partial}{\partial t} \rho u_{lat} + s \frac{\partial}{\partial z}(\rho u_{lat} u_{ax}^*) = -\left(P_j - P_i\right) \cdot \frac{s}{l} - \frac{1}{2} C_{ij} \frac{s}{l} \rho u_{lat}^2 \qquad (2.131)$$

Time t in s, gap width s and lateral length l in m, average axial velocity in gap u_{ax}^* and lateral velocity u_{lat} in m/s, pressure P in Pa, lateral resistance coefficient C_{ij}, density ρ in kg/m³

Substitution of the lateral velocity by the diversion cross-flow w (Eq. 2.106) yields the final COBRA-FLX^{TM} formulation of the lateral momentum balance:

$$\frac{\partial}{\partial t} w + \frac{\partial}{\partial z} w u_{ax}^* = -\left(P_j - P_i\right) \cdot \frac{s}{l} - \frac{1}{2} C_{ij} \frac{s}{l} \frac{w|w|}{\rho^* s^2} \qquad (2.132)$$

Time t in s, diversion cross-flow w in kg/ms, axial direction z in m, average axial velocity in gap u_{ax}^* in m/s, gap width s in m, centroid distance l between sub-channels i and j in m, pressure P in Pa, lateral resistance coefficient C_{ij}, mixture density from donor sub-channel ρ_m^* in kg/m³

Energy conservation equation

The energy conservation equation in COBRA-FLX^{TM} is given in Eq. 2.133. It uses the flowing enthalpy h_m formulation for the mixture instead of the static enthalpy formulation $\hat{h}$. The relation between the two formulations is given by the correlation of Tong [120] in Eq. 2.136. The main assumptions for the energy conservation equation are:

- Viscous dissipation is neglected

- The kinetic and potential energy is small compared to the internal thermal energy

- Work done by the body forces and shear stresses is small compared to the surface heat transfer and convective energy transport

- Heat conduction through the fluid surface is assumed small compared to convective energy transport and heat transfer from solid surfaces

55

$$A_{ax}\rho_m \cdot \frac{\partial h_m}{\partial t} - A_{ax}\Delta h_{lg} \cdot \frac{\partial \Psi}{\partial t} + \dot{m} \cdot \frac{\partial h_m}{\partial z} + \sum_k e_k w h_m =$$
$$\sum_m \phi_m(1 - C_q)q' + \sum_m C_q \phi_m q' - \sum_k w'(h_{m,i} - h_{m,j}) \tag{2.133}$$

Time t in s, diversion cross-flow w in kg/ms, axial direction z in m, mixture density ρ_m in kg/m³, flowing mixture enthalpy h_m in J/kg, heat of vaporization at saturated conditions Δh_{lg} in J/kg, Tong factor Ψ (Eq. 2.136), mass flow $\dot{m}$ in kg/s, sign convention e_k, fraction of rod perimeter ϕ_m facing the sub-channel, fraction of the rod power generated directly in the coolant C_q, local linear heating rate q' in W/m, turbulent mixing w' in kg/ms

$$\hat{h} = \frac{1}{\rho_m} \cdot \left[\alpha_g \rho_g h_g + (1 - \alpha_g) \cdot \rho_l h_l \right] \tag{2.134}$$

$$h_m = x_e h_g + (1 - x_e)h_l \tag{2.135}$$

$$\Psi = \frac{\rho_m}{\Delta h_{lg}} \cdot (h_m - \hat{h}) \tag{2.136}$$

Mixture density ρ_m, gas density ρ_g and liquid density ρ_l in kg/m³, void fraction α_g, gas phase enthalpy h_g and liquid phase enthalpy h_l in J/kg, thermal equilibrium quality x_e, heat of vaporization Δh_{lg} in J/kg, flowing mixture enthalpy h_m and static enthalpy $\hat{h}$ in J/kg

2.4.2 Closure relations

Material properties

The material properties are calculated from the industrial standard IAPWS-IF97 water and steam property table published by Wagner and Kruse [129].

Single-phase wall friction coefficent C_f

The single-phase wall friction factor for turbulent flow is used to model the viscous shear stress on the rod surfaces parallel to the main flow direction. It is formulated as exponential function of Reynolds number, see Eq. 2.137. As alternative, the Lehmann [57] correlation can be used to compute the wall friction factor as function of the surface roughness. Optionally, also entrance effects (Szablewski [116] correction) or wall viscosity corrections can be used.

$$C_f = A \cdot Re^B + C \tag{2.137}$$

Reynolds number Re, empirical model coefficients A, B and C

Two-phase wall friction multiplier C_ϕ

Different options for the definition of the two-phase friction multiplier C_ϕ are available in COBRA-FLX$^{\text{TM}}$. As standard, the homogeneous model in Eq. 2.138 is used in COBRA-FLX$^{\text{TM}}$.

$$C_\phi = \frac{\rho_l}{\rho_m} \text{ for } x_e > 0 \tag{2.138}$$

Liquid phase density ρ_l and mixture density ρ_m in $^{\text{kg}}/_{\text{m}^3}$, thermal equilibrium quality x_e

Spacer drag coefficient C_d

The spacer drag coefficient has to be determined from experimental data or CFD simulations. It can be given optionally as constant or as function of Reynolds number. It has to be provided for each spacer type in every single sub-channel, because of the different blockage ratios.

Lateral resistance coefficient C_{ij}

The lateral resistance coefficient can be regarded as constant value. The standard value is $C_{ij} = 0.5$. No empirical correlation can be selected in COBRA-FLX$^{\text{TM}}$ and this value has to be guessed or determined from experimental data.

Turbulent mixing coefficient C_β

For single phase flows, C_β is assumed to be constant or a function of Reynolds number. An additional model is implemented in COBRA-FLX$^{\text{TM}}$ to account for an axially variable mixing as it occurs in the wake of spacer grids. For two-phase flow, the Beus [8] model can be used or a table with two-phase mixing coefficients can be provided.

Heat transfer coefficient

Several heat transfer correlations are implemented into COBRA-FLX$^{\text{TM}}$. They are selected accounting for different criteria such as the flowing quality and the wall temperature. They are not further discussed here since the heat transfer is not an object of this work.

Void fraction α_g

COBRA-FLX$^{\text{TM}}$ uses different correlations for the sub-cooled boiling and the bulk boiling regime. The quality x_d, at which bubble departure occurs, is computed by the Saha and Zuber [105] correlation, given in Eq. 2.139. The Zuber et al. [137] model is used further to relate the flowing quality x_f to the thermal equilibrium quality x_e, see Eq. 2.141. For bulk boiling, the Chexal et al. [19] model is used that predicts the void fraction. The model formulation is given in Eq. 2.142. The undefined parameters in Eq. 2.142 are explained in [19].

$$x_d = \begin{cases} -0.0022 \cdot \frac{q'' d_{hyd} c_p}{\lambda} & , Pe < 70000 \\ \frac{-154 \cdot \frac{q''}{G}}{\Delta h_{lg}} & , Pe > 70000 \end{cases} \tag{2.139}$$

$$Pe = \frac{d_{hyd} \cdot G \cdot c_p}{\lambda} \tag{2.140}$$

$$x_f = x_e - x_d \cdot \left[1 - \tanh\left(1 - \frac{x_e}{x_d} \right) \right] \tag{2.141}$$

$$\alpha = \frac{x_f}{C_0 \cdot \left(x_f + (1 - x_f) \cdot \frac{\rho_g}{\rho_l} \right) + \frac{V_{gj}\rho_g}{G}} \tag{2.142}$$

Heat flux q'' in $^{\text{W}}/_{\text{m}^2}$, hydraulic diameter d_{hyd} in m, specific heat c_p of liquid phase in $^{\text{J}}/_{\text{kgK}}$, thermal conductivity λ of liquid phase in $^{\text{W}}/_{\text{mK}}$, mass flux G in $^{\text{kg}}/_{\text{m}^2\text{s}}$, heat of vaporization Δh_{lg} in $^{\text{J}}/_{\text{kg}}$, Péclet number Pe, gas phase density ρ_g and liquid phase density ρ_l in $^{\text{kg}}/_{\text{m}^3}$, thermal equilibrium quality x_e, flowing quality x_f, model coefficients C_0 and V_{gj} from [19]

2.4.3 Meshing

The control volume in COBRA-FLX$^{\text{TM}}$ is based on the sub-channel concept. The approach is to divide the rod bundle cross-section into flow sub-channels and to divide the length into finite increments. The result is a set of control volumes that represent the flow region of the rod bundle. The conservation equations are discretized by a first-order Finite Difference Method (FDM). Local geometry features are not resolved in this approach and the sub-channel geometry is described by the hydraulic diameter d_{hyd} and the wetted perimeter p_w.
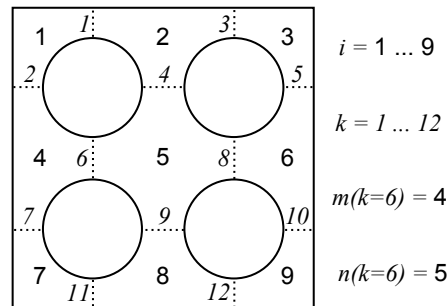
Fig. 2.10: Lateral nodalization in COBRA-FLX$^{\text{TM}}$

Figure 2.10 shows an example for lateral nodalization in COBRA-FLX$^{\text{TM}}$. For the nodalization an index number i is assigned to each sub-channel and the axial nodes are numbered by index j arbitrarily. The convention for lateral direction is positive for growing i-indices and negative for decreasing i-indices. There are also gap numbers assigned. Each gap k has two adjacent sub-channels $m(k)$ and $n(k)$.

Chapter 3

CFD simulations of the rod bundle flow

The results of this work are mainly based on the CFD-RANS simulations of rod bundle two-phase flows. The predictions of this method are based on a number of closure relations with empirical coefficients that were fitted to special boundary conditions. Therefore a calibration of the model coefficients to the desired boundary conditions has to be done and this needs to be validated against available experimental data. A validation exercise for single-phase rod bundle flow is presented in this chapter. Following that, a description of the simulation model is given with details for the geometry, the meshing parameters, the physical modeling and boundary conditions. In the end of this chapter, the CFD simulation results are presented.

3.1   Re-calculation of experimental investigations

In the open literature, the available experimental data for two-phase rod bundle flows at PWR pressure level with mixing vane spacers is very limited and often dedicated to the validation of sub-channel codes[1]. Detailed measurement data of the hydraulic effects of mixing vane spacers was found only for single-phase flow conditions at ambient pressure level. Therefore the CFD simulation results are compared with the data of the MATiS-H benchmark test published by Smith et al. [113] that provides detailed results for the velocity and turbulence field gained by LDV measurements. The main concepts of the simulation model that will be used for this work are examined for their influence on the solution. One of these concepts is the division of the simulation region into a plurality of sub-channel regions connected to each other by interface boundaries. Another concept is the choice of tabulated values as boundary conditions to provide a realistic distribution of the velocity and turbulence field at the edge of the solution domain. In addition, various types of meshing models are examined and the predictions of different turbulence models are compared with the experimental results.

The experimental test section was a 5×5 rod bundle scaled 2.6 times larger than a typical PWR bundle for a better accessibility for the optical measurements. The working fluid was single-

---

[1]De Crécy [24]

59

Tab. 3.1: MATiS-H geometrical specifications and flow conditions

Geometry		Operating Conditions	
Rod diameter	$d = 24.4\,\mathrm{mm}$	Fluid	water
Rod pitch	$p = 33.12\,\mathrm{mm}$	Pressure	$P = 1.569\,\mathrm{bar}$
Hydraulic diameter of bundle	$d_{hyd} = 24.27\,\mathrm{mm}$	Temperature	$T = 35\,^\circ\mathrm{C}$
Grid blockage ratio	$\epsilon_{int} = 0.4$	Bulk velocity	$u_b = 1.5\,\mathrm{m/s}$

phase water. The geometrical and operational conditions are listed in Tab. 3.1. As shown in Fig. 3.1, the test section contains a spacer grid upstream from the measurement section A-A. Two different types of mixing vane spacers were used in the experiments: (1) Split-type and (2) swirl-type mixing vane spacers. The following comparison with CFD results are made only with the split-type spacer. The spacer grid was axially movable to obtain different distances from the measurement section A-A.
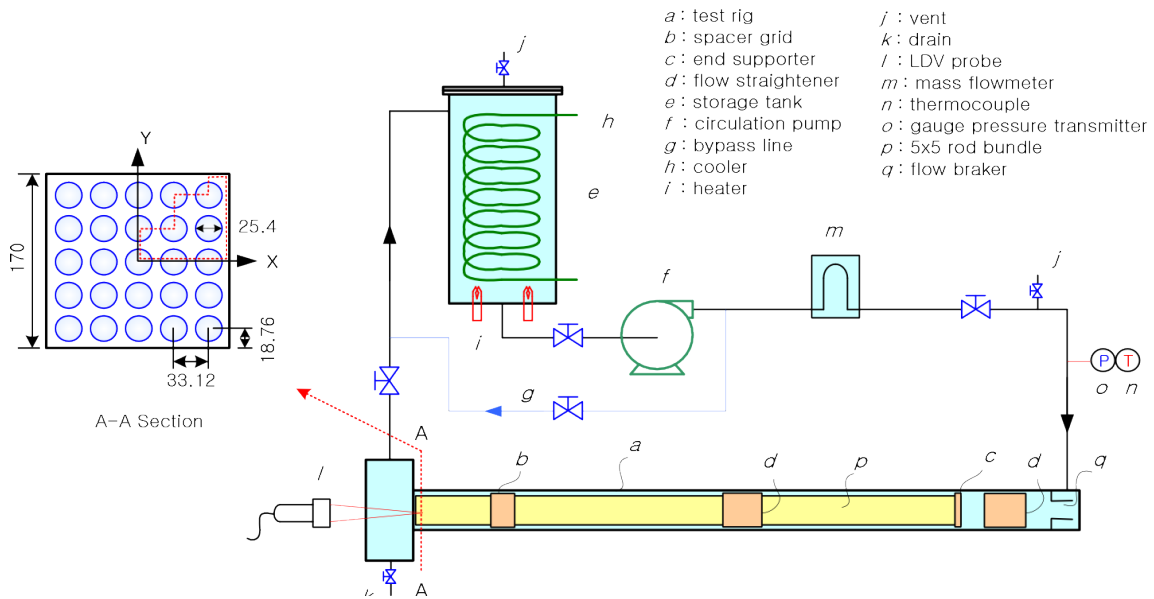
Fig. 3.1: Specifications of the MATiS-H test section

The CFD simulation model consists of a short inflow section upstream of the spacer grid and a downstream outflow section that contains the line probes for comparison with the experimental data. The position of these lines are shown in Fig. 3.2. The CAD model of the spacer grid contains the grid surfaces and the mixing vanes but not such geometrical details as springs or dimples. They were omitted in order to avoid a contact between the grid and the rod wall boundaries what could cause a worse mesh quality. In the following, several simulations were carried out to determine the influences of the inlet boundary conditions, the meshing model, interfaces and the turbulence model. The meshing parameters, except the mesh model, were kept constant using a base size of $l_{base} = 1\,\mathrm{mm}$ and 4 prism layers at the wall in order to obtain a $y^+ \approx 30$. Wall functions were used for the prediction of the velocity profile in the near-wall region. All simulations were calculated as steady state cases.
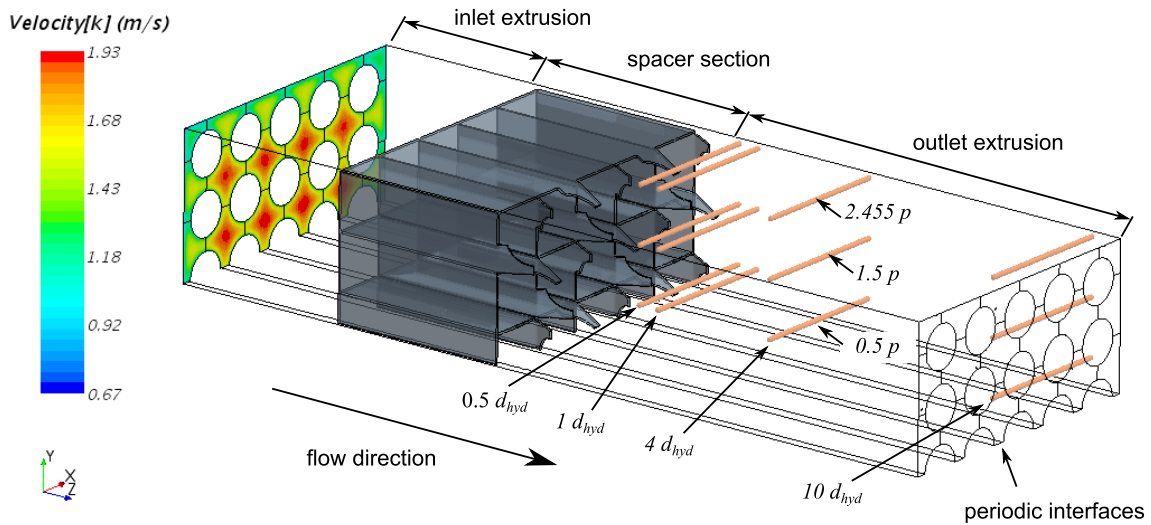
Fig. 3.2: CFD simulation model for the MATiS-H experiment

3.1.1 Influence of inlet boundary conditions

In the first step, the influence of the inlet boundary conditions was investigated. Three simulations were performed with (1) constant velocity profile, (2) periodic boundary conditions in axial direction and (3) a fully developed velocity profile at the inlet. The simulation results of the lateral velocity component u_x/u_b in Fig. 3.3 show that the influence of the three different methods for the boundary conditions is small. A good agreement with experimental data was achieved for all cases, whereas the case with periodic boundaries seems to have a slightly larger deviation than the other two cases.
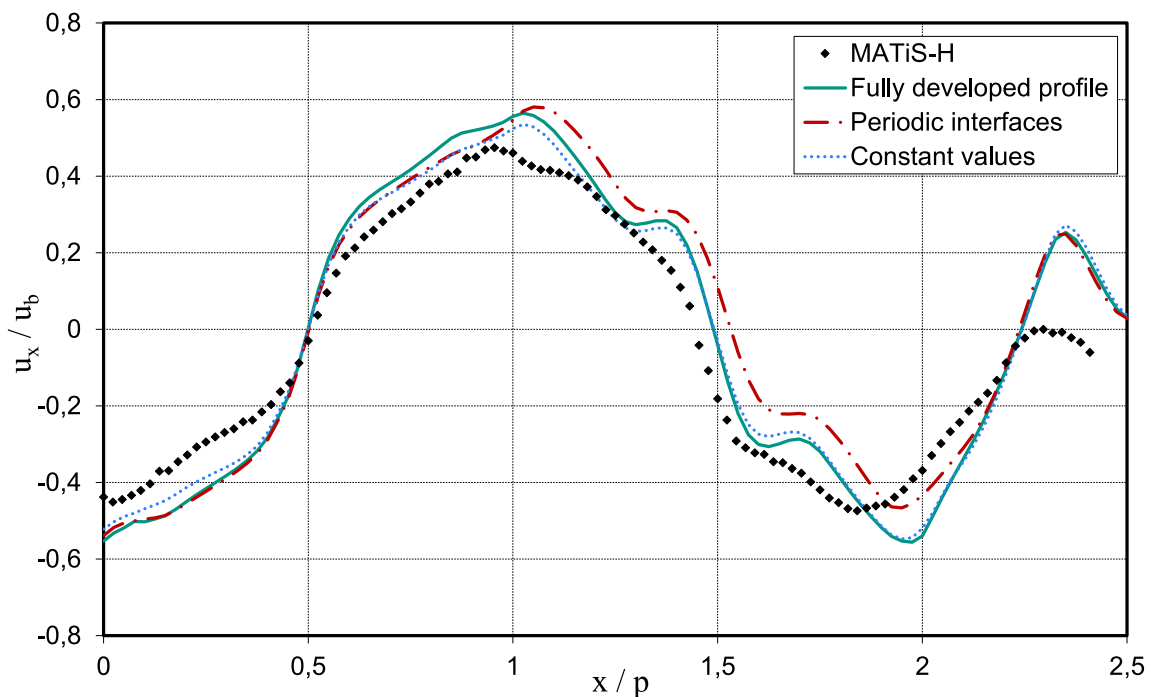
Fig. 3.3: Influence of boundary conditions at line $0.5p$ / $0.5d_{hyd}$

3.1.2 Influence of the meshing model

For the next step, two different meshes were created: (1) A polyhedral mesh, shown in Fig. 3.4a and (2) a trimmed mesh of hexaedras, shown in Fig. 3.4b. The mesh parameters for the cell size and for the prism layers were the same in both simulations. The cell numbers in case of the polyhedral mesh were about $6.3\,\mathrm{M}$ and in case of the trimmed mesh about $6.0\,\mathrm{M}$.

(a) Polyhedral mesh *(b) Trimmed mesh*
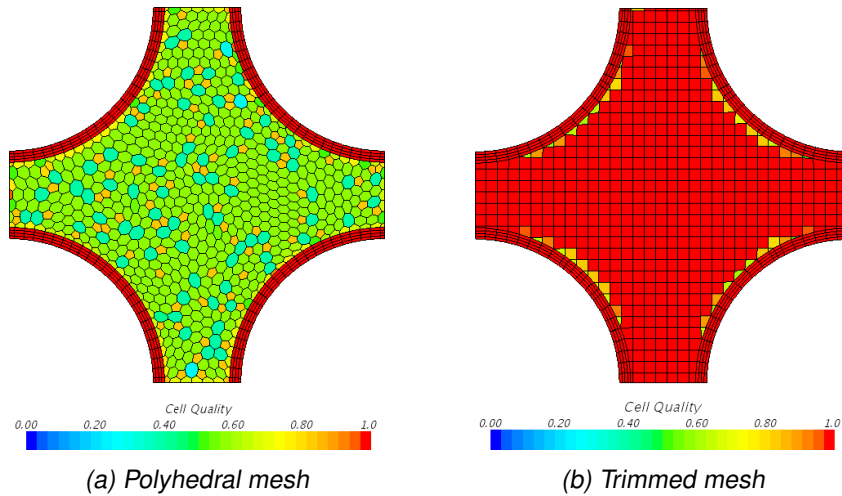
Fig. 3.4: Different volume meshing models and cell quality in an interior sub-channel

The CPU time per iteration step was $103.56\,\mathrm{s}$ in case of the polyhedral mesh and $77.78\,\mathrm{s}$ in case of the trimmed mesh. Convergence was achieved within 800 iteration steps with the polyhedral mesh and 1000 iteration steps with the trimmed mesh. The residuals are smaller and less oscillating in case of the trimmed mesh. This may be the consequence of the better mesh quality in case of the trimmed mesh. The results in Fig. 3.5 show that the trimmed mesh could produce a slightly better prediction of the lateral velocity component u_y/u_b.
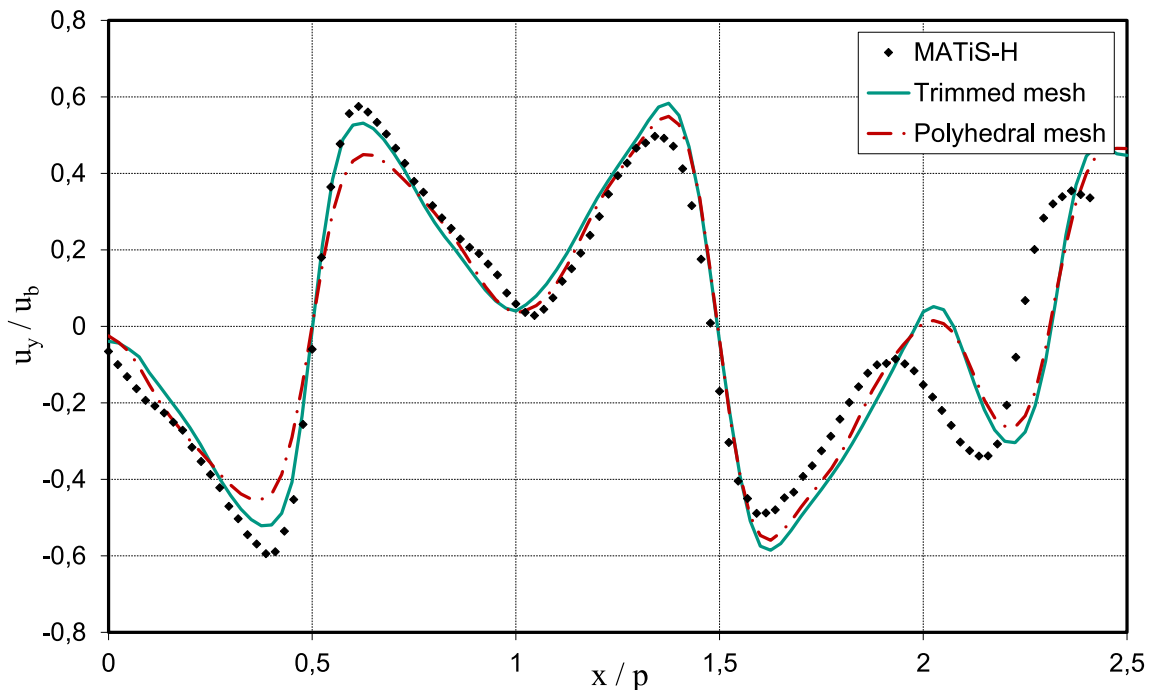
Fig. 3.5: Comparison of different meshing models at line $0.5p\,/\,0.5d_{hyd}$

3.1.3 Influence of a splitted geometry with interface connections

This work is concerned with the model development for sub-channel analysis. Therefore the sub-channel averaged data of the CFD simulation results are of main interest. For this purpose, it is convenient to logically define the individual sub-channel regions within the computational domain. These individual regions are connected by internal interfaces with each other. In this step, it is investigated, if this approach will produce deviations in the results. Two simulations were performed: (1) Computational domain with one single region without interfaces and (2) computational domain with individual sub-channel regions, connected by internal interface boundaries. All other settings were the same for both simulations.
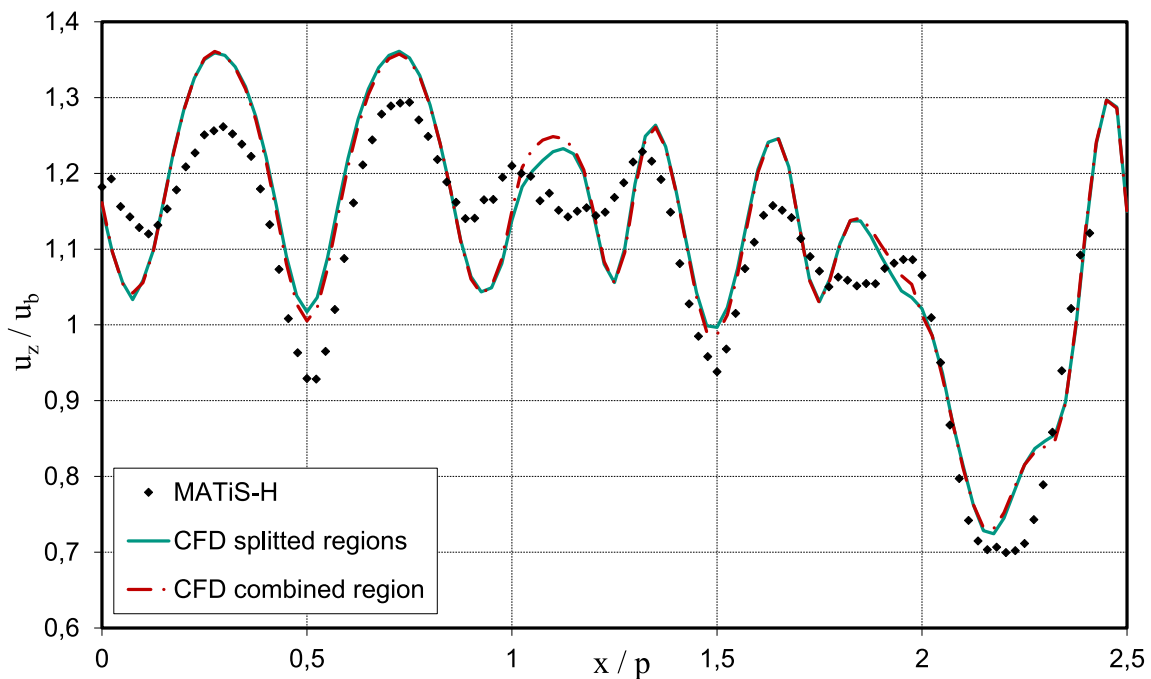
Fig. 3.6: *Influence of interfaces at line* $0.5p$ / $0.5d_{hyd}$. *Wall at* $x/p = 2.5$

The results in Fig. 3.6 show that almost no deviations between the two approaches occur. Only very small differences can be seen in the distribution of the axial velocity u_z/u_b next to an interface boundary at $x/p = 1$ and $x/p = 2$. Generally, there is an over-prediction of the axial velocity peaks in the interior channels of the bundle for all cases.

3.1.4 Influence of the turbulence model

In the next step, the influence of the turbulence model was investigated. The purpose of turbulence models is to predict the elements of the turbulent shear stress tensor resulting from the turbulent velocity fluctuations in the RANS equations. The predictions of four different models that are available in STAR-CCM+® 9.02.005 were compared:

- Realizable k-ε model with two-layer formulation and $y^+ = 1.5$

- Non-linear cubic k-ε model with $y^+ > 30.0$ and wall functions

- SST k-ω model with $y^+ > 30.0$ and wall functions

- SSG Reynolds Stress model with $y^+ > 30.0$ and wall functions
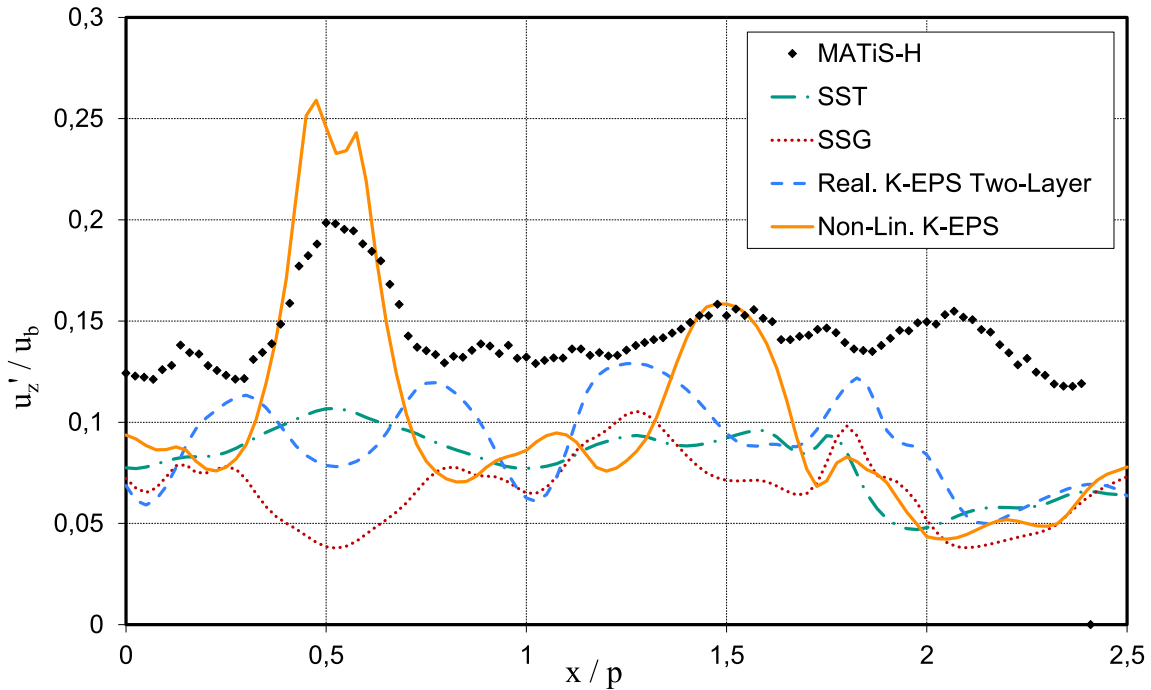
Fig. 3.7: Influence of turbulence model at line $0.5p\,/\,4d_{hyd}$.

In Figure 3.7 the axial velocity fluctuation u_z'/u_b from the experiment is plotted together with the simulation results. The formulation for the velocity fluctuation of the CFD data is different for the isotropic and non-isotropic turbulence models. In case of the SSG and the non-linear k-ε model, the square-root of the Reynolds stress $\sqrt{u_z'u_z'}/u_b$ is used and in case of the SST and Realizable k-ε model, the turbulent kinetic energy $\sqrt{2/3k}/u_b$ is used. The results in Fig. 3.7 show that the turbulence intensity in axial direction is generally under-predicted by nearly all turbulence models. The peaks of turbulence intensity in the center positions of the interior channels at $x/p = 0.5$ and $x/p = 1.5$ due to the swirling flow are only captured by the non-linear cubic k-ε model. In case of the Realizable k-ε model, no improvement can be seen due to a better resolution of the wall boundary layer, so wall functions might be sufficient.

3.1.5 Conclusions of validation exercise

- The mixing vane spacer dominates the mass flow distribution so there is only a little influence of the inflow parameter distribution. Following that, the simulation of only one span without information about the upstream flow can produce sufficiently good results.

- The simulation results are virtually the same for the case of a splitted domain compared to a single domain. Therefore the splitted domain approach will be used for the next simulations what will simplify the evaluation process.

- The trimmed mesh with hexahedral cells achieves smaller residuals and the simulation

results are a little closer to the experimental values compared to the polyhedral mesh. Also the computing time is shorter in case of the trimmed mesh.

- All turbulence models fail to predict the mean turbulence intensity downstream of the grid spacer. The peak of turbulence intensity in the vortex center at $x/p = 0.5$ is only qualitatively predicted by the non-linear cubic k-ε turbulence model. This model will be used for subsequent simulations in conjunction with wall-functions.

3.2 Description of the CFD simulation model

3.2.1 Geometry

This work is aimed to derive a new model for the flow sweeping caused by mixing vane spacers for the application in sub-channel codes. This new model needs to be validated with experimental data. Therefore the geometry of the NUPEC PSBT benchmark published by Rubin et al. [100] is applied to the CFD simulation model for the investigation of the hydraulic effects. The measured void fraction data of these experiments can be used as an indirect validation. The vapor generation and void distribution is, among others, a function of the distribution of mass flux and the mass flux distribution is a hydraulic effect that is strongly influenced by the mixing vanes. Within this publication, a detailed description of the geometry, the boundary conditions and the measurement results is given and all those parameters are within the range of LWR conditions.
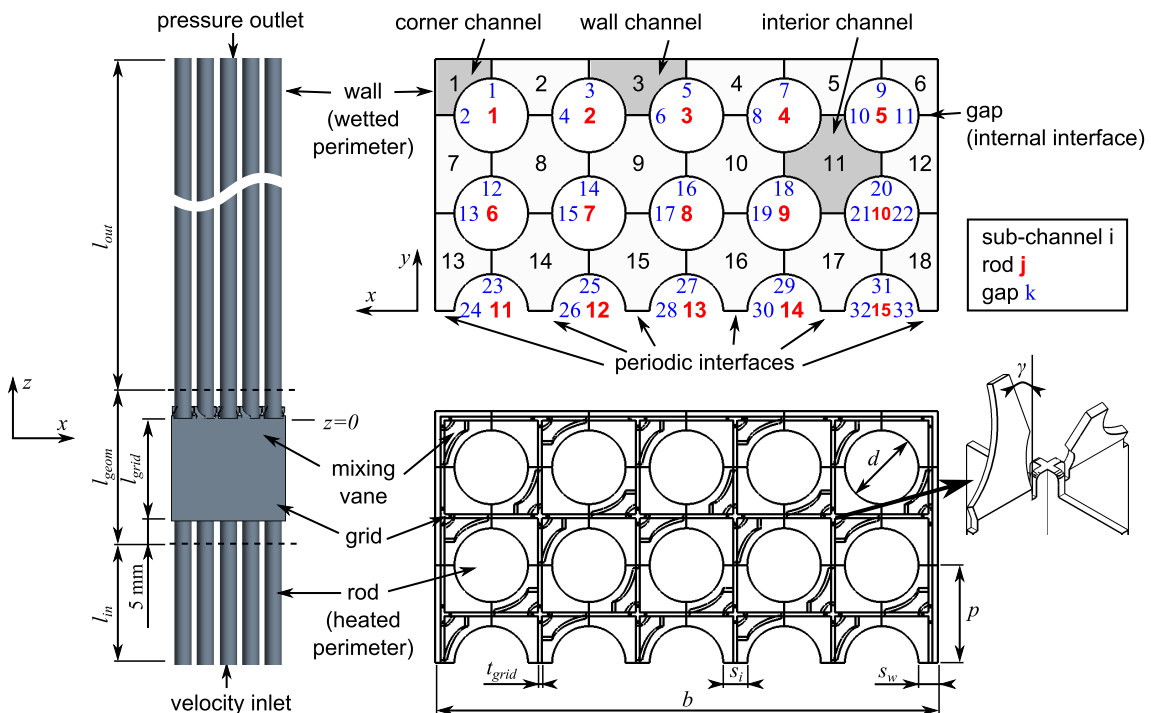
Fig. 3.8: Geometrical configuration of the CFD simulation model

The comparison of CFD results and the MATiS-H experimental data has shown that the simulation of one section of the rod bundle containing only one spacer and using periodic bound-

aries can give sufficiently accurate results. The same setup was used for the simulation model of the NUPEC PSBT geometry and it is shown in Fig. 3.8. The rod diameter $d = 9.5\,\text{mm}$ and rod pitch $p = 12.6\,\text{mm}$ are typical for PWRs. The experimental facility of [100] used a solid bounding box of width b around the rod bundle, which is more typical for BWRs. This configuration yields different shapes of the sub-channels. A CAD model of the rod bundle containing the spacer grid was created with the bundle length l_{geom}. During the meshing process, the inlet section was extruded to the length l_{in} and the outlet section was extruded to the length l_{out}. The angle of the mixing vane relative to the mean flow direction γ was constant. The values for the geometry parameters are given in Tab. 3.2.

Tab. 3.2: Bundle parameter values

Parameter	Value
Rod diameter	$d = 9.5\,\text{mm}$
Rod pitch	$p = 12.6\,\text{mm}$
Interior gap width	$s_i = 3.1\,\text{mm}$
Wall gap width	$s_w = 2.5\,\text{mm}$
Bundle width	$b = 64.9\,\text{mm}$
Spacer thickness	$t_{grid} = 0.5\,\text{mm}$
Mixing vane angle	$\gamma = 28\,°$
Spacer length	$l_{grid} = 55.88\,\text{mm}$
CAD geometry length	$l_{geom} = 75\,\text{mm}$
Inlet extrusion length	$l_{in} = 100\,\text{mm}$
Outlet extrusion length	$l_{out} = 600\,\text{mm}$

For the simulations, two different kinds of spacers were used: (1) A simple spacer without mixing vanes, shown in Fig. 3.9a and (2) a spacer with mixing vanes, shown in Fig. 3.9b. Both spacers have the same thickness t_{grid} and axial length l_{grid}, but in case of the simple spacer, an additional symmetry plane was introduced to reduce the size of the computational domain. That means that, with the simple spacer, one quarter of the whole bundle section was simulated and one half of the section in case of the mixing vane spacer. Additional geometrical features, such as springs and dimples on the spacer were omitted to obtain a better mesh quality as it was done for the MATiS-H geometry. The orientation of the mixing vanes is shown in Fig. 3.8.

Figure 3.8 also shows the convention for the numbering of sub-channels, gaps and rods. This numbering is used both for STAR-CCM+® 9.02.005 as well as for COBRA-FLX™. The CFD simulation model is split into separated regions, each representing a single sub-channel. The regions are connected with each other by internal interface boundaries that represent the gaps. This configuration enables the automated analysis of the simulation results on the base of clearly defined sub-channel regions. Considering the shape of the sub-channel cross-sections it can be distinguished between corner, wall and interior sub-channels. The gap width

(a) 90° *symmetry of the simple spacer*

(b) 180° *symmetry of the mixing vane spacer*
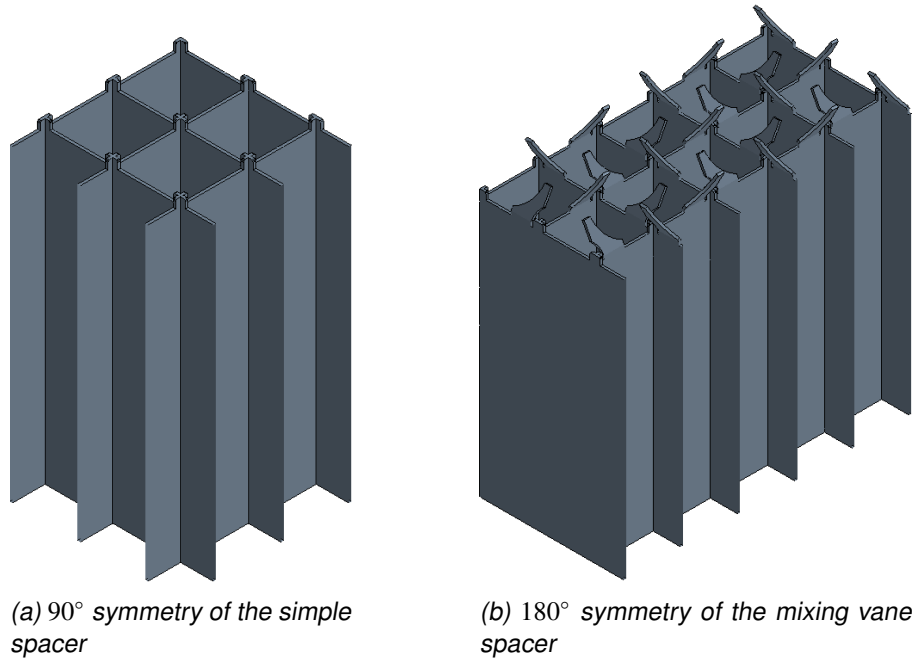
Fig. 3.9: Geometrical features of the grid spacers and cut along the symmetry planes

s_w between wall sub-channels is different from the gap width s_i between interior sub-channels. The values for the sub-channel parameters of cross-section area A, heated perimeter p_h, wetted perimeter p_w, hydraulic diameter d_{hyd} and the blockage ratios ϵ of the simple spacer and the mixing vane spacer for the three sub-channel types are given in Tab. 3.3.

Tab. 3.3: Sub-channel parameter values

Channel	A	p_h	p_w	d_{hyd}	ϵ_{simple}	ϵ_{mv}
Corner	$34.84 \, \text{mm}^2$	$7.46 \, \text{mm}$	$21.96 \, \text{mm}$	$6.35 \, \text{mm}$	0.16	0.39
Wall	$55.91 \, \text{mm}^2$	$14.92 \, \text{mm}$	$27.52 \, \text{mm}$	$8.13 \, \text{mm}$	0.16	0.31
Interior	$87.88 \, \text{mm}^2$	$29.85 \, \text{mm}$	$29.85 \, \text{mm}$	$11.78 \, \text{mm}$	0.14	0.34

3.2.2 Computational mesh

Since the geometric scale and the flow conditions of the simulation model designated for this work differ from the MATiS-H experiment, a complete mesh dependency study was performed for the geometry described above. STAR-CCM+® 9.02.005 provides an automatic meshing tool where the geometry and the mesh parameters have to be specified. In the first step, the meshing tool generates a surface mesh which is a discretized representation of the simulation model surface. In the second step, the mesh for the inner volume is created using a trimmed hexahedral mesh with prismatic cell layers next to solid surfaces. In order to find appropriate meshing parameters, two conflicting requirements must be met: (1) The accuracy of results should be high and it increases with mesh resolution and (2) the computational effort should be low, but it also increases with mesh resolution.

At first, the influence of the radial cell size was investigated. Therefore, three meshes were
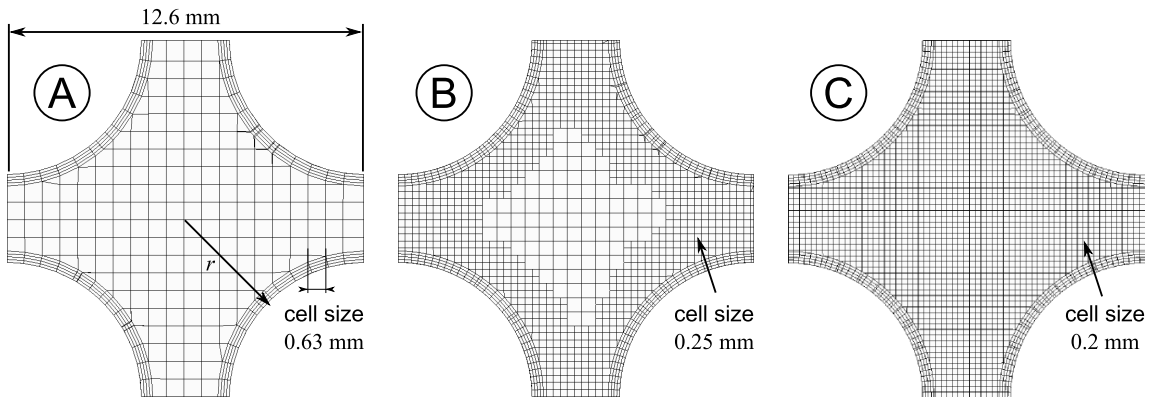
Fig. 3.10: Detail of mesh: Different cell size applied to the simulation

created with different values for the parameter of the surface mesh base size $l_{base} = 5\,\text{mm}$ (Mesh A), $1\,\text{mm}$ (Mesh B) and $0.1\,\text{mm}$ (Mesh C). The value for the relative minimum size was set to $l_{min} = 10\,\%$ and for the relative target size to $l_{target} = 200\,\%$ of the base size. That means that the actual cell size could vary between this range to fit the mesh to the geometry. The volume mesh was derived from the surface mesh and therefore the edge length of the volume mesh cells could be determined only indirect by those parameters. The cell sizes of the volume meshes are shown in Fig. 3.10.

Only a small section of an interior sub-channel with periodic boundaries was simulated. The bulk velocity of the single-phase water flow was set to $u_b = 9\,\text{m/s}$ as it was expected for the sub-channel with the highest mass flux and the highest Reynolds number with $Re = 929000$ within the range of the planned boundary conditions. This case had the highest velocity gradients and required therefore the finest mesh resolution. All cases had four layers of prismatic cells with a distance to the wall of the first mesh node of $\Delta l_{wall} = 0.08\,\text{mm}$. This resulted in a dimensionless wall distance of $y^+ \approx 300$. With this mesh, the minimum y^+ values were greater than 15 even for the smallest Re that was expected within the desired range of boundary conditions. So wall functions could be applied in all subsequent simulations.

The result of the radial cell size study is plotted in Fig. 3.11 and shows that there is only a small influence of the radial cell size on the interpolated axial velocity profile on the line shown in Fig. 3.10. In the case of mesh A with the base size $l_{base} = 5\,\text{mm}$, the axial velocity is slightly smaller in the channel center compared to the other two cases. A base size value of $l_{base} = 1\,\text{mm}$ will produce a mesh with a sufficient resolution. There are no significant changes in the axial velocity profile if the cell size is further decreased.

At next, the influence of the axial cell size l_{ax} is investigated. Three simulations of a single sub-channel containing a spacer with mixing vanes were performed with the same extrusion length $l_{out} = 0.6\,\text{m}$ and different values for the number of extrusion layers. Additionally, in one case a geometric progression of the extrusion layer length was applied with a finer mesh resolution behind the spacer. The ratio of the last extrusion layer length to the first one was $l_n/l_1 = 4.0$. Following cases were simulated:

1. Mesh D: Axial cell size $l_{ax} = 3\,\text{mm}$ and constant node distribution.

2. Mesh E: Axial cell size $l_{ax} = 1.5\,\text{mm}$ and constant node distribution.
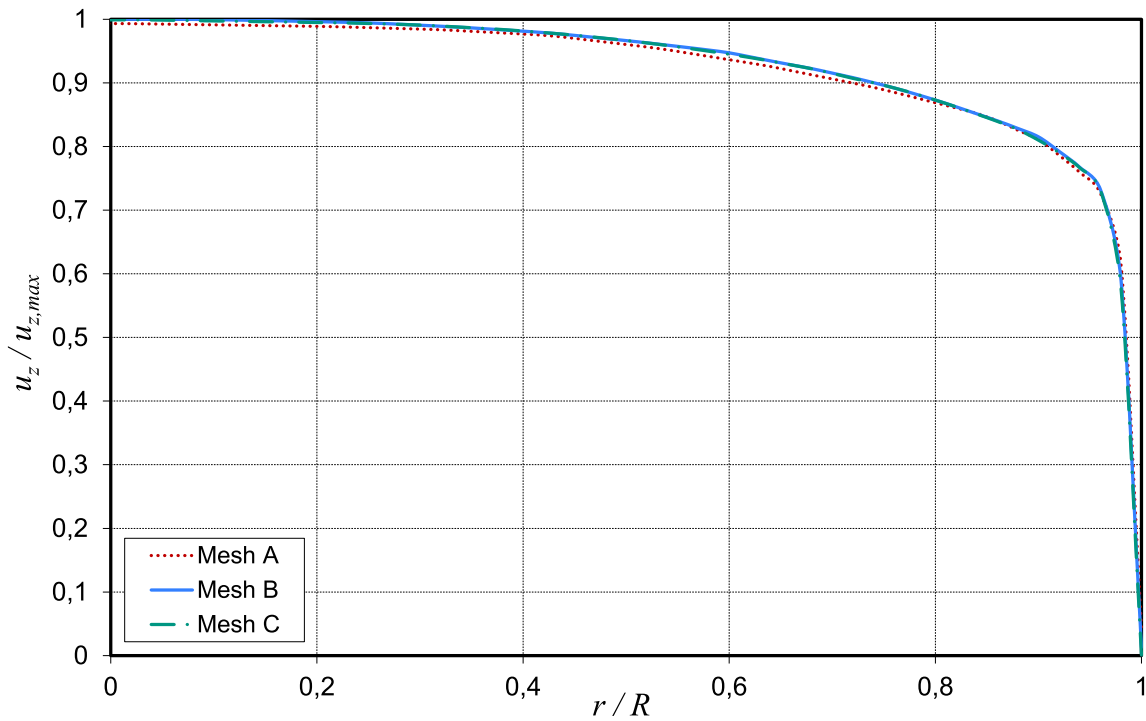
Fig. 3.11: Mesh size study: Radial distribution of axial velocity (single-phase)

3. Mesh F: Axial cell size $l_{ax} = 1\,\text{mm}$ and constant node distribution.

4. Mesh G: Same node number as in mesh D but with progressive cell length. The last cell is four times larger than the first one.
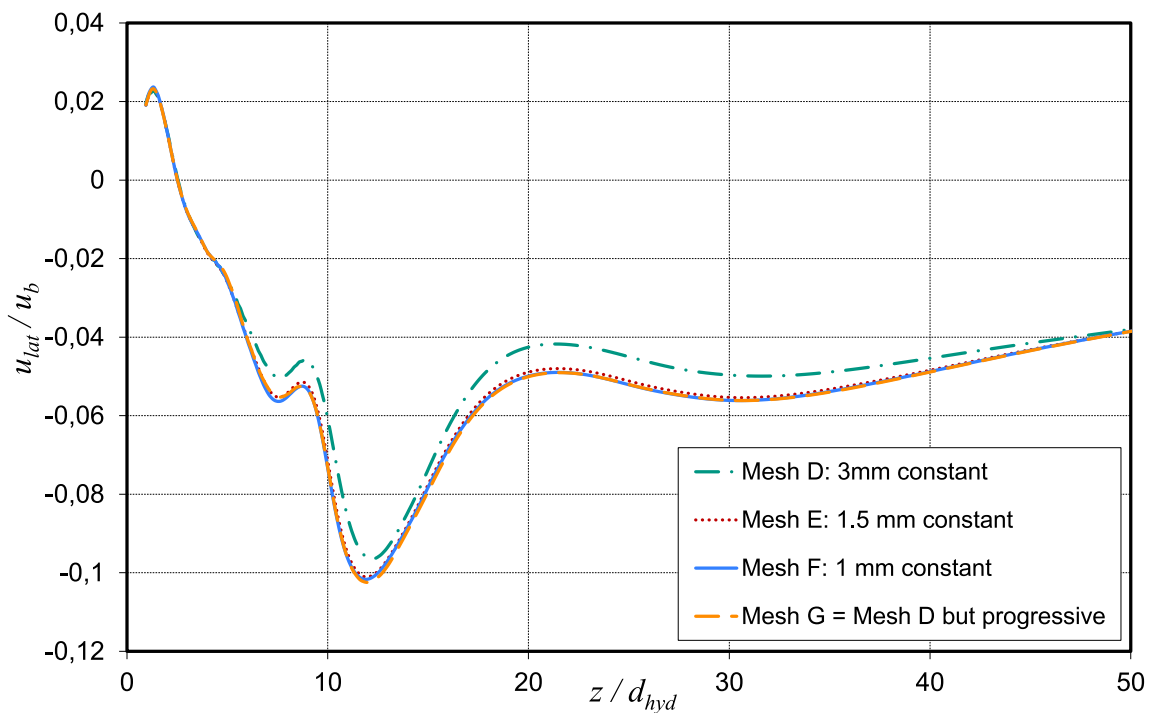
Fig. 3.12: Mesh size study: Axial distribution of radial velocity (single-phase)

The result of the axial cell size study is plotted in Fig. 3.12 and shows the axial distribution of lateral velocity on the center line of the gap behind the mixing vane spacer. In the case

of mesh D a different lateral velocity distribution was predicted compared to the other cases. A significant improvement can be obtained if a geometric progression of the cell lengths is used. This will produce nearly the same results as with an increased number of cells in axial direction.

The mesh for the whole simulation model was created with the parameters found in the mesh dependency study. It contains $2\,\mathrm{M}$ cells in case of the simple spacer geometry and $5.8\,\mathrm{M}$ cells in case of the mixing vane spacer geometry. It meets following quality criteria:

- There are no *negative volume cells* within the mesh continuum

- The maximum *cell skewness angle* is $85.0\,^\circ$.

- All cell faces have a *face validity* of 1. This means that the face normal vectors pointing outward of cell centroid. If some face normal vectors pointing towards the cell centroid, then the face validity is smaller than 1.

- The minimum *volume change* is $1.03{\cdot}10^{-3}$. This is the ratio of the volume of two neighbor cells. A perfect value would be 1 if both cells have the same size.

3.2.3 Physical modeling

All of the 3D-RANS simulations were run under steady state conditions. For the two-phase flow simulations, an Euler-Euler two-fluid model was chosen. The turbulence of the liquid phase was modeled by the non-linear cubic k-ε model that is defined in Eq. 2.56 and was adapted by Baglietto et al. [6] for the application in rod bundle geometries with the coefficients given in Eq. 2.57 – 2.62. This model is able to predict secondary flows in non-circular channels and the prediction of the turbulence intensity at swirling flow in the vicinity of the mixing vane spacer grid of the MATiS-H experiment was better than the standard k-ε or the SST turbulence model, although it showed also large deviations. Compared to a Reynolds stress model, it saves much computational time. Wall functions were used to predict the velocity and turbulent quantities in the near wall region.

The turbulence of the dispersed phase was modeled using the turbulence response model by Issa and Oliveira [40], because at low void fractions under high pressure the bubble diameter is very small and therefore the turbulence field of the dispersed phase is strongly determined by the turbulence of the continuous phase. The model equations were shown in Eq. 2.65 – 2.68. The bubble diameters were influenced by coalescence and breakup effects that were modeled using the S-γ [63] model in Eq. 2.75. The gravity vector $\vec{g}$ was in negative axial direction.

The inter-phase momentum transfer was modeled using the drag force model of Bozzano and Dente [10] that can be applied to high pressure conditions. A drag correction model of Richardson and Zaki [86] was used to account for the effects of bubble swarms. The lift force that acts perpendicular to the flow direction was modeled using the model of Tomiyama et al. [119], because it is sensitive to the bubble size. The wall lubrication force was computed using the model of Antal et al. [2]. The models applied to the CFD simulations are listed in Tab. 3.4.

No wall boiling was simulated in order to avoid a superposition of the hydraulic effects with the heat transfer and evaporation effects.

Tab. 3.4: Modeling of physical effects in the simulation model

Effect	Model
Turbulence of the liquid phase	Baglietto et al. [6]
Gravity	$\vec{g}(x, y, z) = (0.0, 0.0, -9.81)\,\mathrm{m/s^2}$
models only for two-phase flow simulations	
Turbulence of the dispersed phase	Issa and Oliveira [40]
Bubble coalescence and breakup	S/γ model (Lo and Zhang [63])
Drag force	Bozzano and Dente [10], Richardson and Zaki [86]
Turbulent dispersion force	Burns et al. [12]
Lift force	Tomiyama et al. [119]
Wall lubrication force	Antal et al. [2]

3.2.4 Boundary conditions

A wide range of boundary conditions was applied to the simulation model to cover the BWR and PWR operating range. Therefore two different pressure levels, five levels of mass flux and four levels of void fraction were applied. With the two different spacer geometries, a total number of 80 simulations were performed. The average void fraction was limited to $\alpha_g = 15\%$ in order to obtain a bubbly flow regime with a homogeneous distribution of both phases. With larger void fractions, different flow regimes, such as slug flow or annular flow, can be expected. These flow regimes are characterized by a pronounced phase interface and should be better simulated using the VOF method which was not used in this work.

The temperature of the fluids was set to the corresponding saturation temperature for each pressure level, so both phases can exist simultaneously. The no-slip walls were smooth and set as adiabatic, because the modeling of wall boiling was omitted and this work. Therefore the material properties could be assumed to be constant. The range of boundary conditions and the material properties used are shown in Tab. 3.5. The boundary conditions cover a Reynolds number range between $Re = 80000\dots680000$ and a thermal equilibrium quality between $x_e = 0.0\dots0.038$ as Fig. 3.13 shows.

Tables containing data for phase velocity, turbulent quantities and void fraction were applied to the inlet boundaries. In order to obtain these data, simulations were performed in a rod bundle geometry without a spacer but with periodic boundaries in axial direction. This method provides a mass flow and void distribution of a fully developed rod bundle flow and ensures that the redistribution of flow quantities downstream of the grid spacer is only the effect of the spacer itself, but not because of the different sub-channel shapes.

Tab. 3.5: Material properties and boundary conditions

Property	Symbol	Unit	Value	
Pressure	P	bar	80	175
Temperature	T	K	568.16	627.82
Surface tension	σ	N/m	0.015507	0.0028039
Liquid density	ρ_l	kg/m³	722.2	554.66
Vapor density	ρ_g	kg/m³	42.507	126.12
Liquid viscosity	μ_l	Pas	$8.7766 \cdot 10^{-5}$	$6.3466 \cdot 10^{-5}$
Vapor viscosity	μ_g	Pas	$1.9397 \cdot 10^{-5}$	$2.4595 \cdot 10^{-5}$
Void fraction	α_g	–	0.0, 0.05, 0.1, 0.15	
Mass flux	G	kg/m²s	700, 1500, 2500, 3500, 4500	
Heat flux	q''	kW/m²	0.0	
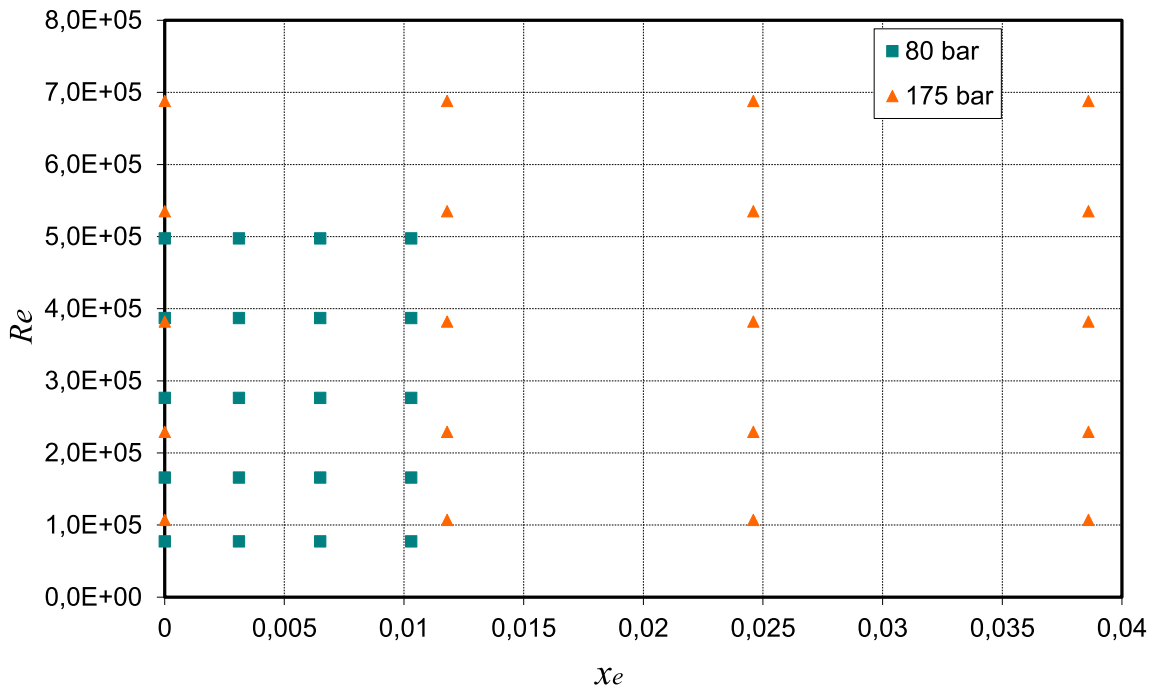
Fig. 3.13: Range of boundary conditions applied to the simulation model

3.2.5 Solver settings and convergence

In STAR-CCM+® 9.02.005, the SIMPLE algorithm is used to solve the discretized basic equations. The gradients are computed by the Hybrid-Gauss-Least-Square method. The discretization of the convection terms were 1st order for the volume fraction and 2nd order for the velocity and turbulence terms. Secondary gradients were included to the diffusion terms. The simulation was assumed to be converged, if the residuals remained constant and have dropped by three orders of magnitude compared to the average value of the first five iterations and if the continuity condition for both the water and vapor phase was fulfilled.

(a) Single-phase

(b) Two-phase
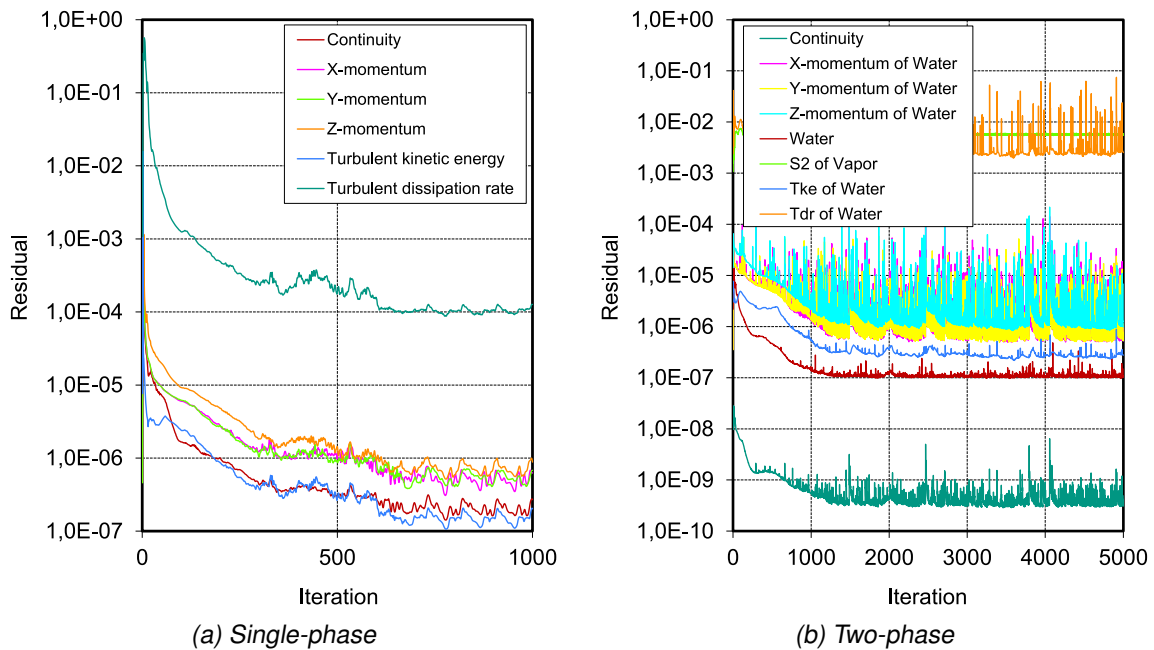
Fig. 3.14: Residuals of iteration steps during convergence

In the single-phase flow simulations, convergence was achieved mainly after 1000 iteration steps as Fig. 3.14a shows. The largest residual remains in the turbulent dissipation equation, but with an order of 10^{-4}, it satisfies the convergence criterion. In the two-phase flow simulations, a larger fluctuation of the residuals compared to single-phase flow can be seen in Fig. 3.14b. The largest residuals remain in the turbulent dissipation equation for water and the interfacial area concentration equation (S2) for the vapor phase.The residuals decrease until 2000 iteration steps what is twice as long as in single-phase flow.

3.3 Post-processing using JAVA macros

After convergence of the simulation runs, the results were evaluated for each individual sub-channel and for each gap. Therefore, several axial positions were defined and the flow parameters shown in Tab. 3.6 were averaged over the whole sub-channel cross-section or the gap section between two axial positions respectively. Those averaged results were written into two text files for further evaluation. The first of these text files had the same format as the COBRA-FLX^{TM} output files and, in this way, the results of both codes could be compared easily. The second text file contained the averaged flow parameters and additional parameters, such as model coefficients. These values could be used to describe the Flow Sweeping effect or to derive the input parameters for the empirical models in COBRA-FLX^{TM}.

Because of the large amount of data, the evaluation of the CFD results was done by using a JAVA macro. The steps of the evaluation algorithm are shown in Fig. 3.15. This macro was applicable both to single-phase and two-phase simulations using the different formulations of the flow parameters shown in Tab. 3.6 that were equivalent to the COBRA-FLX^{TM} formulations. It was self-adapted to the geometry and the computational mesh, so it could be used for arbitrary rod bundle configurations.

73

Tab. 3.6: Field function formulations in STAR-CCM+® 9.02.005

Function	Symb.	Unit	Single-Phase	Two-Phase
Void fraction	α_g	–	0.0	α_g
Pressure	P	Pa		P_{stat}
Density	ρ_m	kg/m³	ρ	$\alpha_g\rho_g + (1-\alpha_g)\rho_l$
Mass flux	G	kg/m²s	ρu_{ax}	$\alpha_g\rho_g u_g + (1-\alpha_g)\rho_l u_l$
Flow quality	x_f	–	0.0	$\frac{\alpha_g\rho_g u_g}{\alpha_g\rho_g u_g+(1-\alpha_g)\rho_l u_l}$
Specific volume	v'	m³/kg	$\frac{1}{\rho}$	$\frac{x_f^2}{\alpha_g\rho_g} + \frac{(1-x_f)^2}{(1-\alpha_g)\rho_l}$
Dynamic Viscosity	μ	Pas	μ	μ_l
Turbulent Viscosity	μ_t	Pas	μ_t	$\mu_{t,l}$
Hydraulic Diameter	d_{hyd}	m		$\frac{4A}{P_w}$
Reynolds number	Re	–		$\frac{G d_{hyd}}{\mu_l}$
Lateral Momentum	$\dot{M}_{lat}$	Pa	$\rho(u_x^2 + u_y^2)$	$\frac{1}{v'}\cdot\left[\left(\alpha_g u_{g,x} + (1-\alpha_g)u_{l,x}\right)^2 + \left(\alpha_g u_{g,y} + (1-\alpha_g)u_{l,y}\right)^2\right]$
Turbulent mixing	C_β	–		$\frac{\mu_t}{l_t \overline{G}}$
Diversion cross-flow	w	kg/ms	$\frac{1}{\Delta z}\cdot\int\rho u_{lat}s\,dz$	$\frac{1}{\Delta z}\cdot\int[\alpha_g\rho_g u_{g,lat}+(1-\alpha_g)\rho_l u_{l,lat}s]dz$

All results obtained from the simulations are documented in the following section. The plots showing the axial development of a flow parameter represent the averaged values of a particular sub-channel or a particular gap on the y-axis and the normalized axial position on the x-axis wherein the hydraulic diameter d_{hyd} of the current sub-channel was used for normalization. The plots showing the radial distribution of a flow parameter always show the smoothed distributed results from CFD.

3.4 Results of the CFD simulations

3.4.1 Pressure distribution

Figure 3.16 shows the axial static pressure distribution within an interior sub-channel with different spacer types and with different void fractions. Both phases share the same pressure field. The pressure decreases monotonically from the inlet to the outlet with a constant rate, except when the flow passes the spacer region. In this region, the pressure drop is strongly increased with a higher pressure drop for the mixing vane spacer than for the simple spacer. This is due to the higher blockage of the sub-channel flow area by the mixing vane spacer with $\epsilon_{mv} = 0.34$ rather than $\epsilon_{simple} = 0.14$ for the simple spacer. The presence of a vapor
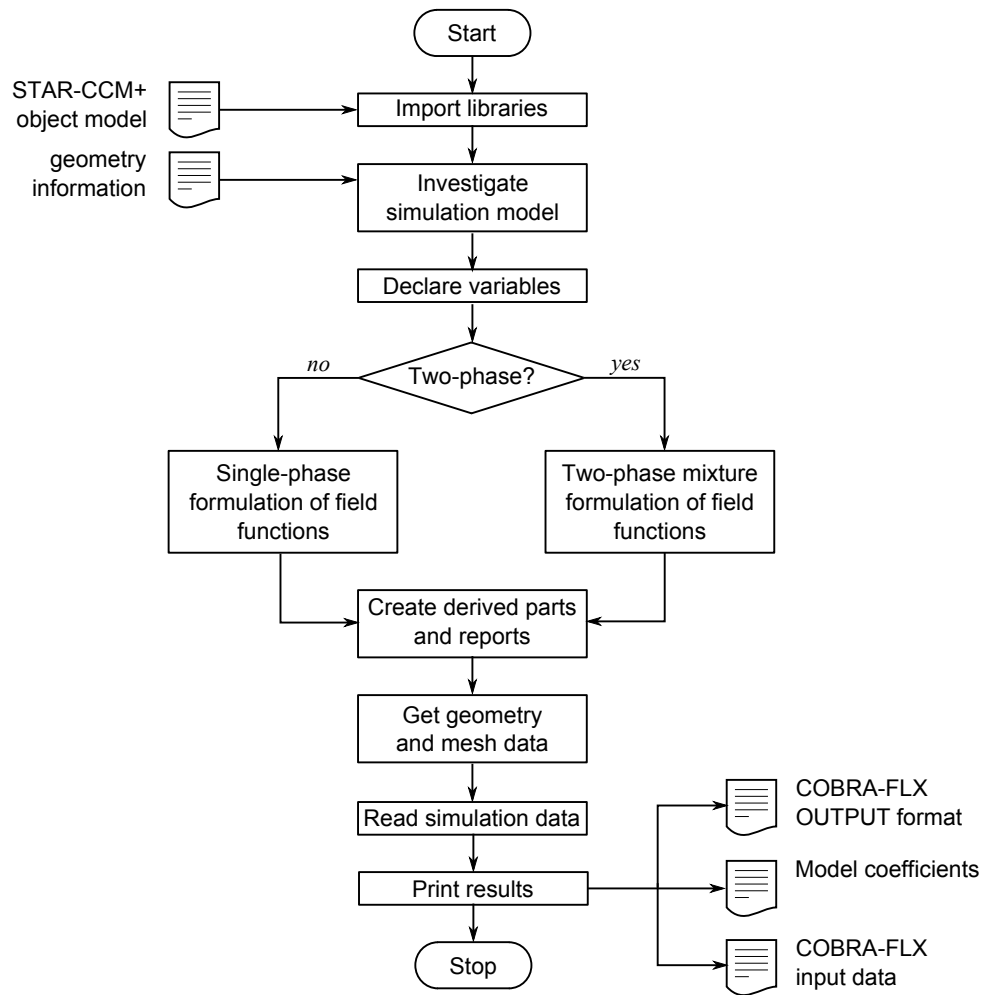
Fig. 3.15: Flowchart of evaluation macro

fraction increases the overall pressure loss. In the region between $0 - 10$ hydraulic diameters downstream of the mixing vane grid, the pressure loss is smaller than in the remainder of the channel. This is assumed to be the result of a strong swirling flow that is caused by the mixing vanes. Vortices are formed around a center of low static pressure. This low pressure area vanishes when the swirl flow intensity is decreasing.

The overall pressure loss is the sum of different effects (Eq. 3.1): (1) An acceleration pressure loss ΔP_a because of area and density changes. In single-phase flow, this part is zero outside of the spacer region due to constant channel cross-sections and a constant density. In the two-phase flow cases, the density changes only with a change of void fraction. Due to the isothermal conditions, the void fraction is redistributed by the grid spacer. (2) A hydro-static pressure loss ΔP_g due to gravity. In single-phase flow this part has the same values in all sub-channels due to constant density. In the two-phase flow cases, the density depends on the void fraction of the sub-channels. (3) The friction and local loss ΔP_f and ΔP_d due to solid boundaries and blockages and the viscosity of the fluid. These parts are investigated herein afterwards. (4) The transfer of momentum to other sub-channels because of cross-flow or turbulent mixing also influences the pressure balance of a sub-channel.
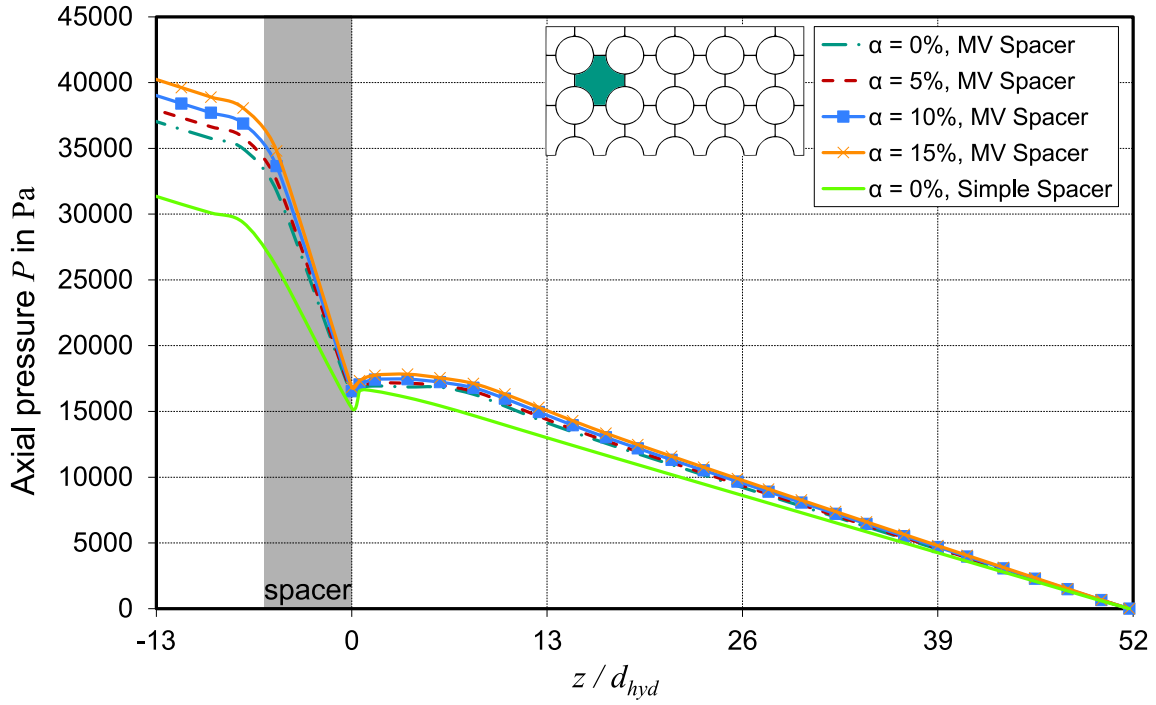
Fig. 3.16: *Axial development of pressure drop in interior channel at different void fractions with P =* 175 bar *and G =* 4500 kg/m²s

$$\Delta P = \sum_k P_k = \Delta P_a + \Delta P_g + \Delta P_f + \Delta P_d + \Delta P_t + \Delta P_{cf} \qquad (3.1)$$

Pressure drop due to acceleration ΔP_a, gravity ΔP_g, wall friction ΔP_f, spacer drag ΔP_d, turbulent mixing ΔP_t, diversion cross-flow ΔP_{cf} in Pa

Wall friction factor for single-phase flow

The pressure loss due to wall friction on the rod surfaces can be described by a wall friction coefficient[2] C_f, defined in Eq. 3.2. The friction pressure loss ΔP_f was computed from CFD by evaluating the wall shear stress in axial direction exerted on the fluid by the rod surface boundaries of each sub-channel, see Eq. 3.3. The axial distribution of the wall friction coefficient is not constant, but influenced by the spacer grid as shown in Fig. 3.17. This results from the disturbance of the velocity field and the breakup of the hydrodynamic boundary layer due to the spacer grid. The section that is influenced by the spacer grid is much longer in case of the mixing vane spacer than in case of the simple spacer. The higher friction coefficient behind the mixing vane spacer is due to a lower Reynolds number.

In order to obtain a correlation for the wall friction coefficient for each sub-channel, averaged values of C_f results were used. Only regions far away from a grid spacer that show a constant value for C_f were considered for the averaging to exclude the spacer influence. Figure 3.18 shows the results for different sub-channel types as function of Reynolds number. The wall friction factor is higher with a greater hydraulic diameter and decreases with increas-

---

[2]also called Darcy friction factor

76
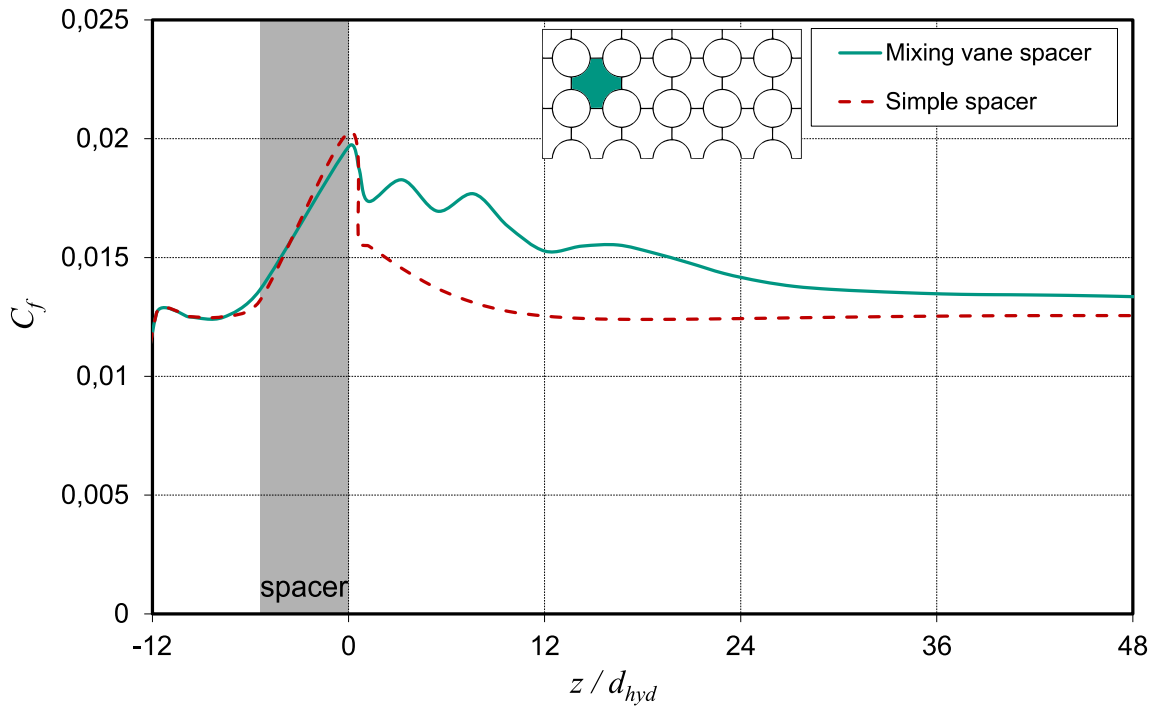
Fig. 3.17: *Axial distribution of the wall friction coefficient in an interior channel with different spacers and with* $P = 175$ bar, $G = 4500$ kg/m²s *and* $\alpha = 0\%$

ing Reynolds number with a constant slope. The results show a good agreement with the correlation developed by Cheng and Todreas [17] (Eq. 3.4) for interior channels of a square array with $p/d = 1.326$ and fully turbulent single-phase flow.

$$C_f = \frac{2\Delta P_f d_{hyd}}{\Delta z \rho u_z^2} \qquad (3.2)$$

$$\Delta P_f = \frac{\tau_{w,rod} \cdot A_{rod}}{A_{ax}} \qquad (3.3)$$

$$C_f = 0.153 \cdot Re^{-0.18} \qquad (3.4)$$

Friction pressure loss ΔP_f in Pa, hydraulic diameter d_{hyd} and axial length of evaluation section Δz in m, density ρ in kg/m³, average axial velocity in sub-channel u_z in m/s, wall shear stress on rod surface $\tau_{w,rod}$ in Pa, rod surface area A_{rod} and sub-channel cross-section A_{ax} in m², Reynolds number Re

The method that was used for the evaluation of the wall friction factor from the CFD results were only applicable for single-phase flow cases in STAR-CCM+® 9.02.005. Therefore the two-phase wall friction was not subject of the current investigations.

Spacer loss coefficient

The pressure loss due to drag forces on the spacer grid can be described by the spacer loss coefficient C_d that is defined in Eq. 3.5. There are two methods to evaluate the local pressure loss ΔP_d from the CFD results. In the first method (Eq. 3.6), the local pressure loss is the difference between the overall pressure drop between two axial positions ΔP, the frictional
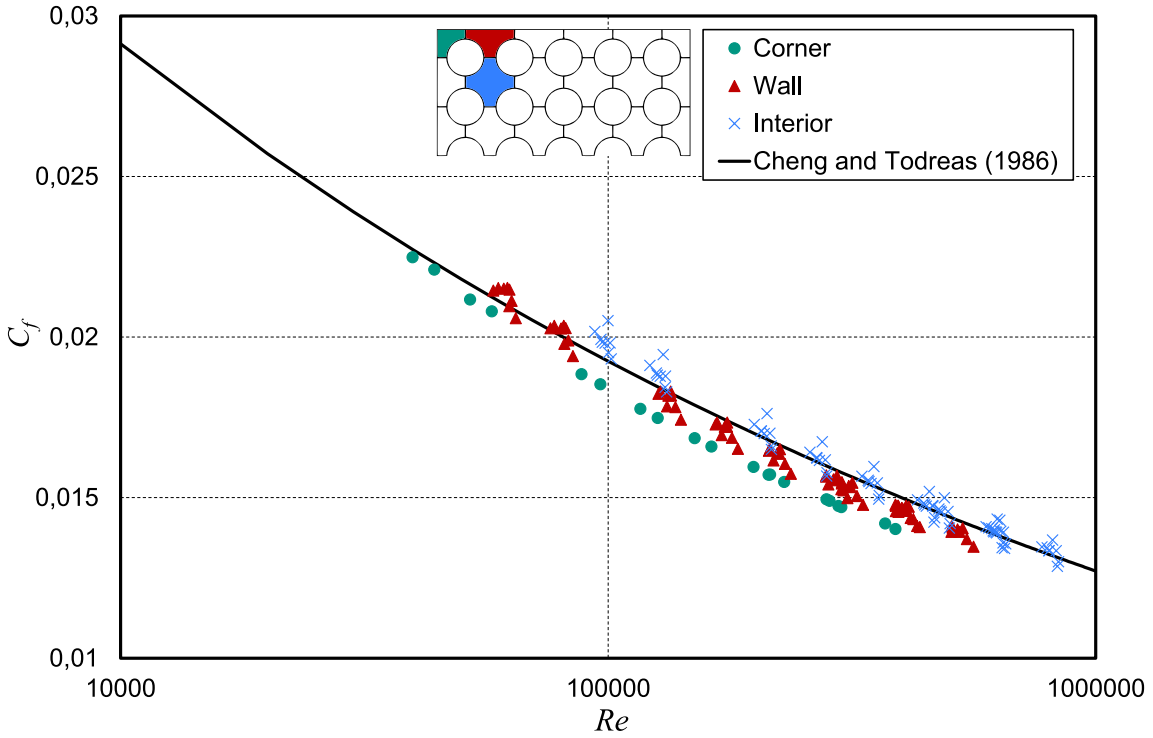
Fig. 3.18: Single-phase flow wall friction coefficient for different sub-channel types

pressure drop ΔP_f (Eq. 3.3) and the gravitational pressure drop ΔP_g (Eq. 3.7). This would be valid in case of flow in a single pipe. In rod bundle flow, there is an interconnection with adjacent sub-channels with a convective cross-flow and also a turbulent mixing over the length Δz that change the axial momentum. Furthermore, the frictional pressure drop ΔP_f is not constant in the spacer region, but it is affected by the spacer itself and also by the cross-flow. Therefore, a second method was developed, shown in Eq. 3.8. This method integrates the wall shear stress and the pressure in axial direction over the grid spacer surface and relates this value to the sub-channel cross-section. This method neglects spacer effects such as a local acceleration and the breakup of streamlines that happen in the flow because it considers only the forces on the spacer surface.

$$C_d = \frac{2\Delta P_d}{\rho u_z^2} \tag{3.5}$$

$$\Delta P_d^{(1)} = \Delta P - \Delta P_f - \Delta P_g \tag{3.6}$$

$$\Delta P_g = \rho g \Delta z \tag{3.7}$$

$$\Delta P_d^{(2)} = \frac{\oint_{A_{grid}} \left(\tau_{w,grid} + P_{grid}\right) dA_{grid}}{A_{ax}} \tag{3.8}$$

Local pressure loss due to channel blockage ΔP_d in Pa, density ρ in kg/m³, average axial velocity in sub-channel u_z in m/s

Figure 3.19 shows the results for different sub-channel types as a function of Reynolds number. The drag coefficient differs between the sub-channel types because of the different block-

age ratio. For $Re < 200000$, there is a strong increase of the drag coefficient with decreasing Reynolds number, whereas for $Re \geq 200000$ the slope of decreasing drag coefficient is much smaller. The results for pressure loss coefficients can be used as input parameters for a COBRA-FLX^{TM} simulation.
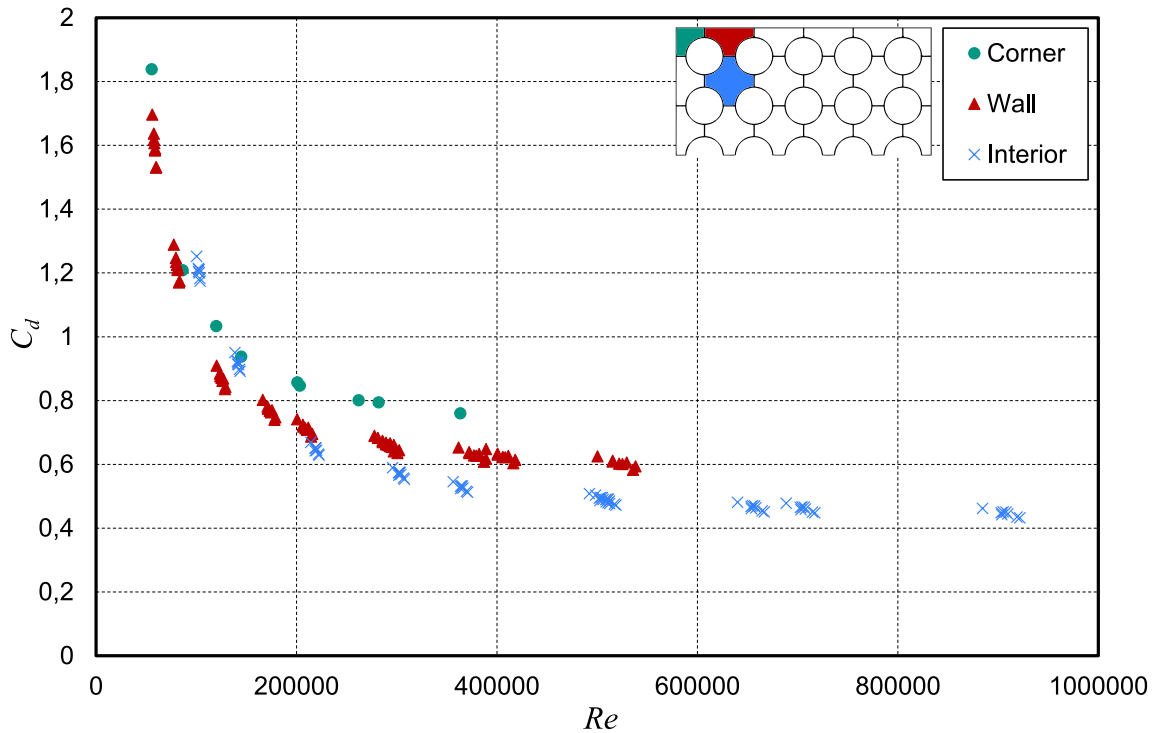
Fig. 3.19: Single-phase flow spacer drag coefficient for different sub-channel types

3.4.2 Velocity distribution

Some details for the influence of mixing vanes on the velocity field are plotted in Fig. 3.20. This figure shows the three velocity components along a line in an interior sub-channel along different axial positions. Due to the mass flow redistribution between the individual sub-channels, the axial velocity and therefore the local Reynolds number changes with the axial position. Due to this reason, the results were normalized with the bulk velocity of the whole bundle, $u_b = G/\rho = 8.11\,\mathrm{m/s}$ that is constant over the whole bundle length outside of the spacer region. Because of this, the normalized axial velocity at $10\,d_{hyd}$ is lower than at $-10\,d_{hyd}$, which is a result of the mass flow redistribution, as Fig. 3.20a shows. The axial velocity profile at $10\,d_{hyd}$ upstream of the spacer has the shape of a fully developed velocity profile. Due to the two mixing vanes in the interior channel, the axial velocity profile has a symmetrical shape with two peaks traveling from the wall towards the channel center between $0.5\,d_{hyd}$ and $1\,d_{hyd}$ downstream of the spacer. After $10\,d_{hyd}$ downstream of the spacer, the axial velocity profile approaches again the shape of the fully developed flow but is still asymmetrical.

The radial velocity components, which are almost zero before the grid, have also a symmetrical shape behind the grid and reveal a strong swirling flow. Later, the radial velocity components become asymmetrical at $10\,d_{hyd}$ behind the grid. Here the velocity field seems to be not longer dominated by the swirling flow.

(a) Axial velocity profile

(b) Radial velocity profile in x-direction

(c) Radial velocity profile in y-direction
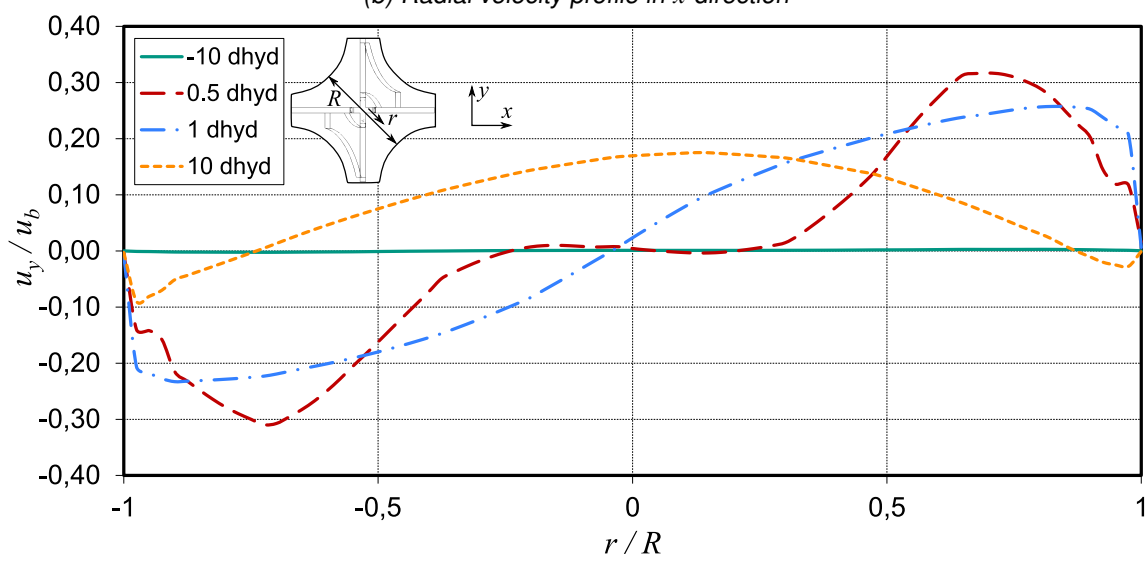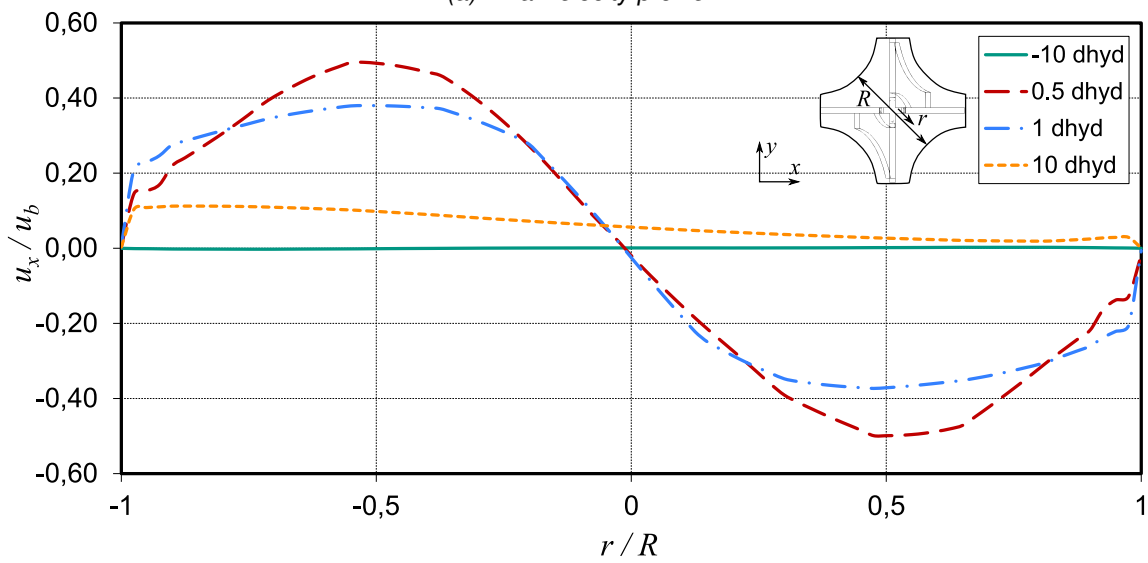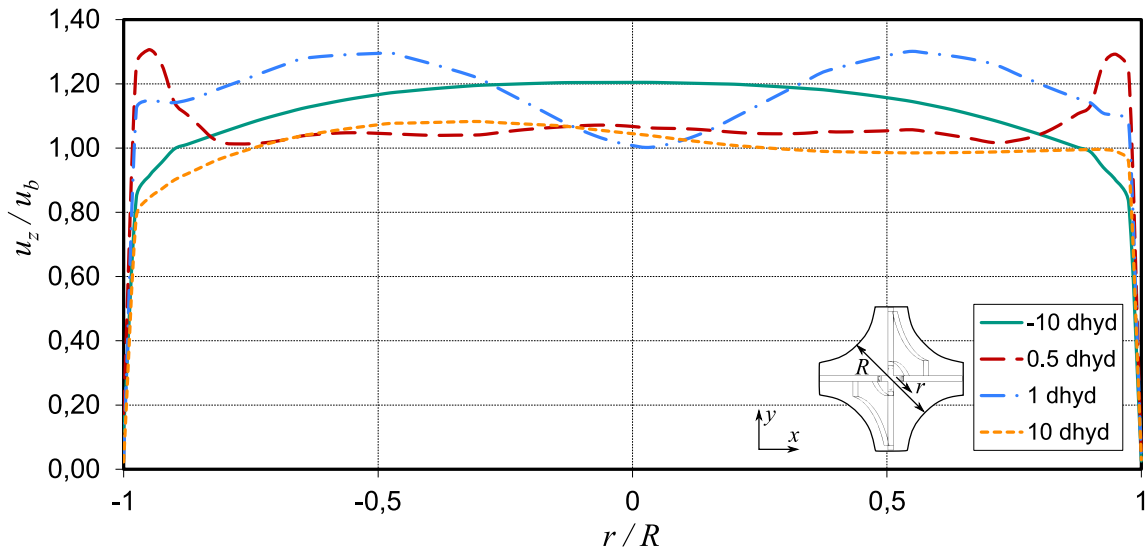
Fig. 3.20: Velocity profiles in an interior sub-channel at $P = 175\,\mathrm{bar}$, $G = 4500\,\mathrm{kg/m^2 s}$ and $\alpha = 0\%$

Mass flux in sub-channels

The mass flux distribution within sub-channels is remarkably affected by the mixing vanes. Figure 3.21 shows the relative mass flux in the two simulated corner channels. The Mass flux is plotted in relation to the bundle averaged mass flux. The difference between the two channels is a mixing vane in Channel 1 (CH 1), whereas Channel 6 (CH 6) has no mixing vane. Before the grid, both channels have nearly the same mass flux that is about 75% of the bundle average mass flux. Due to the blockage of the vane, the mass flux in CH 1 drops strongly down to 55% and in CH 6 the mass flux rises. After a distance of $48p$ downstream from the grid the mass fluxes have not reached the same value as it was before the grid. Figure 3.21 also shows the influence of Reynolds number. With a higher average mass flux through the rod bundle, the relative mass flux in corner channels is higher.
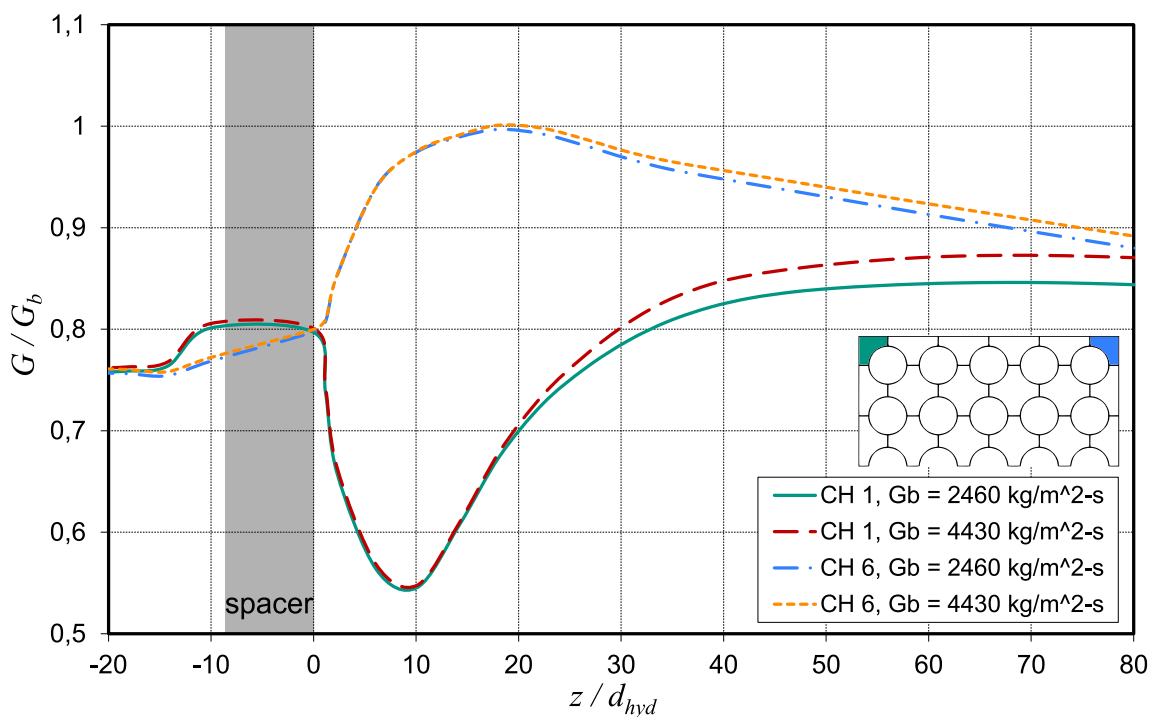
Fig. 3.21: Axial development of mass flux in corner channels with different Reynolds numbers and $\alpha_g = 0\%$

The interior channels have a higher relative mass flux compared to the corner channels, depending on their position within the rod bundle. Channel 8 (CH 8) is neighbored by two other interior channels and two wall channels and has a lower relative mass flux than channel 15 (CH 15) that is neighbored by four interior channels and is located in the center of the bundle. The effect of mixing vanes is that the relative mass flux in the interior channels decreases, after a short region of increase directly behind the grid, see Fig. 3.22.

The mass flux drops faster in CH 8, whereas the mass flux level in CH 15 is maintained by the surrounding interior channels until the . After a long distance the mass flux still not reached the fully developed values what shows the great impact of the mixing vane spacer. The inflow profile for a subsequent spacer would be therefore influenced, depending on the distance between two spacers.
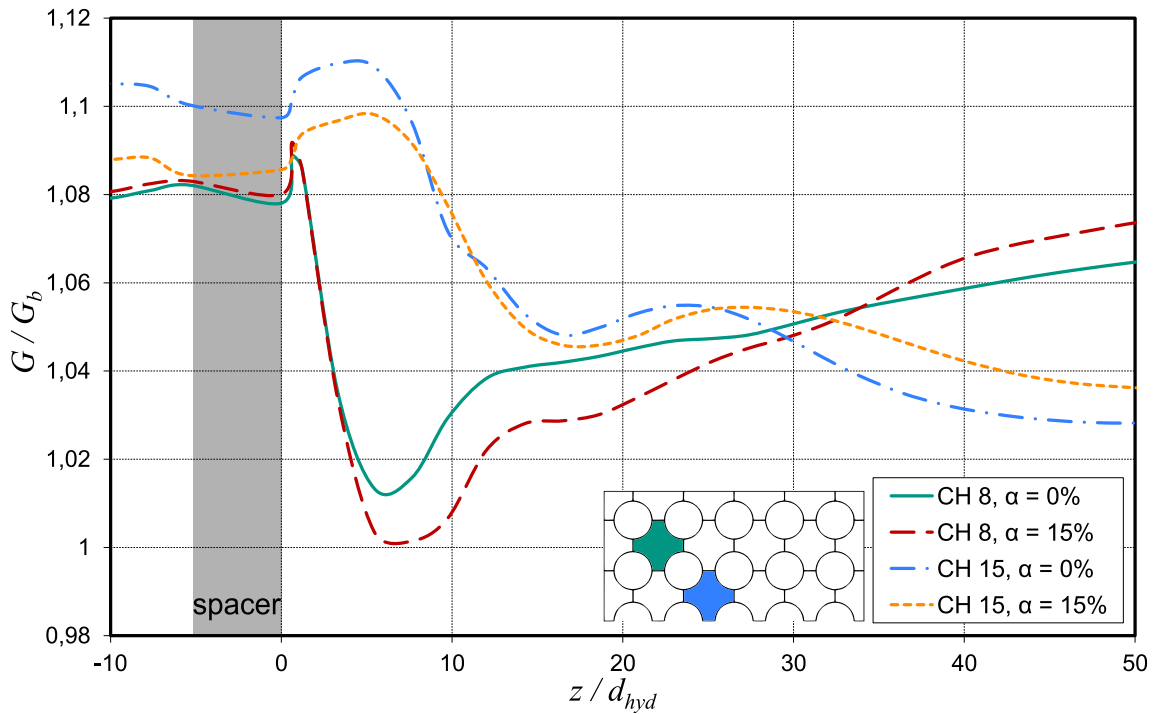
Fig. 3.22: Axial development of mass flux in interior channels with different void fractions and $G = 4430\,\mathrm{kg/m^2s}$

The dashed curves in Fig. 3.22 show that the axial development of the mixture mass flux (defined in Tab. 3.6) also depends on the void fraction. For the understanding of the development of the axial mass flux a closer view to the cross-flows through the gaps is necessary.

Cross-flows through the gaps

The sign convention for the cross-flow is positive, if it flows from the channel with lower ordering number into the channel with higher ordering number and negative vice versa. The channel numbers are defined as shown in Fig. 3.8. As Figure 3.23 shows, the cross-flow velocity u_{lat} in the case of the simple spacer in gap 14 is very small compared to the cross-flow with mixing vane spacers. In the latter case, the peak of cross-flow is located about 3 hydraulic diameters behind the grid edge and is about 20% of the mean axial velocity. The direction is determined by the orientation of the mixing vane. As can be seen in Fig. 3.23, the axial development of cross-flow is different in each gap. In gap 14, there is a change of cross-flow direction, whereas in gap 16 the direction does not change. That might be a consequence of the different position of those gaps within the rod bundle. The dashed curve in Fig. 3.23 shows the void fraction influence. After the position of the maximum, the magnitude of cross-flow in case of $\alpha_g = 15\%$ is smaller than in the single-phase case. That shows that the presence of void decreases the cross-flow velocity what explains the different mass flux distributions in Fig. 3.22.
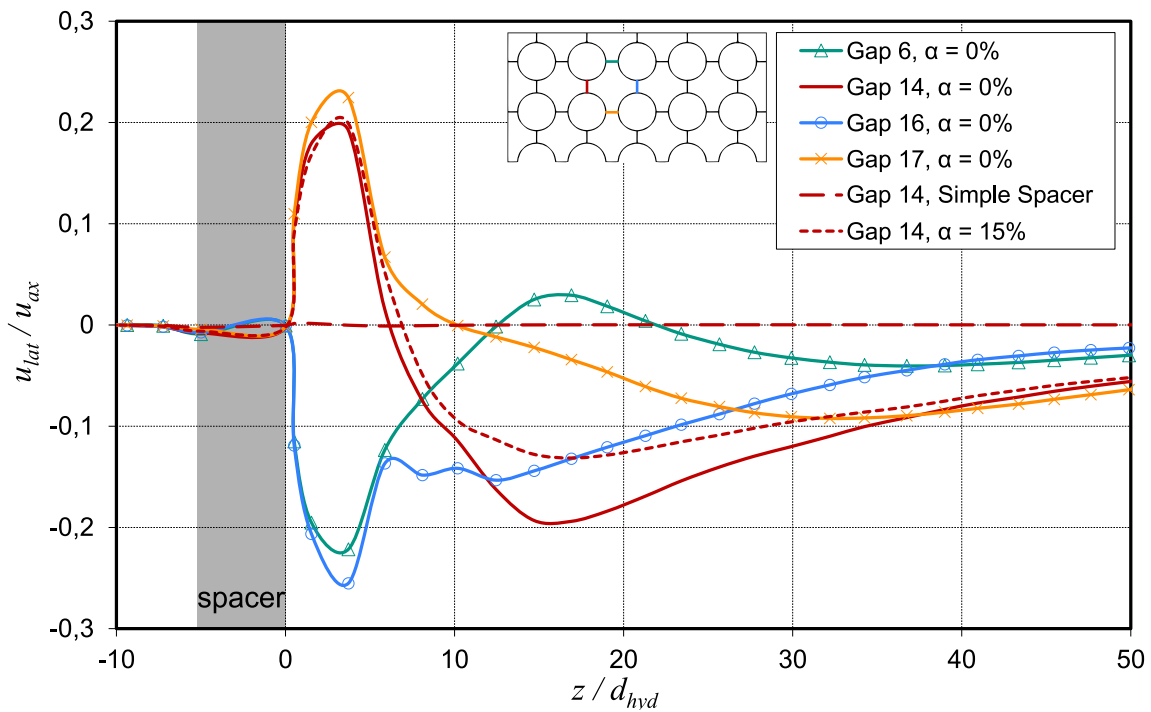
Fig. 3.23: Axial development of cross-flow through different gaps with $P = 175$ bar and $G = 4500\,\mathrm{kg/m^2 s}$

Lateral velocity in sub-channel center

The most significant feature of mixing vanes is the generation of a strong lateral velocity component in the sub-channel flow. Figures 3.24 – 3.27 show the distribution of lateral velocity vectors at different axial positions for the mixing vane and the simple spacer. Upstream of the spacer position, in both cases the flow is undisturbed and contains secondary flow cells (Fig. 3.24b and 3.24a). The magnitude of secondary flow is in the order of 1% of the axial flow velocity. One hydraulic diameter downstream of the top of the spacer grid significant differences between the spacer types can be observed. In case of the simple spacer, the flow structure is only slightly disturbed and the lateral velocity is increased but without showing any regular flow pattern (Fig. 3.25a). In case of the mixing vane spacer, a strong swirling flow is created at the tip of each mixing vane. In the interior sub-channels with two mixing vanes, the two vortices form together a large vortex with an elliptic shape. In the gap regions, there are smaller vortices that are also formed by the mixing vanes (Fig. 3.25b). These flow patterns are also observed experimentally[3]. At $z/d_{dhyd} = 5$ downstream of the mixing vane spacer, the two vortices in the interior sub-channels merge together forming a circular vortex and the vortex center is traveling towards the rod surfaces in some cases (Fig. 3.26b), whereas after the simple spacer the secondary flow cells are redeveloping (Fig. 3.26a). At $z/d_{dhyd} = 20$, the lateral flow field is completely recovered (Fig. 3.27a), but in case of the mixing vane spacer, still a large lateral velocity component exists, but without a regular pattern since the vortices vanished completely (Fig. 3.27b).

---

[3]Conner et al. [22]
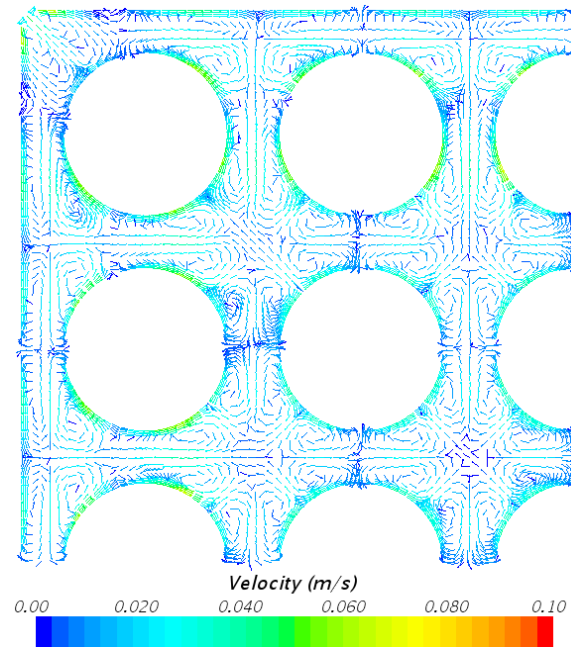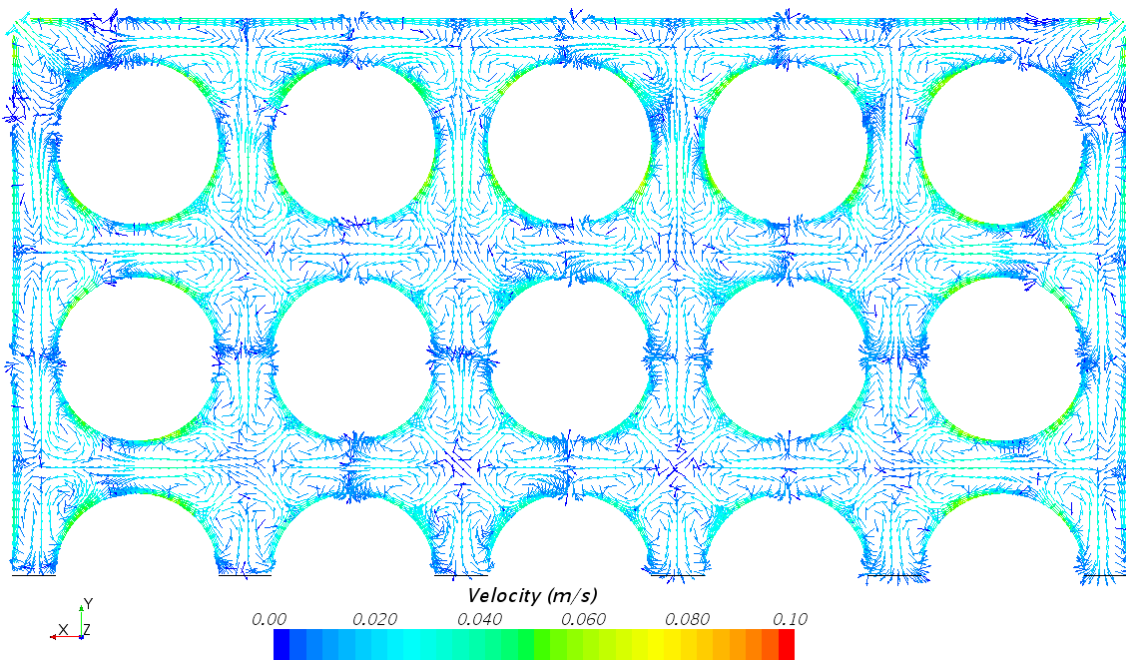
(a) Simple spacer

(b) Mixing vane spacer

Fig. 3.24: Lateral velocity distribution at $P = 175$ bar, $G = 4500\,\mathrm{kg/m^2s}$, $\alpha = 0\%$, $z/d_{hyd} = -10$
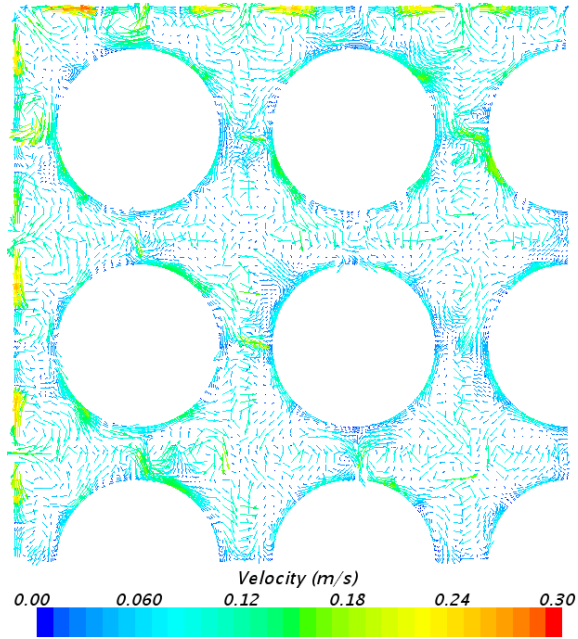
(a) Simple spacer
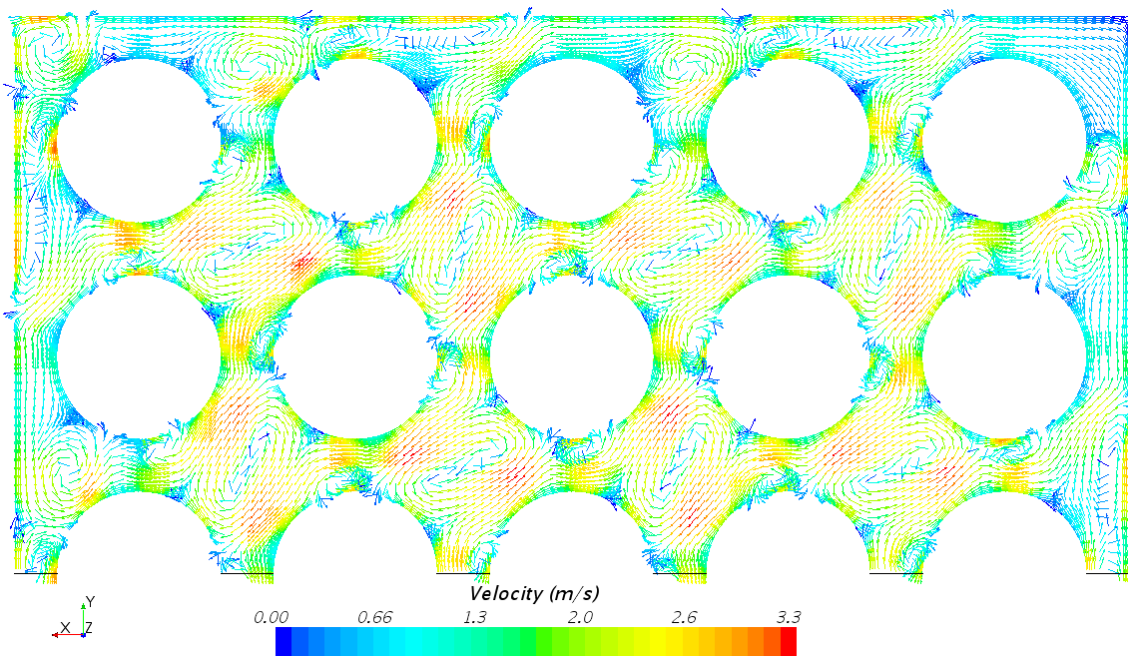
(b) Mixing vane spacer

Fig. 3.25: Lateral velocity distribution at $P = 175\,\mathrm{bar}$, $G = 4500\,\mathrm{kg/m^2 s}$, $\alpha = 0\%$, $z/d_{hyd} = 1$
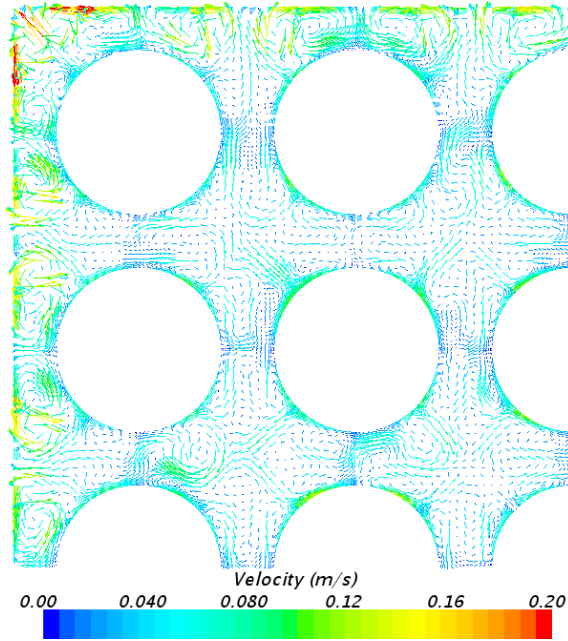
(a) Simple spacer
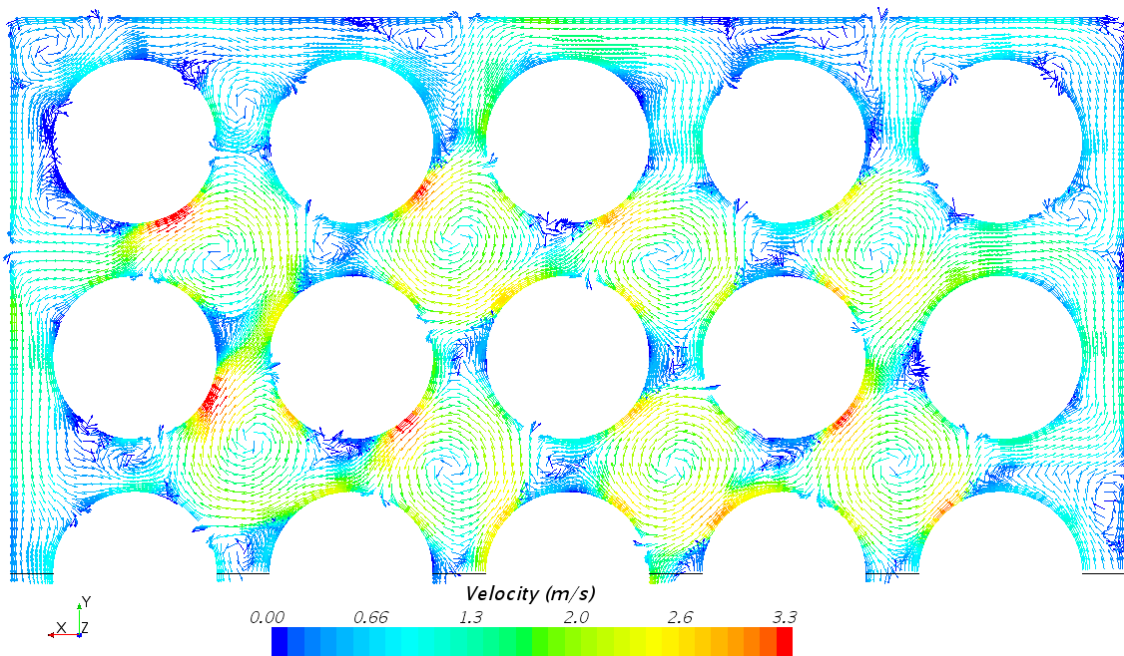
(b) Mixing vane spacer

Fig. 3.26: Lateral velocity distribution at $P = 175$ bar, $G = 4500$ kg/m²s, $\alpha = 0\%$, $z/d_{hyd} = 5$
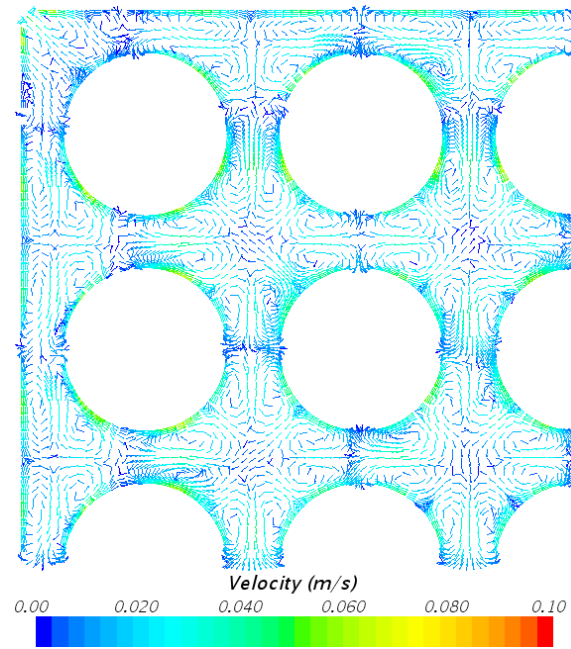
(a) Simple spacer
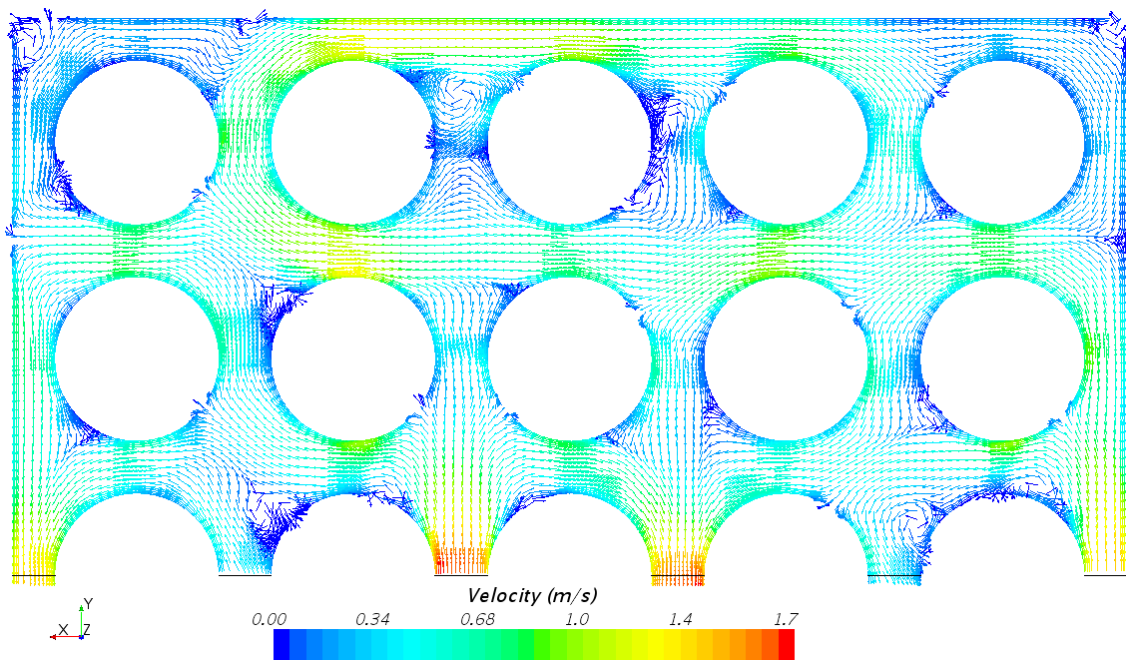
(b) Mixing vane spacer

Fig. 3.27: Lateral velocity distribution at $P = 175$ bar, $G = 4500 \, \mathrm{kg/m^2 s}$, $\alpha = 0\%$, $z/d_{hyd} = 20$

For the quantification of the swirling flow, a formulation has to be found. In literature, the swirling flow is often described by the circulation Γ[4] (Eq. 3.9) or the angular momentum Ω[5] (Eq. 3.10). If the surface integral of these formulations cover the whole sub-channel, then the result would be distorted by the counter-rotating small vortices close to the gap that can be seen in Fig. 3.25b. Therefore the integration should be done only for the main central vortex area, but here the vortex radius $\vec{r}$ and the vortex center position has to be known that can move within the sub-channel as it can be seen in Fig. 3.26b. Because of those limitations, a different and simple definition for the lateral momentum was chosen for this work that represents the sum of all lateral velocity components, see Eq. 3.11. This formulation can be integrated over the whole sub-channel area.

$$\Gamma = \frac{1}{A} \int_A \left(\frac{\partial u_y}{\partial x} - \frac{\partial u_x}{\partial y} \right) dA \tag{3.9}$$

$$\Omega = \frac{1}{A} \int_A \vec{r}_{xy} \times \vec{u}_{lat} dA \tag{3.10}$$

$$\dot{M}_{lat} = \frac{1}{A} \int_A \rho \cdot \left(u_x^2 + u_y^2 \right) dA \tag{3.11}$$

Area A in m^2, velocity u in m/s, position x and y and radius to vortex center $\vec{r}$ in m, density ρ in kg/m^3

In the following, the axial distribution of the lateral momentum is described using the formulation of Eq. 3.11. Figure 3.28 shows the different development of the lateral flow in different sub-channels and with different Reynolds numbers. It can be seen that the magnitude of the initial lateral flow at $z/d_{hyd} = 0$ is nearly independent from Reynolds number but depends on the blockage of the mixing vane in the sub-channel. The swirling flow induced by the mixing vanes is the major contribution to the lateral momentum and so the curves in Fig. 3.28 decrease monotonically with the vortices. Except in the case of wall channels that have a short section of increasing lateral momentum between $z/d_{hyd} = 5 \ldots 10$. Far away from the spacer the lateral momentum approaches a value above zero because there are still secondary flows. In case of the simple spacer only a very small amount of lateral momentum is generated that decays quickly.

3.4.3 Void distribution

Upstream of the lattice at $z/d_{hyd} = -10$, the void fraction is distributed radially with a nearly uniform profile and a small peak in the channel center (Fig. 3.29). After the mixing vane spacer, the void is concentrated in the regions of low pressure in the center of the vortices that are formed by the mixing vanes. This results in a double void peak at $z/d_{hyd} = 0.5$ and later in a single void peak at $z/d_{hyd} = 1$ around the sub-channel center position. The void distribution remains almost symmetrical. Further downstream, the vortex center moves away from the sub-channel center and the void profile is not symmetrical at $z/d_{hyd} = 10$.

---

[4]Smith et al. [113]
[5]Ylönen [135]
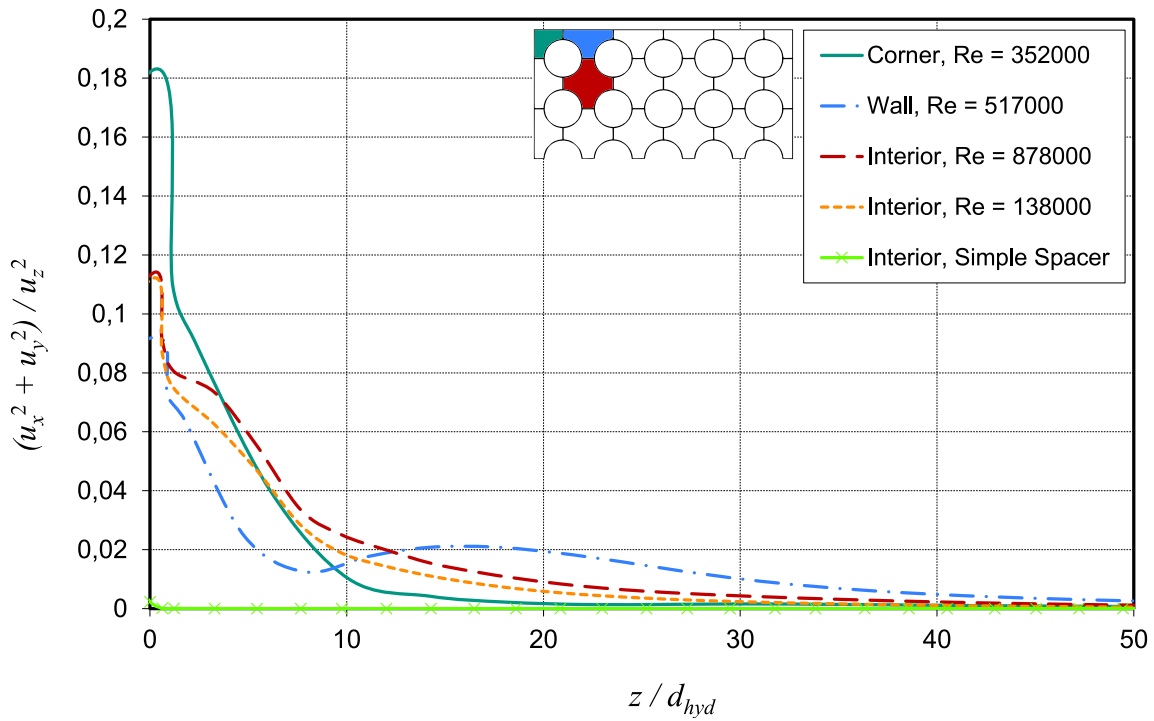
Fig. 3.28: Axial development of lateral velocity in different sub-channel types with different Reynolds numbers for a single-phase flow case
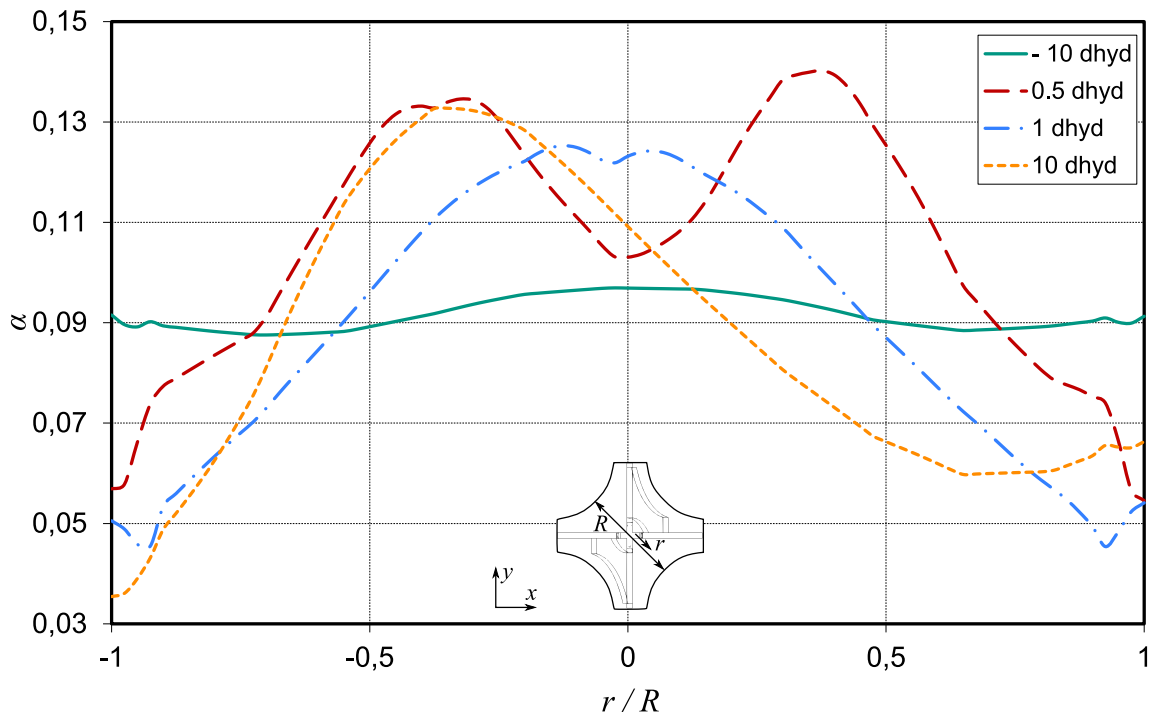
Fig. 3.29: Radial void fraction profiles in interior channel at different axial positions with $\alpha_g = 10\%$ and $Re = 878000$

Contour plots of the development of radial void distribution are shown in Fig. 3.30 − 3.33. The vortex centers can be clearly identified by the high void concentrations. As the vorticity decreases faster in the wall and corner channels, large void pockets remain only in the interior channels. At $z/d_{hyd} = 5$, also the shape of the vortex has changed from elliptical to circular (Fig. 3.32). At $z/d_{hyd} = 20$, the vortices disappeared and no regular pattern of the void fraction

distribution can be identified. It seems that the void fraction close to the rod surface has increased. That might be a consequence of the lift force model used and of the small bubble sizes in high pressure flows. The lift force model of Tomiyama et al. [119] tends to drive small bubbles towards the wall and large bubbles towards the channel center.

The axial distribution of void fraction is different in each sub-channel. For a rough overview, averaged values are shown in Fig. 3.34. The bundle averaged void fraction drops sharply directly before the spacer grid and increases in the vicinity behind the spacer. After an axial distance of about $10\,d_{hyd}$, the bundle average void fraction has again the same value as in fully developed flow. The non-uniformity of the axial void distribution around the spacer position occurs because of a different slip ratio between the liquid and gas velocities when the flow is accelerated due to the channel blockage. Another effect of the mixing vane spacer is a strong redistribution of void fraction between the sub-channels. The void fractions of corner and wall channels decrease and in interior channels they increase. The void redistribution process seems to be slow and is not completed after a distance of $48\,d_{hyd}$ behind the spacer.

The average bubble sizes upstream of the grid, computed by the S-γ model, were about $d_S = 0.4\,\text{mm}$ in case of the $80\,\text{bar}$ pressure level and about $d_S = 0.13\,\text{mm}$ at $175\,\text{bar}$. The spacer notably reduces the bubble sizes. At $z/d_{hyd} = 0.5$ behind the spacer the Sauter mean diameter of the bubbles was reduced to $d_S = 0.16\,\text{mm}$ at $P = 80\,\text{bar}$ and $d_S = 0.05\,\text{mm}$ at $P = 175\,\text{bar}$, respectively. This reduction of bubble size causes an increase of the interaction area density. As consequence, the drag force is increased, slowing down the vapor phase. This increased the void fraction behind the spacer.

3.4.4 Turbulent mixing in single-phase flow

Turbulent mixing is known as a transport process which is caused by the lateral velocity fluctuation in the gap between two sub-channels. In this way, mass, momentum or energy can be transported in lateral direction. This process has a diffusive character. For the description of this process, a diffusion coefficient and a gradient of the transportable flow variable is required. In the case of turbulent mixing of momentum in a transverse direction related on the gap area, the change of momentum in axial direction can be regarded as a turbulent shear force T_t. In COBRA-FLX$^{\text{TM}}$ the turbulent momentum exchange is modeled within the axial momentum conservation equation (Eq. 2.125) with the turbulent mixing coefficient C_β and the difference of the sub-channel-averaged axial velocity between two adjacent sub-channels i and j, see Eq. 3.12. Rowe and Angle [94] derived a model for C_β (shown in Tab. 1.6) by comparing measured and calculated sub-channel exit enthalpies.

$$\frac{T_t^{COBRA}}{\Delta z} = w' \cdot \left[\left(\frac{\dot{m}}{\rho_m A_{ax}} \right)_i - \left(\frac{\dot{m}}{\rho_m A_{ax}} \right)_j \right] = \overbrace{C_\beta \overline{G} s}^{w'} \cdot \Delta \overline{u_{ax}} \tag{3.12}$$

Turbulent fluctuating mass velocity w' in $^{\text{kg}}\!/\!_{\text{ms}}$, axial mass flow $\dot{m}$ in $^{\text{kg}}\!/\!_{\text{s}}$, mixture density ρ_m in $^{\text{kg}}\!/\!_{\text{m}^3}$, sub-channel cross-section A_{ax} in m^2, turbulent mixing coefficient C_β, average mass flux of adjacent sub-channels $\overline{G}$ in $^{\text{kg}}\!/\!_{\text{m}^2\text{s}}$ (Eq. 2.116), gap width s and axial node distance Δz in m, average axial velocity difference $\Delta \overline{u_{ax}}$ in $^{\text{m}}\!/\!_{\text{s}}$
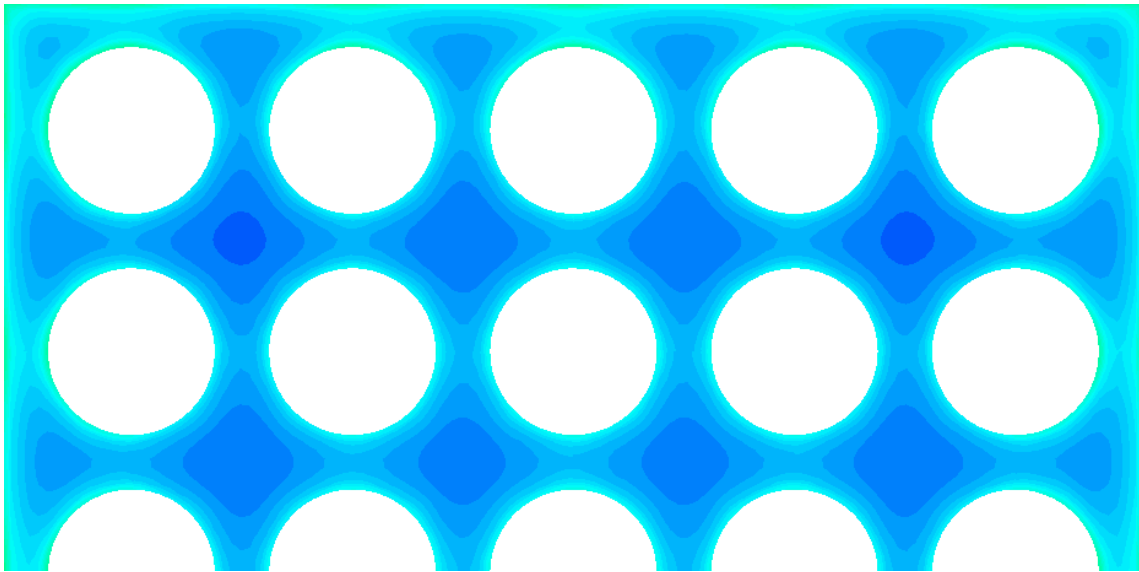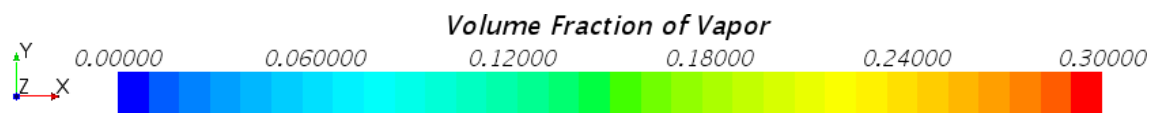
(a) $j_l = 1.247\,\text{m/s}$, $j_g = 0.066\,\text{m/s}$
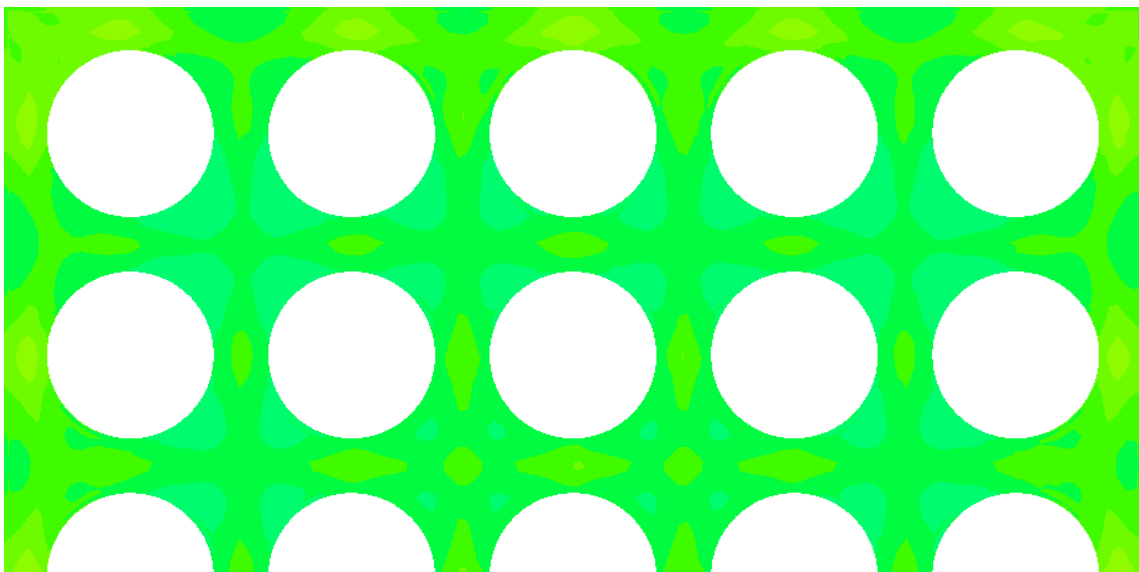
(b) $j_l = 7.8\,\text{m/s}$, $j_g = 1.376\,\text{m/s}$

Fig. 3.30: Radial void distribution with mixing vane spacer at $P = 175\,\text{bar}$, $z/d_{hyd} = -10$
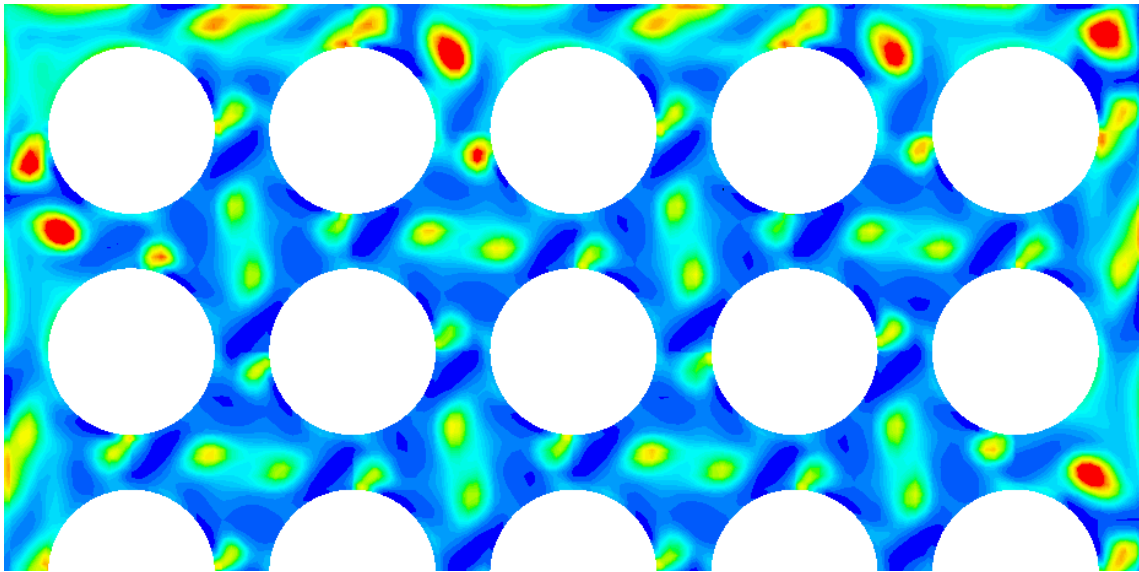
(a) $j_l = 1.247 \, \mathrm{m/s}$, $j_g = 0.066 \, \mathrm{m/s}$
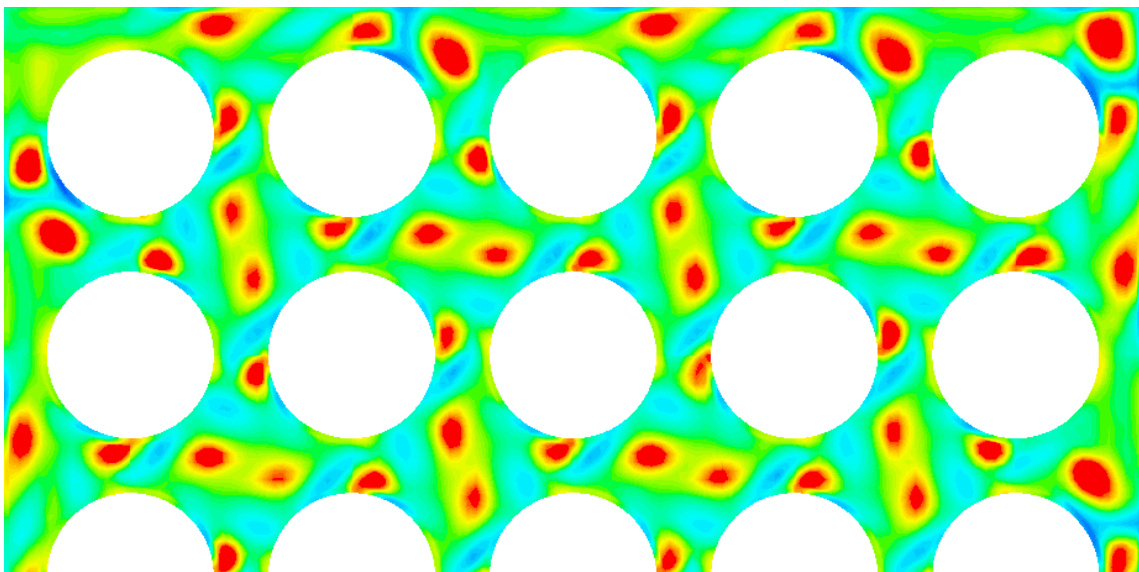
(b) $j_l = 7.8 \, \mathrm{m/s}$, $j_g = 1.376 \, \mathrm{m/s}$

Fig. 3.31: Radial void distribution with mixing vane spacer at $P = 175$ bar, $z/d_{hyd} = 1$
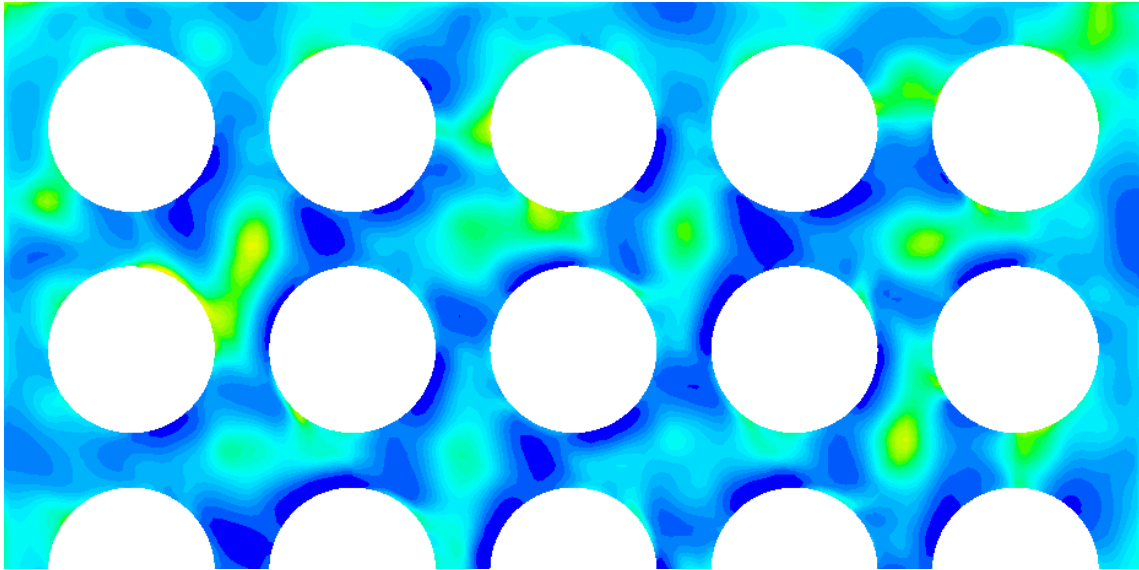
(a) $j_l = 1.247\,\text{m/s}$, $j_g = 0.066\,\text{m/s}$
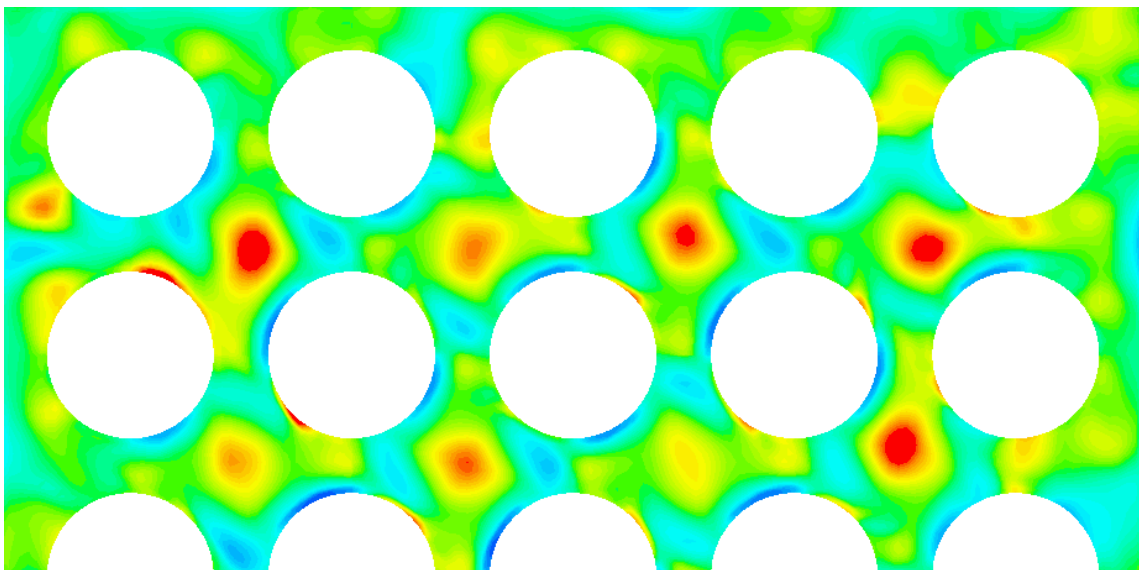
(b) $j_l = 7.8\,\text{m/s}$, $j_g = 1.376\,\text{m/s}$

Fig. 3.32: Radial void distribution with mixing vane spacer at $P = 175\,\text{bar}$, $z/d_{hyd} = 5$
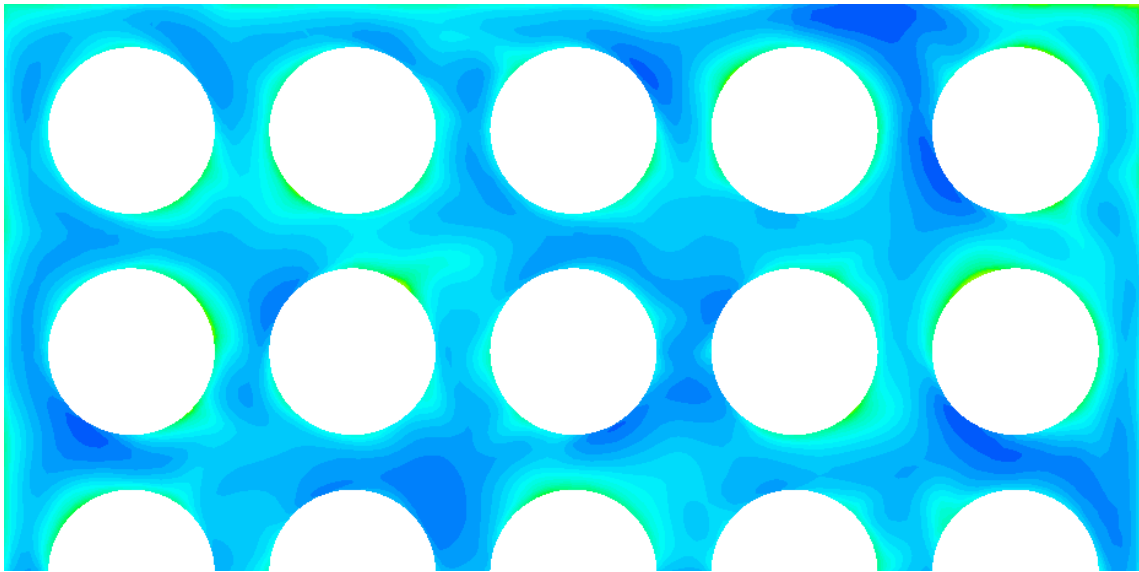
(a) $j_l = 1.247$ m/s, $j_g = 0.066$ m/s
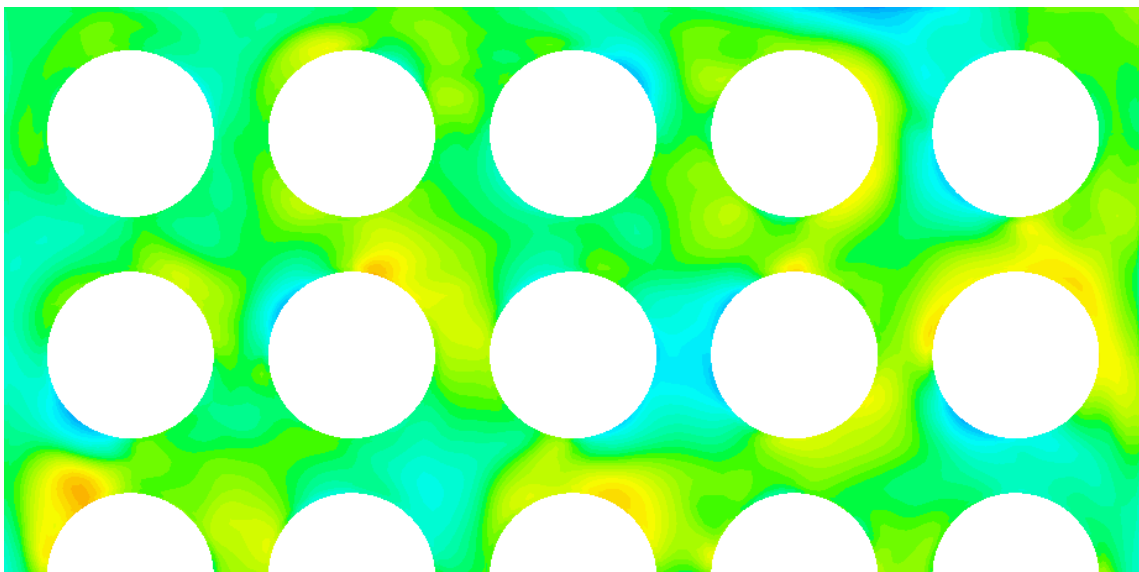
(b) $j_l = 7.8$ m/s, $j_g = 1.376$ m/s

Fig. 3.33: Radial void distribution with mixing vane spacer at $P = 175$ bar, $z/d_{hyd} = 20$
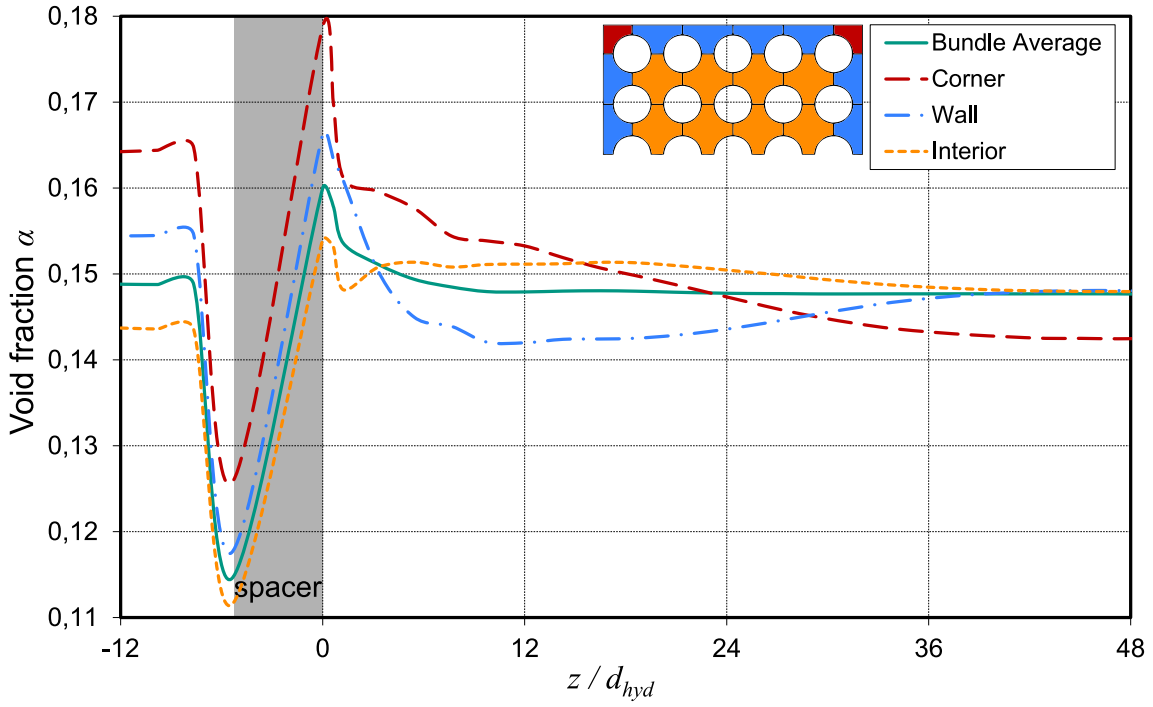
Fig. 3.34: Axial void distributions in different sub-channels at $P = 175$ bar and $G = 4500$ kg/m²s

In STAR-CCM+® 9.02.005 the turbulent shear stress in the gap is based on the correlation of the velocity fluctuations in lateral direction u'_{lat} and axial direction u'_{ax}. Together with the density, these terms are called Reynolds stresses. These are calculated using a turbulence model. In case of an eddy viscosity model, the Reynolds stresses are approximated by the turbulent viscosity μ_t and the shear strain rate, see Eq. 3.13. If the shear strain rate is approximated by the local axial velocity difference over the turbulent length scale l_t an expression for the turbulent mixing coefficient C_β can be derived by setting $T_t^{COBRA} = T_t^{CFD}$, see Eq. 3.14. This expression can be separated into the two components of the velocity fluctuation coefficient C_{β^*} and the velocity difference ratio C_t.

$$\frac{T_t^{CFD}}{s\Delta z} = \rho\overline{u'_{lat}u'_{ax}} \approx \mu_t \cdot \left(\frac{\partial u_{ax}}{\partial x} + \overbrace{\frac{\partial u_{lat}}{\partial z}}^{\approx 0} \right) \approx \mu_t \cdot \frac{\Delta u_{ax}}{l_t} \tag{3.13}$$

$$C_\beta = \underbrace{\frac{\mu_t}{l_t\overline{G}}}_{C_{\beta^*}} \cdot \underbrace{\frac{\Delta u_{ax}}{\Delta\overline{u_{ax}}}}_{C_t} \tag{3.14}$$

$$l_t = C_\mu \frac{k^{3/2}}{\varepsilon} \tag{3.15}$$

Density ρ in kg/m³, velocity fluctuation u' and axial velocity difference Δu_{ax} in m/s, turbulent viscosity μ_t in Pas, turbulent mixing coefficient C_β, averaged mass flux $\overline{G}$ in kg/m²s, gap width s, axial node distance Δz and turbulent length scale l_t in m, $C_\mu = 0.09$, turbulent kinetic energy k in m²/s², turbulent dissipation rate ε in m²/s³

In Equation 3.14, $\Delta\overline{u_{ax}}$ is the difference between the averaged axial velocities of the adjacent sub-channels as they are used in COBRA-FLX™ and Δu_{ax} is the difference of the local axial

95

velocities over the distance l_t as it can be resolved in CFD. The turbulent length scale l_t can be estimated by Eq. 3.15. This length would be in the order of 10^{-5} m. Since the computational mesh in the gap area was too coarse for this distance, the length was set to $l_t = 1$ mm. Thereby it was ensured to use different mesh cells when evaluating Δu_{ax} from the CFD results.

The coefficient C_{β^*} represents the turbulent velocity fluctuations in the transverse direction. The velocity fluctuations are influenced by the grid spacer what is shown in Fig. 3.35. The turbulent fluctuation C_β^* is decreased within the spacer grid and strongly increased behind the grid due to the redistribution of flow. In the gap between a corner and a wall channel, the turbulent fluctuation grows until a peak value $C_{\beta,max}^*$ and then decreases exponentially towards the fully developed value as it is far away from the grid. There is a single peak in case of the simple spacer, but there are two peaks in case of the mixing vane spacer.
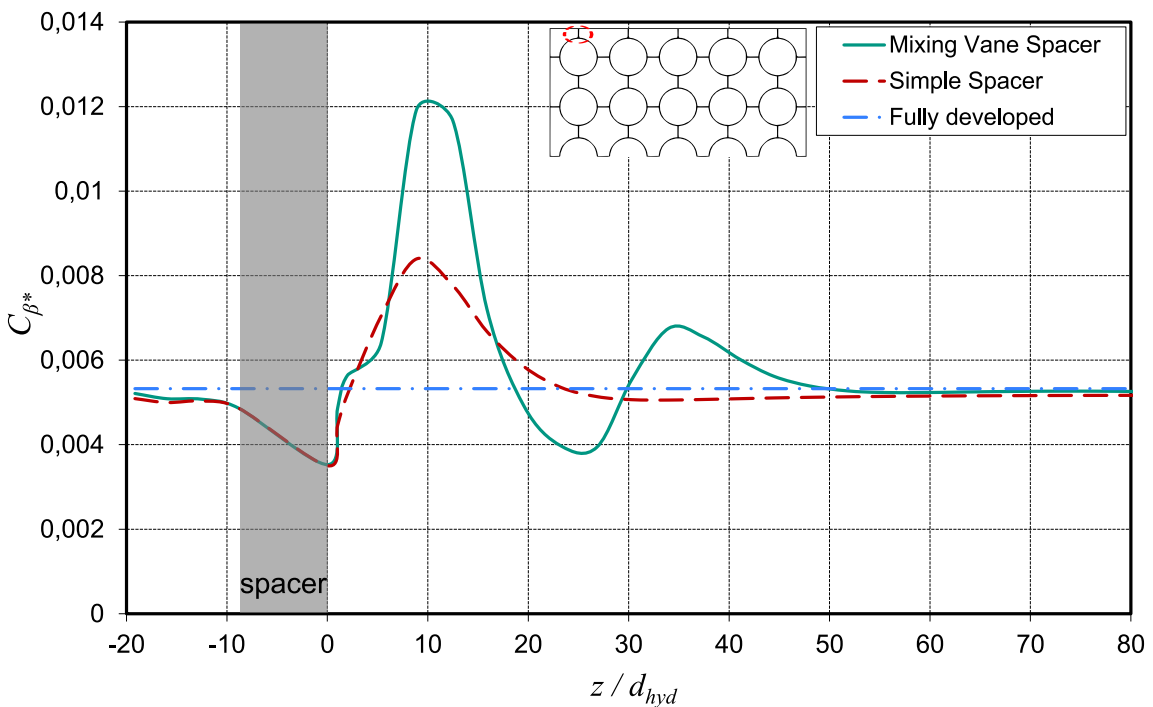
Fig. 3.35: Axial distribution of turbulent fluctuation term with presence of a spacer grid for the gap between a corner and a wall channel at $P = 175$ bar and $G = 4500\,\mathrm{kg/m^2s}$

The average values of C_{β^*} from the last axial positions without the influence of the spacer were evaluated to investigate the influence of Reynolds number. The results are compared in Fig. 3.36 with correlations from the literature. Compared to the correlations of Rowe and Angle [96] and Rogers and Roseheart [87], there is a good agreement for the turbulent fluctuation between two interior channels. The turbulent fluctuation decreases slightly with growing Reynolds number and it is different in each gap type, i.e. it is higher with a larger gap width and it is higher, if the two connected channels have different hydraulic diameters.

The turbulent fluctuation of the liquid phase is affected by the vapor phase. For bubbly flow with $\alpha_g \leq 0.15$, the turbulent fluctuation term has a linear increase with rising void fraction, as Fig. 3.37 shows for the gap between two interior channels. The linear dependency can be expressed by Eq. 3.16. For the evaluation of $C_{\beta^*}^{TP}$ in the two-phase flow simulations, only the values of the liquid phase were considered.
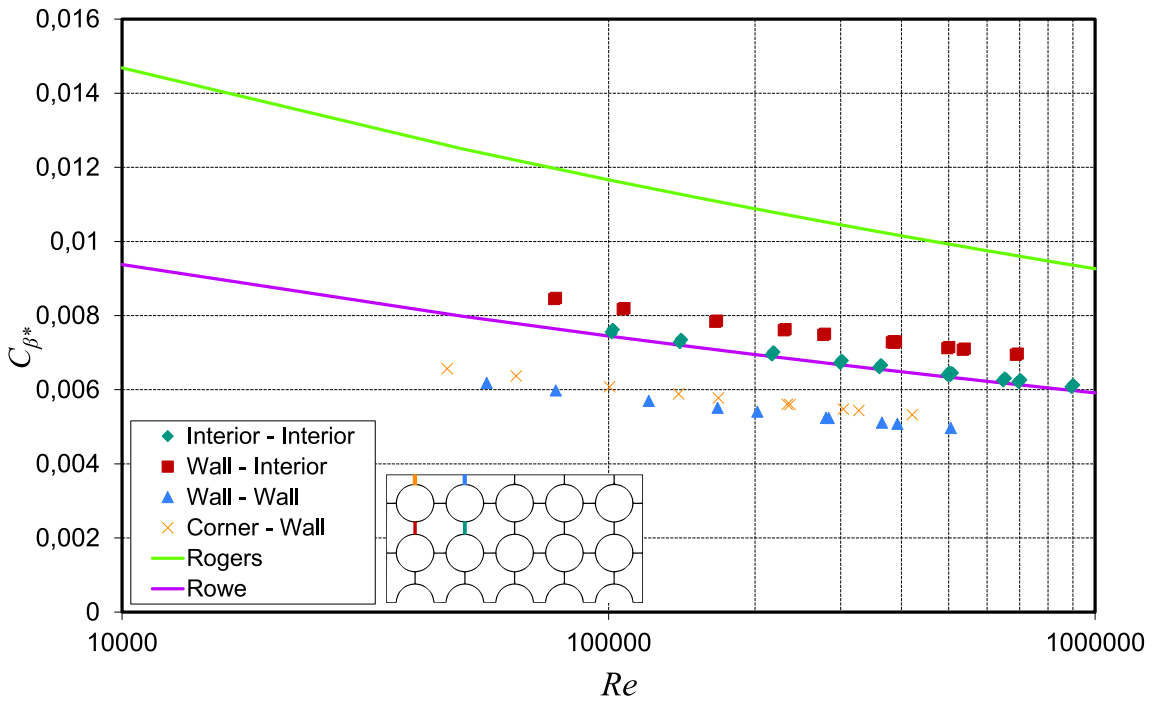
Fig. 3.36: Single-phase flow turbulent mixing coefficient compared to literature correlations
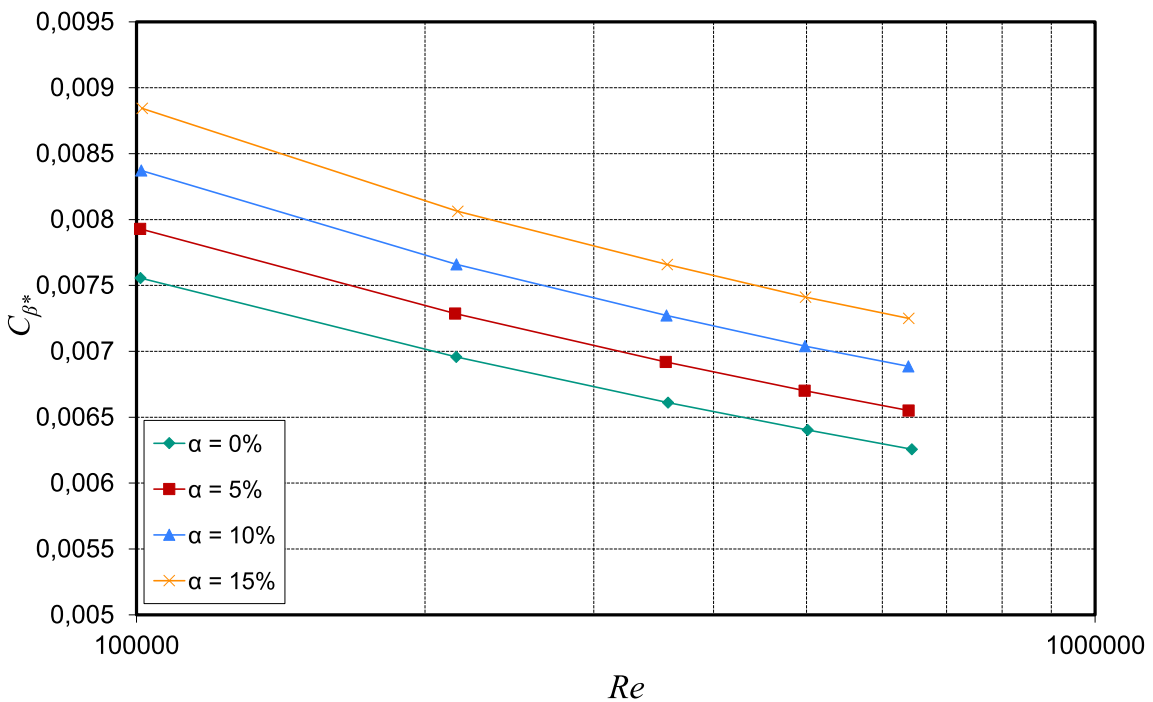
Fig. 3.37: Turbulent mixing coefficient as function of void fraction

$$C_{\beta^*}^{TP} = C_{\beta^*}^{SP} \cdot (1 + \alpha_g) \; ; \; 0 \leq \alpha_g < 0.15 \qquad (3.16)$$

Single-phase turbulent mixing coefficient $C_{\beta^*}^{SP}$, volume fraction of vapor α_g

The turbulent shear stress in a gap is determined not only by the turbulent fluctuation but also by the effective velocity difference in range of the turbulent eddies. In turbulent flows, there is always a turbulent fluctuation but if there are no differences between the axial velocities

97

there would be no momentum transfer due to the turbulent mixing. Within the rough nodal-ization of the sub-channel analysis codes the local velocity gradients cannot be resolved and the average axial velocity difference $\Delta\overline{u_{ax}}$ is used instead to compute the turbulent momentum transfer. The missing information about the local difference Δu_{ax} can be provided by the veloc-ity difference ratio C_t that was defined in Eq. 3.14. CFD resolves the velocity profile through the sub-channel and usually the ratio of the velocity differences is $C_t < 1$. The value of C_t depends strongly on the geometry and flow conditions through the adjacent sub-channels, so C_t is different for each gap and has a different dependency on Reynolds number. Figure 3.38 shows that the velocity difference ratio for different gaps in undisturbed, fully developed turbu-lent flow has only a small dependency on Reynolds number.
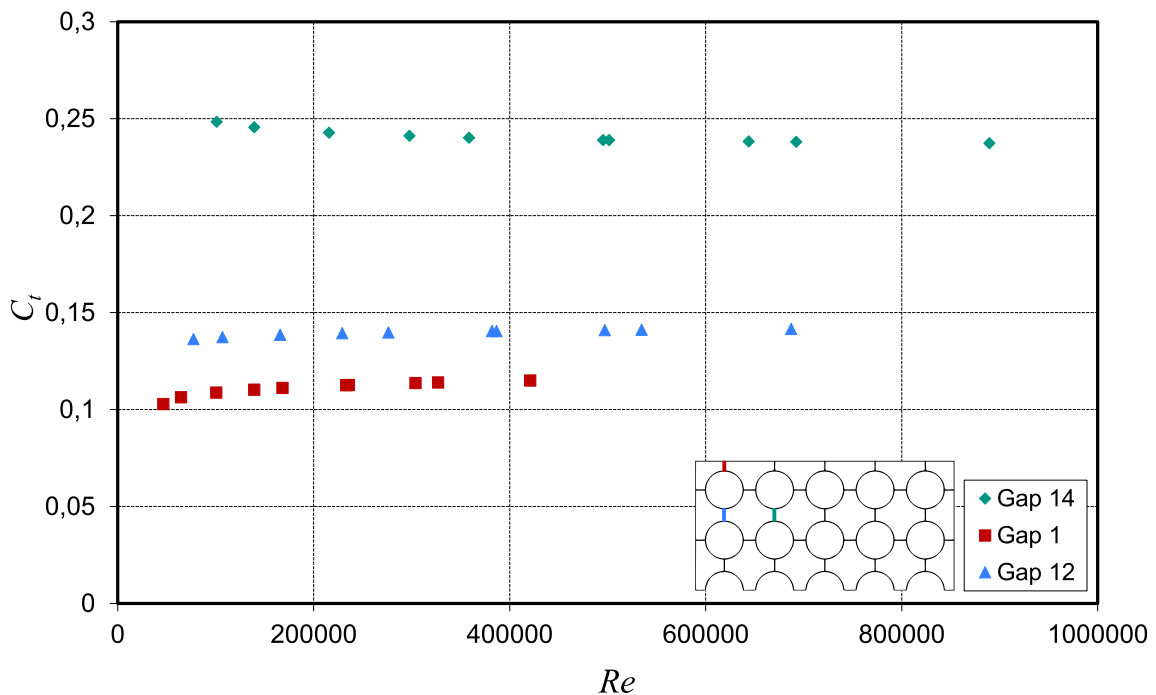
Fig. 3.38: Velocity difference ratio for different gaps as function of Reynolds number in single-phase flow

The axial development of the velocity difference ratio C_t is greatly different for the simple and for the mixing vane spacer. Due to the superposition with a strong convective flow, the velocity difference in the gap can have a different sign than the sub-channel averaged velocity difference, resulting in $C_t < 0$. This is sometimes the case in the vicinity of the mixing vane spacer grid. The simple spacer has only a small effect of the velocity difference in the gap. As consequence, the turbulent shear stress in the gap has not only a different magnitude but also a different direction depending on the spacer geometry.

For proper modeling of the turbulent momentum transfer through the gap in the vicinity of a mixing vane spacer grid the effect of a variable turbulent velocity fluctuation and the effect of a variable local velocity difference has to be taken into account. Meanwhile the magnitude of the resulting turbulent momentum exchange is very small compared to the momentum exchange due to the convective cross-flow in this region. Only in the case of the simple spacer and far away from spacer grids the role of the turbulent mixing is more significant. Therefore the model development in the next chapter will focus on the convective cross-flow effects.

Chapter 4

New model for forced cross-flow in COBRA-FLX$^{\text{TM}}$

The effect of an artificial cross-flow that has a preferred direction is called "Flow Sweeping". It is usually induced by mixing vanes on spacer grids or wire wraps around rods to maintain the gap spacing. This effect needs a special modeling in COBRA-FLX$^{\text{TM}}$ because the scale of the geometric features are not resolved within the rough nodalization of the sub-channels.

4.1 Current COBRA-FLX$^{\text{TM}}$ model

In COBRA-FLX$^{\text{TM}}$, the lateral cross-flow per unit length is denoted as w (Eq. 4.1). It is computed using a momentum balance equation for the lateral direction that was introduced in Eq. 2.132. A detailed derivation of this equation from the local instantaneous Navier-Stokes equations is given in section 2.4.1. This equation considers the lateral pressure gradient between two adjacent sub-channels i and j as driving force for the cross-flow. It also considers an additional resisting force that accounts for the pressure drop due to form drag and shear stress across the gap. The control volume for this equation is placed in the gap region and has the dimensions s (gap width) and l in lateral direction and Δz in axial direction. The definition for l is arbitrary. It can be the sub-channel centroid distance, but the ratio s/l can actually be chosen by the user. It is shown in Fig. 4.1. The parameters of the bottom side of the control volume are indicated with "1" and the parameters of the top side are indicated with "2". The indices for the left and the right side of the control volume are "i" and "j".

$$w = \rho u_{lat} s \tag{4.1}$$

Density ρ in $\mathrm{kg/m^3}$, lateral velocity u_{lat} in $\mathrm{m/s}$, gap width s in m

Only the lateral momentum that is transported by the axial flow through the top and bottom sections of this control volume is considered. It is assumed that a lateral velocity component exists only directly in the gap and that the lateral velocity component is zero in the sub-channel

99
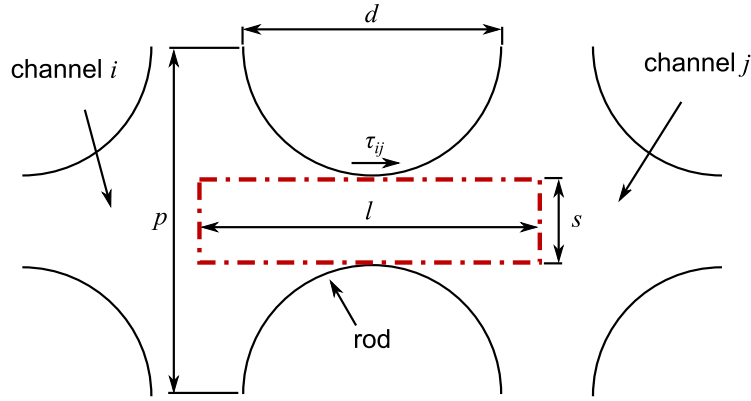
Fig. 4.1: Definition of control volume for the lateral momentum conservation equation in COBRA-FLX™

central regions. Furthermore, no gravity is considered because the lateral flow direction is defined to be orthogonal to the gravity vector. The turbulent shear stress τ_t is neglected. The pressure on the side control sections is assumed to be equal to the sub-channel average pressure. This yields an expression for the cross-flow w that is shown in Eq. 4.2, which represents the finite difference approximation of Eq. 2.132 under stationary conditions. The axial velocity in the gap control volume is computed by Eq. 2.128 as the mean value of the adjacent sub-channels.

$$w_2 = \frac{w_1 u^*_{ax,1} - \left(\overline{P}_j - \overline{P}_i\right) \cdot \Delta z \cdot \frac{s}{l}}{u^*_{ax,2} + \frac{C_{ij}|w|\Delta z}{2\rho^* s^2} \cdot \frac{s}{l}} \tag{4.2}$$

Lateral cross-flow per unit length w at bottom and top axial node 1 and 2 in kg/ms, axial velocity u^*_{ax} in m/s, gap width s, sub-channel centroid distance l and axial length of control volume Δz in m, sub-channel averaged pressure $\overline{P}$ in Pa, density of donor sub-channel ρ^* in kg/m³

The cross-flow resistance is denoted further as τ_{ij} and it is modeled in COBRA-FLX™ with the lateral momentum in the gap and an empirical coefficient C_{ij}, as shown in Eq. 4.3. This term lumps all effects of the rod geometry such as pressure losses and shear stresses on the rod surfaces within the gap area. The cross-flow resistance coefficient is by default $C_{ij} = 0.5$.

$$\tau^{COBRA}_{ij} = \frac{C_{ij}|w|w}{2\rho s^2} \tag{4.3}$$

Resistance coefficient C_{ij}, cross-flow per unit length w in kg/ms, density ρ in kg/m³, gap width s in m

In case of a forced cross-flow, Eq. 4.2 is replaced by Eq. 4.4 for the node that follows the axial position of the spacer downstream edge to compute w. For all subsequent nodes Eq. 4.2 is solved again. The empirical coefficient C_{fc} is user-input and the sign determines the direction of the cross-flow. The major drawback of this model approach is that C_{fc} has to be determined experimentally or by means of CFD simulations for each geometrical configuration and each flow condition separately. The effect of a cross-flow reversion further downstream of the grid that is observed in some cases of the CFD simulations can not be predicted by this model.

$$w_{z=z_{grid}} = C_{fc} \frac{\dot{m}^*}{\Delta z} \tag{4.4}$$

Cross-flow coefficient C_{fc}, mass flow in donor sub-channel $\dot{m}^*$ in kg/s, axial node length Δz in m

4.2 New proposal

For the formulation of an advanced model approach, the flow situation in the gap region is analyzed in detail based on the CFD results. Therefore a different control volume was defined around the gap between two rods and two sub-channels as shown in Fig. 4.2. The momentum balance for this control volume is computed using a volume averaged RANS-equation for the lateral direction. For the evaluation, the governing equations are derived in the following steps. First, a general RANS equation for the two-phase mixture is shown in Eq. 4.5. Due to the mixture formulation, no inter-phase momentum transfer needs to be considered.

$$\frac{\partial}{\partial t} \left(\alpha_l \rho_l \vec{u_l} + \alpha_g \rho_g \vec{u_g} \right) + \nabla \cdot \left(\alpha_l \rho_l \vec{u_l} \vec{u_l} + \alpha_g \rho_g \vec{u_g} \vec{u_g} \right) =$$
$$-\nabla \left(\alpha_l P_l + \alpha_g P_g \right) + \vec{g} \left(\alpha_l \rho_l + \alpha_g \rho_g \right) + \nabla \left[\alpha_l \left(\tau_l + \tau_{t,l} \right) + \alpha_g \left(\tau_g + \tau_{t,g} \right) \right] \tag{4.5}$$

Time t in s, volume fraction α, liquid phase l and gas phase g, density ρ in kg/m³, velocity vector $\vec{u}$ in m/s, gravity vector g in m/s², pressure P, viscous shear stress τ and turbulent shear stress τ_t in Pa

In the second step, following assumptions were applied to the basic equation: (1) The flow is stationary and therefore the temporal derivative term is zero. (2) The void fraction is constantly distributed within the whole control volume and there is no phase transition. (3) The flow is in-compressible and the density is constant. (4) The lateral flow is directed by the gap and the velocity component normal to the gap direction is neglected. (5) The gravity vector has only a component in axial direction. (6) Both phases have the same pressure. (7) Only the viscous shear stress of the liquid phase on the rod walls is considered. (8) Only the turbulent normal stress is considered. (9) The vapor phase is considered as laminar and only the turbulent stress of the liquid phase is taken into account. With these assumptions and after application of the product rule and the continuity condition, the RANS equation becomes for the x-direction:

$$\overbrace{\frac{\partial}{\partial x} \left(\alpha_l \rho_l u_{l,lat} u_{l,lat} + \alpha_g \rho_g u_{g,lat} u_{g,lat} \right)}^{\text{lateral convection}} + \overbrace{\frac{\partial}{\partial z} \left(\alpha_l \rho_l u_{l,lat} u_{l,ax} + \alpha_g \rho_g u_{g,lat} u_{g,ax} \right)}^{\text{axial convection}} =$$
$$- \underbrace{\frac{\partial P}{\partial x}}_{\text{lateral pressure}} + \underbrace{\frac{\partial}{\partial x} \left[\alpha_l \left(\tau_l + \tau_{t,l} \right) \right]}_{\text{shear stress}} \tag{4.6}$$

Volume fraction α, liquid phase l and gas phase g, density ρ in kg/m³, velocity u in m/s, pressure P, viscous shear stress τ and turbulent shear stress τ_t in Pa, direction x and z in m

In the third step, a volume average operation is performed over the control volume shown in Fig. 4.2. Then, the Gauß theorem is used that equals the volume integral of a spatial derivative of a vector with the surface integral of the scalar product of the vector and the surface normal vector. The general expression is written in Eq. 2.102. Furthermore, the lateral velocity of the two-phase mixture is denoted as u_{lat}. Together with the mixture density ρ_m from Eq. 2.17, the equation can be written as:

$$\oint_{A_{lat}} \left(\rho_m u_{lat}^2\right) \vec{n}_{lat} dA_{lat} + \oint_{A_{ax}} \left(\rho_m u_{lat} u_{ax}\right) \vec{n}_{ax} dA_{ax} =$$

$$-\oint_{A_{lat}} P\vec{n}_{lat} dA_{lat} - \oint_{A_{rod}} P\vec{n}_{rod} dA_{rod} + \oint_{A_{rod}} \alpha_l \tau_l \vec{n}_{rod} dA_{rod} + \oint_{A_{lat}} \alpha_l \tau_{t,l} \vec{n}_{lat} dA_{lat} \tag{4.7}$$

Volume fraction α, area A in m, surface normal vector $\vec{n}$, liquid phase l and gas phase g, density ρ in kg/m³, velocity u in m/s, pressure P, viscous shear stress τ and turbulent shear stress τ_t in Pa
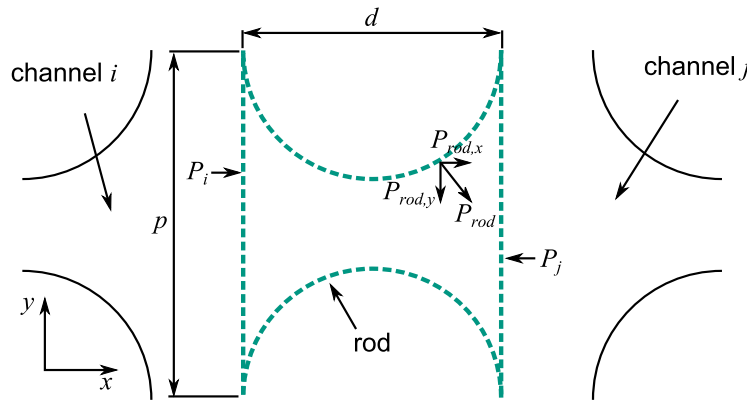
Fig. 4.2: Definition of control volume for the lateral momentum equation in STAR-CCM+® 9.02.005

In the next step, the surface integrals were evaluated for the control volume bounding surfaces. The surfaces of the control volume were defined as $A_{ax} = p \cdot d - \frac{\pi}{4}d^2$ for the surfaces on the bottom and top side in axial direction, $A_{lat} = p \cdot \Delta z$ for the surfaces on the right and left side in lateral direction and $A_{rod} = d \cdot \Delta z$ for the rod surfaces. The axial span of the control volume Δz was fitted to the distance of the CFD mesh nodes and the position of the control volume was moved axially along the gap through the simulation domain in order to evaluate the axial development of the terms of Eq. 4.8. They were evaluated both for the simulation results of the simple spacer and the mixing vane spacer to determine the effect of the mixing vanes.

$$\overbrace{\left(\rho_m u_{lat}^2 A_{lat}\right)_j - \left(\rho_m u_{lat}^2 A_{lat}\right)_i}^{\text{lateral convection}} + \overbrace{\overline{\left(\rho_m u_{lat} u_{ax} A_{ax}\right)_2} - \overline{\left(\rho_m u_{lat} u_{ax} A_{ax}\right)_1}}^{\text{axial convection}} =$$

$$\underbrace{\overline{(PA_{lat})_i} - \overline{(PA_{lat})_j}}_{\text{lateral pressure difference}} \underbrace{- \overline{PA_{rod}} - \overline{\tau_{rod} A_{rod}}}_{\text{forces on rod}} + \underbrace{\overline{(\alpha_l \tau_{t,l} A_{lat})_j} - \overline{(\alpha_l \tau_{t,l} A_{lat})_i}}_{\text{turbulent stress}} \tag{4.8}$$

Mixture density ρ_m in kg/m³, lateral velocity u_{lat} and axial velocity u_{ax} in m/s, area A in m², pressure P, volume fraction of liquid phase α_l, lateral shear stress on rod surface τ_{rod} and lateral turbulent shear stress τ_t in Pa

102

The most significant force in lateral direction is the pressure difference between the sub-channels that is shown for the simple spacer and the mixing vane spacer simulations in Fig. 4.3 for a typical gap between two interior channels by the solid line. After the spacer downstream edge that is marked with position $z/d_{hyd} = 0$, there is only a small increase of lateral pressure difference in case of the simple spacer, resulting from a different pressure drop due to slightly different axial velocities. The range of this spacer influenced section is not longer than $5\,d_{hyd}$. In case of the mixing vane spacer, the magnitude of the lateral pressure difference is much higher. The sign of the lateral pressure difference can change along the axial direction and the range of the spacer influenced section is up to $20\,d_{hyd}$ long, as shown in Fig. 4.3.
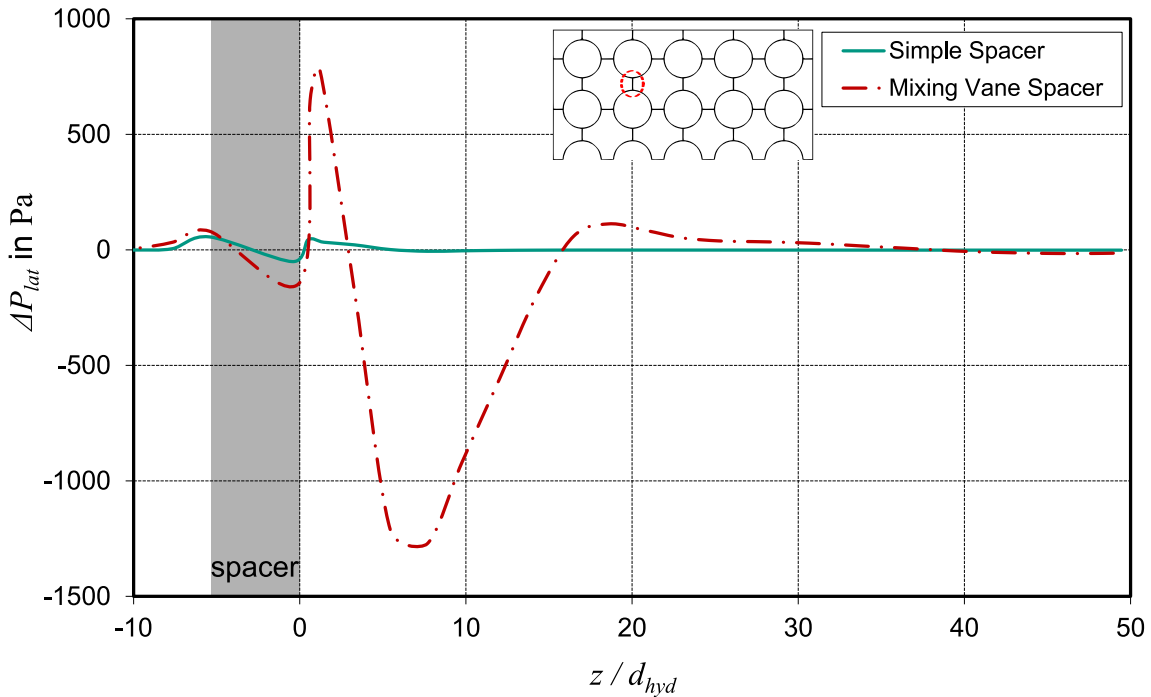
Fig. 4.3: Lateral pressure difference in a gap between two interior channels with different spacer types, $P = 175\,\mathrm{bar}$, $G = 4500\,\mathrm{kg/m^2s}$ and $\alpha = 0\%$

The evaluation of laterally transported lateral momentum shows a similar picture in Fig. 4.4. In case of the simulation with the simple spacer, the lateral convection term is virtually zero at all positions. This supports the assumption of COBRA-FLX^{TM} that there is no lateral velocity component outside of the near gap region. In case of the mixing vane spacer, the lateral momentum convection is very strong within a range of $20\,d_{hyd}$ behind the spacer. The reason for this large magnitude is the swirling flow in the sub-channel centers that is induced by the mixing vanes. The lateral momentum convection through the side control sections has a significant effect on the axial development of the cross-flow velocity and is responsible for the reversion of flow direction that was observed in some cases.

To connect the COBRA-FLX^{TM} lateral momentum balance equation in Eq. 4.2 with the balance equation that was developed for the CFD control volume in Eq. 4.8, an expression for the lateral resistance force τ_{ij} is developed that represents the effects of the rod geometry. It includes the pressure and shear stress in the lateral direction on the rod surface A_{rod}. This expression is shown in Eq. 4.9.
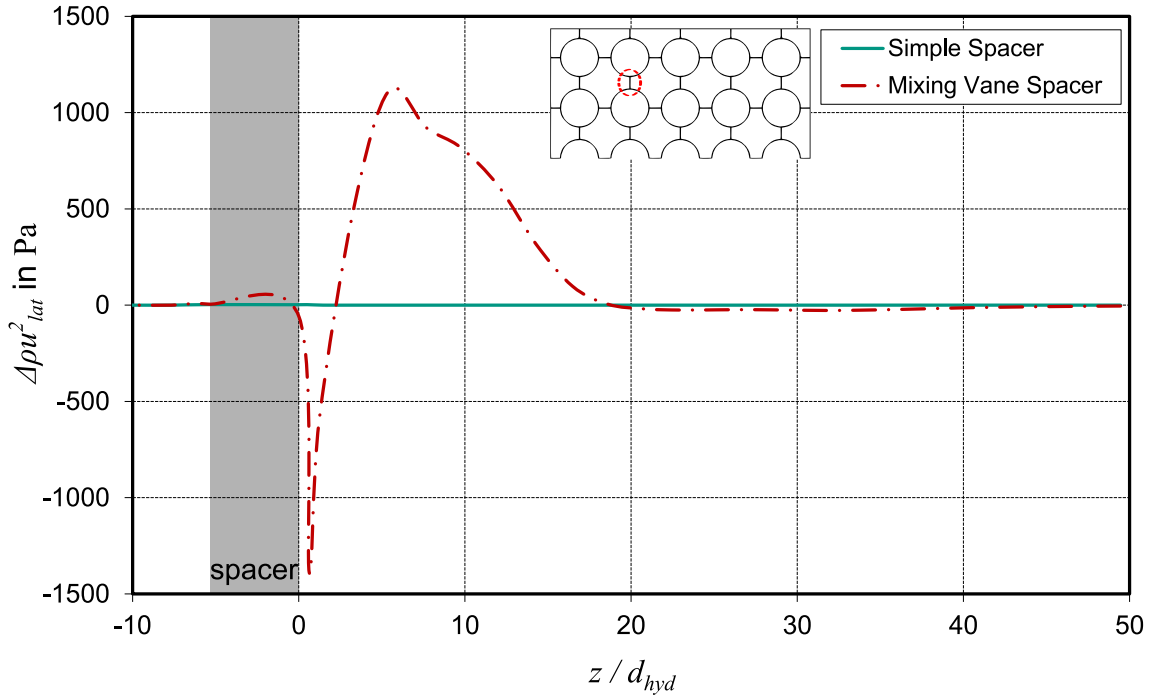
Fig. 4.4: Lateral convection of lateral momentum through the gap control volume with different spacer types, $P = 175\,\mathrm{bar}$, $G = 4500\,\mathrm{kg/m^2s}$ and $\alpha = 0\%$

$$\tau_{ij}^{CFD} = \left(\overline{P}_i - \overline{P}_j\right) - \frac{1}{A_{lat}} \cdot \left[\overline{(PA_{lat})_i} - \overline{(PA_{lat})_j}\right] + \frac{1}{A_{rod}} \cdot \overline{(P + \tau_{rod})\,A_{rod}} \qquad (4.9)$$

Sub-channel averaged Pressure $\overline{P}$, local pressure P and lateral shear stress on rod surface τ_{rod} in Pa, area A in m², axial length of control volume Δz and rod diameter d in m

The CFD results gained with Eq. 4.9 are compared with the predictions of the model used in COBRA-FLX™ in Eq. 4.3 in Fig. 4.5. There is an acceptable agreement between the model predictions and the CFD results. A better model for the cross-flow resistance in the vicinity of the grid spacer is not urgently required. The CFD results for the lateral turbulent shear stresses τ_t in Fig. 4.5 are small compared to τ_{ij} and can be neglected.

The main conclusion from Fig. 4.4 is that the lateral momentum convection in lateral direction cannot be neglected in case of a mixing vane spacer. Hence a new term S_{cf} (Eq. 4.10) is added to the COBRA-FLX™ lateral momentum balance equation that represents the lateral momentum convection in lateral direction as consequence of the swirling flow induced by the mixing vanes. The newly proposed equation for computing the cross-flow w is shown in Eq. 4.11. If this equation is directed to S_{cf}, it can be evaluated from the CFD results.

The term S_{cf} acts as a source term for the forced cross-flow (Flow Sweeping) induced by the mixing vanes. It cannot be computed by COBRA-FLX™ because there is no definition for a lateral momentum balance in the sub-channels with connections to the adjacent sub-channels. So this term has to be provided by an empirical correlation. Two different methods have been developed, how to provide this input information to a COBRA-FLX™ simulation.
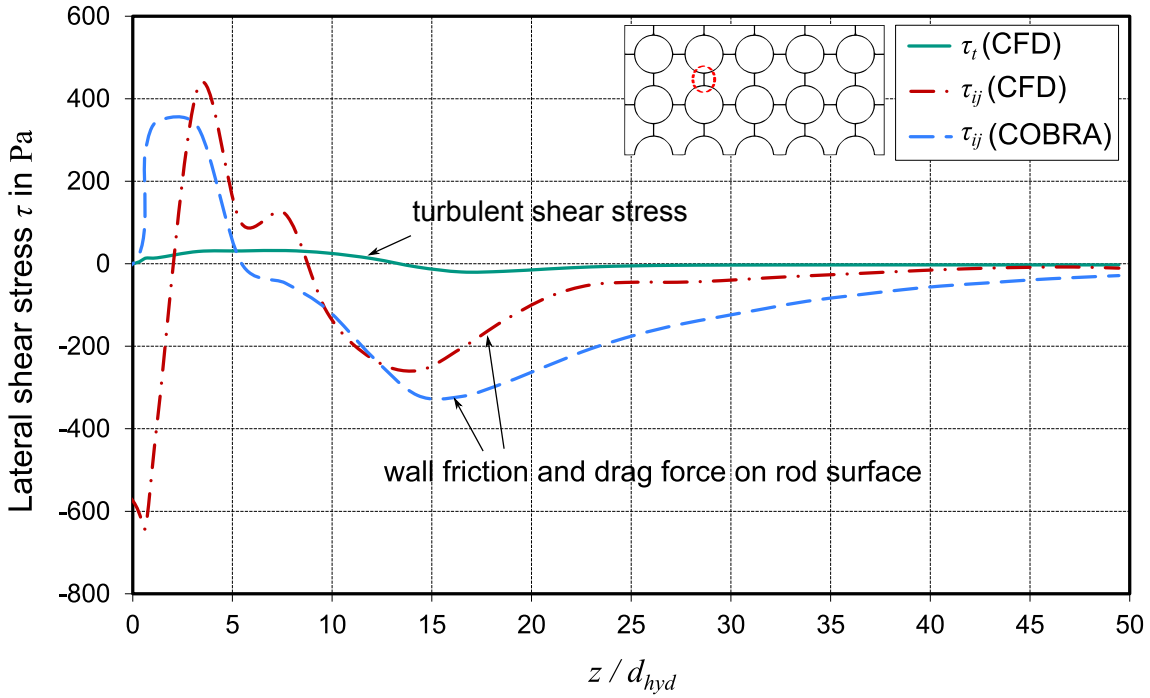
Fig. 4.5: *Lateral cross-flow resistance force in gap with* $P = 175$ bar, $G = 4500$ kg/m²s *and* $\alpha = 0\%$

$$S_{cf} = \left(\rho_m u_{lat}^2\right)_j - \left(\rho_m u_{lat}^2\right)_i \tag{4.10}$$

$$w_2 = \frac{w_1 u_{ax,1}^* - \left(\overline{P}_j - \overline{P}_i + S_{cf}\right) \cdot \Delta z \cdot \frac{s}{l}}{u_{ax,2}^* + \frac{C_{ij}|w|\Delta z}{2\rho^* s^2} \cdot \frac{s}{l}} \tag{4.11}$$

Mixture density ρ_m in kg/m³, lateral cross-flow per unit length w in kg/ms, axial velocity u_{ax} and lateral velocity u_{lat} in m/s, gap width s, lateral length of control volume l and axial length of control volume Δz in m, sub-channel averaged pressure $\overline{P}$ and source term S_{cf} in Pa, lateral resistance coefficient C_{ij}

4.2.1 Method A: Use input data file gained from CFD simulation

In the first method, the values for S_{cf} are evaluated from the CFD results using Eq. 4.11. Then they are related to the axial momentum ρu_{ax}^2 to gain the dimensionless coefficient C_{cf} (Eq. 4.12). These results are stored in an ASCII file for each gap. The axial length of the whole evaluation section behind the spacer can be as long as the distance between two spacers in the bundle, minimum 20 hydraulic diameters. This is the zone with a significant contribution of the lateral momentum convection to the cross-flow, as Fig. 4.4 shows. Usually, a sub-channel code uses a coarser axial nodalization than a CFD code. In this case, COBRA-FLX™ can use an integral term of all CFD values between two of its axial nodes.

$$S_{cf}^A = C_{cf} \cdot \rho u_{ax}^2 \tag{4.12}$$

Forced cross-flow coefficient C_{cf}, density ρ in kg/m³, axial velocity u_{ax} in m/s
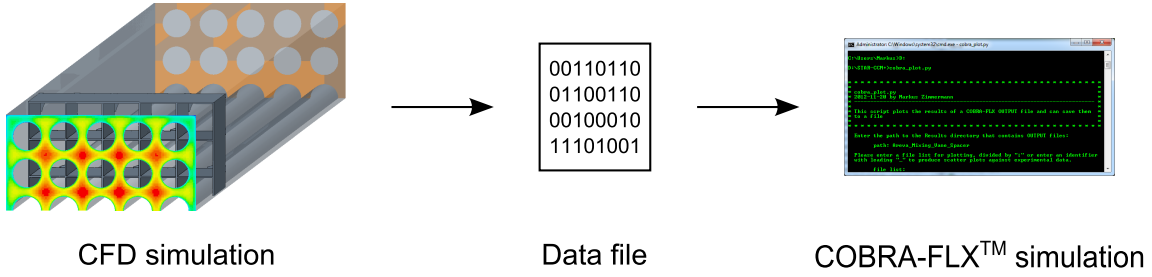
Fig. 4.6: The cross-flow source term S_{cf} is computed from the CFD results and stored in a geometry-specific data file that is used as input by COBRA-FLX^{TM}

With this approach, a CFD simulation has to be performed for each individual spacer geometry to create a specific input data file. In COBRA-FLX^{TM}, the corresponding input file can be selected for each spacer type to provide the input information for the Flow Sweeping effect (Fig. 4.6). Method A is valid for a wide range of operating conditions, because the dimensionless C_{cf} values do not change with Reynolds number. It is also valid for a small amount of void fraction with $\alpha_g < 15\%$.

4.2.2 Method B: Modeling of the lateral momentum

With this method, the forced cross-flow should be computed only from the parameters of the flow and from the geometry of the mixing vane spacer. Therefore, the lateral momentum in each sub-channel is predicted by an empirical correlation and mapped to the gaps by a distribution function Θ. The cross-flow source term S_{cf} is then the difference of the mapped lateral momentum of the adjacent sub-channels (Eq. 4.13). In the following, the modeling of the lateral momentum in the sub-channels and after that the mapping to the gaps is discussed.

$$S_{cf}^{B} = \Theta_j \cdot \left(\overline{\rho u_{lat}^2}\right)_j - \Theta_i \cdot \left(\overline{\rho u_{lat}^2}\right)_i \qquad (4.13)$$

Lateral momentum mapping function Θ, density ρ in kg/m³, lateral velocity u_{lat} in m/s

The lateral momentum in the sub-channels is evaluated from the CFD results using a surface integral over the sub-channel cross-section A_{ax} (Eq. 4.14). The axial development of the lateral momentum behind the mixing vane spacer downstream edge is maintained by the swirling flow but contains also other lateral flow velocities, such as secondary flows. The swirling flow development can be described by an exponential decay function (Eq. 4.17). This function contains two parameters: (1) the initial lateral momentum coefficient C_{lat} and (2) the lateral momentum decay coefficient C_{dec}. The CFD results of the lateral momentum in an interior channel is compared with the model predictions in Fig. 4.7. The CFD results vary around the value predicted by the model. In the first section with $z/d_{hyd} \leq 20$ these deviations arise from the mutual interchange of lateral momentum between the sub-channels through the gaps. In the following section with $z/d_{hyd} > 20$ the CFD results are always higher than the model predictions, which is due to secondary flows. These differences will be defined as additional lateral momentum and are symbolized by the function M_{lv}. It will not be further investigated in

this work and therefore neglected by assuming $M_{lv} = 0$.

The initial lateral momentum coefficient C_{lat} depends on the blockage ratio of the mixing vane in the sub-channel flow area and is independent from Reynolds number (Eq. 4.18). The decay coefficient C_{dec} depends on the Reynolds number. If Equation 4.17 is solved to compute C_{dec}, the axial distribution of this parameter is nearly constant in the region between $5 \leq \frac{z - z_{grid}}{d_{hyd}} < 20$ in an interior sub-channel, as Fig. 4.8 shows. During the first $5\,d_{hyd}$ after the spacer, there is the region of the double vortex that has a stronger decay than the region of the single vortex. The average value of C_{dec} in this region depends on the Reynolds number with the power of -0.0652. The remaining coefficient C_{d1} in Eq. 4.19 depends on the geometry.

$$\left(\overline{\rho u_{lat}^2}\right)^{CFD} = \frac{1}{A_{ax}} \int_{A_{ax}} v' \left(G_x^2 + G_y^2\right) dA_{ax} \tag{4.14}$$

$$G_x = \alpha_g \rho_g u_{g,x} + (1 - \alpha_h)\rho_l u_{l,x} \tag{4.15}$$

$$G_y = \alpha_g \rho_g u_{g,y} + (1 - \alpha_h)\rho_l u_{l,y} \tag{4.16}$$

$$\left(\overline{\rho u_{lat}^2}\right)^{Model} = \frac{1}{2}C_{lat} \cdot \exp\left(-C_{dec} \cdot \frac{z - z_{grid}}{d_{hyd}}\right) \cdot v' G_{ax}^2 + M_{lv} \tag{4.17}$$

Density ρ in kg/m³, lateral velocity u_{lat}, lateral velocity components u_x and u_y in m/s, specific volume v' in m³/kg, Mass flux G in kg/m²s, sub-channel cross-section A in m², lateral momentum coefficient C_{lat} and decay coefficient C_{dec}, axial position z and hydraulic diameter d_{hyd} in m, void fraction α_g, additional momentum M_{lv} in Pa
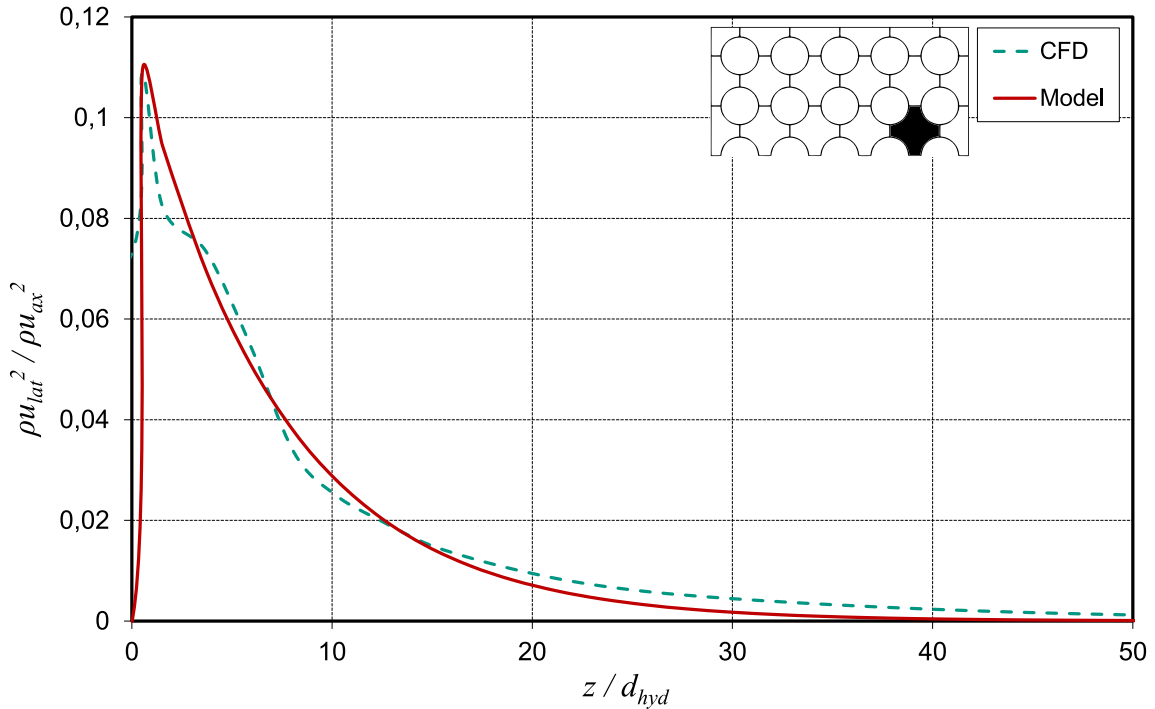
Fig. 4.7: Predictions of model for lateral momentum compared with CFD results with $P = 175\,$bar, $G = 4500\,$kg/m²s and $\alpha = 0\%$
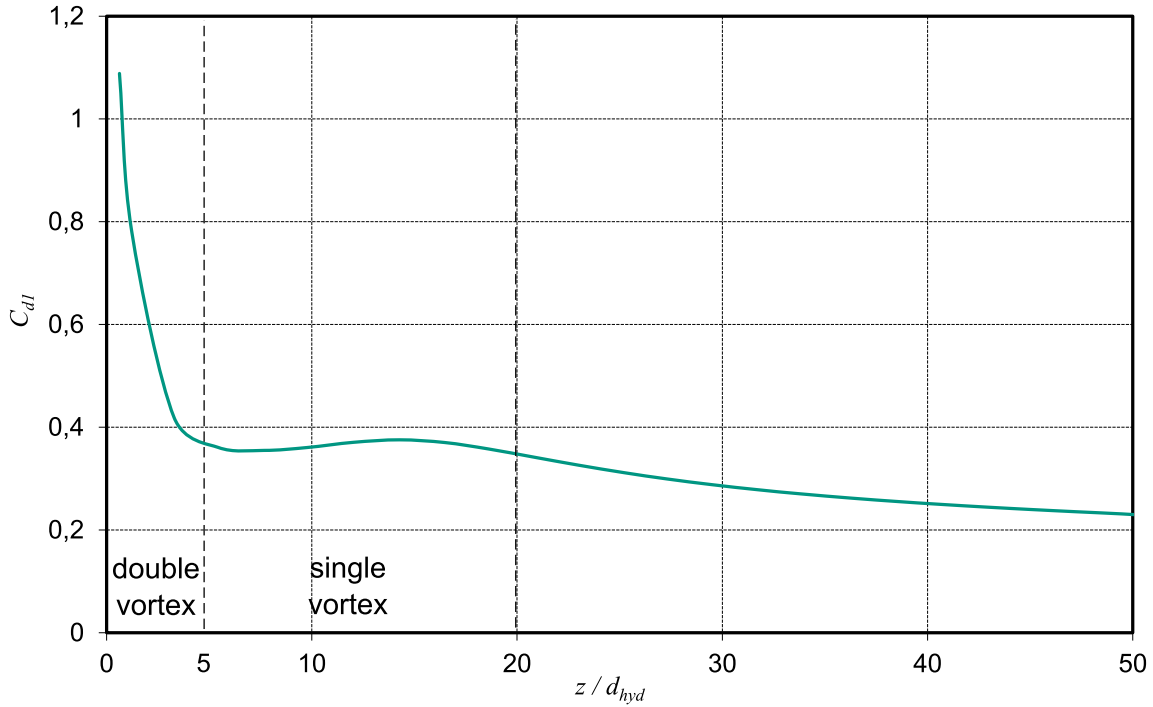
Fig. 4.8: Decay coefficient C_{d1} of swirling flow in interior sub-channel

$$C_{lat} = \frac{n_{vane} \cdot A_{vane} \cdot \sin(\gamma)}{A_{ax}} \qquad (4.18)$$

$$C_{dec} = C_{d1} \cdot Re^{-0.0652} \qquad (4.19)$$

Number of vanes in sub-channel n_{vane}, area of vane A_{vane} and sub-channel cross-section A_{ax} in m^2, mixing vane angle γ in °, Reynolds number Re

The lateral momentum in Eq. 4.14 is defined as the density times the sum of the square of the two lateral velocity components in the x and y direction. Due to the arrangement of the mixing vanes, the lateral velocity components do not have the same values in both directions directly behind the mixing vane tips. There is a preferred direction, which is pretended by the orientation of the mixing vanes (Fig. 4.9a and 4.9b). Due to the swirling flow, this distribution changes over the axial direction. Further downstream, the lateral momentum is more evenly distributed on both directions (Fig. 4.9c and 4.9d).

Due to these reasons, a mapping function Θ has been developed to account for the preferred direction of the lateral momentum due to the vane arrangement and the swirling flow. The definition is given in Eq. 4.20. The physical meaning of Θ is the ratio of one lateral velocity component to the sum of both lateral velocity components. If the mixing vane is directed towards the gap, the distribution is described by Θ_{maj} (Eq. 4.22) and if the mixing vane is directed away from the gap, it is described by Θ_{min} (see Fig. 4.9). Both functions are not independent from each other (Eq. 4.23). The parameters used in Eq. 4.22 depend on the geometry but not on the flow conditions. The CFD results of the axial development of Θ_{maj} and Θ_{min} are plotted for an interior channel in Fig. 4.10. Here only the values that were within a radius of $r = 0.025$ m around the vortex center were considered.

(a) $|u_x|$ at $z/d_{hyd} = 0$

(b) $|u_y|$ at $z/d_{hyd} = 0$

(c) $|u_x|$ at $z/d_{hyd} = 5$

(d) $|u_y|$ at $z/d_{hyd} = 5$
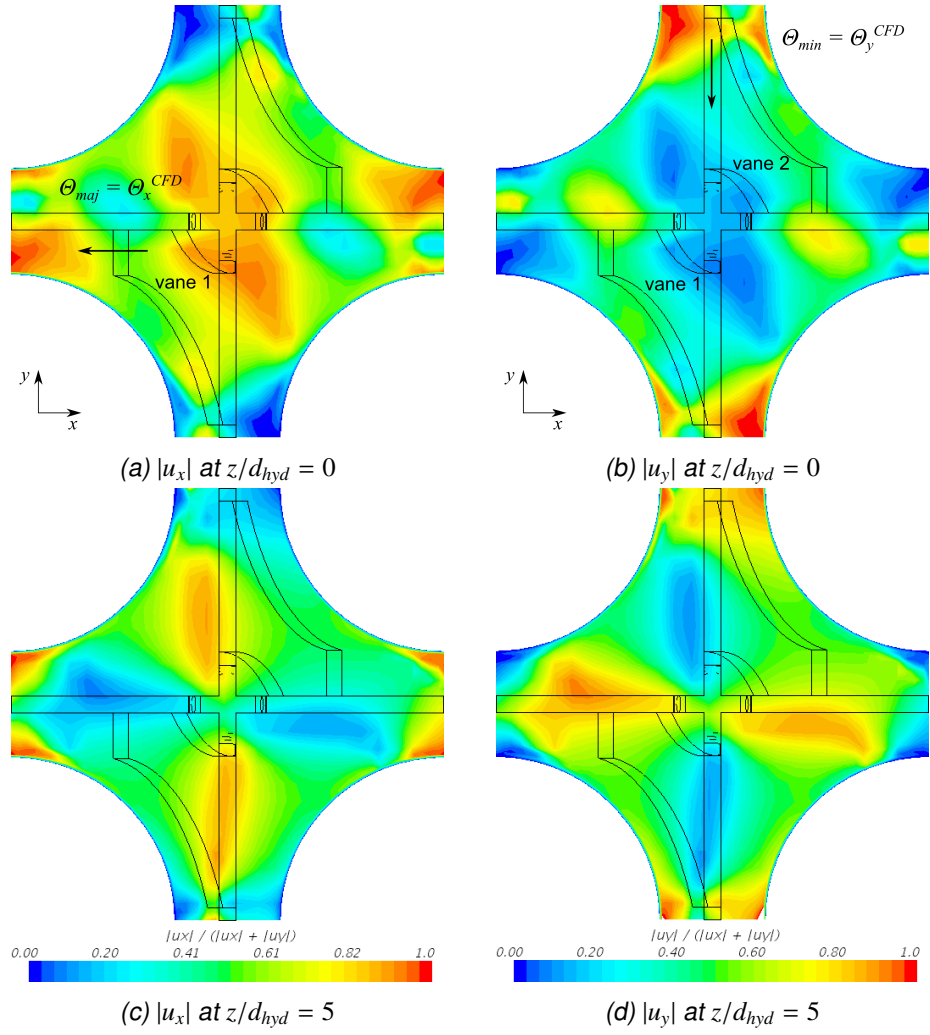
Fig. 4.9: Lateral velocity distribution in interior channel with mixing vanes at two different axial positions behind the grid for single-phase flow conditions

$$\Theta_{i,j}^{CFD} = \begin{cases} \frac{u_x^2}{u_x^2 + u_y^2} & \text{if gap is oriented in } x\text{-direction} \\ \frac{u_y^2}{u_x^2 + u_y^2} & \text{if gap is oriented in } y\text{-direction} \end{cases} \qquad (4.20)$$

$$\Theta_{i,j}^{Model} = \begin{cases} \Theta_{maj} & \text{if vane is directed towards the gap} \\ \Theta_{min} & \text{if vane is directed away from the gap} \end{cases} \qquad (4.21)$$

$$\Theta_{maj} = \max\left(0.2; 1.0 - \frac{z - z_{grid}}{6 \cdot d_{hyd}}\right) \qquad (4.22)$$

$$\Theta_{min} = 1 - \Theta_{maj} \qquad (4.23)$$

Lateral velocity components u_x and u_y in m/s, lateral momentum distribution function Θ, axial position z and hydraulic diameter d_{hyd} in m
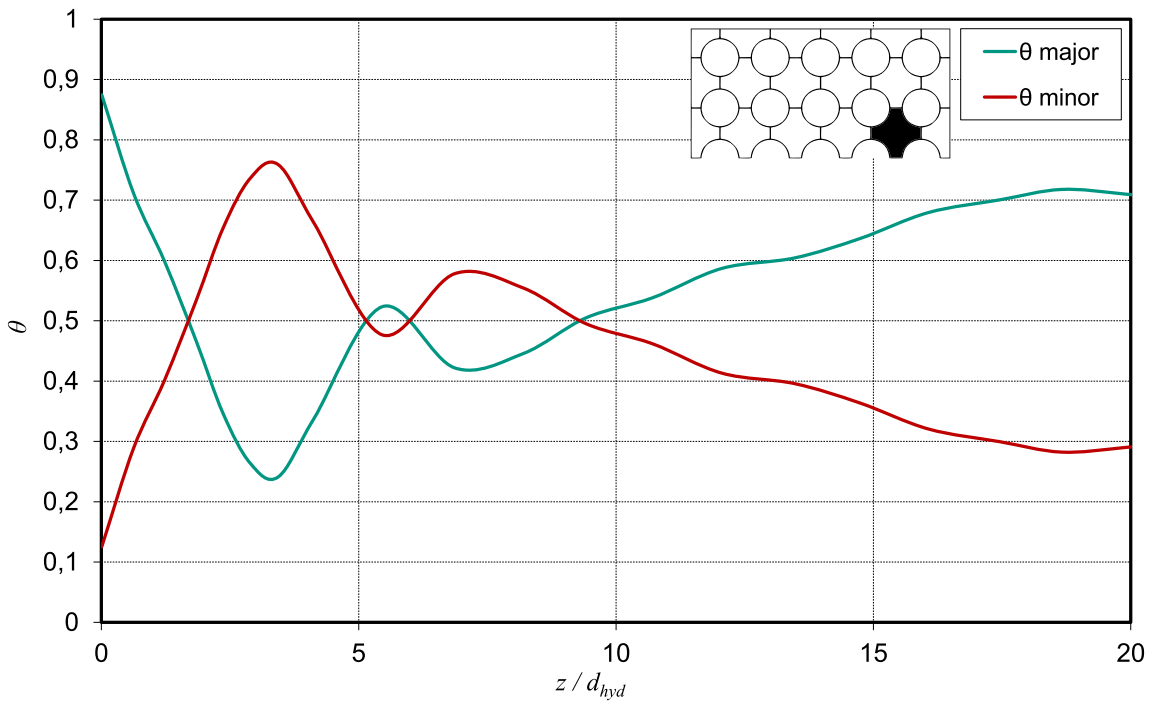
Fig. 4.10: Lateral momentum distribution due to swirling flow

Figure 4.11 shows the CFD results for the cross-flow source term S_{cf} that is used for Method A (solid line) compared to the predictions of the model proposed by method B (dash-dotted line, Eq. 4.13). These results show the axial distribution of the forced cross-flow caused by the mixing vanes and the swirling flow for a gap between two interior channels.
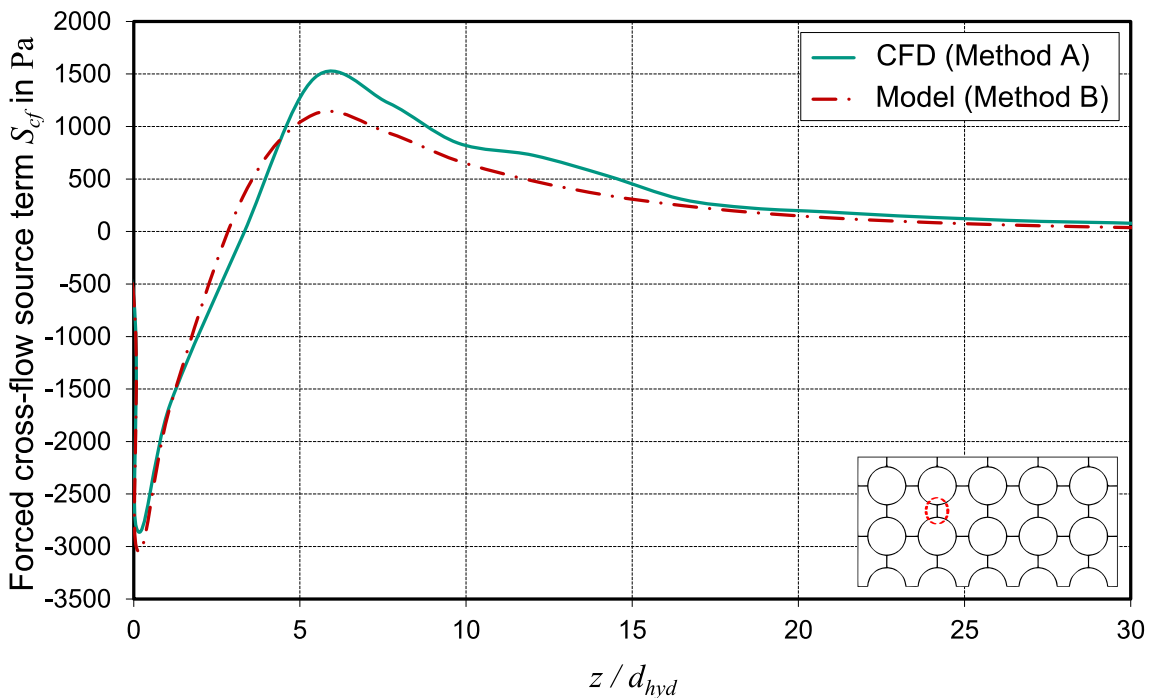
Fig. 4.11: Forced cross-flow source term evaluated from CFD and prediction of model in Eq. 4.13

The initial direction of this term is determined by the orientation of the mixing vanes but the further axial development is influenced by the swirling flow that causes a change of the direction of the forced cross-flow. There is a good agreement between the two curves for this gap. The

deviations are probably the effect of the additional lateral momentum M_{lv} in the sub-channels that require further modeling to improve the predictions.

4.2.3 Verification

The source code of COBRA-FLX^{TM} was modified in order to include the newly proposed models for the simulation runs. Each model requires different inputs. The old Flow Sweeping model needs the coefficient C_{fc} for each gap that can be estimated from the CFD results. The input for method A of the new model is a data file that contains values for S_{cf} for each gap on several axial positions. The input for method B are geometry parameters that describe the mixing vane geometry.

After the implementation, the predictions with the new model were checked against CFD results. Therefore the simulation case of the mixing vane spacer geometry with $P = 175\,\text{bar}$, $T_{in} = 627.82\,\text{K}$, $G = 4500\,\text{kg/m}^2\text{s}$, $q'' = 0\,\text{kW/m}^2$ and $\alpha_g = 0\%$ was selected. An input file for method A was created from this simulation and the other simulation parameters, such as spacer drag coefficients, wall friction factors and turbulent mixing coefficients were derived from this simulation. Table 4.1 shows the input parameters for the COBRA-FLX^{TM} simulation.

Tab. 4.1: Input parameters for COBRA-FLX^{TM} verification run with new models

Parameter	Value		
Material properties	IAPWS IF-97		
Mixing vane angle γ	28°		
Mixing vane area A_{vane}	0.231 cm^2		
Grid position z_{grid}/L	0.2182		
Cross-flow resistance coeff. C_{ij}	0.5		
Turbulent mixing coeff. C_β	$0.0055 Re^{-0.075}$		
Sub-channel parameter	Corner	Wall	Interior
Wall friction coeff. C_f	$0.167 Re^{-0.19}$	$0.153 Re^{-0.182}$	$0.142 Re^{-0.174}$
Spacer drag coeff.	1.4	0.82	0.65
Swirl decay param. C_{d1}	0.54	0.57	0.37

Some examples for the results of the different flow sweeping models are shown in Fig. 4.12 – 4.14. The axial distribution of pressure drop in the corner sub-channel is shown in Fig. 4.12. Compared to the CFD results, the simulation with the new flow sweeping models provides a better prediction of the pressure distribution in the vicinity of the spacer grid that is strongly affected by the cross-flow. The pressure field has an important impact on the lateral cross-flow calculation and its correct prediction is therefore very important.

The predictions for the axial development of the mass flux in the corner sub-channel are plotted in Fig. 4.13. Due to the mixing vane, there is a strong decay of mass flux in the vicinity of the grid. Further downstream, the mass flux recovers to the level as it was before the grid.
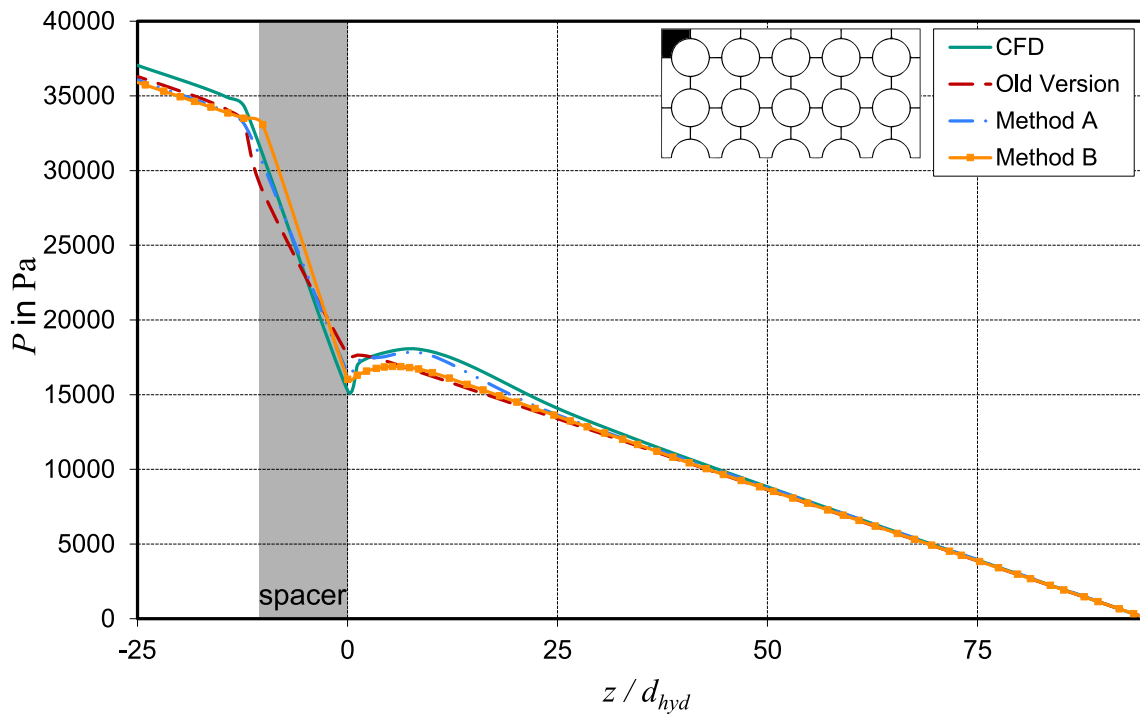
Fig. 4.12: *Predictions of COBRA-FLX^{TM} for the pressure drop within the corner sub-channel with different models for the forced cross-flow (P = 175 bar, G = 4500 kg/m²s and α = 0%)*
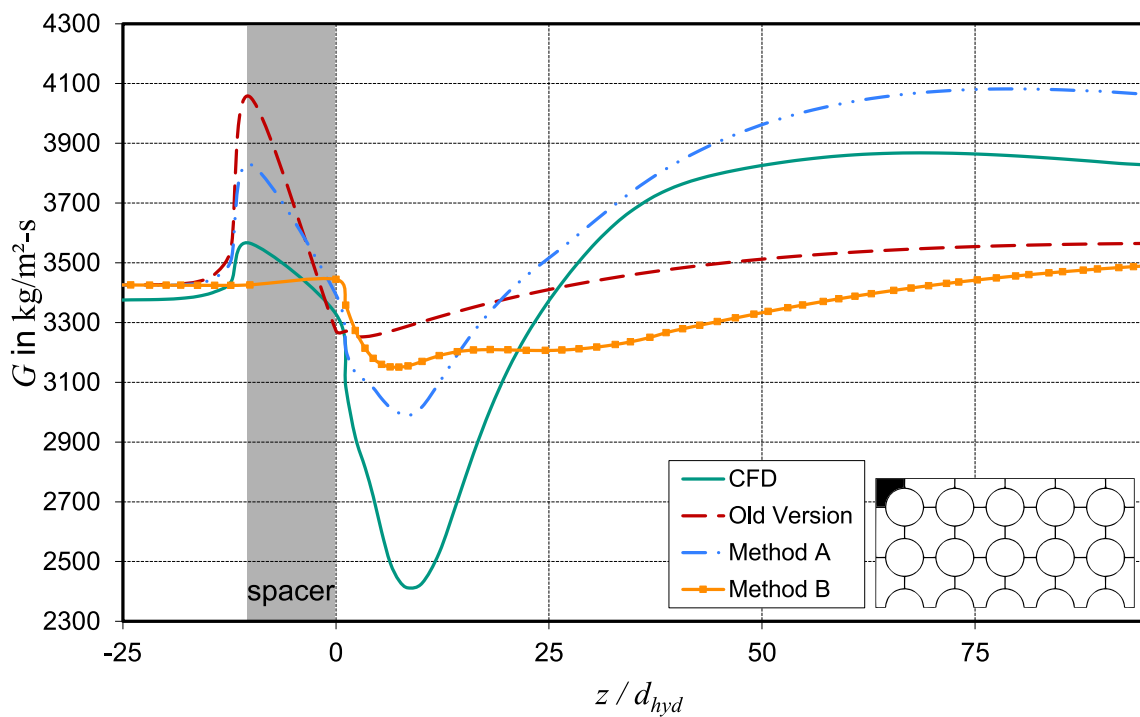
Fig. 4.13: *Predictions of COBRA-FLX^{TM} for the mass flux within the corner sub-channel with different models for the forced cross-flow (P = 175 bar, G = 4500 kg/m²s and α = 0%)*

This strong decay is captured by the new proposal for the flow sweeping model, whereas the old version shows large deviations from the CFD results. Also the predictions of method B are not satisfying. Method B is developed for the forced cross-flow between two interior channels. In a corner channel that is neighbored by two wall channels, there is a different behavior of the swirling flow that is not included yet in this version.
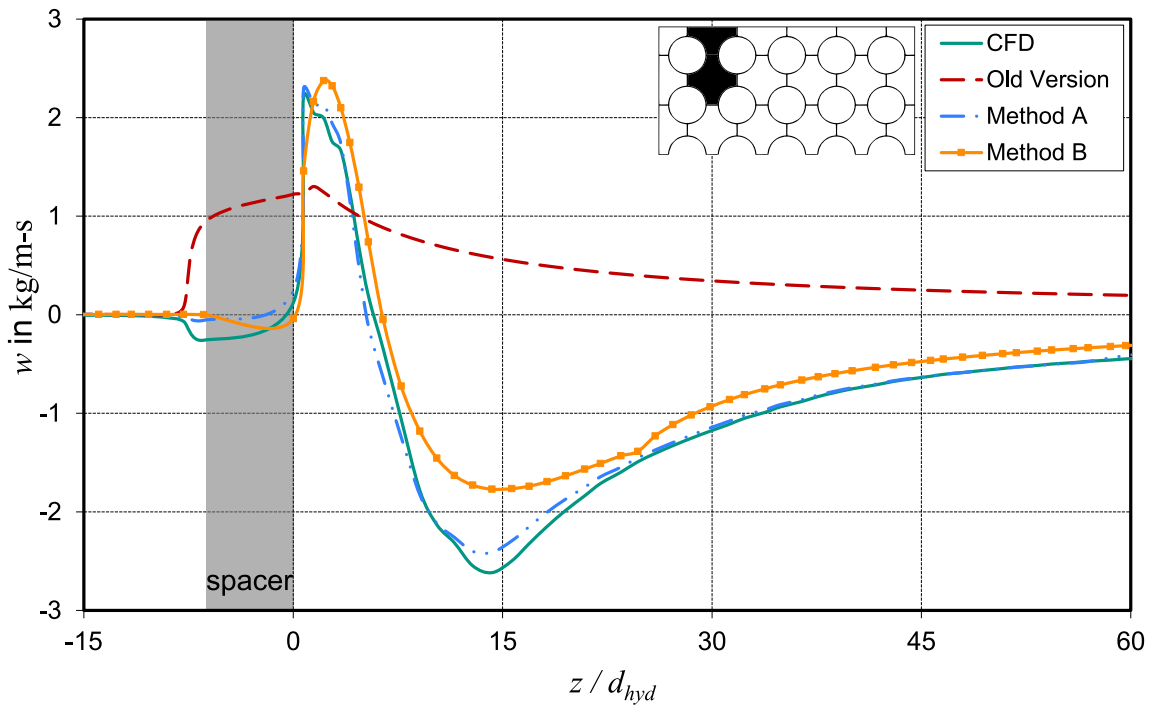
Fig. 4.14: Predictions of COBRA-FLX^{TM} for the cross-flow between two interior channels with different forced cross-flow models ($P = 175$ bar, $G = 4500\,^{kg}/_{m^2s}$ and $\alpha = 0\%$)

Figure 4.14 shows the predictions of COBRA-FLX^{TM} for the cross-flow in a typical gap between two interior channels. Obviously, the old model fails to predict the change of cross-flow direction in the vicinity of the grid that results from the swirling flow in the adjacent sub-channels. Both of the new model versions are able to predict this effect and as consequence, COBRA-FLX^{TM} is able to compute a better prediction for the cross-flows in the gaps and the mass flows in the sub-channels. The agreement of method A is better than of method B, because method A provides direct CFD input for this specific geometry for the forced cross-flow source term. The reason for the small differences can be explained with a slightly different pressure distribution in COBRA-FLX^{TM}. Method B can be applied to many more spacer geometries due to its parametrization but this advantage is paid with a slightly greater inaccuracy.

For a judgment of the overall performance of the new model approaches, the mass flux predictions of COBRA-FLX^{TM} for all sub-channels on a plane with an axial distance of $z/d_{hyd} = 20$ behind the mixing vane spacer were compared to the CFD results. After this distance, the major part of the spacer influenced section should be included in the results. Figure 4.15 shows the percentage of the sub-channel averaged mass flux deviations of the both proposed new methods and the old version of the Flow Sweeping model. It is shown that the deviations range from $< 1\%$ up to 15% of the mass flux that was predicted by CFD. Generally, the mass flux is over-predicted in the interior channels $8 - 11$ and $14 - 17$ and under-predicted in the wall and corner channels. Apparently method A performs best, this means, the deviations are the smallest, except for the wall channels 7 and 12.
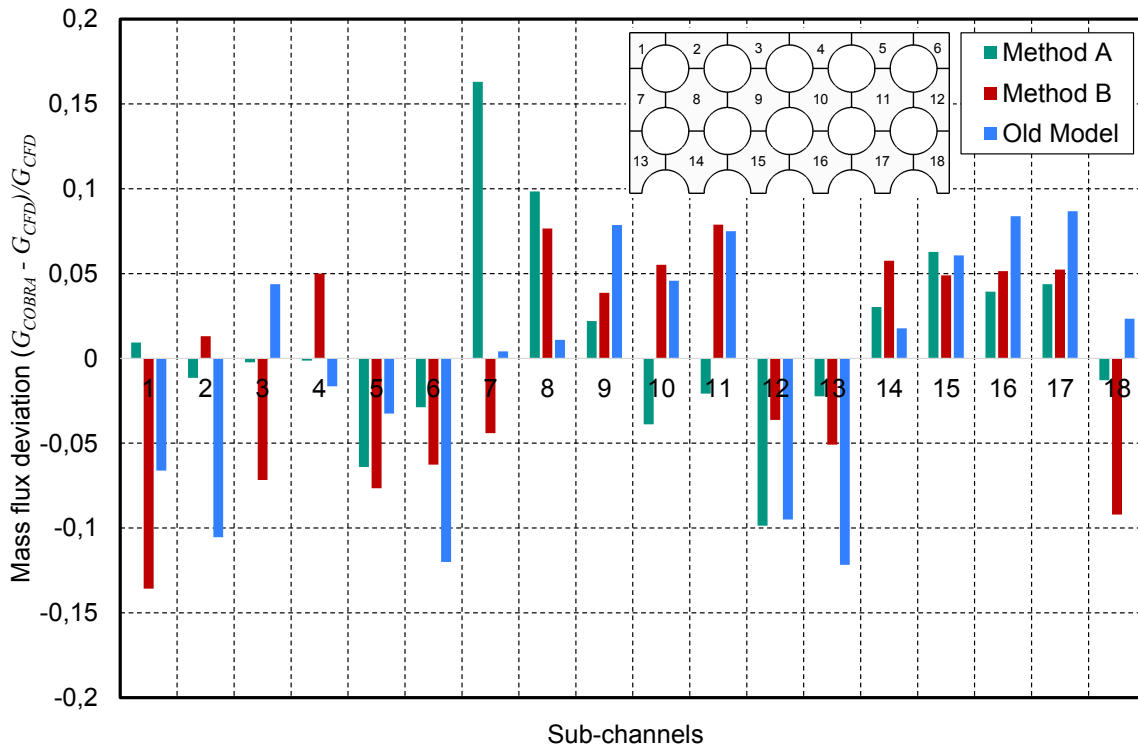
Fig. 4.15: Deviation of COBRA-FLX^{TM} mass flux predictions with different Flow Sweeping models ($P = 175$ bar, $G = 4500 \, \mathrm{kg/m^2s}$ and $\alpha = 0\%$)

4.2.4 Validation

As a validation case, a series of tests of the NUPEC PSBT benchmark published by Rubin et al. [100] was selected. It contains specifications for several test series for steady state and transient conditions. For this report, the steady state test series 5 and 8 including 105 data points were simulated with COBRA-FLX^{TM}. The operating conditions for these test series ranged for the pressure from $P = 48 \ldots 165$ bar, for the mass flux from $G = 550 \ldots 4200 \, \mathrm{kg/m^2s}$, for the bundle inlet temperature from $T_{in} = 150 \ldots 320 \, ^\circ$C and for the heat flux from $q'' = 375 \ldots 1200 \, \mathrm{kW/m^2}$. The geometrical specifications are given in Tab. 4.2. Data were sampled on three planes at the axial positions $z_1 = 221.6$ cm, $z_2 = 266.9$ cm and $z_3 = 317.7$ cm, averaged over the four central sub-channels of the 5×5 rod bundle (Fig. 4.16). These data are void fractions computed from the density of the flow that was measured with a gamma-ray transmission method. A direct conclusion about the quality of the new Flow Sweeping model is thereby not possible because the models for steam generation and distribution are of greater importance. However, an important parameter in steam generation is the mass flow distribution within the rod bundle and, due to the new model, there should be visible changes in the void distribution.

The 5×5 rod bundle was maintained by three different kinds of spacer grids, namely simple spacers, non-mixing vane spacers and mixing vane spacers that were assembled in alternately order with the rods. Details of the spacer geometries are given by Rubin et al. [100]. The effect of mixing vanes on the mass flow distribution is integrally included in the measurement results of the void fraction. For the prediction of the void fraction, the Levy [60] sub-cooled void correlation and the Chexal et al. [19] bulk-void correlation was used. The

Fig. 4.16: Geometry of NUPEC PSBT 5×5
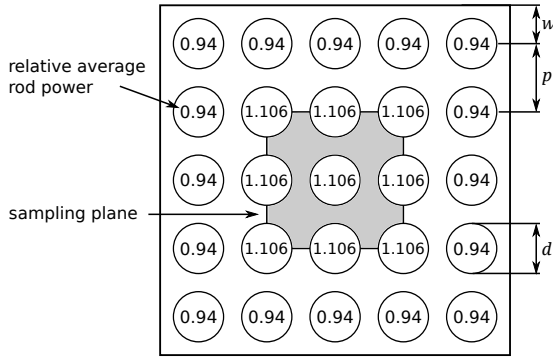
Tab. 4.2: NUPEC PSBT 5×5 geometry data

Parameter	Value
d	9.5 mm
p	12.6 mm
p_w	7.25 mm
l_h	365.8 cm

Zuber et al. [137] model was used to compute the flowing quality x_f from the thermal equilibrium quality x_e. The two-phase friction multiplier was computed using the model of Jones [42]. The material properties were taken from the IAPWS-IF97 property table given by Wagner and Kruse [129]. For the validation, three simulations with different Flow Sweeping modeling were performed for the entire test series: (1) Without model for the forced cross-flow, (2) with the old version of the forced cross-flow model given in Eq. 4.4 and (3) with the new version of the forced cross-flow model using method A (Eq. 4.12). The comparison of the results are made on two different evaluation planes located at different axial positions at z_2 and z_3 of the rod bundle. For these planes, the averaged void fractions of the four central sub-channels were measured experimentally. The results are shown in Fig. 4.17a and 4.17b.

(a) Void fractions at $z_2 = 266.9\,\text{cm}$

(b) Void fractions at $z_3 = 317.7\,\text{cm}$
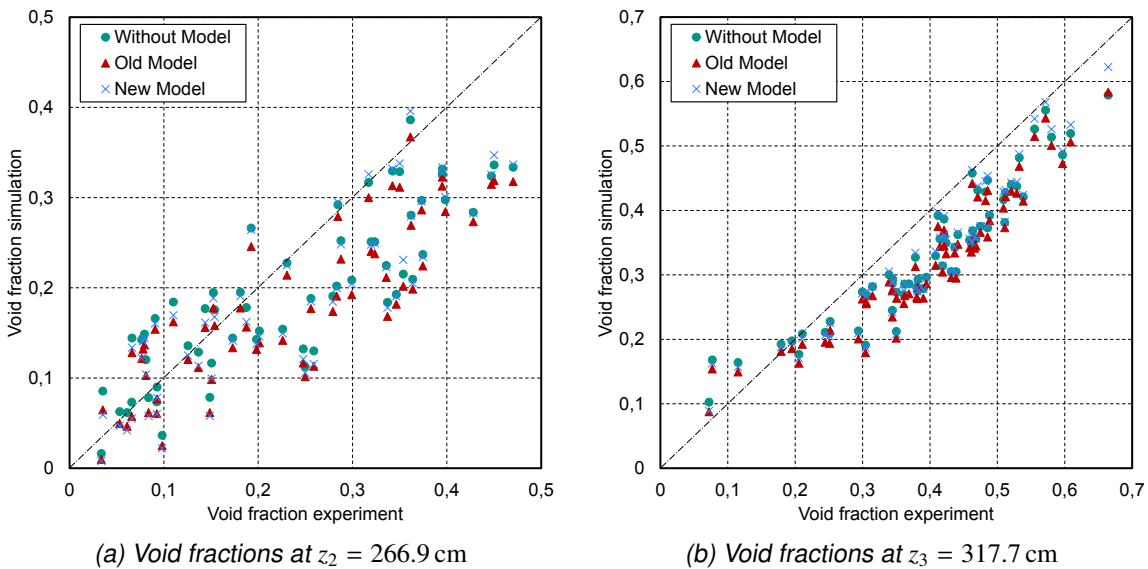
Fig. 4.17: COBRA-FLX^{TM} predictions with new Flow Sweeping model compared to the old approach

In terms of the standard deviation σ_D, defined in Eq. 4.24, there is a slight improvement of the prediction for the averaged void fraction in the four central sub-channels of the bundle with the new model, compared to the old model or the simulations without a Flow Sweeping model, as shown in Tab. 4.3. The standard deviation of the experimental results due to measurement inaccuracies are specified with $\sigma_D = 4\dots5\%$ in [100]. The improvement results from a better prediction of the mass flow distribution that is affected by the new model. Obviously, the

results from the simulations with the old model for Flow Sweeping are even worse than the simulations without model.

$$\sigma_D = \sqrt{\frac{1}{n-1} \cdot \sum_{i=1}^{n} \left(\alpha_i^{COBRA} - \alpha_i^{EXP} \right)^2} \qquad (4.24)$$

Number of experimental results n, void fraction data α

Tab. 4.3: Standard deviation σ_D of simulation results with different Flow Sweeping models compared to experimental data

Plane	Without model	Old model	New model
z_2	0.08	0.086	0.08
z_3	0.081	0.091	0.078

It should be considered that the results shown in Fig. 4.17a and 4.17b include also data for high void fractions. At high void fractions, different flow regimes can be established, such as slug flow ($0.15 < \alpha \leq 0.5$) or annular flow ($0.5 < \alpha < 1$). These flow regimes were not investigated in this work by means of CFD simulations and therefore the validity range of the newly proposed model is limited to the parameter range that was used for this work. Nevertheless also for high void fractions an improvement of the prediction accuracy can be observed. This indicates that the mechanisms that are responsible for the Flow Sweeping are still in effect at high void fractions.
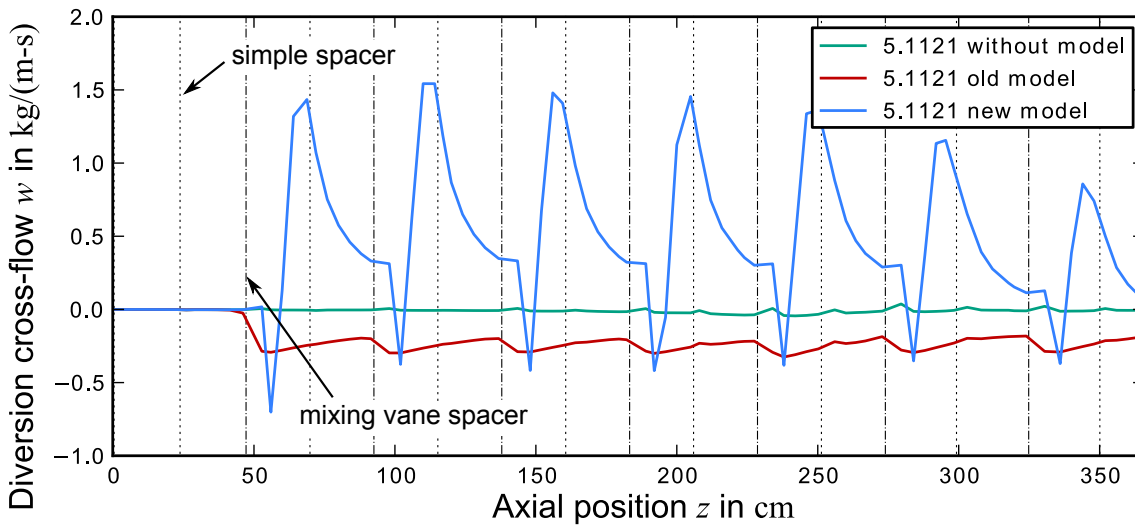
Fig. 4.18: Predictions of COBRA-FLX^{TM} for the cross-flow between two interior sub-channels ($P = 175$ bar, $G = 4500$ kg/m²s and $\alpha = 0\%$)

For the test case number 5.1121 ($P = 164$ bar, $T_{in} = 590$ K, $G = 4156$ kg/m²s, $q'' = 1096$ kW/m²), there are detailed results of the COBRA-FLX^{TM} simulations given for the axial development of the cross-flow. Along the bundle axis, there are alternately simple spacers and mixing vane spacers, indicated by different vertical lines in Fig. 4.18. After the mixing vane spacer, there is a strong increase of the cross-flow, determined by the vane. Later, the cross-flow

turns to the opposite direction. This effect of cross-flow reversion is not captured by the old model, it predicts the cross-flow always to be directed into the same direction. Without a Flow Sweeping model, the cross-flows are computed only with the pressure difference. In this case, the magnitude of the cross-flow is very small compared to the simulations with Flow Sweeping model.

Due to the strong cross-flow, the mass flux in the interior channels is strongly increased compared to the simulation without Flow Sweeping model. In other sub-channels it is decreased therefore. According to the experimental results, the void fractions on the lower plane z_1 and the middle plane z_2 are zero and, because of the heating, $\alpha(z_3) = 17.9\%$ on the upper plane. Due to the different mass flows, the predicted void generation is also different in the three simulations. As result, the average void fractions on the evaluation sections are closer to the experimental data in case of the new model compared to the simulations without cross-flow model or with the old model.

Chapter 5

Summary and Outlook

COBRA-FLX^{TM} is used by AREVA GmbH for thermal-hydraulic design of nuclear reactor cores. Here, a precise prediction of the cross-exchange of mass, momentum and energy between the sub-channels is necessary to calculate the mass flow and temperature distribution within the fuel assembly. In the sub-channel analysis program COBRA-FLX^{TM}, the cross-exchange mechanisms "Turbulent Mixing" and "Diversion Cross-flow" are considered. Due to a spacer grid, such as those typically used in fuel assemblies, there are additional cross-exchange mechanisms which have a strong influence on the mass flow and temperature distribution. Because of the blockage of the flow channel, there is a change in the velocity distribution within the channel. Therefore additional turbulence is created which can increase the cross-exchange in the wake of a spacer grid. This effect is called "Flow Scattering". In modern lattice geometries, often so-called mixing vanes are used. These are shaped to deflect a fraction of the axial mass flow in the transverse direction and thus produce a forced convection into adjacent sub-channels. This effect is called "Flow Sweeping". Furthermore, the mixing vanes generate a strong vortex flow inside of a sub-channel. These phenomena must be taken into account in the calculation of the cross-exchange.

Until now, the possibilities of COBRA-FLX^{TM} to include these phenomena in the calculations are very limited. The Flow Sweeping could be approximately calculated if the proportion of the axial mass flow, which is deflected by the mixing vanes, is directly determined as the cross-flow. For this reason, the lateral momentum conservation equation used by COBRA-FLX^{TM} is replaced at the calculation node behind the spacer position by another equation. This method is not sufficient to determine the axial development of the cross-flow.

The objective of this work was to investigate the possibilities of the high-resolution, numerical 3D-CFD tool STAR-CCM+$^{®}$ 9.02.005 for the analysis of these cross-exchange phenomena. In this case, the wake flow of a grid spacer was studied in detail among several reactor operating conditions in a single-phase water and two-phase water-vapor flow. As a result, guidelines should be developed for the setup of a CFD simulation model for this purpose and how the simulation results can be evaluated in order to use the obtained data as input parameters for COBRA-FLX^{TM} simulations. In addition, the cross-exchange should be systematically examined in the wake of a grid spacer. Based on the CFD data, a model shall be proposed to compute the Flow Sweeping effect.

As geometry for the CFD simulation model PWR-typical dimensions were chosen with a rod diameter of $d = 9.5\,\text{mm}$ and a rod pitch $p = 12.6\,\text{mm}$ for the bundle that is consisted of a square array of 5×5 fuel rods. The decreased number of fuel rods, compared to 17×17 bundles in the reality, can be explained with the limited computing capacity, so the simulation model has been reduced to its essential characteristics. The axial length of the bundle was therefore $l_B = 77.5\,\text{cm}$. This length contained a grid spacer with a short inflow section and a long outflow section for evaluating the simulation results. Two different grid geometries were used with the difference that one grid has mixing vanes and the other one does not. This allowed to explicitly show the influence of the mixing vanes. As operating conditions, two different pressure levels with $P_1 = 80\,\text{bar}$ and $P_2 = 175\,\text{bar}$ were selected. The temperature was set as the respective saturation temperature of water at each pressure level so that both phases can coexist simultaneously. This corresponds to temperatures of $T_1 = 568.16\,\text{K}$ at pressure level P_1 and $T_2 = 627.82\,\text{K}$ at pressure level P_2. As a result of these conditions, the material properties were considered as constant and the temperature was set to be isotherm. Accordingly, the walls were assumed as adiabatic. The influence of a heated fluid has been omitted in order not to superimpose the cross-exchange phenomena by boiling phenomena. These processes can be reproduced only inaccurately by current CFD programs anyway. The considered mass flux was five-fold between $G = 700\ldots4500\,\text{kg/m}^2\text{s}$. In the two-phase flow simulations, the velocities of the water and vapor phases at the inlet boundary were chosen in order to obtain a 4-stage void fraction between $\alpha_g = 0\%$ (single phase) and $\alpha_g = 15\%$. Under these conditions, it is ensured that a bubbly flow regime is established, where a uniform distribution of the two phases within the flow area can be assumed.

For the spatial differentiation of the individual sub-channels of the rod bundle, the simulation area was divided into a plurality of regions that are connected by interface boundaries. This approach has enabled the the evaluation of simulation results in the individual sub-channels separately from each other without overlap or different sized sub-channels caused by the spatial extent of the computational grid cells. As inlet boundary condition data tables were used with the data of a fully developed flow. These data were obtained from previous simulations with bundle geometries without spacers and with periodic boundary conditions in the axial direction. This ensured a realistic and well-defined inflow of the spacer grid.

At first, a selection was made from the available models in the CFD program STAR-CCM+® 9.02.005 with which the expected flow phenomena could be simulated. In the two-phase simulations, an Euler-Euler two-fluid model has been used. The turbulence of the continuous phase was simulated using a cubic non-linear k-ε model and the turbulence of the dispersed phase was calculated with a turbulence response model that depends on the turbulence parameters of the continuous phase. The inter-phase momentum transfer was calculated using models for the Drag Force, Lift Force, Turbulence Dispersion Force and Wall Lubrication Force. The bubble sizes were determined by the S-Gamma model. The predictions of the used models in the considered parameter range were checked by different validation exercises. For this purpose, after a comprehensive literature study, experimental data were selected. It has been found that there is an acute shortage of highly qualitative and quantitative measurements of cross-exchange under the desired operating conditions. Therefore, the used models can be carefully

considered as validated. Nevertheless, it has been shown that the mass flow distribution, the vorticity and the vortex structure of the simulations agrees very well qualitatively with experimental measurements. The concept of a separated simulation region affects equally marginal the simulation results, such as the choice of boundary condition formulation or limitation of the simulation domain to a single span of a rod bundle with one spacer grid.

At next, a grid study was performed. STAR-CCM+® 9.02.005 provides several models that define the kind of meshing of the simulation region. The cell size and mesh quality can be adjusted by several parameters. These parameters were optimized in several simulations regarding mesh quality, mesh independence of results and computational effort. As meshing model a trimmed hexahedral mesh was chosen. In this mesh type, adjacent cells are similar in size and most cell faces are orthogonal to each other. This ensures a high mesh quality. Solid walls are approximated by a number of layers of prismatic cells which are orthogonal to the wall surface. Thereby strong gradients occurring near the wall can be reflected better. The wall distance is chosen so that there are dimensionless wall distances in the range $15 < y^+ \leq 200$ among the bandwidth of the flow conditions. Wall functions are used therefore to model the velocity profile in the wall-adjacent mesh-layer.

The simulation results include data for pressure drop across the grid, the pressure loss due to wall friction, the cross-flow velocity, the turbulent fluctuating velocity in the gap, the velocity gradient in the gap, the distribution of the void fraction and the lateral momentum in the sub-channels. The pressure drop across the grid depends on the blockage ratio and on the Reynolds number. The greater the blockage of the flow passage by the spacer, the higher the pressure drop. With increasing Reynolds number, the pressure loss coefficient, however, falls. This behavior is also reflected in the wall friction coefficient, which depends also on the hydraulic diameter. The cross-flow velocity in the case of the grid with mixing vanes is much stronger than with the simple spacer. The direction is specified directly behind the grid by the alignment of the mixing vanes, but it can be reversed along the axial direction under certain conditions. The turbulent fluctuation velocity in the gap rises sharply behind the spacer and then decreases exponentially. Wherein the mixing vane spacer, this effect is more pronounced than with the simple grid. Thus, fluctuations with several peaks may occur. The velocity difference in the gap depends on many factors and is very different from the difference of the sub-channel averaged velocities. In the wake of the grid, their ratio may even reverse. The void is accumulated in areas of lower pressure. In the vortex centers, there is a higher void fraction as outside of the vortices. Directly behind the spacers the void fraction is also higher than further downstream. Due to the mixing vanes, a strong lateral velocity component is generated in the wake of the grid which decays exponentially and greatly influences the cross-flow in its axial development. As the highlights of this work, following results were obtained:

- On the basis of extensive CFD simulation results, a model has been proposed to calculate the forced cross-flow induced by mixing vanes (Flow Sweeping).

- An additional source term was introduced into the lateral momentum balance equation of COBRA-FLX™. This term is determined by the geometry of the mixing vane and the lateral momentum in the adjacent sub-channels.

- Two methods have been proposed how to quantify the new source term:

  - Method A: Dimensionless values for the source term are evaluated from the CFD results and stored in an ASCII file to be used as input data for COBRA-FLX^{TM}. This record is geometry-specific, so appropriate simulations have to be performed for each grid type. It has been described how the CFD simulations are to be evaluated in order to obtain these data.

  - Method B: The source term is evaluated from the lateral momentum of the adjacent sub-channels of a gap, that is induced by the mixing vanes. A mapping function was developed to consider the non-isotropic distribution of lateral momentum due to the mixing vane orientation and the rotation of the flow.

- The new model is applicable to high Reynolds number flows with void fractions of $\alpha_g \leq 15\%$ and split-type mixing vane spacer geometries.

- The verification of the COBRA-FLX^{TM} implementation of the model shows that a very good agreement can be obtained with the CFD results. With this new model, COBRA-FLX^{TM} is able to qualitatively and quantitatively predict better the axial profile of the transverse mass flow with forced cross flow as with the old version of the model.

- Validation calculations based on experimental data for the void fraction averaged over the four central channels of a 5×5 rod bundle show an improvement in predictive accuracy over the old model.

In the next steps, the validation of the new model should be extended for the desired operating conditions based on explicit measurement data for mass flow distribution or the transverse flow rate. The necessary data were not available for this work. For the practical applicability of the newly proposed model, a further investigation of the numerical stability and accuracy, even at low spatial resolution of the flow area by the sub-channel program, is still required.

Bibliography

[1] Norbert Alleborn, R. Reinders, S. Lo, and A. Splawski. Analysis of two-phase flows in pipes and subchannels under high pressure. In *7th World Conference on Experimental Heat Transfer, Fluid Mechanics and Thermodynamics*, 2009.

[2] S. P. Antal, R. T. Lahey, and J. E. Flaherty. Analysis of of phase distribution in fully developed laminar bubbly two-phase flow. *International Journal of Multiphase Flow*, 17: 635 – 652, 1991.

[3] AREVA GmbH. *COBRA-FLX: A Core Thermal-Hydraulic Analysis Code*, ANP-10311P edition, March 2010. Proprietary.

[4] T. R. Auton, J. C. R. Hunt, and M. Prud'Homme. The force exerted on a body in inviscid unsteady non-uniform rotational flow. *Journal of Fluid Mechanics*, 197:241 – 257, 1988.

[5] Maria Avramova. *Development of an innovative spacer grid model utilizing computational fluid dynamics within a subchannel analysis tool*. PhD thesis, Pennsylvania State University, 2007.

[6] E. Baglietto, H. Ninokata, and Takeharu Misawa. CFD and DNS methodologies development for fuel bundle simulations. *Nuclear Engineering and Design*, 236:1503 – 1510, 2006.

[7] Abbes Bellil, A. Teyssedou, L. Bonnet, and P. Tye. Void drift in two interconnected subchannels. In *9th Int. Topical Meeting on Nuclear Reactor Thermal Hydraulics, NURETH-9*, San Francisco, USA, 1999.

[8] S. G. Beus. A two-phase turbulent mixing model for flow in rod bundles. Technical Report WAPD-T-2438, Bettis Atomic Power Lab., 1971.

[9] T.J. Blasing. Recent greenhouse gas concentrations. http://cdiac.ornl.gov/pns/current_ghg.html, February 2014.

[10] G. Bozzano and M. Dente. Shape and terminal velocity of single bubble motion: a novel approach. *Computers & Chemical Engineering*, 25:571 – 576, 2001.

[11] Bundesanstalt für Geowissenschaften und Rohstoffe (BGR). Energierohstoffe 2009 - Reserven, Ressourcen, Verfügbarkeit. Technical report, 2009.

[12] Alan D. Burns, Thomas Frank, Ian Hamill, and Jun-Mei Shi. The Favre-averaged drag model for turbulent dispersion in Eulerian multi-phase flows. In *5th International Conference on Multiphase Flow, ICMF04*, number Paper No. 392, Yokohama, Japan, 2004.

[13] Diana Caraghiaur. Experimental study and modelling of spacer grid influence on flow in nuclear fuel assemblies. Technical report, KTH Stockholm, 2009.

[14] Pedro Carajilescov. *Experimental and analytical study of axial turbulent flows in an interior subchannel of a bare rod bundle*. PhD thesis, Massachusetts Institute of Technology, 1976.

[15] Frank S. Castellana, Wilton T. Adams, and Joseph E. Casterline. Single-phase subchannel mixing in a simulated nuclear fuel assembly. *Nuclear Engineering and Design*, 26:242 – 249, 1974.

[16] Seok Kyu Chang, Sang Ki Moon, Won Pil Baek, and Young Don Choi. Phenomenological investigations on the turbulent flow structures in a rod bundle array with mixing devices. *Nuclear Engineering and Design*, 238:600 – 609, 2008.

[17] Shih-Kuei Cheng and Neil E. Todreas. Hydrodynamic models and correlations for bare and wire-wrapped hexagonal rod bundles - bundle friction factors, subchannel friction factors and mixing parameters. *Nuclear Engineering and Design*, 92:227 – 251, 1986.

[18] Xu Cheng and U. Müller. Turbulent mixing and critical heat flux in thight 7-rod bundles. *International Journal of Multiphase Flow*, 24:1245 – 1263, 1998.

[19] B. Chexal, G. Lellouche, J. Horowitz, and J. Healzer. A void fraction correlation for generalized applications. *Progress in Nuclear Energy*, 27:255 – 406, 1992.

[20] Ji Bum Chung, Won-Pil Baek, and Soon Heung Chang. Effects of the spacer and mixing vanes on critical heat flux for low-pressure water at low-velocities. *International Communications in Heat and Mass Transfer*, 23:757 – 765, 1996.

[21] J. G. Collier and J. R. Thome. *Convective Boiling and Condensation*. Oxford Science Publications, 1996.

[22] Michael E. Conner, Yassin A. Hassan, and Elvis E. Dominguez-Ontiveros. Hydraulic benchmark data for PWR mixing vane grid. *Nuclear Engineering and Design*, 264:97 – 102, 2013.

[23] Xiang-Zhe Cui and Kwang-Yong Kim. Three-dimensional analysis of turbulent heat transfer and flow through mixing vane in a subchannel of nuclear reactor. *Journal of Nuclear Science and Technology*, 40:719 – 724, 2003.

[24] F. De Crécy. The effect of grid assembly mixing vanes on critical heat flux values and azimuthal location in fuel assemblies. *Nuclear Engineering and Design*, 149:233 – 241, 1994.

[25] Elvis E. Dominguez-Ontiveros, Yassin A. Hassan, Michael E. Conner, and Zeses Karoutas. Experimental Benchmark data for PWR rod bundle with spacer-grids. *Nuclear Engineering and Design*, 253:396 – 405, 2012.

[26] P. A. Durbin. On the k-e stagnation point anomaly. *IntInternation Journal of Heat and Fluid Flow*, 17:89 – 90, 1996.

[27] W. Eifler and R. Nijsing. Experimental investigation of velocity distribution and flow resistance in a triangular array of parallel rods. *Nuclear Engineering and Design*, 5:22 – 42, 1967.

[28] ExxonMobil. The Outlook for Energy: A View to 2040. http://www.exxonmobil.com/energyoutlook, 2013.

[29] A. Faya, L. Wolf, and N. Todreas. Development of a method for BWR subchannel analysis. Technical Report MIT-EL 79-027, Massachusetts Institute of Technology, 1979.

[30] A. Gandhir and Yassin Hassan. RANS modeling for flow in nuclear fuel bundle in pressurized water reactors (PWR). *Nuclear Engineering and Design*, 241:4404 – 4408, 2011.

[31] M. M. Gibson and B. E. Launder. Ground effects on pressure fluctuations in the atmospheric boundary layer. *Journal of Fluid Mechanics*, 86:491 – 511, 1978.

[32] H. Herkenrath, W. Hufschmidt, U. Jung, and F. Weckermann. Experimental investigation of the enthalpy and mass flow-distribution in 16-rod clusters with BWR + PWR geometries and conditions. Technical report, Joint Research Center ISPRA Establishment, 1981.

[33] Mary V. Holloway, Heather L. McClusky, Donald E. Beasley, and Michael E. Conner. The effect of support grid features on local, single-phase heat transfer measurements in rod bundles. *Journal of Heat Transfer*, 126:43 – 53, February 2004.

[34] Mary V. Holloway, Donald E. Beasley, and Michael E. Conner. Single-phase convective heat transfer in rod bundles. *Nuclear Engineering and Design*, 238:848 – 858, 2008.

[35] J. D. Hooper. Developed single-phase turbulent flow through a square-pitch rod cluster. *Nuclear Engineering and Design*, 60:365 – 379, 1980.

[36] J. D. Hooper, D. H. Wood, and W. J. Crawford. Developed single-phase turbulent flow through a square-pitch rod cluster for an extended range of reynolds numbers. Technical Report AAEC/E558, Australian Atomic Energy Commission, 1983.

[37] Akitoshi Hotta, Hiroshi Shirai, Mie Azuma, Michio Sadatomi, Akimaro Kawahara, and Hisashi Ninokata. A modified equilibrium void distribution model applicable to subchannel-scale vapor-liquid cross flow model for conventional square and tight lattice bwr fuel bundles. *Nuclear Engineering and Design*, 235:983 – 999, 2005.

[38] Wang Kee In. Numerical study of coolant mixing caused by the flow deflectors in a nuclear fuel bundle. *Nuclear Technology*, 134:197 – 205, 2001.

[39] Wang Kee In, Dong Seok Oh, and Tae Hyun Chun. Flow analysis for optimum design of mixing vane in a PWR fuel assembly. *Journal of the Korean Nuclear Society*, 33(3): 327 – 338, June 2001.

[40] R. I. Issa and P. J. Oliveira. Numerical prediction of phase separation in two-phase flow through t-junctions. *Computers Fluids*, 23:347 – 372, 1994.

[41] J. W. Jackson and N. E. Todreas. COBRA-IIIC/MIT-2: A Digital Computer Program for Steady State and Transient Thermal-Hydraulic Analysis of Rod Bundle Nuclear Fuel Elements. Technical Report MIT-EL 81-018, Massachusetts Institute of Technology, 1981.

[42] A. B. Jones. Hydrodynamic stability of a boiling channel. Technical Report KAPL-2170, Knolls Atomic Power Laboratory, 1961.

[43] W. P. Jones and B. E. Launder. The prediction of laminarization with a two-equation model of turbulence. *International Journal of Heat and Mass Transfer*, 15:301 – 314, 1972.

[44] Zeses Karoutas, Chun-Yuan Gu, and Bertil Schölin. 3-d flow analyses for design of nuclear fuel spacer. In *Proceedings of the 7th International Meeting on Nuclear Reactor Thermal-Hydraulics NURETH-7*, pages 3153 – 3174, Saratoga Springs, USA, 1995.

[45] Akimaro Kawahara, Yoshifusa Sato, and Michio Sadatomi. The turbulent mixing rate and the fluctuations of static pressure difference between adjacent subchannels in a two-phase subchannel flow. *Nuclear Engineering and Design*, 175:97 – 106, 1997.

[46] Akimaro Kawahara, Michio Sadatomi, Hiroyuki Kudo, and Keiko Kano. Single and two-phase turbulent mixing rate between subchannels in triangle tight lattice rod bundle. *JSME International Journal*, 49:287 – 295, 2006.

[47] Kwang-Yong Kim and Jun-Woo Seo. Numerical optimization for the design of a spacer grid with mixing vanes in a pressurized water reator fuel assembly. *Nuclear Technology*, 149:62 – 70, 2005.

[48] Ákos Horváth and Bernd Dressel. Numerical simulations of square arrayed rod bundles. *Nuclear Engineering and Design*, 247:168 – 182, 2012.

[49] T. Krauss. *Experimentelle Untersuchung des turbulenten Wärme- und Impulstransports in einem beheizten Stabbündel.* PhD thesis, Universität Karlsruhe, 1996.

[50] R. T. Lahey and F. J. Moody. *The thermal-hydraulics of a boiling water nuclear reactor*. American Nuclear Society, 1993.

[51] Richard T. Lahey, B. S. Shiralkar, and D. W. Radcliffe. Two-phase flow and heat transfer in multirod geometries: Subchannel and pressure drop measurements in a nine-rod bundle for diabatic and adiabatic conditions. Technical report, General Electric, 1970.

[52] Richard T. Lahey, B. S. Shiralkar, D. W. Radcliffe, and E. E. Polomik. Out-of-pile sub-channel measurements in a nine-rod bundle for water at 1000 psia. *Progress in heat and mass transfer*, 6:345 – 363, 1972.

[53] M. Lance and J. Bateille. Turbulence in liquid phase of a uniform bubbly air-water flow. *Journal of Fluid Mechanics*, 222:95 – 118, 1991.

[54] B. E. Launder and D. B. Spalding. The numerical computation of turbulent flows. *Computer Methods in Applied Mechanics and Engineering*, 3:269 – 289, 1974.

[55] M. Leberig, N. Alleborn, M. Glück, J. Jones, Ch. Kappes, C. Lascar, and G. Sieber. AREVA NP's Advanced Thermal Hydraulic Methods for Reactor Core and Fuel Assembly Design. In *Top Fuel 2009*, Paris, France, September 2009.

[56] C. M. Lee and Y. D. Choi. Comparison of thermo-hydraulic performances of large scale vortex flow (LSVF) and small scale vortex flow (SSVF) mixing vanes in 17x 17 nuclear rod bundle. *Nuclear Engineering and Design*, 237:2322 – 2331, 2007.

[57] J. Lehmann. Widerstandsgesetze der turbulenten Strömung in geraden Stahlrohren. *Gesundheit, Zeitschrift für angewandte Hygiene und Gesundheitstechnik in Stadt und Land*, 82:Heft 6, 1961.

[58] Yu. D. Levchenko, V. I. Subbotin, and P. A. Ushakov. Experimental investigation of averaged characteristics of turbulent flow in cells of rod packs. *Atomnaya Energiya*, 33: 893 – 899, 1972.

[59] S. Levy. Prediction of two-phase pressure drop and density distribution from mixing length theory. *Journal of Heat Transfer*, 5:137 – 152, 1963.

[60] S. Levy. Forced convection subcooled boiling - prediction of vapor volumetric fraction. *International Journal of Heat and Mass Transfer*, 10:951 – 965, 1967.

[61] Xiaochang Li and Ye Gao. Methods of simulating large-scale rod bundle and application to a 17 x 17 fuel assembly with mixing vane spacer grid. *Nuclear Engineering and Design*, 267:10 – 22, 2014.

[62] F. S. Lien, W. L. Chen, and M. A. Leschziner. Low-Reynolds number eddy-viscosity modelling based on non-linear stress-strain/vorticity relations. In *Proceedings of the 3rd Symposium on Engineering Turbulence Modelling and Measurements*, pages 27 – 29, Crete, Greece, 1996.

[63] Simon Lo and Dongsheng Zhang. Modelling of break-up and coalescence in bubbly two-phase flows. *Journal of Computational Multiphase Flows*, 1:23 – 38, 2009.

[64] J. N. Loomis and W. D. Hinkle. Reactor core thermal-hydraulic analysis – Improvement and application of the code COBRA-IIIC/MIT. Technical Report MIT-EL 80-027, Massachusetts Institute of Technology, September 1980.

[65] Heather L. McClusky, Mary V. Holloway, Donald E. Beasley, and Michael E. Conner. Development of a swirling flow in a rod bundle subchannel. *Journal of Fluids Engineering*, 124:747 – 755, 2002.

[66] Heather L. McClusky, Mary V. Holloway, Timothy A. Conover, Donald E. Beasley, Michael E. Conner, and L. David Smith III. Mapping of the lateral flow field in typical subchannels of a support grid with vanes. *Journal of Fluids Engineering*, 125:987 – 996, November 2003.

[67] F. R. Menter. Two-equation eddy-viscosity turbulence models for engineering applications. *AIAA Journal*, 32:1598 – 1605, 1994.

[68] E. Merzari, H. Ninokata, and E. Baglietto. Numerical simulation of flows in tight-lattice fuel bundles. *Nuclear Engineering and Design*, 238:1703 – 1719, 2008.

[69] Leonhard Meyer. From discovery to recognition of periodic large scale vortices in rod bundles as source of natural mixing between subchannels. *Nuclear Engineering and Design*, 240:1575 – 1588, 2010.

[70] Kaichiro Mishima and Mamoru Ishii. Flow regime transition criteria for upward two-phase flow in vertical tubes. *International Journal of Heat and Mass Transfer*, 27:723 – 737, 1984.

[71] Sergio Vicosa Möller. Single-phase turbulent mixing in rod bundles. *Experimental Thermal and Fluid Science*, 5:26 – 33, 1992.

[72] J. Nikuradse. Untersuchung über turbulente Strömungen in nicht-kreisförmigen Querschnitten. Technical report, Kaiser-Wilhelm-Institut für Strömungsforschung, Göttingen, Germany, 1930.

[73] H. Ninokata, T. Anegawa, M. Aritomi, T. Hara, H. Kamo, S. Kusuno, K. Mishima, S. Morooka, K. Nishida, M. Sadatomi, A. Sou, Y. Yabushita, and Y. Yamamoto. Development of the NASCA code for predicting transient BT phenomena in BWR rod bundles. Technical Report R(2001)2 vol. 2, NEA / CSNI, 2001.

[74] Bo Pang. *Numerical study of void drift in rod bundle with subchannel and CFD codes*. PhD thesis, Karlsruhe Institute of Technology, 2014. KIT scientific reports 7669.

[75] K. Podila, Y. F. Rao, M. Krause, and J. Bailey. A CFD simulation of 5 x 5 rod bundles with split-type spacers. *Progress in Nuclear Energy*, 70:167 – 175, 2014.

[76] C. W. Rapley and A. D. Gosman. The prediction of fully developed axial turbulent flow in rod bundles. *Nuclear Engineering and Design*, 97:313 – 325, 1986.

[77] Klaus Rehme. Experimentelle Untersuchungen der turbulenten Strömung in einem Wandkanal eines Stabbündels. Technical Report KFK 2441, Kernforschungszentrum Karlsruhe, 1977.

[78] Klaus Rehme. Turbulente Strömung in einem Wandkanal eines Stabbündels. Technical Report KFK 2617, Kernforschungszentrum Karlsruhe, 1978.

[79] Klaus Rehme. The structure of turbulent flow through subchannel of a rod bundle. *Nuclear Engineering and Design*, 45:311 − 323, 1978.

[80] Klaus Rehme. The pressure drop of spacer grids in rod bundles of 12 rods with smooth and roughened surfaces. Technical Report KfK 2697, Kernforschungszentrum Karlsruhe, 1978.

[81] Klaus Rehme. Turbulent momentum transport in rod bundles. *Nuclear Engineering and Design*, 62:137 − 146, 1980.

[82] Klaus Rehme. The structure of turbulent flow through rod bundles. *Nuclear Engineering and Design*, 99:141 − 154, 1987.

[83] H. Reichardt. Messung turbulenter Schwankungen. *Die Naturwissenschaften*, 24:404 − 408, 1938.

[84] M. Renksizbulut and G. I. Hadaller. An experimental study of turbulent flow through a square-array rod bundle. *Nuclear Engineering and Design*, 91:41 − 55, 1986.

[85] Osborne Reynolds. On the dynamical theory of incompressible viscous fluids and the determination of the criterion. *Philosophical Transactions of the Royal Society of London*, 186:123 − 164, 1895.

[86] J. Richardson and W. Zaki. Sedimentation and Fluidisation: Part 1. *Transactions of the Institution of Chemical Engineers*, 32:35 − 53, 1954.

[87] J. T. Rogers and R. G. Roseheart. Mixing by turbulent interchange in fuel bundles. correlations and interfaces. Technical Report 72-HT-53, ASME, 1972.

[88] J. T. Rogers and N. E. Todreas. *Coolant Mixing in Rod Bundles*, chapter 1, pages 1 − 56. The American Society of Mechanical Engineers, 1968.

[89] M. Roidt, M. J. Pechersky, R. A. Markley, and B. J. Vegter. Experimental determination of turbulent exchange coefficients in a model reactor rod bundle. Technical report, Westinghouse Research Laboratories, 1973.

[90] E. R. Rosal, J. O. Cermak, L. S. Tong, J. E. Casterline, S. Kokolis, and B. Matzner. High pressure rod bundle DNB data with axially non-uniform heat flux. *Nuclear Engineering and Design*, 31:1 − 20, 1974.

[91] D S Rowe. COBRA-II: A digital computer program for thermal-hydraulic subchannel analysis of rod bundle nuclear fuel elements. Technical Report BNWL-1229, Battelle Pacific Northwest Laboratories, February 1970.

[92] D. S. Rowe. COBRA-III: A digital computer program for steady state and transient thermal-hydraulic analysis of rod bundle nuclear fuel elements. Technical Report BNWL-B-82, Battelle Pacific Northwest Laboratories, 1971.

[93] D. S. Rowe. COBRA-IIIC: A digital computer program for steady state and transient thermal-hydraulic analysis of rod bundle nuclear fuel elements. Technical Report BNWL-1695, Battelle Pacific Northwest Laboratories, March 1973.

[94] D. S. Rowe and C. W. Angle. Cross-flow mixing between parallel flow channels during boiling - Part II: Measurement of flow and enthalpy in two parallel channels. Technical Report BNWL-371 PT 2, Battelle Pacific Northwest Laboratories, Richland, Washington, USA, December 1967.

[95] D. S. Rowe and C. W. Angle. Cross-flow mixing between parallel flow channels during boiling - Part I: COBRA - Computer program for coolant boiling in rod arrays. Technical Report BNWL-371 PT 1, Battelle Pacific Northwest Laboratories, Richland, Washington, USA, March 1967.

[96] D. S. Rowe and C. W. Angle. Cross-flow mixing between parallel flow channels during boiling - Part III: Effect of spacers on mixing between two channels. Technical Report BNWL-371 PT 3, Battelle Pacific Northwest Laboratories, Richland, Washington, USA, January 1969.

[97] D. S. Rowe and C. C. Chapman. Measurement of turbulent velocity, intensity and scale in rod bundle flow channels containing a grid spacer. Technical Report BNWL-1757, Batelle Northwest Laboratories, Richland, Washington, USA, June 1973.

[98] D. S. Rowe, B. M. Johnson, and J. G. Knudsen. Implications concerning rod bundle crossflow mixing based on measurements of turbulent flow structure. *International Journal of Heat and Mass Transfer*, 17:407 − 419, 1974.

[99] D. S. Rowe, R. B. Macduff, and R. E. Collingham. Thermal hydraulic subchannel model based on void drift. In *Proc. Nat. Heat Transfer Conf.*, volume 1, pages 401 − 406, 1990.

[100] A. Rubin, A. Schoedel, M. Avramova, H. Utsuno, S. Bajorek, and A. Velazquez-Lozada. OECD/NRC Benchmark based on NUPEC PWR subchannel and bundle tests (PSBT). Technical report, NEA Nuclear Science Committee, 2010.

[101] Michio Sadatomi, Akimaro Kawahara, and Yoshifusa Sato. Flow redistribution due to void drift in two-phase flow in a multiple channel consisting of two subchannels. *Nuclear Engineering and Design*, 148:463 − 474, 1994.

[102] Michio Sadatomi, Akimaro Kawahara, and Yoshifusa Sato. Prediction of the single-phase turbulent mixing rate between two parallel subchannels using a subchannel geometry factor. *Nuclear Engineering and Design*, 162:245 − 256, 1996.

[103] Michio Sadatomi, Akimaro Kawahara, Keiko Kano, and Y. Sumi. Single- and two-phase turbulent mixing rate between adjacent subchannels in a vertical 2x3 rod array channel. *International Journal of Multiphase Flow*, 30:481 − 498, 2004.

[104] Michio Sadatomi, Keiko Kano, Akimaro Kawahara, and Naoki Mori. Void fraction and pressure drop in two-phase equilibrium flows in a vertical 2x3 rod bundle channel - as-

sessment of correlations against present subchannel data. *JSME International Journal*, 49:279 – 286, 2006.

[105] P. Saha and Novak Zuber. Point of net vapor generation and vapor void fraction in subcooled boiling. In *Proc. 5th Int. Heat Transfer Conference Vol. 4*, 1974.

[106] S. Sarkar and L. Balakrishnan. Application of a Reynolds-stress turbulence model to the compressible shear layer. Technical Report ICASE Report 90 - 18, 1990.

[107] Y. Sato. Cross flow of gas-liquid mixture between sub-channels. In *Sub-channel analysis in nuclear reators. Proc. of the Int. Seminar on Sub-channel Analysis ISSCA'92*, 1992.

[108] W. J. Seale. Turbulent diffusion of heat between connected flow passages - part 1: Outline of problem and experimental investigations. *Nuclear Engineering and Design*, 54:183 – 195, 1979.

[109] W. J. Seale. Turbulent diffusion of heat between connected flow passages - part 2 - predictions using the k-epsilon turbulence model. *Nuclear Engineering and Design*, 54: 197 – 209, 1979.

[110] Yue Fen Shen, Zi Dong Cao, and Qing Gang Lu. An investigation of crossflow mixing effect caused by grid spacer with mixing blades in a rod bundle. *Nuclear Engineering and Design*, 125:111 – 119, 1991.

[111] Byung Soo Shin and Soon Heung Chang. Experimental study on the effect of angles and positions of mixing vanes on CHF in a 2×2 rod bundle with working fluid R-134a. *Nuclear Engineering and Design*, 235:1749 – 1759, 2005.

[112] Joseph Smagorinsky. General Circulation Experiments with the Primitive Equations. *Monthly Weather Review*, 91:99 – 164, 1963.

[113] B. L. Smith, C.-H. Song, S.-K. Chang, J. R. Lee, and J. W. Kim. Report of the oecd/nea kaeri rod bundle cfd benchmark exercise. Technical report, OECD/NEA, July 2013.

[114] C.G. Speziale, S. Sarkar, and T.B. Gatski. Modelling the pressure-strain correlation of turbulence: an invariant dynamical systems approach. *Journal of Fluid Mechanics*, 227: 245 – 272, 1991.

[115] S. Sugawara and Y. Miyamoto. FIDAS - Detailed sub-channel analysis code based on the three-fluid model. *Nuclear Engineering and Design*, 120:147 – 161, 1990.

[116] W. Szablewski. Der Einlauf einer turbulenten Rohrströmung. *Ingenieur-Archiv*, 21:323, 1953.

[117] Yehuda Taitel, Dvora Bornea, and A. E. Dukler. Modelling flow pattern transitions for steady upward gas–liquid flow in vertical tubes. *AIChE Journal*, 26:345 – 354, 1980.

[118] A. Tapucu. Studies on diversion cross-flow between two parallel channels communicating by a lateral slot. *Nuclear Engineering and Design*, 42:297 – 306, 1977.

[119] Akio Tomiyama, Hidesada Tamai, Iztok Zun, and Shigeo Hosokawa. Transverse migration of single bubbles in simple shear flows. *Chemical Engineering Science*, 57:1849 – 1858, 2002.

[120] L. S. Tong. *Boiling Heat Transfer and Two-Phase FLow*. Wiley, 1966.

[121] A. A. Troshko and Y. A. Hassan. A two-equation turbulence model of turbulent bubbly flows. *International Journal of Multiphase Flow*, 27:1965 – 2000, 2001.

[122] A. C. Trupp and R. S. Azad. The structure of turbulent flow in triangular array rod bundles. *Nuclear Engineering and Design*, 32:47 – 84, 1975.

[123] Y. S. Tseng, Y. M. Ferng, and C. H. Lin. Investigating flow and heat transfer characteristics in a fuel bundle with split-vane pair grids by CFD methodology. *Annals of Nuclear Energy*, 64:93 – 99, 2014.

[124] Theodoor Van der Ros. *On two-phase flow exchange between interconnected hydraulic channels*. PhD thesis, Technische Hogeschool Eindhoven, November 1970.

[125] Veloso and Mistelberger. COBRA 3-CP: An improved version of COBRA-IIIC/MIT-2. Technical Report ST 112/86/e332, Siemens/KWU, November 1986.

[126] P. Venkateswararao, R. Semiat, and A. E. Dukler. Flow pattern transition for gas-liquid flow in a vertical rod bundle. *International Journal of Multiphase Flow*, 8:509 – 524, 1982.

[127] Th. Von Kármán. Mechanische Ähnlichkeit von Turbulenz. *Nachrichten von der Gesellschaft der Wissenschaften zu Göttingen*, 5:58 – 76, 1930.

[128] V. Vonka. Measurement of secondary flow vortices in a rod bundle. *Nuclear Engineering and Design*, 106:191 – 207, 1988.

[129] Wolfgang Wagner and Alfred Kruse. *Properties of water and steam - The industrial standard IAPWS-IF97 for the thermodynamic properties and supplementary equations for other properties*. Springer Verlag Berlin, 1998.

[130] G. B. Wallis. *One-Dimensional Two-Phase Flow*. McGraw-Hill, 1969.

[131] D. C. Wilcox. *Turbulence Modeling for CFD*. DCW Industries, Inc., 1998.

[132] Sun Kyu Yang and Moon Ki Chung. Spacer grid effects on turbulent flow in rod bundles. *Journal of the Korean Nuclear Society*, 28(1):56 – 71, February 1996.

[133] Sun Kyu Yang, Heung June Chung, Se Young Chun, and Moon Ki Chung. Measurements of turbulent flow in 5x5 PWR rod-bundles with spacer grids. *Journal of the Korean Nuclear Society*, 24:263 – 273, 1992.

[134] Arto Ylönen, Wilhelm-Martin Bissels, and Horst-Michael Prasser. Single-phase cross mixing measurements in a 4x4 rod bundle. *Nuclear Engineering and Design*, 241:2484 – 2493, 2011.

[135] Arto Ylönen. *High-resolution flow structure measurements in a rod bundle*. PhD thesis, ETH Zürich, 2013.

[136] Novak Zuber. On the dispersed two-phase flow in the laminar flow regime. *Chemical Engineering Science*, 19:897 – 917, 1964.

[137] Novak Zuber, F. W. Staub, and G. Bijwaard. Vapor void fraction in subcooled boiling and in saturated boiling systems. In *Proceedings of the 3rd International Heat Transfer Conference*, 1966.